Development and Application of an Eulerian Density Function Methodology coupled to Flamelet Progress Variable Approach for the Simulation of Oxyfuel Combustion

Dem Fachbereich Maschinenbau
an der Technischen Universität Darmstadt
zur
Erlangung des Grades eines Doktor-Ingenieurs (Dr.-Ing.)
genehmigte

Dissertation

vorgelegt von

Dip.Ing. Rihab Mahmoud

aus Gafsa/Tunesien

Berichterstatter:	Prof. Dr-Ing. Amsini Sadiki
Mitberichterstatter:	Prof. Dr-Ing. Andreas Dreizler
Mitberichterstatter:	Prof. Dr-Ing. Benoît Fiorina
Tag der Einreichung:	11.08.2020
Tag der mündlichen Prüfung:	01.12.2020

Darmstadt 2020

D17

Mahmoud, Rihab: Development and Application of an Eulerian Density Function Methodology coupled to Flamelet Progress Variable Approach for the Simulation of Oxyfuel Combustion,
Darmstadt,Technische Universität Darmstadt,
Jahr der Veröffentlichung der Dissertation auf TUprints: 2021
Tag der mündlichen Prüfung: 01.12.2020

Erklärung

Hiermit erkläre ich, dass ich die vorliegende Arbeit, abgesehen von den in ihr ausdrücklich genannten Hilfen, selbständig verfasst habe.

Datum, Unterschrift

Acknowledgements

The research presented in this dissertation is the result of my time as doctoral candidate within the European CLEAN-Gas project. The main part of the work was carried out at the Institute of Energy and Power Plant Technology (currently merged in Reactive Flows and Diagnostics institute), at the Technical University of Darmstadt. Therefore, I would like to express my sincerest gratitude to Prof. Dr.-Ing. Johannes Janicka, the former head of the institute, and my advisor Prof. Dr. rer. Amsini Sadiki for the great opportunity to be part of their research team.

I am particularly grateful to Prof. Dr. rer. Amsini Sadiki for the confidence placed in me from the very beginning when he invited me to pursue my Ph.D under his guidance. With his vast experience and knowledge, he was constantly encouraging and helping me with great scientific advice. In addition, Prof. Sadiki was always understanding and supportive advisor specially during my pregnancy and post birth periods when my productivity had decreased. I am glad to be one of his Ph.D students.

During my 11 month-secondment at the Macroscopic Molecular Energy and Combustion Laboratory (EM2C) of CentraleSupélec at the University of Paris-Saclay, another part of my thesis has been achieved under the co-guidance of Prof. Benoît Fiorina. Hence, I would like to sincerely express my deepest gratitude to him for his great contribution to my studies especially through his valuable advice and remarks during the weekly seminars that were held at the institute.

I would like to sincerely thank Prof. Dr.-Ing. Andreas Dreizler the head of the Reactive Flows and Diagnostics institute for accepting to be a reviewer and a potential member of the disputation committee. I deeply thank Prof. Alessandro Parente and Prof. Alberto Cucio from University libre de Bruxelles and Politecnico di Milano, respectively, for accepting to review my thesis work. I would like also to thank Prof. Ronan Vicquelin from the University of Paris-Saclay for accepting my invitation to be a potential member in the disputation committee.

I am deeply grateful for Prof. Dr. rer. nat. Michael Pfitzner for his significant contribution to this thesis by sharing the first version of the reacting solver (*FPVFoam*). Moreover, I have benefited from intensive discussions with him and his research team during my short visits to the Thermodynamic Institute.

Within the different research stays kindly encouraged by the CLEAN-Gas project, I had the opportunity to visit Dr. Mehdi Jangi and his research team at the university of Birmingham, UK. I am indebted to him as he was intensively involved in the cooperation with TU Darmstadt. Only with his valuable contribution I could achieve most simulation parts where he showed great physical and mathematical knowledge during the numerical

implementations.

Special thanks to my former supervisors in Tunisia: Pr. Mouldi Chrigui and Dr. Ammar Hidouri who taught me the first steps towards the numerical combustion.

I would further like to thank all my colleagues at the L1|08 building (RSM/EKT). Among them I would like to thank my office-mates: Henriette, Martin, Alija, Florian Z. and Pascal, for the great working atmosphere that we shared and for the good enriching discussions specially with Alija. My gratitude also goes to Florian R. who introduced me to the OpenFOAM world and intensively helped me with his ready answers for all my questions. I would like to thank Pedro, Mary, Flavia and Agnes for their friendship during this time in Germany/France and also my colleagues in Tunisia (Hassan and Nesrine) for memorable moments we had shared together. I thank also my friend Senda who deeply encouraged me during the defense preparation weeks.

The main gratitude goes to my family. I would like to deeply thank my parents Bahija and Said for their endless love and confidence in me. They have been constantly supportive and encouraging. I enormously thank my sweet sister and brothers for their endless care and support. Very special thanks to my dear husband Soufiane who believed in me and motivated me to complete this work and never give up.

Rihab Mahmoud
Darmstadt, August 2020

Dedicated to
Yanis.

List of Publications

The content of this work is partly based on the publications listed below which have been published during the PhD project.

1 Journal Publications

[**P1**] R. Mahmoud, M. Jangi, B. Fiorina, M. Pfitzner, A. Sadiki, Numerical Investigation of an Oxyfuel non-premixed combustion using a Hybrid Eulerian Stochastic Field/Flamelet Progress Variable approach: Effects of H2/CO2 enrichment and Reynolds number, *Energies* 11 (2018) 3158.

[**P2**] R. Mahmoud, M. Jangi, F. Ries, B. Fiorina, J. Janicka, A. Sadiki, Combustion Characteristics of a Non-Premixed Oxy-Flame Applying a Hybrid Filtered Eulerian Stochastic Field/Flamelet Progress Variable Approach, *Applied Sciences* 9 (2019) 1320.

2 Conference Publications

[**P3**] M. Jangi, R. Mahmoud, A. Sadiki, J. Wen, A Hybrid Eulerian Stochastic Field/Flamelet Progress Variable approach for Large Eddy Simulations of LNG pool fires, *11th Mediterranean Combustion Symposium (MCS11)* (2019).

[**P4**] R. Mahmoud, M. Jangi, B. Fiorina, A. Sadiki, Hybrid Flamelet Progress Variable tabulated chemistry approach/Eulerian Stochastic Field method for non-premixed Oxy-fuel jet flame, *17th International Conference on Numerical Combustion* (2019).

[**P5**] Z. Li, R. Mahmoud, A. Sadiki, A. Parente, Numerical Investigation of Lifted Turbulent Flame with PASR and FPV models, *12th International ERCOFTAC Symposium on Engineering Turbulence Modelling and Measurements* (2018).

[**P6**] R. Mahmoud, A.S. Doost, F. Ries, S. Bürkle, A. Sadiki, and J. Janicka, Large Eddy Simulation of Complex Flow in Combustion Chamber and Residence Time Distribution Calculation, *International Congres on materials and energy (CIMATEN)* (2016).

Contents

List of Figures

List of Tables

Nomenclature

This nomenclature summarizes the variables used in this work, while those that are locally employed are not included.

Upper case latin letters		**Unit**
A^a	Pre-exponential constant of the Arrhenius law	$*$
$A^a_{fr/br}$	Constant of the Arrhenius law for forward/backward reaction	$*$
C_s	Smagorinsky coefficient	$*$
C_ζ	Micro-mixing constant	$-$
$\mathcal{D}$	Diffusion number	$-$
$\mathcal{D}_\alpha$	Diffusion coefficient of the component α	$\mathrm{m^2\,s^{-1}}$
$\mathcal{D}_\Phi$	Diffusion coefficient of scalar Φ	$\mathrm{m^2\,s^{-1}}$
dW_i^n	n^{th} vector Wiener term in direction i	$\mathrm{s^{0.5}}$
E^α	Activation energy	$\mathrm{J\,mol^{-1}}$
G	Low-pass spatial filtering operator	$\mathrm{m^{-3}}$
$\widetilde{G}_k$	Production of turbulent kinetic energy	$*$
$J_{i\alpha}$	Mass flux vector of species α	$\mathrm{Kg\,m^2s}$
L	Characteristic length scale	m
$\mathcal{M}$	Molar mass of the mixture	$\mathrm{kg\,kmol^{-1}}$
$\mathcal{M}_\alpha$	Molar mass of the species α	$\mathrm{kg\,kmol^{-1}}$
N_r	Number of reactions	$-$
N_s	Number of stochastic fields	$-$
N_α	Number of species α	$-$
$N(0,1)$	Random number with normal distribution	$-$
$\mathcal{P}(\Phi)$	Probability density function of the variable Φ	$-$
$\overline{P}$	Modified pressure within the LES	Pa
$\mathcal{R}$	Perfect gas constant	$\mathrm{J\,kmol^{-1}K^{-1}}$
S	General surface	$\mathrm{m^2}$
S_{f_i}	Specific flat surface	$\mathrm{m^2}$

S_{ij}	Rate-of-strain tensor	s^{-1}
T	Temperature	K
$\mathcal{U}$	Characteristic velocity	$\mathrm{m\,s}^{-1}$
V	General volume	m^3
Y_α	Mass fraction of the species α	–
$\mathcal{Z}_k$	Element mass fraction of the element k	–

Lower case latin letters		**Unit**
a	strain rate	s^{-1}
c_p	Isobaric specific heat capacity of the mixture	$\mathrm{J\,kg}^{-1}\mathrm{K}^{-1}$
c_α	Concentration of species α	$\mathrm{mol\,m}{-}3$
d_i	Distance between two cell center points	m
d	General diameter	m
f	Mixture fraction	–
f_l	Flame length	m
g_i	Acceleration of gravity into direction i	$\mathrm{m\,s}^{-2}$
h	Specific enthalpy of the mixture	$\mathrm{J\,kg}^{-1}$
h_α	Specific enthalpy of the species α	$\mathrm{J\,kg}^{-1}$
k	Turbulent kinetic energy	$\mathrm{m}^2\,\mathrm{s}^{-2}$
k_f, k_b	Rate coefficient of forward/backward reaction	$*$
l	Turbulent length scale	m
l_I	Integral length scale	m
l_η	Kolmogorov length scale	m
m_α	Mass of the species α	kg
p	Pressure	$\mathrm{kg\,s}^{-2}\mathrm{m}^{-1}$
p^{ref}	constant reference pressure	$\mathrm{kg\,s}^{-2}\mathrm{m}^{-1}$
pv	Reaction progress variable	–
q_i	Energy flux in direction i	$\mathrm{J\,m}^2\mathrm{s}$
r_f, r_b	Reaction rate of the forward/backward reaction	$\mathrm{mol\ m}^{-3}\mathrm{s}^{-1}$
s_l	Laminar flame speed	m
t	Time	s
t_s	Simulation time step	s
u_i	Velocity in direction i	$\mathrm{m\,s}^{-1}$
x_i (x, y, z)	Cartesian coordinates	m

Upper case greek letters		**Unit**
Δ	Filter width	m
Δ_f	Mixture fraction range	–

Δt	Time step size	s
Δx	Grid size	m
Φ	General scalar	$*$

Lower case greek letters

		Unit
δ_{ij}	Kronecker-symbol	–
ε	Dissipation of the turbulent kinetic energy	$\mathrm{m^2\,s^{-3}}$
υ	Wave number (in the energy spectrum)	$\mathrm{m^{-1}}$
λ	Thermal conductivity	$\mathrm{W\,m^{-1}\,K^{-1}}$
μ	Dynamic viscosity	$\mathrm{kg\,s^{-1}\,m^{-1}}$
μ_{eff}	effective dynamic viscosity	$\mathrm{kg\,s^{-1}\,m^{-1}}$
μ_{t}	Turbulent dynamic viscosity	$\mathrm{kg\,s^{-1}\,m^{-1}}$
ν	Kinematic viscosity	$\mathrm{m^2\,s^{-1}}$
ν_{t}	Turbulent kinematic viscosity	$\mathrm{m^2\,s^{-1}}$
ν'_α	Stoichiometric coefficient of species α on the reactant side	–
ν''_α	Stoichiometric coefficient of species α on the product side	–
ξ^n_α	n^{th} stochastic field of the species α	–
π	Number pi	–
ρ	Density of the mixture	$\mathrm{kg\,m^{-3}}$
τ_c	Chemical time scale	s
τ_f	Diffusion time scale	s
τ_t	General time scale	s
τ_η	Kolmogorov time scale	s
τ_{ij}	Components of the viscous stress tensor	$\mathrm{kg\,s^{-2}\,m^{-1}}$
ϕ	Equivalence ratio	–
χ	Scalar dissipation rate	$\mathrm{s^{-1}}$
χ_α	General species	–
ψ_α	Sample space for species α	–
$\dot{\omega}_\alpha$	Chemical source term for species α	$\mathrm{kg\,m^{-3}\,s^{-1}}$
$\dot{\omega}_\Phi$	General chemical source term of the component α	$\mathrm{kg\,m^{-3}\,s^{-1}}$

Indices

$\cdot_c$	Co-flow
$\cdot_f$	Fuel
$\cdot_{max}$	Maximum
$\cdot_{norm}$	Normalized value
$\cdot_O$	Oxidizer

$\cdot_{rms}$	Root mean square
$\cdot^{sgs}$	Subgrid-scale
$\cdot_{st}$	Stoichiometric conditions
$\cdot_{T}$	Turbulent
$\cdot_{P}$	Value at point P

Operators

$\bar{\cdot}$	Spatial filter (LES) or temporal average (RANS)
$\tilde{\cdot}$	Density weighted filtered/averaged value

Dimensionless numbers

Da	Damköhler number
Ka	Karlovitz number
Le	Lewis number
Le_{α}	Lewis number of species α
Ma	Mach number
Re	Reynolds number
Re_t	Turbulent Reynolds number
Re_c	Critic Reynolds number
Sc	Schmidt number
Sc_{α}	Schmidt number of the species α

Abbreviations

BP	British Petroleum company
CFD	Computational fluid dynamics
CFL	Courant-Friedrichs-Lewy (courant number)
CSSA	Correlation set by simulated annealing
DNS	Direct numerical simulation
EMST	Euclidean minimum spanning tree
ESF	Eulerian stochastic field
FGM	Flamelet generated manifolds
FPI	Flame prolongation of intrinsic low-dimensional manifolds
FPV	Flamelet progress variable
FVM	Finite volume method

IEA	International Energy Agency
IEM	Interaction by exchange with the mean
ILDM	Intrinsic low-dimensional manifolds
IPCC	Intergovernmental Panel on Climate Change
LES	Large eddy simulation
LMSE	Linear mean-square estimation mixing model
MPI	Message passing interface
PDF	Probability density function
PISO	Pressure Implicit with Splitting of Operator
RANS	Reynolds averaged Navier Stokes
RQL	Rich-Quench-Lean
SDE	Stochastic differential equation
SIMPLE	Semi-implicit method for pressure-linked equations
SLF	Steady laminar flamelet
SMLD	Statistically most likely distribution
TNF	International Workshop on Measurement and Computation of Turbulent Non-premixed Flames
TPDF	Transport Probability density function

Chapter 1

Introduction

Being one of the most essential technologies in the modern civilization, the combustion process has been generally described as a fast exothermic reaction where besides flames, consequential amount of energy as heat is released. Since the beginning of industrialization, this combustion thermal energy has been converted into mechanical energy serving for multitude of necessities intending to improve the increasing living standards and to respond to the modern industry requirements. To this day, the combustion of fossil fuels has gained an important role in a sustainable energy framework covering mostly the global energy demand. The combustion processes comprise approximately 82% of the global primary energy consumption according to the recent BP's statistical review of world energy [13] as depicted in Figure 1.1. With the continuous evolution of the industrialized world and the remarkable growth of population, the demand for energy that depends on the fossil fuel combustion is largely rising specially for electricity and transportation sectors. Consequently, the global energy consumption which has doubled since 2010, will be more increasing with 1.3% each year in the next two decades as stated by the International Energy Agency (IEA) [74]. Unfortunately, this trend is profoundly related to many issues.

The first problem is connected to the fossil fuel resources which are considered limited and not renewable. With the high rate of energy consumption, these resources are expected to be entirely depleted within decades. According to the last BP's statistical review (2019) [13], the production of coal may last for about 115 years while both crude oil and natural gas supply may held for approximately only 51 years. Consequently, the modern industrialization is gradually directed to the usage of renewable energy sources. The most common examples involve wind, solar energy, geothermal, biomass and hydro power. However, electricity generated from the renewable energy supplies is completely dependent on weather conditions which is considered a big challenge to satisfy the global energy demand. Additionally, generating some types of renewable energies is strongly linked to combustion, like the bio-fuels production.

The second issue is related to the undesirable effect of some of the combustion products. Fossil fuels combustion produces pollutants such as carbon monoxide (CO), carbon dioxide (CO_2), nitric oxides (NO_x) and other unburnt substances (UHC) released into the atmosphere. These discharged gases which degrade dramatically the air quality, present a huge threat not only to human health, plants and animals but also to the global climate. Among several greenhouse gases (GHG), the CO_2 is considered the major heat-trapping

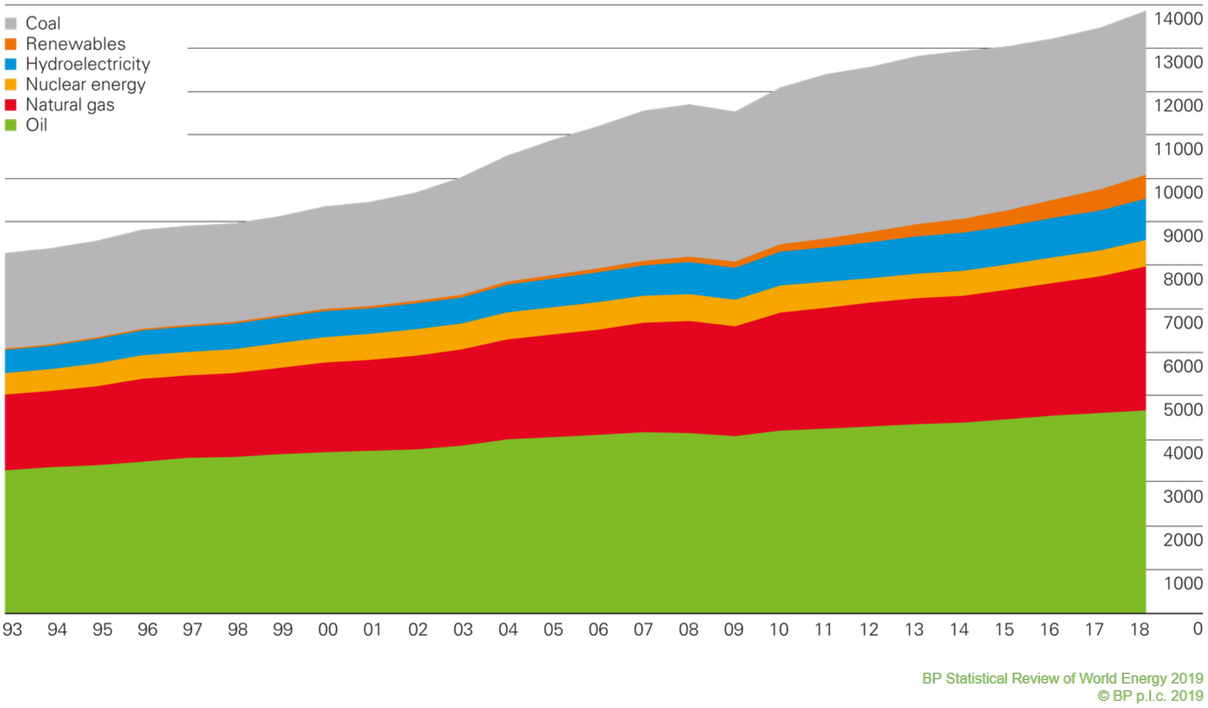

Figure 1.1: Primary energy world consumption in 2019 (million tonnes oil equivalent)[13].

gas that contributes to the global warming. The continuous increase of these gases concentrations lead to several hazardous effects such as the increase of global mean temperatures, the rise of sea level, numerous droughts and floods, wildfire and other undesired consequences for the ecosystem [48; 141]. These emissions are mainly released through human industrial activities because of the large growth in the energy consumption. The IEA expected in the CO_2 Status Report (2019) that "Global energy-related CO2 emissions grew 1.7% in 2018 to reach a historic peak of 33.1 Gt CO2 which was 70% higher than the average increase since 2010" [13]. Therefore, international agreements with various goals have been set recently in order to scale down the level of CO_2 and other polluting gases emissions.

In this context, the carbon capture and storage (CCS) plays an important role as an accepted energy strategy for increasing the efficiency of fossil fuel combustion and the development of sustainable energy from its application. Within the CCS process, the CO_2 released from fossil fuel power plant is initially separated to be captured and compressed to liquid form. Then, it follows several transport systems to be injected and stored in suitable and permanent underground sites. The storage systems are generally composed of geological formations (saline reservoir or depleted oil and gas fields)[1]. In comparison with renewable energy technology costs, the implementation expenses of CCS systems are less expensive [17]. Thereby, many efforts have been made to apply and improve the CCS technologies. The IPCC estimates that by 2040 more than 70% of electrical energy remain produced from power plants where CCS systems are implemented [75].

Depending on the industrial process under consideration, several options have been suggested and currently employed to capture and store the CO_2 released gas. The methods are post-combustion capture, pre-combustion capture and oxy-fuel combustion (during-combustion process) [99]. In the first method, a specific chemical process is followed where an appropriate solvent is used in order to separate the CO_2 from the flue gas. For the pre-combustion method, the fuel is transformed to syngas (mixture of carbon monoxide and hydrogen) where the CO is converted to CO_2 to be later captured, while the H_2 is used for heat production. Although these technologies are suited to various applications, they are considered expensive and challenging CO_2 capture options [17].

In the oxy-fuel combustion, the fossil fuel is burned with free-nitrogen oxidizer by replacing the air with oxygen enriched environment or pure oxygen. The obtained flue gas is composed essentially of CO_2 and H_2O, from which CO_2 can be easily captured, stored or recycled [99; 106; 172]. Based on various significant benefits over other conventional combustion systems, the oxy-combustion technology has been notably developed. This combustion technology contributes primarily in the reduction of nitric oxides (NO_x) pollutants gas emissions since reactions are occurring within free-nitrogen atmosphere. Additionally, compared to other CCS methods, old fuel power plants with oxy-fuel combustion can be retrofitted for CO_2 capture with better efficiency and lower implementation costs. Moreover, the other advantage of this method is the capability to control the flames temperature, structure and heat transfer fostering oxy-fuel combustion to be largely applied in high thermo-chemical processes with faster chemical reaction and burning velocity. In fact, the flame temperature control is mainly achieved by adding the recycled CO_2 as a diluent in the oxidizer stream to vary the O_2 level [172].

Given the significant importance of gas fuel combustion and specifically the challenging changes concerning the traditional combustion environment, it is mandatory to deepen the understanding of the combustion process under oxy-fuel conditions in order to better describe flow properties, the flame stability and the flame structure, among others. In this regard, experimental and numerical methods are the common used tools to develop and optimize the efficiency of combustion related systems. Most advanced measurement techniques can largely contribute to the understanding of combustion phenomena by providing accurate experimental results. However, prototype experiments are generally high priced and encounter measurement limitations due to inaccessibility or critical conditions of studied flows which may require longer construction time line. Additionally, not all quantities of interest can be reproduced. Therefore, numerical simulations of combustion systems offer a great potential in this respect. The computational Fluid dynamics (CFD) technique presents several benefits: It needs relatively lower costs and shorter development phase. Furthermore, multiple parametric studies and design analysis can be carried out without limitations within state of the art CFD codes.

1.1 State of Research

Most of combustion technical applications deal with turbulent flows in order to increase the mixing mechanism and consequently the efficiency of the process in question. On the other hand, the chemical reactions involving the temperature rise change the density and affect the flow itself. Therefore, aside of mass and heat transfer (including radiation), the coupling between turbulence and chemistry plays a crucial role in combustion based energy systems. Due to the multi-scale character of the phenomena in space and time [132], combustion appears as a challenging task for numerical predictions where the uncertainties in model performance is complicated by the interactions between turbulence and chemistry. These interactions have not been addressed sufficiently yet for oxy-combustion due to the weaknesses of the models involved and limitations on computational time.

For turbulence properties prediction, Direct Numerical Simulation (DNS) is one of the CFD numerical methods in which the underlying equations are numerically calculated solving the whole range of spatial and temporal scales without including modeling approaches. Although DNS results are accurate and considered as references, the method is significantly expensive in terms of computational effort. The second method is the Reynolds Averaged Navier-Stokes based approach (RANS) which presents the state of art of industrial applications. It emerges as the compromise between acceptable results and computational costs. However, very fine details of complex turbulent flow can not be predicted using RANS method since all reacting-flow scales are rather modeled.

During the last four decades, the Large Eddy Simulation (LES) approach has emerged as the appropriate alternative for simulating reacting turbulent flows [152]. Within LES models, large flow eddies are classically separated from small ones by means of filtering. Consequently, large structures are explicitly calculated taking account for unsteady effects, while the influence of sub-grid turbulent structures are modeled. Although LES requires more computational effort than RANS models, it provides more accurate results and can be combined with combustion approaches. Further, LES shows great potential as a robust approach combining accuracy and efficiency. It was initially introduced by Smagorinsky [157] in order to suggest a new mathematical approach to describe the meteorologic flow phenomena. Later, the model was exploited by Lilly [102] and Deardorff [28]. Recently, the LES approach has been employed as well to part of industrial applications as computing resources capacities have been increased.

Nevertheless, with both RANS and LES approaches, numerical investigations of industrial-scale combustion systems are considered complex and computationally expensive, in particular for the case of oxy-fuel combustion applications [50]. Therefore, studying laboratory-scale burners presents the large trend for most of research activities including model development and numerical validation [93]. In this aspect, multiple generic configurations have been properly designed and experimentally investigated in the framework of the *'International Workshop on Measurement and Computation of Turbulent Non premixed Flames'* (TNF) [163]. The main goal of the TNF workshop is to provide valuable observations and quantitative results which significantly contribute to enrich reference data bases and consequently can be further employed for modeling validation.

Additionally to the outlined turbulence methods, the chemistry has to be considered by employing appropriate combustion modeling which allows to take into account the range of scales ensuing from turbulence, chemistry interaction (TCI) and to handle consequently the different arising unclosed terms. Divers research groups have been developing and improving numerical methods to study the effect of TCI within RANS and LES contexts. Available models such as the eddy-breakup (EBU) model and Eddy-Dissipation-Concept

(EDC) model are widely used in commercial CFD codes, but cannot capture TCI effects adequately without ad-hoc tuning. Eddy-break-up and eddy-dissipation models are usually used with the assumption of infinitely fast chemistry (mixing controlled). Occasionally, they have been applied with one step or two-steps global chemical mechanisms. When finite-rate chemistry is important (e.g., for CO, NO_x predictions, flames with intermittency), the EDC model is usually used [151]. However, in an environment where interactions between turbulence and chemistry are unknown, the ad-hoc parameter-tuning models are not ideal candidates. Other turbulent combustion models, such as laminar flamelet model, conditional moment closure, and one-dimensional turbulence models are then used as described in [123; 133]. However, in view of the reported limitations of these models the transported PDF models are getting more and more important. A detailed review of this research state will be provided below where the focus will lie on non-premixed turbulent combustion evolving in laboratory-scale burners (see section 4.2).

In order to consider the chemistry within both RANS and LES frameworks, the integration of the required chemistry equations needs special care aiming to reduce the overall computational effort related with detailed chemistry computations that are essential for fully describing the evolving chemical process [107]. Accordingly, many combustion models that are in conjunction with specific chemical mechanism reductions and chemistry tabulation techniques have been suggested and employed to reproduce most important flame properties. These approaches are currently accessible in the literature and widely utilized [44; 125; 152]. A very popular approach for non-premixed combustion calculations is the flamelet method. The common idea behind flamelet models is to separate the numerical solution of the turbulent flow and mixture fields from that of the chemistry [123]. As one of the conserved scalar methods, transport equations for the moments of a conserved variable are solved when applying the flamelet approach. The conserved variable is chosen such that it describes the local mixture and is therefore called the mixture fraction. Turbulent mean/filtered values of the mass fractions of chemical components can then be calculated by using a PDF of the mixture fraction. Besides the PDF, the only requirement of the model is that there exists locally a unique relation between the mixture fraction and all scalar quantities like the species mass fractions and the enthalpy.

In the context of tabulated chemistry strategies, most applied methods in different numerical investigations include ILDM (Intrinsic Low Dimensional Manifold) as explained in [104], REDIM (Reaction-Diffusion Manifold) which is the extension form of ILDM as stated in [18], FPV (Flamelet/Progress variable) as first introduced by Pitsch et al. in [129] and Pierce and Moin in [125] proposing the unsteady form of the FPV approach, FGM method (Flamelet Generated Manifold) as explained in [115] and F-TACLES (Filtered tabulated chemistry for LES) for which detailed description of the approach is given in [44; 167]. By applying the mentioned techniques for simulating turbulent combustion systems, generated chemical tables are coupled either to RANS- or to LES-based CFD codes.

Focusing on the Flamelet/Progress Variable method which is adopted in this study, the two pre-selected controlling variables of the chemical table are the mixture fraction and the reaction progress variable when adiabatic flames are considered. This chemistry reduction technique can be extended with additional table controlling parameters, for example with enthalpy or temperature to account for heat transfer in non adiabatic flames [88]. In the FPV approach, the equation system is significantly reduced where only the transport equations of the table controlling variables are added to the classical governing equations in single phase reacting flow cases (see [58; 72; 106; 125; 143]). The FVP-based combustion model has been widely applied, especially for methane/air jet flame Sandia D within many studies (e.g. [38; 73; 85; 143]) and for predicting the extinction phenomena in piloted jet flames E and F [72].

In the context of oxy-fuel combustion, several advanced techniques have been assessed and employed but very few contributions using the FPV technique have been documented in the literature. One of early turbulent investigations integrating the FPV approach in the LES framework has been reported in [58] where it was revealed the great potential of the FPV approach in addressing differential diffusion issues in the reacting turbulent regimes under study. However, the application of tabulated chemistry reduction methodology calls for assumptions concerning the flame structure along with the statistical turbulence-chemistry interaction phenomena. Therefore, a probability density function (PDF) of the table controlling variables is usually employed for this purpose.

Mainly two approaches are introduced in the literature in order to describe the PDF [132; 133]. The first method is based on the assumption of a presumed shape of the PDF on each cell in RANS framework and on the sub-grid level of each cell in the LES context. In this context, different numerical studies have been reported where presumed PDF is applied in conjunction with FPV approach and a common shape assumption for the mixture fraction following the so-called β-function is used [58; 60; 72; 73; 125]. However, the aforementioned presumed PDF calls generally to account for statistical independence between single PDF which is not correct. Furthermore, the chemical source term is described in an unclosed form and need to be modeled.

Therefore, the second method which is adopted in this work is considered as more sophisticated and efficient alternative. It determines the PDF by solving a transported probability density function (T-PDF) equation [134]. This method has been applied in several studies, for example in [62; 78; 79; 110; 111; 135]. Transporting the PDF equations is based on two major formulations that have been introduced in the literature, namely the Lagrangian Monte-Carlo as reported in [93; 139] and the Eulerian based approach as the cases in [111; 140]. In the current work, the Eulerian stochastic field (ESF) methodology is utilized. According to Valińo et al. in [165] and Sabel'nikov et al. in [148], the solution of the stochastic differential equation in turbulent reacting flow is defined by using multiple smooth stochastic fields for each control variable to describe the PDF undergoing diffusion, turbulent convection and chemical reaction. These stochastic fields (SFi) are continuous and differentiable in space which make the ESF methodology as one attractive technique to model the PDF equations (see [82; 84]). Moreover, by employing the ESF method, the chemical source term appears in a closed form. In this study, the ESF method is essentially coupled to the reduced chemical mechanism according to the FPV approach since it is revealed that the choice of the chemical mechanism methods has an enormous effect in terms of computational requirements [4].

The wide range of ESF numerical investigations have been extended from jet flames in air environment [79; 84] to bluff body flames [93]. However, no oxy-combustion studies have been reported yet. Hence, the current study presents for the first time numerical investigations where the FPV/ESF combustion model in the context of both RANS and LES turbulent models is applied in order to investigate non-premixed oxy-flames.

1.2 Objectives

The present work aims at the development and the application of an advanced numerical approach for the simulation of oxy-fuel combustion in which the TCI is adequately accounted for within non-premixed combustion regimes using the OpenFOAM platform. The suggested model which is designed for both RANS and LES applications, consists of a combination of a transported probability density function approach following the Eulerian Stochastic field methodology and the flamelet progress variable (FPV) chemistry reduction mechanism. In the LES framework, the proposed method accurately represents the effect of the sub-grid fluctuations on the flame structure and on combustion characteristics along with the interaction between turbulence and chemistry.

The implemented developed combustion model is first verified, validated and then applied to different turbulent non-premixed combustion configurations featuring an increasing order of complexity. In particular, Sandia flame D which consists of a turbulent piloted methane-air jet flame [127], is first employed for model validation in both RANS and LES contexts. The next flames are more challenging cases, namely the non-premixed Sandia oxy-flame series (A & B), which are operated under different *Re* numbers and characterized by various CO_2 and H_2 enrichments in the oxidizer and fuel streams, respectively [154]. All investigated cases are well documented with available experimental measurements.

The objectives of this work can be summarized as follows:

- Development and implementation of the Eulerian Stochastic Field combustion model in conjunction with the flamelet progress variable (FPV) approach. This combination with the FPV chemistry reduction technique is essentially applied to reduce the computational effort required. The resulting model is referred as hybrid ESF/FPV method.

- Verification of the hybrid ESF/FPV method in one-dimensional laminar flame. The results are compared to solutions of detailed chemistry.

- Validation of the combustion model by simulating the well-known Sandia flame D within RANS and LES contexts, respectively.

- Application of the novel method to relatively more complex and challenging cases of oxy-fuel flame series (A & B). The prediction capability of the combustion model in reproducing main oxy-flame properties is evaluated and the influence of some operating conditions on the combustion characteristics is analyzed.

1.3 Thesis Outline

Aside from this introduction, the thesis consists of 7 chapters that are structured as follows:

Chapter 2 outlines the basic theoretical background and mathematical description of turbulent flows. The main turbulent flow properties are presented, and different modeling approaches are described. The fundamental governing equations are derived and listed in the context of LES and RANS modeling, respectively.

Chapter 3 provides the fundamentals of combustion. Mathematical description and basic theoretical concepts are discussed. General chemical reaction kinetics and reaction mechanisms are explained, and different flame modes are introduced. The FPV chemistry reduction technique is described to provide more insights on chemical table generation.

Chapter 4 discusses the interaction between turbulence and combustion with the description of different regime diagrams of turbulent combustion. It outlines the different techniques for coupling chemistry reduction methods with CFD turbulent flow code. In particular, the Eulerian Stochastic field (ESF) approach coupled to FPV technique is first introduced and deeply described.

Chapter 5 consists on presenting the different numerical approaches involved in the implementation of the suggested hybrid ESF/FPV model. Thereby, general solution procedure including the overall solution of the solver is outlined. In order to first assess the implemented method, a simple one-dimensional verification test is performed, and obtained results are compared to solutions of detailed chemistry.

Chapter 6 investigates the jet-flame Sandia D as a validation case. For this purpose, simulations are carried out within RANS and LES frameworks, respectively. The appraisal of the model is achieved by means of comparison between experimental data and numerical results. In particular, comparisons of RANS simulations using 2D and 3D computational domains are reported for future use.

Chapter 7 deals with the application of the validated ESF/FPV approach to complex oxy-fuel flame series. The simulations of these flames are performed within RANS and LES contexts and obtained results are compared to available measurements. Thereby the capability of the novel combustion model in predicting turbulent flame properties is assessed. The significant effects of different operating conditions on the oxy-combustion properties are then analyzed and quantified by means of RANS only for saving the computational costs.

Chapter 8 summarizes the main concluding remarks of the current numerical study and suggests an outlook on how to improve and further develop the implemented turbulent combustion model.

Chapter 2

Description and Modeling of turbulent flows

The current chapter provides the essential theoretical background to describe the turbulent fluid flows. In the first part, the physics of turbulent flows are stated along with fundamental governing equations based on law-conservation of transported equations. The second section provides the properties of turbulent flows corresponding to time and length scales of flow and scalars, and also an overview of the energy spectrum. In the third section of this chapter, different numerical approaches allowing the understanding and prediction of the behavior of turbulent flows are listed and described. More details on the numerical description of turbulent flows that would go beyond the scope of this work can be found in these books [49; 56; 132].

2.1 Fundamental Governing Equations

In the present work, compressible, Newtonian Fluids flows are derived exclusively from a macroscopic point of view following Euler's approach. This means that instead of identifying individual particles of the fluid, large discrete control volumes are designated to describe the contained fluid by means of macroscopic quantities, such as velocity, temperature, pressure, density and other properties. Numerically, with the change of time, the considered flows can be described using the partial differential conservation equations for mass, momentum, species transport and energy, known as the Navier-Stokes equations. Their introduction is the subject of this section where most of the notations used are in agreement with Poinsot and Veynante [130], however detailed derivation of the Navier-Stokes equations can be found in these books [2; 132; 162].

It is necessary to specify that all of this work was done with pressure based solvers treating applications with only weakly compressible flows where Mach numbers $\mathcal{M}a$, defined as the ratio of the speed of the flow to the speed of sound, do not reach 0.3. Hence, due to the typically low Mach numbers in combustion chambers, the system of equations used is rigid and preconditioning methods are sometimes required in order to be able to solve the flow equations efficiently.

Thereby the transported equations, presented in coming sections, will follow the derivation operator below, reading:

$$\frac{D}{Dt} = \frac{\partial}{\partial t} + u_i \frac{\partial}{\partial x_i}. \tag{2.1}$$

2.1.1 Conservation of Mass

In accordance with the mass conservation law, mass cannot be generated or destroyed. Within the mass conservation equation (defined also as *continuity equation*), the temporal change in mass in a control volume corresponds to the convective flow across its limits. This connection leads to the following differential expression :

$$\frac{\partial \rho}{\partial t} + \frac{\partial}{\partial x_i}\left(\rho u_i\right) = 0. \tag{2.2}$$

In Eq. 2.1, the Einstein summation convention is employed for the compact representation of the differential equations. The position and the velocity vector are denoted in the Cartesian coordinate system with x_i and u_i respectively. The density is marked with ρ and the time with t.

2.1.2 Conservation of Momentum

Similarly to the continuity equation, the conservation of momentum ρu_i can be expressed applying the form of the Eq 2.2. The basis for the conservation of momentum was postulated by Newton in his laws of motion, which states that if a body remains fixed or moves uniformly, there are no external forces acting on it and appositely correct. The relevant forces present in case of change in the motion of the fluid, are the surface force caused by the pressure gradient $\partial p/\partial x_i$ and the viscous stress tensor τ_{ij} (defined in Eq. 2.4). The balancing of these forces on a control volume leads to the momentum conservation law:

$$\frac{\partial\left(\rho u_i\right)}{\partial t} + \frac{\partial\left(\rho u_i u_j\right)}{\partial x_j} = -\frac{\partial p}{\partial x_i} + \frac{\partial \tau_{ij}}{\partial x_j} + \rho g_i. \tag{2.3}$$

Where p represents the pressure and τ_{ij} states for to the viscous stress tensor. The stress tensor τ_{ij} can be estimated according to the Stoke's hypothesis reported in [47] with the following formula:

$$\tau_{ij} = 2\mu(S_{ij} - \frac{1}{3}\frac{\partial u_k}{\partial x_k}\delta_{ij}). \tag{2.4}$$

With μ stands for the dynamic viscosity, δ_{ij} is the Kronecker Delta and S_{ij} expresses the strain rate which is defined as:

$$S_{ij} = \frac{1}{2}\left(\frac{\partial u_i}{\partial x_j} + \frac{\partial u_j}{\partial x_i}\right). \tag{2.5}$$

2.1.3 Transport of Species

Besides the mixing properties of the fluid flow, characterizing and evaluating the concentrations of individual species within the mixture is crucial. Hence, additionally to the continuity and momentum equation, the multiple species of the fluid flow are conserved and transported. The mass fractions Y_α are employed to describe the composition of a mixture using the following definition:

$$Y_\alpha = \frac{m_\alpha}{m}. \tag{2.6}$$

Where m_α and m stand for the mass of species α and the total mass in the control volume, respectively. In a mixture, the summation of all species mass fractions is equal to one.

Then, the general form of the species transported equation is written as:

$$\frac{\partial(\rho Y_\alpha)}{\partial t} + \frac{\partial(\rho u_j Y_\alpha)}{\partial x_j} = -\frac{\partial J_{j\alpha}}{\partial x_j} + \dot{\omega}_\alpha. \tag{2.7}$$

By comparing the transported equation Eq 2.7 with the continuity one in Eq 2.2, two additional terms appeared in the right side of the equation. The first one represented by $J_{i\alpha}$ and expressed in Eq. 2.8, stands for the diffusive mass flow, which is approximated based on the Fick's law of diffusion according to Poinsot and Veynante in [130]. Here the Dufour and Soret terms are not considered. The second term $\dot{\omega}_\alpha$ refers to the change of mass fractions Y_α of species α as a result of multiple occurring chemical reactions. It is generally called reaction source term and can be calculated by solving a kinetic reaction mechanism. More details about this topic are reported in section 3.1.

$$J_{i\alpha} = -\rho D_\alpha \frac{\partial Y_\alpha}{\partial x_i}. \tag{2.8}$$

where $\mathcal{D}_\alpha$ denotes for the diffusion coefficient for species α and can be described as a function of viscosity and density quantities and the Schmidt number Sc_α as follows:

$$\mathcal{D}_\alpha = \frac{\mu}{\rho Sc_\alpha}. \tag{2.9}$$

The diffusion coefficient $\mathcal{D}_\alpha$ can also be described as a function of the dimensionless Lewis number Le_α , which indicates the ratio of heat conduction to diffusion. It is written as:

$$\mathcal{D}_\alpha = \frac{\lambda/\rho}{c_p Le_\alpha}. \tag{2.10}$$

Where c_p stands for the isobaric heat capacity of the mixture and λ is the thermal conductivity.

In furtherance of consistency with the chemical tabulation (see subsection 3.3.2), it was assumed that the Lewis number of all species is $Le_k = 1$. This is an assumption has to be carefully checked for reacting flows where species of very different molar masses are involved. Another assumption is considered in the present work is regarding the Schmidt number Sc_α in Eq. 2.9, where all chemical components are assumed to have the same Schmidt number with $Sc_\alpha = Sc = 0.7$.

2.1.4 Transport of Enthalpy

According to Poinsot and Veynante [130], within an isolated system, the energy cannot be destroyed nor created, but it can change its form by the application of the first law of thermodynamics. Thereby a further conservation equation can be derived. Broadly in the numerical fluid mechanics field and specifically in computational fluid dynamics (CFD) applications, the energy transported equation describing the energy balance within a specific reacting system, includes the total energy or enthalpy (h). Other thermodynamics properties formulations carrying the entropy or temperature can also be employed. The general enthalpy form of the mixture follows the equation below:

$$\frac{\partial(\rho h)}{\partial t} + \frac{\partial(\rho h u_i)}{\partial x_i} = \tau_{ij}\frac{\partial u_i}{\partial x_j} + \frac{Dp}{Dt} - \frac{\partial q_i}{\partial x_i} + \dot{w}_h. \tag{2.11}$$

In the Eq. 2.11 the last term $\dot{w}_h$ stands for the external volumetric enthalpy sources (e.g. radiation) and it is neglected if there are no external sources considered. However, the first and the second terms on the right hand side of the equation represent the enthalpy change due to pressure forces variations and viscous heating, respectively. As clearly addressed in [130], generally these two terms are neglected within low Mach number flow conditions. Regarding the third term on the right hand side q_i, it stands for the heat flux vector depending on material characteristic and described by Fourier's heat conduction law as:

$$q_i = -\lambda\frac{\partial T}{\partial x_i} - \sum_{\alpha=1}^{N_\alpha} \rho h_\alpha D_\alpha \frac{\partial Y_\alpha}{\partial x_i}, \tag{2.12}$$

With the unity Lewis number assumptions and as smoothly reported in [130] and [81], the final simplified form of the transported equation of the enthalpy balance is written as:

$$\frac{\partial(\rho h)}{\partial t} + \frac{\partial(\rho u_j h)}{\partial x_j} = \frac{\partial}{\partial x_j}\left(\frac{\lambda}{c_p}\frac{\partial h}{\partial x_j}\right). \tag{2.13}$$

At this level, it is highly substantial to mention that the enthalpy equation (Eq.2.11) is just presented as a part of the commonly used Navier-Stokes equations in the CFD calculations, but it won't be implemented within the numerical method used to simulate the treated reacting turbulent cases. In fact, this is by reasons of considering, so far, only *adiabatic* numerical investigations in this study which adheres to the applied hybrid Eulerian Stochastic Field/Flamelet Progress Variable Approach (see chapter 4 for all details).

2.1.5 The Equation of State

In order to solve the transport equations introduced, an equation describing the thermodynamic state of the fluid is required. In the context of this work, ideal gases exclusively are assumed for which the equation of state includes pressure, temperature and density together and it reads:

$$\rho = \frac{p}{T}\frac{\mathcal{M}}{\mathcal{R}}. \tag{2.14}$$

where $\mathcal{R}$ is the ideal gas constant with $\mathcal{R} = 8.314\ J/molK$, and $\mathcal{M}$ stands for the mixture mean molar mass. As reported in [51], following the Eq. 2.15, any significant pressure variation in a flow leads to a significant variation in density and that occurs even with small temperature changes. And as Poinsot and Veynante addressed in [130], for flows with low Mach number not exceeding 0.3, pressure variations can be neglected and a constant reference pressure (p^{ref}) in the ideal gas equation can be used. The last assumption can be adequately applied in the current work since all flow velocities for studied cases are far below the speed of sound. Hence the equation of state is written as:

$$\rho = \frac{p^{ref}}{T}\frac{\mathcal{M}}{\mathcal{R}}. \tag{2.15}$$

2.1.6 Summary of the Applied Equations

In this section, all transported equations that need to be solved are gathered as follows. Nevertheless, it is important to mention that generally in case of adiabatic chemical tabulation, which will bee seen in section 3.1, the enthalpy equation is not included.

1. Continuity equation

$$\frac{\partial \rho}{\partial t} + \frac{\partial(\rho u_i)}{\partial x_i} = 0 \tag{2.16}$$

2. Conservation of momentum

$$\frac{\partial(\rho u_i)}{\partial t} + \frac{\partial(\rho u_i u_j)}{\partial x_j} = -\frac{\partial p}{\partial x_i} + \frac{\partial}{\partial x_j}\left[\mu\left(\frac{\partial u_i}{\partial x_j} + \frac{\partial u_j}{\partial x_i}\right) - \frac{2}{3}\mu\frac{\partial u_k}{\partial x_k}\delta_{ij}\right] + \rho g_i \tag{2.17}$$

3. Species transport

$$\frac{\partial(\rho Y_\alpha)}{\partial t}(\rho Y_\alpha) + \frac{\partial(\rho u_j Y_\alpha)}{\partial x_j} = \frac{\partial}{\partial x_j}\left(\rho D_\alpha \frac{\partial Y_\alpha}{\partial x_j}\right) + \dot{\omega}_\alpha \tag{2.18}$$

4. Equation of state

$$\rho = \frac{p^{ref}}{T} \frac{\mathcal{M}}{\mathcal{R}} \tag{2.19}$$

2.2 Turbulence

Fluid flows are classified under three regimes: laminar, transitional and turbulent flows. In order to differentiate these regimes, a generally non-dimensional number, called Reynolds number, Re is evaluated and applied as introduced in [144]. The Re number is resolved based on the characteristic flow velocity u , a characteristic length scale L and the specific kinematic viscosity of the flow ν. Its formula is written as:

$$Re = \frac{uL}{\nu}. \tag{2.20}$$

Following the Re number estimations, the regimes addressed above can be briefly described as follows.

- *Laminar flow* : Re values are sufficiently low and the flow is characterized by an orderly, linear movement of fluid particles.
- *Turbulent flow* : Re values increased in a way that the flow presents irregular vortex structures showing different length scales and with three-dimensional unsteady motions. This regime is commonly reached once the Re is higher than a certain value known as the critic number with $Re_c = 2300$ (pipe case). Within this regime, the transfer of mass, momentum, and also energy is highly improved by the randomly vortex structures.
- *Transitional flow* : Re values ares on the limit of the critic value Re_c but the flow do not reach the turbulence regime. This phase stands for the intermediate scenario that occur between the laminar and the turbulent regimes.

In the current study, attention is given to turbulent flow since almost all technical applications are operating under strong turbulent conditions of the considered fluid flow. Correspondingly, It is relevant to understand this phenomena by explaining the mathematical description of turbulent flows, their properties and major modeling techniques applied to solve them. The following parts will be then focusing on the turbulence topics related to our numerical investigations and for more comprehensive details, the reader is referred to these textbooks [27; 132; 162].

2.2.1 Turbulent flow properties

According to Davidson in [27] and to Tennekes & Lumley in [162], there is no literal and clear definition of turbulence, however it is smoothly described through many specific properties. Among these properties we cite the dissipative stochastic behavior of the turbulent flow. Hence, it is preferable to split the instantaneous variables (velocity, pressure, temperature, ...) into two parts: Mean value and a fluctuating value. For the velocity components, the time averaged part is denoted with $\overline{u}$ and it is determinated over a sufficiently large period Δt, while the fluctuation element is designated with u'. The expressions of instantaneous parts are itemed as follows:

- a time-averaged part :

$$\overline{u} = \frac{1}{\Delta t} \int\limits_{0}^{\Delta t} u(t) \mathrm{d}t, \tag{2.21}$$

- and a fluctuating part :

$$u' = u - \overline{u}. \tag{2.22}$$

With the words of Davidson [27], the instantaneous variables are generally decomposed, when the flow quantities are measured, on the grounds that investigations are more focusing on mean values rather than time histories. Furthermore, in order to smoothly solve numerically the transport equations listed in 2.1.6, all turbulent scales should be resolved requiring very fine mesh and fine resolution in time since turbulence is always unsteady. Additionally, fluctuating part of the velocity can be applied to define the turbulent kinetic energy with the expression below:

$$k = \frac{1}{2}\overline{u_i' u_i'}. \tag{2.23}$$

According to [81; 132], within a turbulent flow, an energy spectrum can illustrate how the turbulent kinetic energy (k) is dispersed among many eddies. These turbulent eddies are characterized with various lengths l and characteristic speed $u(l)$ along different time scales expressed with $\tau(l) = l/u(l)$. Hereby, large eddies are unstable and derive the kinetic energy k from the flow that has time scale proportionate to large scales ([27]. Hence, once the large scales break-up, a part of the kinetic energy is transferred to the slightly smaller scales. This process, known as *the energy cascade process*, continues in a way that k is always transferred from the largest to the smallest scales until that the frictional forces become large and the kinetic energy is converted to thermal energy in consequence of dissipation process. This dissipation phenomena between interacted eddies is characterized by the *dissipation rate* denoted by ε with dimensions $[m^2/s^3]$. It is proportional to the kinematic viscosity ν and the fluctuating velocity gradient, and it can also be defined in terms of the integral length scale l_I identifying the characteristic length scale of the large eddies and its corresponding velocity $u'(l_I)$ ([5; 81]). Then, the formula of the dissipation ε follows :

$$\varepsilon = \frac{u'(l_I)^2}{l_I/u'(l_I)} = \frac{u'(l_I)^3}{l_I}. \tag{2.24}$$

With Davidson notes in [27], the most part of the viscous stresses exist at the smallest eddies where the dissipation occurs. These scales are called *Kolmogorov scales* whose velocity scale is expressed with u_η, length scale by l_η and time scale by τ_η. These quantities are assumed to be described in terms of the viscosity ν and the dissipation rate ε as follows:

$$l_\eta = \left(\frac{\nu^3}{\varepsilon}\right)^{1/4}, \qquad u_\eta = (\varepsilon\nu)^{1/4}, \qquad \tau_\eta = \left(\frac{\nu}{\varepsilon}\right)^{1/2}. \tag{2.25}$$

Another quantity that is important to be estimated is the turbulent Reynolds number Re_t that characterizes the turbulent flow field and reads:

$$Re_t = \frac{u'(l_I)l_I}{\nu}. \tag{2.26}$$

From which another relation can be extracted combining the Re_t and the Kolmogorov length scales of the considered flow. This relation is obtained by inserting both l_η and τ_η in Eq.(2.25) and the previous Eq.(2.26) into the Eq.(2.24). The obtained ratio has the following expression :

$$\frac{l_I}{l_\eta} = \frac{u'(l_I)^3/\varepsilon}{(\nu^3/\varepsilon)^{1/4}} = Re_t^{3/4}. \tag{2.27}$$

The last ratio reveals the influence of the turbulence on the range of length scales that need to be evaluated which is strongly paramount in the case of defining the grid generation during numerical simulations.

The *energy cascade process* with all aforementioned range of different scales in the turbulent flow can be schematically resumed via *the spectrum of the turbulent kinetic energy* which is depicted in Figure 2.1. The corresponding diagram shows the evolution of the turbulent kinetic energy k in the wavenumber space v where $v = 2\pi/l$. It can be noticed that the kinetic energy evolves toward the smaller eddies until the viscous stresses are adequately large in order to dissipate the energy and convert it to heat as reported above. Following [27], mainly three different zones are characterizing the spectrum:

- Large energy containing eddies : This region contain the large eddies carrying most part of the kinetic energy. These vortices interact and extract energy from the mean flow which part of it is transferred (per unit time) to slightly smaller scales. The spectrum attains its maximum value at a wavenumber that adjusts the integral length scale l_I. This region is called also the production zone
- Inertial subrange : This region is achieved once the flow is considered fully turbulent flow (high Reynolds number). This zone is known as "the transport zone" or "the inertial subrange" in cascade process in which the energy is transferred from large scales to smaller ones by vortex stretching processes and the spectrum decays with a characteristic constant slope of $v^{-5/3}$ (see [132]).
- Viscous subrange : The dissipation occurs in this zone where eddies are isotropic and the scales are small and described by the Kolmogorov scales. The kinetic energy is converted to thermal energy resulting in increased temperature and no more small eddies are formed.

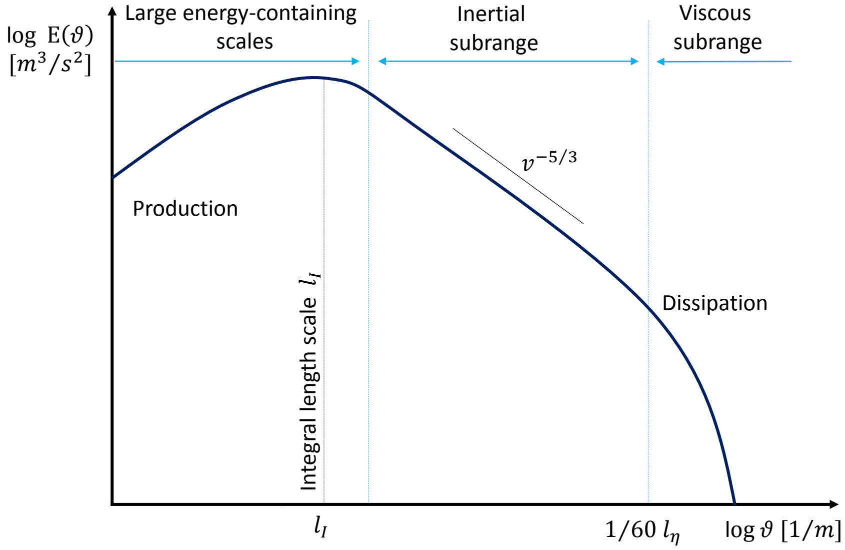

Figure 2.1: Schematic diagram of the evolution of the kinetic energy spectrum as a function of the wavenumber v illustrating the energy cascade of turbulent flows.

2.3 Modelling approaches

The Navier-Stokes equations listed in the previous section (2.1.6) are applied equally to the calculation of different types of fluid flows. However, in the current study, the focus is pointed to the turbulent flows since the investigated cases are operated under turbulence conditions and generally laminar flows are rarely found in combustion systems. In this case, and by considering the complexities of turbulent reacting flows, several numerical approaches are employed in order to solve the corresponding equations since analytical methods could not be applicable in current cases. Thence, in the following subsections, the different frequently used numerical approaches are mathematically defined and described. Three major numerical strategies are commonly implemented in *Computational Fluid Dynamics* (CFD) solvers and applied for the simulation of turbulent flows:

- Direct Numerical Simulation (DNS)
- Large Eddy Simulation (LES)
- Reynolds Averaged Navier-Stokes (RANS)

These numerical methods are distinguishable from each other according to many aspects which can be based on the way of modeling, the computational grid generated and the mesh quality used and also the computational effort required.

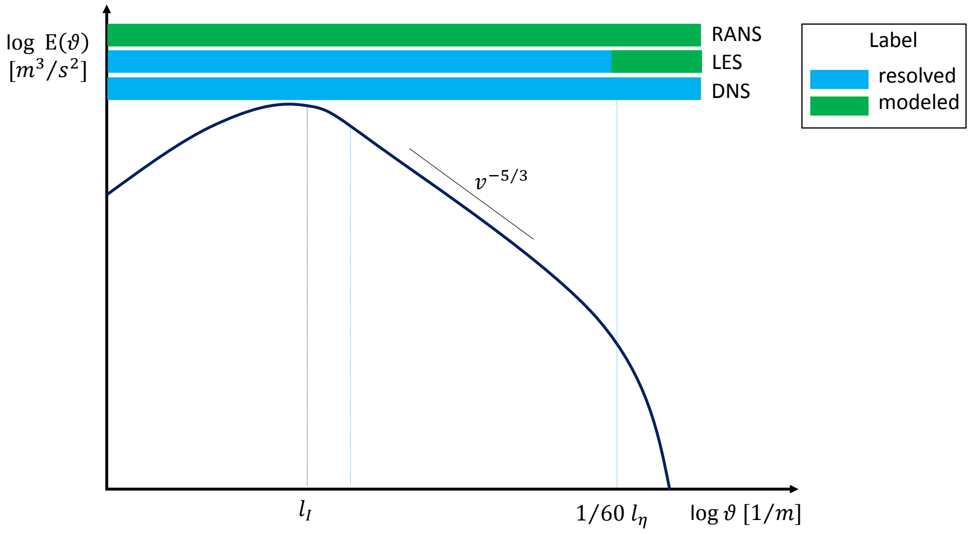

Figure 2.2: Schematic diagram of the kinetic energy spectrum illustrating the basic difference among the three numerical approaches. The directly resolved area is depicted with blue color and the green color denotes the modeled region of the turbulent scales.

2.3.1 Direct Numerical Simulation (DNS)

In order to completely solve the fluid flow equations presented in section 2.1.6, the DNS is the most accurate numerical method to be adopted. It is a direct calculation approach rather than modeling technique. For a direct numerical simulation, all turbulent flow structures are fully resolved by the applied numerical computational grid. This implies all involved turbulent scales even the smallest ones which are characterized by the Kolmogorov length scale (see 2.25). These turbulent scales as directly resolved on the computational grid in order to correctly simulate the complete flow without considering the numerical errors. Hence no modeling techniques are used for the turbulent fluctuations determinations.

As depicted in Figure 2.2, the DNS method resolves the entire energy spectrum of a turbulent flow. However, the effort involved in direct numerical simulation is extremely significant due to the necessary fine computational grid generated to cover all scales including kolmogorov scales. This is proportionally reflected in the computing time since the spatial resolution is directly connected to the temporal resolution following the CFL number (Courant-Friedrichs-Lewy) (see [25; 93]). Consequently, the computational costs increase. The computing time of a DNS is proportional to $Re_t^{3/4}$, in every direction and therefore with $Re_t^{9/4}$ for a three-dimensional simulation. For all previous reasons, the DNS method application is particularly limited to special applications where simple geometries are investigated or within the areas where measurements can not be derived during an experimental investigation.

In order to simulate more complex realistic systems, not all turbulent structures are considered and only specific range of scales is to be considered. This can be done by either averaging the transported equations in time or by filtering them in space ([81]). The first procedure is called **Reynolds Averaged Navier-Stokes (RANS)** modeling and the second one is referred to as **Large Eddy Simulation (LES)**. Both previously mentioned approaches are employed in the current study to investigate different turbulent reacting cases and will be more detailed in the following subsections.

2.3.2 Reynolds Averaged Navier-Stokes (RANS)

The Reynolds averaged Navier-Stokes (RANS) method is widely used for turbulence calculations and frequently implemented in all industrial CFD codes on account for its low computational costs comparing to other approaches. In opposition to the DNS method, where all turbulent scales are exactly calculated, the entire range of wavenumber is modeled as illustrated in Figure 2.2. As already defined for the velocity components in equations (2.21) and (2.22), any other physical quantity Φ within a turbulent flow can adhere to the same concept and be averaged over time into a mean part denoted generally with $\overline{\Phi}$ and a stochastic fluctuating part designated with Φ'. Thereby, applying this averaging concept, only flow time-averaged quantities are described by the modeled Navier-Stokes equations leading to a significant decrease in terms of numerical computational requirements ([126]). Reminding of the decomposition formulation, for each quantity Φ in turbulent flow, it reads:

$$\Phi(x_i, t) = \overline{\Phi}(x_i) + \Phi'(x_i, t). \tag{2.28}$$

Furthermore and by employing this averaging concept on transported equations, the unclosed term $\overline{\Phi' u'}$ appeared and modeling tools are required to calculate it. In the momentum equation the unknown unclosed term $\overline{{u_i}'{u_j}'}$ is called Reynolds stress tensor. Within the modeling steps, a specific mass-weighted averaging is applied, known as Favre averaging (see [37; 81]) and has the following form:

$$\widetilde{\Phi} = \frac{\overline{\rho \Phi}}{\overline{\rho}}. \tag{2.29}$$

Several approaches in RANS framework were introduced as reported in ([132]) in order to model these unclosed terms. In the current study, the standard two equations k-ε model is applied. Additionally to the Navier-stokes equations listed in subsection 2.1.6, two further equations are transported. One equation is for solving the turbulent kinetic energy k and the other one for the dissipation rate ε. Solving these two quantities, the characteristic length scale l and time scale τ can be calculated as follows:

$$l = \frac{k^{3/2}}{\varepsilon} \qquad \tau = \frac{k}{\varepsilon} \tag{2.30}$$

After applying the averaging tools to all balance equations and adopting the k-ε model, the following modeled set of equations are the ones implemented in the CFD-code to be solved.

1. Conservation of mass

$$\frac{\partial\overline{\rho}}{\partial t} + \frac{\partial\overline{\rho}\widetilde{u}_i}{\partial x_i} = 0 \tag{2.31}$$

2. Conservation of momentum

$$\frac{\partial\overline{\rho}\widetilde{u}_i}{\partial t} + \frac{\partial\overline{\rho}\widetilde{u}_i\widetilde{u}_j}{\partial x_j} = -\frac{\partial}{\partial x_i}(\overline{p} + \frac{2}{3}\overline{\rho}\widetilde{k}) + \frac{\partial}{\partial x_j}\left[\overline{\rho}(\mu + \mu_t)(\frac{\partial\widetilde{u}_i}{\partial x_j} + \frac{\partial\widetilde{u}_j}{\partial x_i} + \frac{2}{3}\delta_{ij}\frac{\partial\widetilde{u}_k}{\partial x_k})\right] \tag{2.32}$$

3. Species transport

$$\frac{\partial\overline{\rho}\widetilde{Y_\alpha}}{\partial t} + \frac{\partial\overline{\rho}\widetilde{u}_i\widetilde{Y}_\alpha}{\partial x_i} = \frac{\partial}{\partial x_j}\left[\overline{\rho}(\frac{\mu}{Sc} + \frac{\mu_t}{Sc_t})\frac{\partial\widetilde{Y}_\alpha}{\partial x_j}\right] + \overline{\dot{\omega}}_\alpha \tag{2.33}$$

4. Turbulent kinetic energy transport

$$\frac{\partial\overline{\rho}\widetilde{k}}{\partial t} + \frac{\partial\overline{\rho}\widetilde{u}_i\widetilde{k}}{\partial x_i} = \frac{\partial}{\partial x_j}\left[\overline{\rho}(\mu + \frac{\mu_t}{Sc_k})\frac{\partial\widetilde{k}}{\partial x_j}\right] + \widetilde{G}_k - \overline{\rho}\widetilde{\varepsilon} \tag{2.34}$$

5. Dissipation rate of turbulent kinetic energy transport

$$\frac{\partial\overline{\rho}\widetilde{\varepsilon}}{\partial t} + \frac{\partial\overline{\rho}\widetilde{u}_i\widetilde{\varepsilon}}{\partial x_i} = \frac{\partial}{\partial x_j}\left[\overline{\rho}(\mu + \frac{\mu_t}{Sc_\varepsilon})\frac{\partial\widetilde{\varepsilon}}{\partial x_j}\right] + C_{\varepsilon 1}\widetilde{G}_k\frac{\widetilde{\varepsilon}}{\widetilde{k}} - C_{\varepsilon 2}\frac{\widetilde{\varepsilon}^2}{\widetilde{k}} \tag{2.35}$$

In the equations above, the $(\widetilde{\cdot})$ stands for the Favre weighted quantity and the symbol $(\overline{\cdot})$ for the mean quantity. The dynamic molecular viscosity is referred with μ while the term μ_t stands for the turbulent one with the expression : $\mu_t = \rho C_\mu k^2/\varepsilon$. The coefficients Sc and Sc_t present the laminar and the turbulent Schmidt numbers respectively. The term $\widetilde{G_k}$ stands for the production of the turbulent kinetic energy, its expression is a function of the strain rate tensor $\widetilde{S_{ij}}$ and reads:

$$\widetilde{G_k} = 2\mu_t\widetilde{S_{ij}}\widetilde{S_{ij}}. \tag{2.36}$$

For the standard turbulent k-ε model, and according to ([97]) and the author's previous studies in ([106]), the constant coefficients are set in the following manner :

$$C_{\varepsilon 1} = 1.44, \qquad C_{\varepsilon 2} = 1.92, \qquad C_\mu = 0.09$$

$$Sc = Sc_t = 0.71, \qquad Sc_k = 1.0, \qquad Sc_\varepsilon = 1.3.$$

2.3.3 Large Eddy Simulation (LES)

Conceptually, the large eddy simulations (LES) are classified between the RANS and DNS turbulence methods following scale separation technique as exemplified in Figure 2.2. The flow largest scales, so called high-energy scales, are explicitly resolved on the numerical grid while the smaller structures corresponding to the low-energy scales called also sub-grid scales (SGS) are modeled applying a suitable sub-grid model. The most discussed point is the choice of the wavenumber at which the scale separation is made. This is numerically associated to the grid width properties applied for the flow simulations. The criterion for choosing the grid width is that approximately 80% of the turbulent kinetic energy spectrum is resolved which corresponds to the blue area in the LES segment in Figure 2.2.

2.3.3.1 Filtering of Navier-Stokes Transport Equations

The function of fine structure modeling is to map the dissipation of the turbulent kinetic energy k on the sub-grid scales. This numerical modeling can be implemented by using a vortex viscosity approach based on the Boussinesq hypothesis [130]. Regarding the coarse structure simulations, contrary to the temporal averaging for the static turbulence models, an implicit spatial filtering is applied in the LES context. The advantage of this filtering technique, is the persistent location and time dependency of the filtered quantities (see [49; 91]).

As aforementioned, the LES numerical model has the capability to describe transient processes by considering the spatial filtering instead of temporal one which is based on a separation of the scales performed on the conservation equations listed in subsection 2.1.6. This filtering function generally referred to the G low pass filter which was presented by Leonard [98]. By applying the G filter, an arbitrary filtered quantity Φ is described as:

$$\overline{\Phi}(x) = \int_V G(x - x')\Phi(x')dx'. \tag{2.37}$$

Here the two variables $\overline{\Phi}$ and Φ represent respectively a filtered and unfiltered quantities at a position x. In following, the one-dimensional notation is employed for simplifying reasons. Among many used different standard filters that can be reported in Sagaut's book in [153], a rectangular filter is applied for all calculations which is achieved by using the numerical grid length Δ as selected filter size, conforming the following definition:

$$G(x - x') = \begin{cases} \frac{1}{\Delta} & : |x - x'| < \frac{\Delta}{2} \\ 0 & : otherwise \end{cases} \tag{2.38}$$

Additionally to RANS description, in the LES context and for both compressible and incompressible flows, it is an advantage to use the same density-weighted Favre filtering already prescribed in equation (2.29). This filtering technique allows all Φ quantities to be split into two parts: the filtered part presented by $\widetilde{\Phi}$ and the unresolved part or the subgrid-scale (SGS) fluctuations designated with Φ^{sgs} :

$$\Phi = \widetilde{\Phi} + \Phi^{sgs}. \tag{2.39}$$

The filtered part in the equation above characterizes the flow properties on the resolved scales which cover all length scales that are larger than the selected filter size Δ.

Herein, in LES context, only the filtered quantities are calculated directly, whereas all sub-grid quantities are modeled. Applying the filter described above, the conservation equations for the filtered variables can be derived from the Navier-Stokes equations in subsection (2.1.6) leading to the following set of filtered balance equations:

1. Conservation of mass

$$\frac{\partial \overline{\rho}}{\partial t} + \frac{\partial (\overline{\rho}\widetilde{u}_i)}{\partial x_i} = 0 \tag{2.40}$$

2. Conservation of momentum

$$\frac{\partial (\overline{\rho}\widetilde{u}_i)}{\partial t} + \frac{\partial (\overline{\rho}\widetilde{u}_i\widetilde{u}_j)}{\partial x_j} = -\frac{\partial \overline{p}}{\partial x_i} + \frac{\partial \overline{\tau}_{ij}}{\partial x_j} - \frac{\partial \tau_{ij}^{sgs}}{\partial x_j} \tag{2.41}$$

3. Species transport

$$\frac{\partial (\overline{\rho}\widetilde{Y_\alpha})}{\partial t} + \frac{\partial (\overline{\rho}\widetilde{u}_i\widetilde{Y}_\alpha)}{\partial x_i} = \frac{\partial \overline{J}_{i\alpha}}{\partial x_i} - \frac{\partial J_{i\alpha}^{sgs}}{\partial x_i} + \overline{\dot{\omega}}_\alpha \tag{2.42}$$

In the filtered equations above, the filter function G employed leads to the apparition of additional new terms once compared to original Navier-Stokes unfiltered equations. The influence of the fine scales of the turbulent flow reflects on the filtered quantities. Hereof, in the filtered moment equation (2.41), we find the turbulent shear stress tensor with the following expression:

$$\tau_{ij}^{sgs} = \overline{\rho}\widetilde{u_i u_j} - \overline{\rho}\widetilde{u}_i\widetilde{u}_j \tag{2.43}$$

However in the species transport filtered equation (2.42), the sub-grid scale species flux of the species under consideration reads:

$$J_{i\alpha}^{sgs} = \overline{\rho}\widetilde{u_i Y_\alpha} - \overline{\rho}\widetilde{u}_i\widetilde{Y_\alpha} \tag{2.44}$$

The additional terms listed above are in unclosed form and then must be determined by applying a suitable sub-grid scale model which will be discussed in the next subsection. However, there is another unclosed term in the species transport equation Eq.2.42 which is designated with $\overline{\dot{\omega}}$ and refers to the filtered chemical source term. The modeling of this term is achieved by different proposed approaches where the main used method in this work will be discussed with details in chapter 4. The determination of this quantity presents a huge challenge because it strongly depends on the non-linear interaction between unresolved time and length scales for both chemical reactions and turbulence.

2.3.3.2 Modeling of sub-grid scale

The objective of this section is to determine the unclosed terms created during filtering the transport equations in the subsection (2.3.3.1) and that by using suitable modeling techniques for sub-grid scale quantities. The reader is referred to Sagaut's book in [153] for detailed overview of these applied techniques. However, only the LES sub-grid model employed in the current work is reported in this section. The applied sub-grid scale model belongs to the class of the eddy viscosity approaches which are based on the Boussinesq approximation as already mentioned above. Herein, it is presumed that the subgrid-scale stress tensor performs as an additional diffusion term [145]. An effective dynamic eddy viscosity is introduced in Eq.2.45 and is determined from both turbulent and molecular dynamic viscosities represented with μ_{sgs} and μ respectively.

$$\mu_{eff} = \mu_{sgs} + \mu \tag{2.45}$$

Thereby, following the eddy viscosity approach with the Boussinesq approximation, the SGS stress tensor is postulated as:

$$\tau_{ij}^{sgs} - \frac{1}{3}\tau_{kk}^{sgs}\delta_{ij} = -2\mu_{sgs}\left(\widetilde{S}_{ij} - \frac{1}{3}\widetilde{S}_{kk}\delta_{ij}\right) \tag{2.46}$$

where the first two terms τ_{ij}^{sgs} and $\frac{1}{3}\tau_{kk}^{sgs}\delta_{ij}$ denote the anisotropic and isotropic parts of the Reynolds stresses respectively. Nonetheless, the isotropic part of the stress tensor is usually included into the modified filtered pressure as:

$$\overline{P} = \overline{p} + \frac{1}{3}\overline{\rho}\tau_{kk}^{sgs}. \tag{2.47}$$

The $\widetilde{S}_{ij}$ term in Eq (2.46) stands for the filtered rate of strain with the following expression:

$$\widetilde{S}_{ij} = \frac{1}{2}\left(\frac{\partial \widetilde{u}_j}{\partial x_i} + \frac{\partial \widetilde{u}_i}{\partial x_j}\right). \tag{2.48}$$

Regarding the subgrid-scale flux $J_{i\alpha}^{sgs}$ in the species transport equations, it is closed as follows:

$$J_{i\alpha}^{sgs} = -\frac{\mu_{sgs}}{Sc_{\alpha,sgs}}\frac{\partial \widetilde{Y}_\alpha}{\partial x_i}. \tag{2.49}$$

where $Sc_{\alpha,sgs}$ is the turbulent Schmidt number for different species α. However, in this study the assumption that all flow species have the same Schmidt number is adopted. The common value of the turbulent Schmidt number applied in all calculations is 0.7.

Algebraic eddy viscosity model: The Smagorinsky model

The algebraic subgrid-scale viscosity model proposed by Smagorinsky in 1963 [157] is considered one of the most popular eddy viscosity model utilized in the CFD applications. It is used in the current work and it consists mainly on employing the Δ filter size to describe the characteristic length scale as:

$$\mu_{sgs} = \overline{\rho}(C_s\Delta)^2|\widetilde{S}_{ij}| \qquad with \qquad |\widetilde{S}_{ij}| = \sqrt{2\widetilde{S}_{ij}\widetilde{S}_{ij}}. \tag{2.50}$$

where C_s is a model constant coefficient, generally approximated between the values 0.065 and 0.2, while in the current work $C_s = 0.17$. The filter size Δ is defined with the expression: $\Delta = (\Delta_x\Delta_y\Delta_z)^{1/3}$. As reported in [132], the definition proposed by Smagorinsky regarding the length scale is justifiable only for specific range of Δ; those within the inertial subrange only. Therefore, and accounting for stream jet's wall surface, the van Driest wall damping function is proposed [35] in order to slightly modify the Smagorinsky model. The modification comprises the definition of the grid filter width in the near-wall region where it is replaced by the following formula:

$$\Delta_{VD} = min[\Delta, \frac{k_r}{C_\Delta}(1 - e^{-r.A^+/r^+})] \tag{2.51}$$

where k_r stands for the Karman constant and r^+ is the dimensionless wall distance. According to [28; 35; 107] the values of model coefficients applied in this study read:

$$k_r = 0.41 \qquad C_\Delta = 0.158 \qquad A^+ = 26.$$

2.4 Summary

In this chapter the fundamentals transport equations describing the turbulent flows were reported and the numerical models solving these equations were presented.

In the first section, the generally applied governing equations in the CFD calculations were introduced and the techniques used for their simplifications and derivation were explained. Also, the necessary equations set implemented in the CFD code employed in the current work was specified since not all equations are considered. Thereafter, an overview of turbulence was briefly described highlighting main turbulent flow characteristics. Finally, the turbulence modeling part is addressed by describing the three most used numerical methods for turbulent flows : DNS, LES and RANS. The focus was appended to the two models used in this work which are the LES and RANS methods taking into account the optimum ratio between the good grid resolution and the computational costs.

However, and among many numerical assumptions presented so far to determine different terms in the filtered transport equations, the closure approach of the filtered chemical source term $\overline{\dot{\omega}}$ appeared in Eq.(2.33) and in Eq.(2.42) will be discussed in details in the next chapter where the turbulence-combustion interaction topic is addressed.

Chapter 3

Description and Modelling of Combustion

In this chapter, the mathematical description of combustion and the basic theoretical concepts of turbulent reacting flows are presented. Herein, the combustion process is known as a rapid oxidation of the fuel and the oxygen generally found in air. Through a variety of exothermic elementary chemical reactions, the energy presented in chemical bonds is converted into heat and light. Depending on the industrial application, the generated heat can be additionally reformed into different energy forms (electric, mechanical, ...).

In the current study, we are focusing on the methane as principal fuel for the combustion process. Hence, in the first section, chemical reaction kinetics and reaction mechanisms of methane are addressed. In the second section, the combustion modes and its different regimes are explained and presented according to the two flame types: non-premixed flames and premixed flames.

3.1 Chemical reaction kinetics and reaction mechanisms

In order to study the combustion process, it is highly important to understand the fundamentals about chemical reaction kinetics. Generally, the combustion reaction is simplified and described with one global reaction where fuel and oxidizer as initial reactants transformed into final combustion products in one step. Thereby, since methane CH_4 is the chosen fuel for this study, the global reaction mechanism of CH_4 oxidized with air (gas mixture of O_2 and inert N_2) can be depicted as the following example :

$$\nu_1' \mathrm{CH_4} + \nu_2' (\mathrm{O_2} + 3.76\mathrm{N_2}) \rightarrow \nu_3'' \mathrm{CO_2} + \nu_4'' \mathrm{H_2O} + \nu_5'' \mathrm{N_2}. \tag{3.1}$$

Theoretically, in Eq 3.1, if there is just enough oxidant then the mixture is described as *stoichiometric mixture.* Thence, the stoichiometric coefficients ν_i' and ν_j'' are evaluated as follows:

$$\begin{pmatrix} \nu'_1 \\ \nu'_2 \\ \nu''_3 \\ \nu''_4 \\ \nu''_5 \end{pmatrix} = \begin{pmatrix} 1 \\ 2 \\ 1 \\ 2 \\ 7.52 \end{pmatrix}$$

The global reaction simplifies the expression of the complex combustion process in one step, but in reality, numerous sub-reactions are present to transform a molecule of CH_4 collided with O_2 to finally result in CO_2 and H_2O. As reported in [164] and other studies [5; 81; 149], many radicals and species are transformed into new ones after breaking and consequently forming several bonds. Herein many sequential steps happen simultaneously including hundreds of intermediate species. Following [5], the general form to describe the collection of N_r underlying elementary reactions involving N_α intermediate species designated with χ_i, reads:

$$\sum_{i=1}^{N_\alpha} \nu'_{i,\kappa} \chi_i \rightleftharpoons \sum_{i=1}^{N_\alpha} \nu''_{i,\kappa} \chi_i \qquad \kappa \in \{1, \dots, N_r\}. \tag{3.2}$$

According to Stephen Turns in [164], the combustion's rate is conducted by the chemical reaction rates in all combustion process where they control the formation and the destruction of different species. These processes may occur involving some elementary reversible reactions which clarify the use of double arrow in Eq 3.2. Consequently, for each chemical reaction, a forward and backward reaction rates denoted respectively with $r_{f,\kappa}$ and $r_{b,\kappa}$, are defined to resolve the reaction source term $\dot{\omega}_\alpha$ (see Eq 2.7) [5; 81]. Thus, the general form of these reaction rates can be revealed as follows:

$$r_{f,\kappa} = k_{fr,\kappa} \prod_{\alpha=1}^{N_\alpha} \left(c_\alpha^{\nu'_{i,\kappa}} \right) \qquad r_{b,\kappa} = k_{br,\kappa} \prod_{\alpha=1}^{N_\alpha} \left(c_\alpha^{\nu''_{i,\kappa}} \right). \tag{3.3}$$

Where the considered species concentration c_α is defined as function of the mass fraction Y_α and the molar mass $\mathcal{M}_\alpha$ of each specie α with:

$$c_\alpha = \rho \frac{Y_\alpha}{\mathcal{M}_\alpha}. \tag{3.4}$$

And the chemical rate coefficients $k_{fr,\kappa}$ and $k_{br,\kappa}$ are estimated following the Arrhenius law reading:

$$k_{fr,br} = A^a_{fr/br} T^{n^a_{fr/br}} \exp\left(-\frac{E^a_{fr/br}}{\mathcal{R}T} \right). \tag{3.5}$$

In Eq 3.5, the coefficient $A^a_{fr/br} T^{n^a_{fr/br}}$ states for pre-exponential factor and E^a is the activation energy. The average kinetic energy is expressed with the factor $\mathcal{R}T$. Thence, with a combination of different elementary reaction rates, the progress reaction rate $\dot{\omega}_\alpha$ can be determined following the coming expression:

$$\dot{\omega}_\alpha = \mathcal{M}_\alpha \sum_{\kappa=1}^{N_r} \left(\nu''_{\alpha,\kappa} - \nu'_{\alpha,\kappa} \right) \left(r_{f,\kappa} - r_{b,\kappa} \right). \tag{3.6}$$

In this context, N_α transport equations, including each one a chemical reaction rate coming out as a source term, are added to the equation system (RANS (2.31 –2.35), LES (2.40 –2.42)) that are required to be solved. However, many chemical processes involve hundreds of species and sub-reactions, leading to define thousands of implicated parameters for transporting and resolving thousands of equations. Some of these species and underlying reactions have minor importance than other within the same chemical process. Thereby, detailed mechanisms can be considered as a very expensive reaction mechanism. As alternatives, many techniques were proposed in the literature (see [170]) where species and reactions with major influence on the global chemical process are considered. Hence, the GRI3.0-mechanism (see [64]) which is generally employed for methane-oxygen/air combustion is applied in this study. Only 53 species and 325 involved reactions are considered in this reaction mechanism.

3.2 Flame Modes

In the framework of practical applications of the combustion process, it is highly important to understand the basic of reacting flows and flame characteristics. This starts with categorizing the flame under multiple modes according to how the fuel and the oxidizer are delivered before combustion process takes place (see [164]). The flame modes are commonly identified as:

- Premixed flames: Fuel and oxidizer are perfectly mixed prior the reaction zone
- Non-premixed flames: Fuel and oxidizer are not mixed prior the reaction zone
- Partially-premixed flames: Fuel and oxidizer are partially mixed prior the reaction zone

Other than fuel/oxidizer distribution mode to categorize the flame types, many features are strongly considered such as local flame structure, pollutant destruction and/or formation and temperature distribution. Therefore, in order to study and present these flame modes in the coming subsections, we need to define first important properties. The first property is known as the equivalence ratio ϕ which characterize the reactants mixture. It is described as the actual fuel-oxidizer ratio normalized by the stoichiometric fuel-oxidizer ratio. The expression of the equivalence ratio ϕ reads:

$$\phi = \left(\frac{Y_{fuel}}{Y_{oxi}}\right) / \left(\frac{Y_{fuel}}{Y_{oxi}}\right)_{st} . \tag{3.7}$$

The stoichiometric fuel-oxidizer ratio denoted with the subindex (st) in Eq 3.7 corresponds to the reaction conditions where present reactants (methane and oxygen) are fully consumed. Hence, it is referred as stoichiometric mixture with $\phi = 1$. However the fuel-air/oxygen is considered lean mixture in case $\phi < 1$, and reach if $\phi > 1$. More details can be also found in (see [109]).

Additionally to the equivalence ratio, the mixture fraction, which is a passive scalar, can be applied to measure the combustion reactants mixing and to define the local fuel/oxidizer ratio as smoothly stated by Poinsot and Veynante in [132]. In order to adopt same notations as in [132], the mixture fraction is denoted with f. This parameter is defined in function of mass fractions of involved atomic elements denoted with Z_p with the following expression:

$$Z_p = \sum_{\alpha=1}^{N_\alpha} a_{\alpha p} \frac{\mathcal{M}_p}{\mathcal{M}_\alpha} Y_\alpha \qquad p \in \{1, \ldots, P\}. \tag{3.8}$$

where $\mathcal{M}_p$ is the molar mass of the element type p and Y_α is the mass fraction of the species α. However, $a_{\alpha p}$ states for the number of atomic elements p in the involved species α. We can take methane (CH_4) as an example of species α, so if (H) is the element p then $a_{(CH_4)p} = 4$.

The mixture fraction f, as a function of Z_p, corresponds to one in pure fuel and to zero in pure oxidizer after being normalized according to:

$$f = \frac{Z_p - Z_{p,Ox}}{Z_{p,fuel} - Z_{p,Ox}} \qquad p \in \{1, \ldots, P\}. \tag{3.9}$$

Likewise, as comprehensively explained in [164; 173] and also in [22], a relation of mixture fraction and equivalence ratio ϕ can be introduced with the next formula:

$$\phi = \frac{f}{1-f} \frac{1-f_{st}}{fst}. \tag{3.10}$$

With the appropriate application of these parameters measuring the fuel/oxidizer ratio, the main characteristics of the generic flame types are reported in the next subsections.

3.2.1 Premixed Flames

As its name indicates, the premixed flame states for flames type where a fresh fuel and oxidizer are perfectly mixed with an ignitable ratio before entering the reaction zone prior to their burning. As introduced in (see [109]), an ignition from a spark or the existence of pilot within the combustion system can establish the burning phase which creates a propagating flame in the direction of unburned gases. The propagation of the flame is generally referred to the flame speed s_l.

The Figure 3.1 (left) illustrates schematically the reaction process with isolines of a standardized controlling variable that represents the progress of the reaction from fresh gas with value equal to zero increasing towards the combustion products side with the value of one. Nevertheless, the diagram in Figure 3.1 (right) illustrates the structure of one-dimensional premixed CH_4/air flame, whereby three flame zones can be distinguished. In the preheat zone, also called diffusion zone, the gas mixture is preheated and receives heat from the reaction zone. Most of the reactions and most of the heat release take place in the reaction zone in which the activation energy is exceeded which is also shown in Figure 3.1 (right)

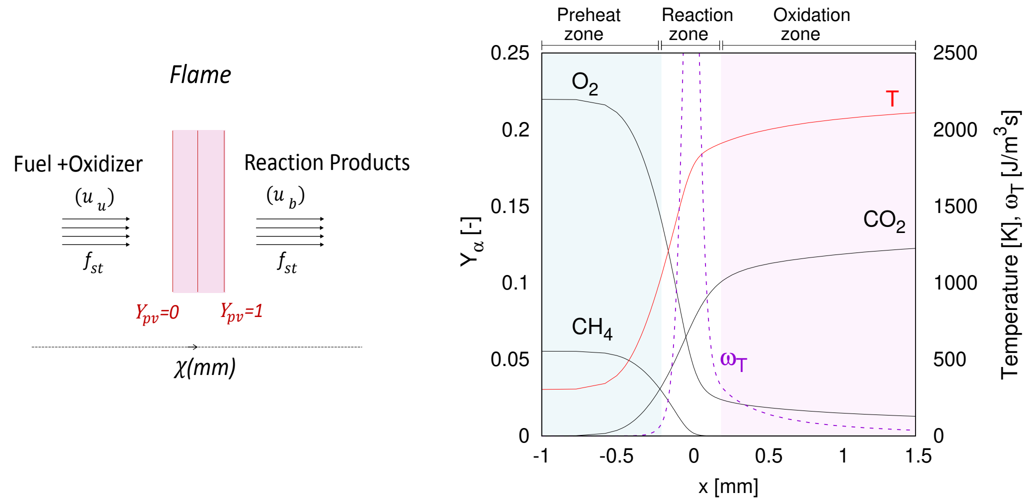

Figure 3.1: Basic schematic drawing of a premixed flame (left) and profiles of some species and temperature of a one-dimensional premixed CH_4/air flame (right).

As briefly mentioned above, the flame speed s_l is an important characteristic of premixed flames. It depends on the thermodynamic conditions and the degree of mixing. Generally in many common hydrocarbons and specifically for CH_4, the flame speed, as well as the adiabatic flame temperature, reach the maximum values at the stoichiometric degree of mixing which is depicted in Figure 3.1 (right). Another parameter characterizing premixed flames is the thickness of reaction zone, commonly referred to the flame thickness which strongly depends on the operating conditions and reaches its minimum value at the stoichiometric mixture fraction. More comprehensive explanation can be found in (see [109]).

According to [81] and [51], operating under lean mixture in the premixed flames can help significantly in minimizing the formation of nitrogen oxides by avoiding high temperatures. This represents a significant advantage over diffusion flames (see Subsection (3.2.2)), in which combustion takes place inherently under stoichiometric conditions and correspondingly high temperature. However, there are disadvantages due to the flame stabilization that is difficult to achieve. Since the ignitable mixture is not only present in the flame itself, but fills a larger area in front of the flame, it raises the risk of flashback where the flame propagates in the direction of the fuel stream.

3.2.2 Non-Premixed Flames

Contrary to the premixed flames type, the non-premixed combustion states for the flame type where fresh fuel and oxidizer are perfectly separated before entering the reaction zone. Once both streams are mixed and under flammability limits, the burning phase may occur. As described in [109], this type of flames is traditionally known as diffusion flames since both reactants are mainly transported independently by the diffusion process towards the reaction region. One of various configurations of the non-premixed flame burners is the planar counterflow arrangement as depicted in Figure 3.2 (left) where fuel and oxidizer streams are feeding the combustion chamber from opposite directions as the name implies.

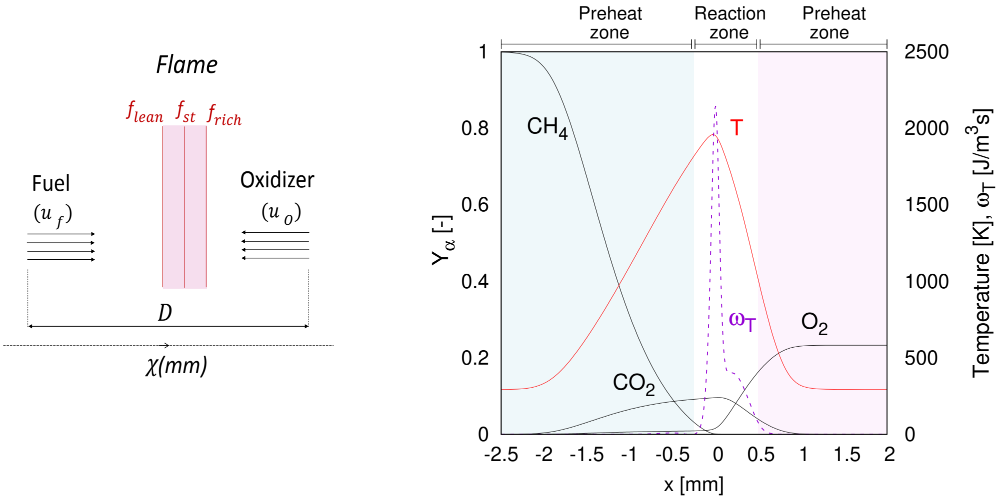

Figure 3.2: Basic schematic drawing of a non-premixed flame (left) and profiles of some species and temperature of a one-dimensional non-premixed CH_4/Air flame (right).

In Figure 3.2 (left) the velocity of the fuel and the burner are denoted by u_f and u_O respectively. These velocities define the strain rate a which is an important parameter that characterizes diffusion flames and largely determines how much the flame is compressed. Thereby it has the following expression:

$$a = \frac{u_f + u_O}{L}, \tag{3.11}$$

where L stands for the distance between both streams inlets.

According to [109], chemical reactions occur at molecular level thus the mixing has to take place just before the reaction phase where the combustion establishes almost around the interface separating both reactants. Chemical reactions are usually fast hence the transport and the mixing process control the burning rate instead of chemical kinetics.

Based on some combustion species evolutions and on the temperature profile, Figure 3.2 (right) illustrates a typical diffusion flame structure where the used fuel is methane and the strain rate $a = 100s^{-1}$. The preheat zones present the diffusion zones of the flame which are outside the ignition limits. In these regions, the diffusive mixing of the considered flows takes place, so that a combustible mixture is created. In the middle we have the reaction zone, where all mixture fraction values within the ignition limits including the stoichiometric mixture fraction are contained. Therein, the temperature and the chemical source term of the reaction reach their maximum values as shown in the diagram.

Unlike premixed flames, the flame speed and the flame thickness can not be considered in the case of diffusion flames. However, the flame position can be easily determined based on the velocity value of the reactant flows since the reactions can only take place in a small area, which presents the major advantage of diffusion flames in terms of flame stability.

As it was stated above, the diffusion and the mixing process are crucial aspects to be treated for non-premixed flames. Hence, in order to describe the mixing and reproduce properly the flame structure in reactive cases, the mixture fraction approach expressed in Eq 3.9 can be employed similarly to the studies in [5; 81; 95; 173]. In [173], with the application of the mixture fraction approach and transporting the variable f, the number of variables can be reduced. This has huge benefits especially if the used chemical mechanism involves hundred of species.

Among many definitions of the variable f, we adopt in this work the definition suggested by Bilger [9] which seemed to be more suitable in the case of hydrocarbon-oxygen reactions and is in accordance to many numerical studies [5; 81; 95; 149; 159]. This definition is based on the Z_p already presented in Eq 3.9 and considering the element mass fractions of carbon, hydrogen, and oxygen as with Z_C, Z_H and Z_O respectively. Thence the definition of Bilger mixture fraction f reads:

$$f = \frac{Z_p^* - Z_{p,Ox}^*}{Z_{p,fuel}^* - Z_{p,Ox}^*} \qquad \text{where} \qquad Z^* = 2Z_C + \frac{1}{2}Z_H + Z_O. \tag{3.12}$$

with $Z_{p,fuel}$ and $Z_{p,Ox}$ state for the element mass fractions of the element p in the fuel and the oxidizer, respectively.

Following the work of Künne in [95], dealing with reacting cases and in order to describe the mixing state in the considered domain, it is more appropriate to apply the passive scalar mixture fraction rather than the equivalence ratio (see Eq 3.7) since the last parameter is only valid for unburnt mixture. Thereby, the transported equation of this passive scalar f is defined as follows:

$$\frac{\partial(\rho f)}{\partial t} + \frac{\partial(\rho u_j f)}{\partial x_j} = \frac{\partial}{\partial x_j}\left(\frac{\mu}{Sc}\frac{\partial f}{\partial x_j}\right). \tag{3.13}$$

And by applying the Favre filter, the equation above reads:

$$\frac{\partial(\overline{\rho}\widetilde{f})}{\partial t} + \frac{\partial(\overline{\rho}\widetilde{u}_j\widetilde{f})}{\partial x_j} = \frac{\partial}{\partial x_j}\left[\frac{\overline{\mu}}{Sc}\frac{\partial \widetilde{f}}{\partial x_j} - \overline{\rho}(\widetilde{u_j f} - \widetilde{u}_j\widetilde{f})\right]. \tag{3.14}$$

3.2.3 Partially-Premixed Flames

Real industrial applications often operate in one combined form instead of the two idealized flame modes presented in subsections above. For these cases, "If the fuel and oxidizer enter separately, but partially mixed by turbulence before combustion, the turbulent flame propagates through a stratified mixture. Such a mode of combustion has traditionally been called partially premixed combustion" (Peters in [123]).

The RQL (Rich-Quench-Lean) strategy described in aircraft engine combustion chambers where a combination of non-premixed and premixed mixed combustion types can be employed to create a stable flame and to ensure pollutant-reduced combustion. Other technique like the Lean Partially Pre-vaporized (LPP) turbulent spray flames is employed to reduce the emission of NO_x for combustion engines [150].

3.3 Chemistry Reduction Techniques

The chemistry reduction plays a huge role for the numerical investigations of reacting flows specially for the hydrocarbon fuels combustion. The available simplification methods save enormously the time and the computational efforts since, contrary to the detailed reaction mechanisms, they do not involve thousands of complex elementary reactions with hundreds of species. This is highly important to be considered in the current study specially that the methane is employed as fuel in all investigated cases. Thereby, combining combustion chemistry reduction methods with the computational fluid dynamics (CFD) framework is necessary for the simulation of detailed technical cases.

One of many suggested approaches is the reduced chemical mechanisms where only certain elementary reactions and species are considered for the numerical calculations and not all elements that are involved in the reaction process. As reported in [81; 170], these mechanisms can be constructed based on two assumptions: some chemical elementary reactions are in partial equilibrium and certain species are considered in a quasi-steady state. Applying this technique can scale down noticeably the computational costs but restricts the application of the obtained chemical mechanisms only to the related-problem conditions. In addition, certain fine details connected to the combustion process are neglected which may affect the obtained results .

The Intrinsic Low-Dimensional Manifolds (ILDM) method for combustion process is a different chemistry reduction technique. It was first described and reported in 1992 by Maas and Pope [104] and it is based on the dynamical systems approach. By applying the same quasi-steady state and partial equilibrium assumptions, and based on an analysis of the eigenvalues, a mathematical scheme is followed where only the desired dimension of the reaction composition space is specified. However, this method does not involve diffusive processes which also affects its performance in the low-temperature zones as pointed out in [81].

Other simplification techniques are the chemistry tabulation/storage/retrieval approaches which are based on the manifolds arrangement. Depending on the employed reactants, the detailed reaction kinetics are computed in a preprocessing phase after solving laminar flames in physical space applying specific flamelet generators. The obtained results are arranged in function of two specified scalars, so-called controlling variables, and stored in a chemical look-up table to be exploited later on. All information about reaction species and flame thermodynamic states are then associated with the controlling variables. Thereby, the number of governing equations to be solved in the CFD code are limited to the number of the controlling variables used and based on the obtained solution, other features can be retrieved from the chemical look-up table.

As documented by Sadiki et al. in [152], these reduced chemical schemes are widely employed and different numerical investigations have been published to be common representatives of these methods. Kempf et al. in [87] and others in [14; 23] used a Steady Laminar Flamelet (SLF) model which is a classical model involving the mixture fraction and the scalar dissipation rate χ as controlling variables. However, due to the steady state assumption, missing information regarding the flame properties are noticed. In order to overcome these limitations, van Oijen and de Goey in [116] have introduced the Flamelet Generated Manifolds (FGM) tabulation technique where additionally to the mixture fraction f, a progress variable pv is defined as a controlling variable instead of the scalar dissipation χ. Following the same methodology, the flame Prolongation of ILDM (FPI) approach was documented by Gicquel et al. in [57]. These chemistry models were used in different studies as in [5; 68; 81; 115]. Fiorina et al. have introduced another approach for the chemistry simplifications where filtering techniques are employed to the chemical values stored in the look-up tables as reported in [43–45] and also employed in [167].

How the TCI is described in all these models depends on the solved transport equations. For this purpose, let us recall that the local composition of a non-premixed flame is strongly influenced by turbulent mixing, which itself causes kinetic effects in the chemical processes. Likewise chemical reactions and the resulting volume expansion lead to strong spatial and temporal density changes [96]. Due to a strong non-linear dependence of the averaged/filtered functions (e.g. chemical source terms) on the temperature and the species concentration of the gas mixture and to their strong fluctuations in turbulent flow due to the influence of turbulent processes on the chemical kinetics, the mean/filtered values of the function is not equal to the function of the mean/filtered values that are indeed employed to access the lookup table. To retrieve the required statistical information about the influence of turbulent processes on the kinetics and a statistical description that accounts for the turbulence-chemistry interaction, the concept used is based on the statistical description of the interaction by means of the PDFs for which a presumed based PDF approach is rather usually adopted.

3.3.1 Flamelet/Progress Variable (FPV) Model

The chemistry reduction was grounded also following the flamelet/progress variable (FPV) method which was developed by Pierce & Moin in [125] in order to overcome the problems and limitations of previous chemistry simplification models specially the Steady Laminar Flamelet approach. The mixture fraction f and the progress variable pv, tracing the local chemical reaction evolution, are likewise the controlling variables for the multidimensional chemistry. On the grounds that this model has shown good capability on reproducing the non-premixed turbulent flame properties as reported in several numerical investigations [71; 72; 142], it is then adopted in the current study and implemented in the CFD solver that is used for the simulation of the reacting cases. This approach applies a non-premixed freely-propagating laminar flames to generate the appropriate chemical data base. Once the flamelets equations are resolved in physical space, the filtered scalar quantities obtained (e.g chemical species composition, chemical rates of formation/destruction, temperature and density) are arranged along a look-up table where all chemical values are mapped into the two controlling variables space: mixture fraction f and progress variable pv. Additionally to that, the other flame thermo-chemical characteristics related to the burned and unburned states can be parameterized by using the advantage that the reaction progress variable permits the determination of local extinctions and re-ignition phenomena.

3.3.2 Adiabatic Tabulation Using FPV Approach

In the current study, the generation of the detailed reaction kinetics is done after solving in physical space adiabatic and laminar counter-flow steady flamelets at different strain rates from very small to extinguishing values and the state of the unsteady flamelet at the extinguishing strain rate. The calculations were done using the one-dimensional flamelet Flame-Master code which was developed by Heinz Pitsch (see [46]). During the simulations, the assumption of the unity Lewis number $Le = 1$ is followed where all chemical species have equal diffusion coefficients. Consequently, the effects of preferential diffusion is underestimated and the complexity of the reaction process is lowered. As reported in Künne [95], variations and discrepancies due to the unity Lewis number assumption are tolerable for simple fuel such as methane which is used in this investigation. The chemical mechanism used for the flamelets creation consists of 325 reactions and 53 species available in GRI-MECH 3.0 [64].

In fact, the creation of the FPV manifold from the generated flamelet tables is achieved in this study by means of Matlab code scripts. In the first steps, these flamelets are sorted according to the highest temperature in a given 2D f-pv space with 401 data points in the mixture fraction and 401 in the progress variable direction. With the assumption that at the highest temperature T_{max} there is also pv_{max} in way that with descending T_{max} the pv vectors descend over f. The pv_{max} values then are stored for all flamelets to be used for the normalization of the reaction progress variable in order to establish a statistical independence from the mixture f. The normalized pv_{norm} reads:

$$pv_{norm} = \frac{pv}{pv_{max}} \tag{3.15}$$

However, only non-normalized pv transport equation is solved within the applied CFD solver. By applying several interpolations on the used f-pv grid, all species concentrations and thermo-chemical properties are, after that, mapped into two-dimensional manifold in function of the controlling variables. Regarding the choice of the reaction progress variable, certain conditions should be fulfilled to properly define it as pointed out in [81]. These conditions concern:

- The monotonicity behavior of the pv variable over the flame front. Thereby the computed flame quantities are properly parametrized in function of pv.
- Covering the entire flame range.
- The high resolvability of the chosen pv to avoid numerical issues.

For reacting numerical investigations which follow the FPV model for chemistry reduction, the number of reaction progress variables should not be superior to two in favor of reducing the computational effort, but for most commonly studied cases, only one additional progress variable beside the mixture fraction is defined and employed. Hence, many different definitions of the reaction progress variable have been considered, but the frequently applied description involves a molar mass weighted combination of specific species concentrations. In the current study, and depending on the investigated case, two definitions of the variable pv have been adopted and expressed as follow:

- The Piloted Sandia flame-D case:

$$pv_{(FD)} = \frac{Y_{CO_2}}{M_{CO_2}} + \frac{Y_{CO}}{M_{CO}} + \frac{Y_{H_2O}}{M_{H_2O}}. \tag{3.16}$$

- The oxyfuel cases ($A1$, $A3$, $B3$):

$$pv_{(OX)} = \frac{Y_{H_2O}}{M_{H_2O}}. \tag{3.17}$$

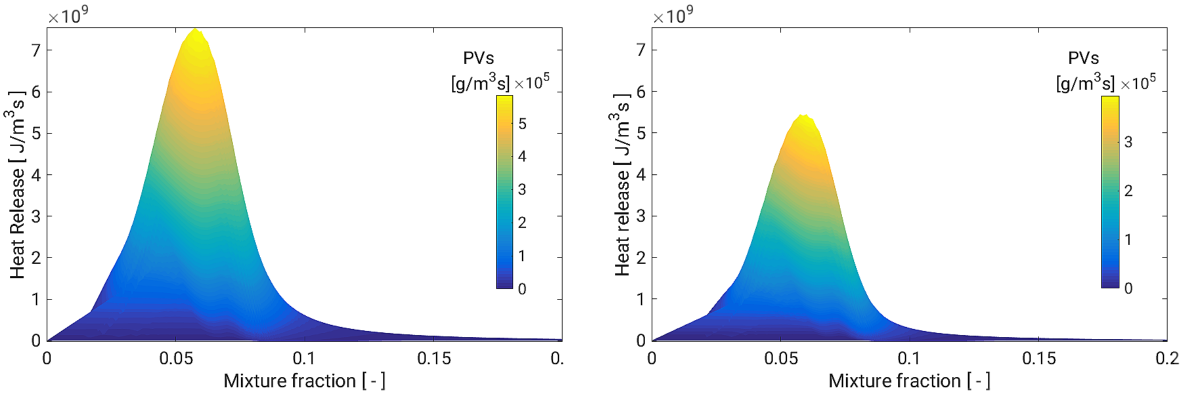

(a) **(b)**

Figure 3.3: Production rate of heat release in the mixture fraction space colored with source term $\dot{\omega}_{pv,OX}$. (a) distribution of heat release in flames $A1$, $B3$ tables, (b) distribution of heat release in flame $A3$ table [106].

For the Piloted Sandia flame-D case and contrary to Jesch and Cavalcanti in [19; 81] who have defined the reaction progress variable by the mass fraction of CO_2, the species CO and H_2O are currently added for several argumentations. Fiorina et al. demonstrated in [42] that CO mass fraction should be added in the definition of the reaction progress variable to ensure a completely monotonic behavior for different equivalence ratio values. Furthermore, the common addition of the H_2O specie concentration to the formulation

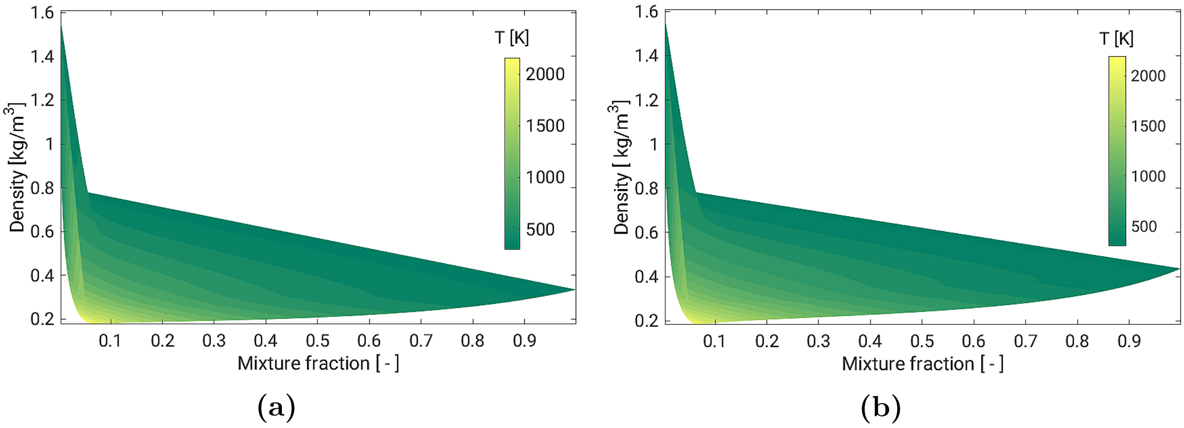

Figure 3.4: Density distributions in the mixture fraction space colored with temperature T. (a) density distribution in flames $A1$, $B3$ tables, (b) density distribution in flame $A3$ table [106].

above Eq 3.16 contributed to good results in the prediction of main flame features as documented by Pierce in [83] and the works of [72; 143].

In the case of the oxy-fuel flames ($A1$, $A3$, $B3$) the progress variable was defined according to the numerical investigation of Garmory & Mastorakos in [55] which is found that it is the appropriate definition for the corresponding oxy-flame cases as shown also in [7; 58]. For instance, Figure 3.3 and Figure 3.4 depict some properties from the FPV tables generated for the different oxy-flame series using the chosen pv. Figure 3.3 exhibits the distribution of the production rate of heat release colored by the source term of the progress variable in the mixture fraction space. However, Figure 3.4 illustrates the density distribution in oxy-flame series colored by the temperature in the mixture fraction space. As both fuel and oxidizer compositions are different from one case to another, the maximum value of heat release production rate is varying significantly and a change of the density distribution at high mixture fractions values is recorded [106].

After describing the tabulation procedure and properly defining the progress variables, the two-dimensional chemical manifold generated with f and pv is ready to be utilized in the CFD reacting solver where necessary parameters can be retrieved. Among these quantities, the chemical source term $\dot{\omega}_\alpha$ in Eq 2.18 can be than retrieved and exploited. As an example, the 3D diagram in Figure 3.5 illustrates the two-dimensional adiabatic manifold applied for the piloted jet Sandia flame-D case, where the chemical source term is plotted in function of the two controlling variables: the progress variable pv and the mixture fraction f. As shown in this representation, the source term varies significantly in the direction of the progress variable where the reaction zone occurs. The plot is colored with the temperature T that reaches its maximum in the vicinity of the stoichiometric mixture fraction value.

In some other works where the heat losses are taken into account, the enthalpy is merged in the chemical look-up table as third controlling variable, which is so far not considered in this study since we are limited in the first steps for the investigations of turbulent reacting cases with the application of only adiabatic chemical tables.

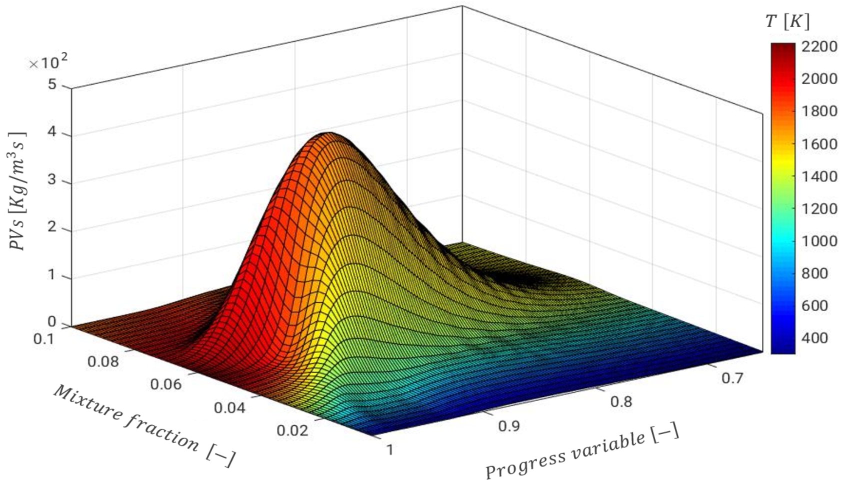

Figure 3.5: Visualization of the adiabatic two-dimensional chemical table applied in the current work for the Sandia flame D. The chemical source term $\dot{\omega}_{pv,FD}$ is given in function of f and pv and is colored with T values.

During the coupling with the CFD solver, only the two transport equations for the mixture fraction and the progress variable are added to the Navier-Stokes governing equations to be solved instead of solving all chemical species transport equations, as in the case of using the detailed chemistry. Below, we found the expressions of the applied equations which are properly implemented in both RANS and LES contexts. For the LES simulations filtered terms and sub-grid scale stresses and fluxes are considered.

$$\frac{\partial(\bar{\rho}\tilde{f})}{\partial t} + \frac{\partial(\bar{\rho}\tilde{u}_j\tilde{f})}{\partial x_j} = \frac{\partial}{\partial x_j}\left[\bar{\rho}\left(\frac{\bar{\mu}}{Sc} + \frac{\mu_t}{Sc_t}\right)\frac{\partial \tilde{f}}{\partial x_j}\right] \tag{3.18}$$

$$\frac{\partial(\bar{\rho}\widetilde{pv})}{\partial t} + \frac{\partial(\bar{\rho}\tilde{u}_j\widetilde{pv})}{\partial x_j} = \frac{\partial}{\partial x_j}\left[\bar{\rho}\left(\frac{\bar{\mu}}{Sc} + \frac{\mu_t}{Sc_t}\right)\frac{\partial \widetilde{pv}}{\partial x_j}\right] + \bar{\dot{\omega}}_{pv} \tag{3.19}$$

3.4 Summary

This chapter presents a general description of reacting turbulent flows where commonly used modeling approaches were reported. First, the theoretical background of chemical reactions and kinetics were presented. Then, the different flame types raised in the combustion process are addressed which are the premixed flames, non-premixed or so-called diffusion flames and partially premixed flames. In the last section, different chemistry reduction techniques were briefly introduced and the modeling approach employed in this work which is the Flamlet/Progress Variable (FPV) tabulated technique was outlined. Furthermore, the description of the whole procedure and the definitions of the reaction progress variables used for both investigated cases (Sandia flame D and oxy-fuel flame series) were presented. In order to couple the CFD combustion solver with turbulence models, flame-turbulence interaction model should be addressed in favor of obtained correct quantities while accessing the look-up table. This topic will be the focus of the following chapter.

Chapter 4

Turbulence-Combustion Interaction

Over the preceding chapters, both turbulence and chemistry topics have been individually addressed and described in detail reporting the modeling approaches and the simulation methods needed to investigate numerically the proposed cases. Hence, the subject of this chapter is mainly understanding the interaction between turbulence and combustion citing the different techniques in the context of coupling chemistry reduction approaches with the CFD solver. These techniques allow, with different degrees of performance, the determination of the unclosed terms that appear in the balance equations. The mean chemical source quantity is one of these unclosed terms and its determination presents a challenging task because of the strong non-linearity of chemical reaction rates. Thereby the focus here lies on the statistical approaches to turbulent combustion modeling which are the probability density functions (PDF) that will be then extensively described below. But, before establishing these approaches, different diagrams of the turbulent combustion will be presented and explained first.

4.1 Regime Diagrams of Turbulent Combustion

Different classical structures are proposed in the literature in order to characterize the different turbulent combustion regime diagrams. Many investigations based on DNS results and experimental data have been achieved in order to provide more details and extension of the classical combustion diagrams in [131]. For the turbulent premixed combustion, the widely accepted diagram is the representation that was originally suggested by Borghi [12] and later modified by Peters [122]. However, Poinsot & Veynante have intensively discussed and documented the turbulent non-premixed combustion diagram as shown in [130].

4.1.1 Premixed Combustion

The turbulent premixed combustion diagram presented in this section pursues the classical structure suggested by Peters in [122] as mentioned above. According to [149], the conception of the premixed combustion representation is mainly based on the ratios of relevant length and time scales which are the integral length scale l_I, the laminar flame thickness known as δ_l, the root mean square (rms) of the velocity fluctuation u' and the laminar flame speed s_l. The ratios of these quantities can be described according to certain non-dimensional numbers allowing the classification of different combustion regimes within the diagram.

- The Damköhler number Da [26] is the ratio of the characteristic turbulent integral time scale τ_t and chemical time scale τ_c . It is determined as:

$$Da = \frac{\tau_t}{\tau_c} = \frac{(l_I/u')}{(\delta_l/s_l)}. \tag{4.1}$$

- The Ka Karlovitz number [166] characterizes the relation between the time scales of the smallest turbulent eddies and the chemical time scales. This term is also formulated as the ratio of the laminar flame thickness and the Kolmogorov scale (η_κ) :

$$Ka = \frac{\tau_c}{\tau_\kappa} = \left(\frac{\delta_l}{\eta_\kappa}\right)^2. \tag{4.2}$$

- The turbulent Reynolds number Re_t :

$$Re_t = \frac{u' l_t}{\nu} = \frac{(l_I/\delta)}{(u'/s_l)}. \tag{4.3}$$

The different regimes of the turbulent premixed combustion can be distinguished through a combination of the above mentioned non-dimensional numbers in the diagram suggested by Peters [122], and illustrated in Figure 4.1. According to the description in [149], these regimes are essentially defined as follow :

- **The laminar combustion region**: As shown in Figure 4.1, this zone is the starting side of the diagram where no turbulence-flame interaction occurs. It is characterized by the laminar flamelets and delimited by $Re_t < 1$.
- **The flamelet regime**: It corresponds to the area of the region bounded by the lines $Ka < 1$ and $Re_t > 1$. In this region, which leads to a Damköhler number $Da < 1$, the chemical time scale are lower than the turbulent integral time scales.
- **The thickened-wrinkled flame regime**: This zone is outlined in the region where $1 < Ka \leq 100$ and it is also called as the **thin reaction zone**. Thus the smallest turbulent structures are able to affect the preheat zone of the flame, but the reactions are not disturbed by turbulence.
- **The thickened flame regime**: As sketched in Figure 4.1, this is the remaining part of the diagram where $Ka > 100$ and $Da < 1$. Here the turbulence disturbs the reaction zone and local extinctions may occur. Moreover, no laminar flame structures can be identified.

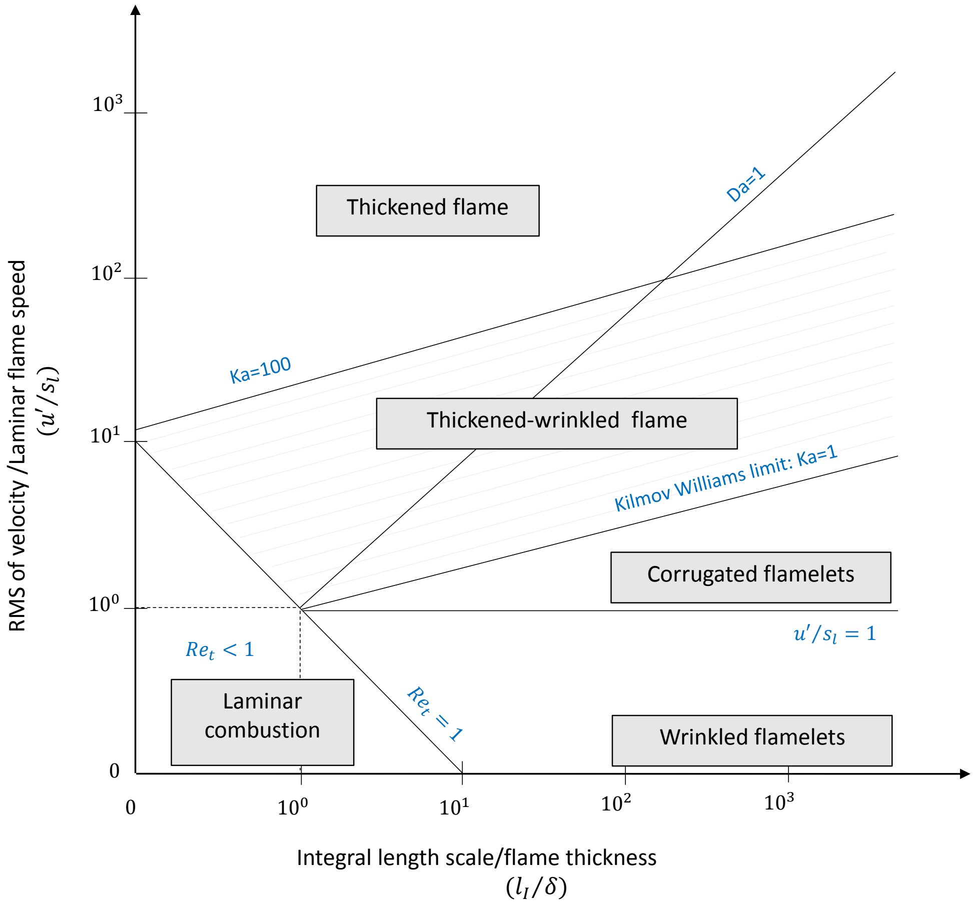

Figure 4.1: Premixed combustion regimes

4.1.2 Non-premixed Combustion

According to Poinsot & Veynante in [130], the construction of turbulent non-premixed combustion diagram with distinguished regimes is challenging and not easy once compared to the previous premixed combustion regime. The difficulties behind are related to the lack of well-defined length, time and velocity scales for the diffusion flames as they depend strongly on the flow conditions. Hence, the exact description of turbulent flame regimes and the precise construction of the corresponding diagram are still an open question. Consequently, additional assumptions are considered to interact the different flame-turbulence scales.

The different regimes in the non-premixed combustion diagram proposed by [130], are distinguished based on the comparison between certain quantities that have the following expressions:

- The mean scalar dissipation rate for the stoichiometric mixture fraction which is used to estimate the diffusion time scale τ_f:

$$\widetilde{\chi}_{st(f=f_{st})} \approx \frac{1}{\tau_f}. \tag{4.4}$$

- The local flame Damköhler number Da^{fl} which is the ratio of the characteristic time scale τ_f and chemical time scale τ_c and determined as:

$$Da^{fl} = \frac{\tau_f}{\tau_c} \approx \frac{1}{\widetilde{\chi_{st}}\tau_c}. \tag{4.5}$$

- The turbulent Reynolds number Re_t as formulated previously in Eq.(4.3).

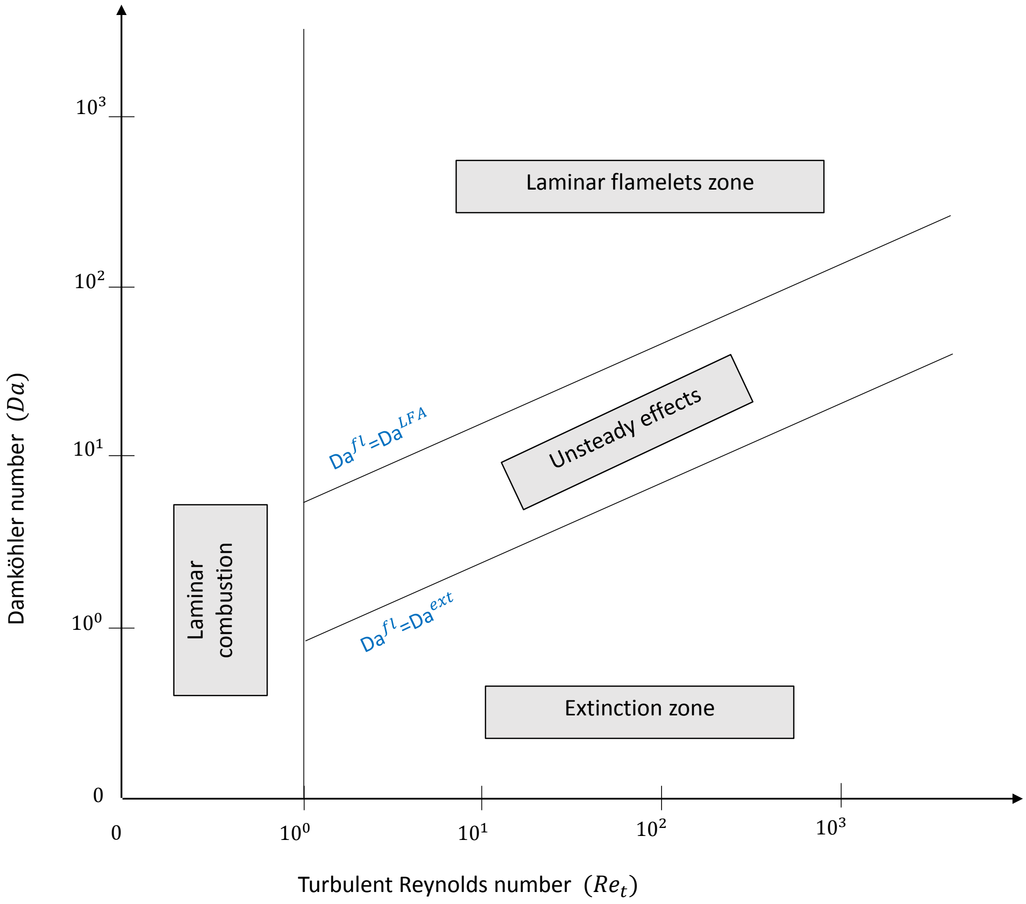

Figure 4.2: Non-premixed combustion regimes

Analogically to the preceding section, and conforming to the digram proposed in [130], the different regimes of the turbulent non-premixed combustion can be classified through relations between non-dimensional numbers described above as depicted in Figure 4.2. Basically, these regimes are delineated along these lines :

- **The laminar combustion region**: Similar to the Figure 4.1, this zone is outlined by the laminar flamelets and delimited by $Re_t < 1$.
- **The laminar flamelet assumption**: It conforms to the area limited by the curves ${D_a}^{fl} = {D_a}^{LFA}$ and $Re_t = 1$.
- **The Flame extinction zone**: As illustrated in Figure 4.2, this zone is defined for ${D_a}^{fl} = {D_a}^{ext}$ where extinction occurs for large chemical times τ_c.

Despite the fact that Poinsot & Veynante in [130] formulated the diagram in a comprehensive manner to explain qualitatively the turbulent diffusion flame regimes, it was notified that the corresponding diagram should be utilized with great care.

Furthermore, in the following sections, the focus will lie only on the non-premixed turbulent combustion and its modeling approaches since, as already mentioned, only diffusion flames are used for the current investigations.

4.2 Turbulence Combustion Interaction Modeling

As discussed in the previous sections, in order to calculate the different turbulent flow properties, the corresponding equations are generally expressed with averaged or filtered values for the RANS or LES contexts, respectively, instead of using the flow instantaneous values. The new unclosed terms that arise in the updated balance equations are defined based on the resolved quantities or on the proposed numerical approaches. However, the averaged/filtered unclosed source term $\dot{\omega}_\alpha$ can not be calculated directly based on the Arrhenius law due to the high non-linearity of the chemical reaction rates. Therefore, in order to account for the turbulence-chemistry interaction, various numerical methods have been suggested in the literature and they are generally based on physical and geometrical analysis (ATF [95], presumed PDF [81]), turbulent mixing approach (PaSR [39]) and local statistical analysis (Transported PDF [93]).

Among these combustion modeling approaches that have been proposed and can be also found in [130; 159; 166], the PDF methods are applied in this study with different techniques. The first method is the presumed PDF which is based on the beta-function (β-PDF) and the second approach is the transported probability density function (TPDF). More focus will lie essentially on the latter model which is combined with the Flamelet Progress Variable (FPV) technique. This hybrid method, newly proposed in the current work, is mainly applied for the investigated reacting cases and is compared to the classical β-PDF model for both RANS and LES frameworks. Nevertheless, for the sake of clarity and considering the different numerical difficulties levels, all details that concern the PDF approaches in the coming subsections will be described for the LES model but the final implemented PDF-equations will be expressed for both turbulent models in the summary.

4.2.1 Artificially Thickened Flame model (ATF)

The artificially thickened flame model was first introduced by Butler and O'Rourke [16] for premixed flames. Its fundamental concept consisted on considering an artificial flame thicker instead the real one which is typically between 0.1 and 0.5 mm. The goal of the ATF model is to allow the flame to be resolved on relatively affordable LES mesh including multiple computational cells with typical sizes larger than the real flame thickness (0.5 mm). Thereby, a thickening factor F is introduced into scalar transport equations to rescale the spatial and temporal flame coordinates keeping the laminar flame speed unaltered.

Although this TCI model has been applied in many studies ([95],[5], [81]), according to Kassinos et al. in [86], the major shortcoming of the ATF method is the reduction of the Damköhler number that changes the turbulence flame interaction. Similar observation is reported by Proch et al. in [136] where the response of the artificially thickened reaction zone to turbulence differs from the real one. Hence, it is always necessary to include additional wrinkling approaches to counteract this limitation. Attempts for non-premixed are being undertaken [103; 114].

4.2.2 Partially stirred reactor model (PaSR)

The PaSR combustion model, suggested by Golovitchev [61], is one of the well-known TCI methods that is based on the Eddy Dissipation Concept (EDC) model first introduced by Magnussen [105]. In this model it is assumed that main molecular-level mixing process and chemical reactions occur intensively within fine structures of the turbulent flow. The PaSR is conceptually similar to EDC method, but the reacting volume fraction is differently described [39]. Here, each computational control volume can be divided into two zones: reacting and non-reacting portions where each portion is characterized by its specific concentration [100].

Despite the large application of the PaSR model for the simulation of turbulent combustion systems, the original form of the method suffers from some drawbacks that are mainly related to the absence of state history account of fine structures. According to Shiryaeva and Sabelnikov [156], the smallest structures do not have sensitivity to the surrounding phenomena beyond the zone under consideration. Moreover, the change in time is not considered. Due to such shortcomings, different studies, where the PaSR combustion model was applied, have reported limitations in capturing some flame characteristics [65] especially in the prediction of NO_x species [101]. Thereby, different formulations have been proposed to extend the PaSR model in order to overcome the mentioned constraints [147; 156]. Also works by Alessandro and al. [101; 137] at ULB.

4.2.3 PDF Methods

According to the FPV method described in section 3.3.1, the different dependent scalars ϕ_α can be extracted from the chemical look-up table based on the filtered controlling variables $(\widetilde{f}, \widetilde{pv})$ with the knowledge that a filtered quantity does not acquire details on its corresponding sub-grid values. This fact leads, together with the high non-linearity relation, to the difficulties of determining the thermo-chemical state from the filtered values of a defining chemical scalar. Therefore, the sub-grid distribution has to be considered and the sub-filter probability density function (PDF) should be known in order to properly characterize the properties of the combustion products: mainly the mean chemical source term $\bar{\dot{\omega}}_\alpha$ that is required in the species equations. This can be mathematically described as:

$$\widetilde{\phi_\alpha(\psi)} \neq \phi_\alpha(\widetilde{\psi}) \qquad \text{but} \qquad \widetilde{\phi_\alpha} = \int_\psi \phi_\alpha(\psi)\mathcal{P}(\psi)\mathrm{d}\psi. \tag{4.6}$$

Here, $\mathcal{P}(\psi)$ stands for the probability density function (PDF) of the defining species $\widetilde{\phi_\alpha}$. The ψ represents a sample space of the species ϕ_α. The $\mathcal{P}(\phi_\alpha)$ evaluates the probability that the species ϕ_α takes values between ϕ_α and $\phi_\alpha + \mathrm{d}\phi_\alpha$, and in the LES framework, it refers to the sub-filter distribution of the quantity within a control volume not spatially, but statistically [93]. As a consequence, the normalization of the PDF reads:

$$\int \mathcal{P}(\phi_\alpha)\mathrm{d}\phi_\alpha = 1. \tag{4.7}$$

and the statistical moments can be estimated as follows:

$$\widetilde{\phi_\alpha} = \int \phi_\alpha \mathcal{P}(\phi_\alpha)\mathrm{d}\phi_\alpha \qquad \text{and} \qquad \widetilde{\phi_\alpha''^2} = \int \left(\phi_\alpha - \widetilde{\phi_\alpha}\right)^2 \mathcal{P}(\phi_\alpha)\mathrm{d}\phi_\alpha. \tag{4.8}$$

A realistic description of the filtered PDF is therefore an important part of modeling turbulent flames in order to define the unclosed terms. However, both PDF methods modeling and the reaction kinetics calculation are computationally expensive; hence, more simplifications and reduction approaches are adopted. Two different modeling techniques for the PDF methodology are presented:

- The transported Monte Carlo PDF approach which follows the Eulerian stochastic fields (ESF) method and coupled to the FPV model. This new hybrid approach (ESF/FPV) represents the essential part of the numerical modeling of the current study.
- The classical presumed PDF (β-PDF).

For the introduction into the basics, Pope in [132–134] and Haworth in [67] have explained with details the different PDF methods and their general applications for numerical problems.

4.2.3.1 Transported PDF: The Eulerian Stochastic Fields Method

The transport of the filtered composite PDF of the scalar fields $\mathcal{P}$ in the flow field is considered as one approach that allows the description of the chemical reactions on the unresolved scales. The temporal change of the PDF can be expressed using a transport equation, which has the advantage that the chemical source term $\bar{\dot{\omega}}_\alpha$ is expressed in closed form and no further closure modeling is required. In the following, the basics of the transport equation of the PDF (TPDF) are explained and the Eulerian stochastic fields approach is described in details in order to simplify the application of the TPDF equations.

Joint Probability Density Function

According to the description given by Avdić in [5] and also explained in references [133; 134; 160], for a specific instance of time t and at a fixed point x_i, the species ϕ_α implicated in the chemical reaction process can be described by a marginal probability density function $\mathcal{P}_\alpha$ which can be presented as follows:

$$\mathcal{P}_\alpha(\psi_i; x_i, t) = \delta(\psi_\alpha - \phi_\alpha(x_i, t)). \tag{4.9}$$

where δ stands for the Dirac delta function. Consequently, the joint PDF for all involved species is expressed by the product of all marginal probabilities density function $\mathcal{P}_\alpha$ in the following way:

$$\mathcal{F}(\psi; x_i, t) = \prod_{\alpha=1}^{N_\alpha} \mathcal{P}_\alpha(\psi_i; x_i, t) = \prod_{\alpha=1}^{N_\alpha} \delta(\psi_\alpha - \phi_\alpha(x_i, t). \tag{4.10}$$

Filtered Probability Density Function

In order to compute the filtered variables, it is also necessary to apply the spatial filter function G, described in subsection (2.3.3.1), on the fine-grained PDF $\mathcal{F}(\psi; x_i, t)$. The filtered (or the density weighted) joint subgrid probability density function $\widetilde{\mathcal{P}}_{sgs}(\psi)$ can be then expressed as:

$$\widetilde{\mathcal{P}}_{sgs}(\psi) = \frac{1}{\overline{\rho}} \int_V \rho(x_i - x'_i)\mathcal{F}(\psi; x'_i, t)G(x_i - x'_i)\mathrm{d}x'_i. \tag{4.11}$$

The transport equation for $\widetilde{\mathcal{P}}_{sgs}(\psi)$ can be obtained explicitly following the derivation proposed by Gao et al. in [52] and it reads:

$$\begin{aligned}
\underbrace{\frac{\partial \overline{\rho}\widetilde{\mathcal{P}}_{sgs}(\psi)}{\partial t}}_{\textbf{(1)}} + \underbrace{\frac{\partial \overline{\rho}\widetilde{u}_j\widetilde{\mathcal{P}}_{sgs}(\psi)}{\partial x_j}}_{\textbf{(2)}} - \underbrace{\sum_{\alpha=1}^{N_\alpha} \frac{\partial}{\partial \psi_\alpha}(\dot{\omega}_\alpha \overline{\rho}\widetilde{\mathcal{P}}_{sgs}(\psi))}_{\textbf{(3)}} = \\
- \underbrace{\frac{\partial}{\partial x_j}[((\widetilde{\rho u_j} - \overline{\rho}\widetilde{u}_j)|\phi_\alpha = \psi_\alpha)\widetilde{\mathcal{P}}_{sgs}(\psi)]}_{\textbf{(4)}} \\
- \underbrace{\sum_{\alpha=1}^{N_\alpha}\sum_{\beta=1}^{N_\beta} \frac{\partial^2}{\partial \psi_\alpha \psi_\beta}\left[\left(\overline{\rho}\widetilde{\mathcal{D}}\overline{\frac{\partial \phi_\alpha}{\partial x_i}\frac{\partial \phi_\beta}{\partial x_i}|\phi_j = \psi_j}\right)\widetilde{\mathcal{P}}_{sgs}(\psi)\right]}_{\textbf{(5)}}
\end{aligned} \tag{4.12}$$

The different terms of Eq 4.12 are clearly presented in order to explain the significations of each part. The first term (1) stands for the temporal evolution in the physical space, and, the convection by cause of mean velocity is represented by the second term (2). The third term of the equation (3) reveals the chemical source term in the sample space. All these three parts in the left side of the expression are in closed form and no further modeling is required, but the two terms in the right side are unclosed and some modeling approaches should be applied to estimate their values. Thence, a gradient approach is used for the fourth term (4) which describes the turbulent transport of the probability density function due to unresolved velocity fluctuations. This gradient diffusion approach is detailed and documented in [160] and the diffusion coefficient $\mathcal{D}$ is defined using the turbulent viscosity and the Schmidt numbers (Sc, Sc_{sgs}) as already shown in subsection 2.3.3.2.

The term (5) characterizes the micro-mixing which corresponds to the turbulent transport of the probability density function as a result of the molecular mixing. Generally, the modeling approach utilized to close this term is based on the Interaction by Exchange with the Mean model (IEM), which is discussed in [33; 168] and reported under the Linear Mean-Square Estimation named by Dopazo in [34; 55]. This approach (IEM or LMSE) was employed in numerous published studies [76; 106; 107]. Hence, by using this model, the last term is expressed as follows:

$$\sum_{\alpha=1}^{N_\alpha}\sum_{\beta=1}^{N_\beta}\frac{\partial^2}{\partial\psi_\alpha\psi_\beta}\left[\left(\overline{\rho}\widetilde{\mathcal{D}}\overline{\frac{\partial\phi_\alpha}{\partial x_i}\frac{\partial\phi_\beta}{\partial x_i}|\phi_j=\psi_j}\right)\widetilde{\mathcal{P}}_{sgs}(\psi)\right]=-\frac{\overline{\rho}}{\tau_{sgs}}\sum_{\alpha=1}^{N_\alpha}\left[(\psi_\alpha-\widetilde{\phi}_\alpha)\widetilde{\mathcal{P}}_{sgs}(\psi)\right]. \quad (4.13)$$

Here, the τ_{sgs} states for the time scale of the turbulent mixture which is evaluated in the current study based on mixing time model referring to Jones et al in [83]. Thence, this term reads:

$$\frac{1}{\tau_{sgs}}=C_\zeta\left(\frac{\mu+\mu_{sgs}}{\overline{\rho}\Delta^2}\right)\quad\text{where}\quad C_\zeta=2. \quad (4.14)$$

Various other micro-mixing approaches have been proposed in literature [69; 77] with different values of the constant C_ζ, but according to Jones et al. in [83] and Avdić in [5], the suitable value of the coefficient is given as $C_\zeta = 2$. Furthermore, after applying the equal diffusivity in the current work, the final expression of the modeled filtered joint probability density function $\mathcal{P}_{sgs}(\psi)$ reads:

$$\begin{gathered}\frac{\partial\overline{\rho}\widetilde{\mathcal{P}}_{sgs}(\psi)}{\partial t}+\frac{\partial\overline{\rho}\widetilde{u}_j\widetilde{\mathcal{P}}_{sgs}(\psi)}{\partial x_j}-\sum_{\alpha=1}^{N_\alpha}\frac{\partial}{\partial\psi_\alpha}(\dot{\omega}_\alpha\overline{\rho}\widetilde{\mathcal{P}}_{sgs}(\psi))=\\ \frac{\partial}{\partial x_j}\left[\left(\frac{\widetilde{\mu}}{Sc}+\frac{\mu_{sgs}}{Sc_{sgs}}\right)\frac{\partial\widetilde{\mathcal{P}}_{sgs}(\psi)}{\partial x_i}\right]-\frac{\overline{\rho}}{\tau_{sgs}}\sum_{\alpha=1}^{N_\alpha}\left[(\psi_\alpha-\widetilde{\phi}_\alpha)\widetilde{\mathcal{P}}_{sgs}(\psi)\right]\end{gathered} \quad (4.15)$$

Eulerian Stochastic Fields Approach

Toward solving the modeled transport probability density function $\mathcal{P}_{sgs}(\psi)$ in equation (4.15), a more recent formulation of the Eulerian stochastic fields (ESF) method introduced by Valińo in [165] and Jones and Martinez [83] is applied in the current study. This methodology is adopted also in the published reviews by Mahmoud et al. in [106; 107]. In this formulation, and in conjunction with the FPV chemistry reduction approach, the temporal evolution of the sub-grid joint PDF is expressed by an ensemble of N_s Eulerian stochastic fields $\xi_\alpha^n(x_i,t)$ constructed for each tabulated controlling parameter $\alpha \equiv (f, pv)$ for the complete considered domain. Therefore, the stochastic differential equation (SDE) that is obtained to describe the transport PDF equation is expressed in Itô-form as follows:

$$\begin{aligned}\underbrace{\mathrm{d}(\overline{\rho}\xi_\alpha^n)}_{\textbf{(1)}} + \underbrace{\frac{\partial(\overline{\rho}\widetilde{u}_i\xi_\alpha^n)}{\partial x_i}\mathrm{dt}}_{\textbf{(2)}} - \underbrace{\frac{\partial}{\partial x_i}\left[\left(\frac{\widetilde{\mu}}{Sc} + \frac{\mu_{sgs}}{Sc_{sgs}}\right)\frac{\partial \xi_\alpha^n}{\partial x_i}\right]\mathrm{dt}}_{\textbf{(3)}} &= \underbrace{\overline{\rho}\dot{\omega}_\alpha^n(\xi_\alpha^n)\mathrm{dt}}_{\textbf{(4)}} \\ &- \underbrace{\frac{\overline{\rho}}{2\tau_{sgs}}(\xi_\alpha^n - \widetilde{\phi}_\alpha)\mathrm{dt}}_{\textbf{(5)}} + \underbrace{\sqrt{2\overline{\rho}(\frac{\mu_{sgs}}{Sc_{sgs}})}\frac{\partial \xi_\alpha^n}{\partial x_i}\mathrm{dW_i^n}}_{\textbf{(6)}}.\end{aligned} \tag{4.16}$$

with $1 \leqslant n \leqslant N_s$ and $1 \leqslant \alpha \leqslant N_\alpha$.

Similarly to the Eq (4.15), the first term (1) in Eq 4.16 is for the temporal variation, the second term (2) is the convective transport in real space, the term (3) expresses the diffusive transport while the term (5) is the molecular mixing. Additionally, the chemical source term, defined by term (4), is finally in closed form and is determined based on the evolution of the controlling variables, and its value can be retrieved from the chemical table.

However, the term (6) is newly raised after derivation and stands for the stochastic term. Following the recent formulation proposed by Valińo in [165], only the subgrid diffusivity $(\frac{\mu_{sgs}}{Sc_{sgs}})$ is included in this term in order to avoid unphysical fluctuations generated from the stochastic term within laminar regimes. The $\mathrm{dW_i^n}$ in term (6) presents the vector Wiener term that is spatially uniform, varies in time and is different for each stochastic field according to [5; 53; 106; 107]. Hence, for N_s stochastic fields the Wiener term is determined by multiplying the time-step Δt and the dichotomic vector following the relation:

$$\mathrm{dW_i^n} = N(0,1)\sqrt{\Delta t} \quad \text{with} \quad N(0,1) \approx [-1,+1] \tag{4.17}$$

Here the discrete time-step Δt is defined between the temporal sample t_n and t_{n+1}. It is important to note that the N_s stochastic fields do not reflect N_s physical flow realizations, but represents a stochastic system where the differential equations of the transported PDF are solved according to the number of controlling variables and N_s. The filtered mean and variances of species ϕ_α can be calculated as :

$$\widetilde{\phi}_\alpha = \frac{1}{N_s}\sum_{n=1}^{N_s} \xi^n_\alpha \qquad \text{where} \quad \alpha \equiv (f, pv). \tag{4.18}$$

$$\widetilde{\phi}^2_{\alpha,sgs} = \frac{1}{N_s}\sum_{n=1}^{N_s} (\xi^n_\alpha)^2 - (\widetilde{\phi}^2_\alpha). \tag{4.19}$$

4.2.3.2 Presumed PDF: The β-PDF Method

In the present work, the classical presumed probability density function approach is chosen to be applied in order to be compared with the previous proposed method in terms of prediction capability of the numerical technique for capturing main flame properties. This approach is used based on the two chemical table controlling variables (f, pv) and on the variance of the mixture fraction (f''^2) which allows the description of the distribution of the mixture within each control volume. Consequently, the mean value of a ϕ scalar in the given cell can be estimated based on the corresponding filtered probability density function as:

$$\widetilde{\phi} = \int\int \phi(f, f''^2, pv)\widetilde{\mathcal{P}}(f, f''^2, pv)\mathrm{d}f\mathrm{d}pv. \tag{4.20}$$

where the $\phi(f, f''^2, pv)$ values are extracted from the pre-integrated chemical look-up table that is generated anteriorly to the numerical simulations. In the context of presumed-PDF, the variables are generally considered statistically independent. Therefore, the joint PDF can be described as the product of a presumed Beta-function (β)-PDF for the mixture fraction (see [93; 130; 152] for more details) and a Dirac delta-function (δ)-PDF for the reaction progress variable. Consequently, the $\widetilde{\phi}$ scalar is obtained according to:

$$\widetilde{\phi} = \int\int \phi(f, pv)\widetilde{\mathcal{P}}_\beta(\widetilde{f}, \widetilde{f''^2})\widetilde{\mathcal{P}}_\delta(\widetilde{pv})\mathrm{d}f\mathrm{d}pv. \tag{4.21}$$

The β-function of the mixture fraction is defined by the following equation :

$$\widetilde{\mathcal{P}}_\beta(\widetilde{f}, \widetilde{f}''^2) = \frac{f^{(\alpha-1)}(1-f)^{(1-\beta)}}{\int_0^1 f^{(\alpha-1)}(1-f)^{(\beta-1)}\mathrm{d}f} \tag{4.22}$$

where certainly the two parameters α and β are determined using the statistical moments of the mixture fraction f as:

$$\alpha = \widetilde{f}\left(\frac{\widetilde{f}\left(1-\widetilde{f}\right)}{\widetilde{f''^2}} - 1\right) \qquad \text{and} \qquad \beta = (1-\alpha). \tag{4.23}$$

4.2.3.3 Summary of resolved equations

By using the newly proposed hybrid ESF/FPV method and with the generation of only adiabatic chemical look-up tables, N_s stochastic transport equations for each controlling variable (f, pv) are additionally considered. This set of stochastic differential equations is implemented in the CFD solver and require to be solved with Navier-Stokes governing equations.

The corresponding stochastic differential equations are:

$$\begin{aligned} \mathrm{d}(\overline{\rho}\xi_f^n) + \frac{\partial(\overline{\rho}\widetilde{u}_j\xi_f^n)}{\partial x_i}\mathrm{dt} - \frac{\partial}{\partial x_i}\left[(\frac{\widetilde{\mu}}{Sc} + \frac{\mu_{sgs}}{Sc_{sgs}})\frac{\partial \xi_f^n}{\partial x_i}\right]\mathrm{dt} = &-\frac{\overline{\rho}}{2\tau_{sgs}}(\xi_f^n - \widetilde{\phi}_f)\mathrm{dt} \\ &+\sqrt{2\overline{\rho}(\frac{\mu_{sgs}}{Sc_{sgs}})}\frac{\partial \xi_f^n}{\partial x_i}\mathrm{dW_i^n}. \end{aligned} \tag{4.24}$$

$$\begin{aligned} \mathrm{d}(\overline{\rho}\xi_{pv}^n) + \frac{\partial(\overline{\rho}\widetilde{u}_j\xi_{pv}^n)}{\partial x_i}\mathrm{dt} - \frac{\partial}{\partial x_i}\left[(\frac{\widetilde{\mu}}{Sc} + \frac{\mu_{sgs}}{Sc_{sgs}})\frac{\partial \xi_{pv}^n}{\partial x_i}\right]\mathrm{dt} &= \overline{\rho}\dot{\omega}_{pv}^n(\xi_{pv}^n)\mathrm{dt} \\ -\frac{\overline{\rho}}{2\tau_{sgs}}(\xi_{pv}^n - \widetilde{\phi}_{pv})\mathrm{dt} &+ \sqrt{2\overline{\rho}(\frac{\mu_{sgs}}{Sc_{sgs}})}\frac{\partial \xi_{pv}^n}{\partial x_i}\mathrm{dW_i^n}. \end{aligned} \tag{4.25}$$

for $1 \leqslant n \leqslant N_s$.

Furthermore, by applying the classical β-PDF approach and in conjunction with the FPV model, three transport equations are added to the continuity and momentum equations. They correspond to the mixture fraction, the variance of mixture fraction and the reaction progress variable. These equations read:

$$\frac{\partial(\overline{\rho}\widetilde{f})}{\partial t} + \frac{\partial(\overline{\rho}\widetilde{u}_j\widetilde{f})}{\partial x_j} = \frac{\partial}{\partial x_j}\left[\overline{\rho}\left(\frac{\overline{\mu}}{Sc} + \frac{\mu_{sgs}}{Sc_{sgs}}\right)\frac{\partial \widetilde{f}}{\partial x_j}\right], \tag{4.26}$$

$$\begin{aligned} \frac{\partial(\overline{\rho}\widetilde{f''^2})}{\partial t} + \frac{\partial(\overline{\rho}\widetilde{u}_j\widetilde{f''^2})}{\partial x_j} =& \frac{\partial}{\partial x_j}\left[\overline{\rho}\left(\frac{\overline{\mu}}{Sc} + \frac{\mu_{sgs}}{Sc_{sgs}}\right)\frac{\partial \widetilde{f''^2}}{\partial x_j}\right] + \\ & 2\overline{\rho}\frac{\mu_{sgs}}{Sc_{sgs}}\left(\frac{\partial \widetilde{f}}{\partial x_j}\right)^2 - C_f\frac{\mu_{sgs}}{Sc_{sgs}}(\frac{\widetilde{f''^2}}{\Delta^2}), \end{aligned} \tag{4.27}$$

$$\frac{\partial(\overline{\rho}\widetilde{pv})}{\partial t} + \frac{\partial(\overline{\rho}\widetilde{u}_j\widetilde{pv})}{\partial x_j} = \frac{\partial}{\partial x_j}\left[\overline{\rho}\left(\frac{\overline{\mu}}{Sc} + \frac{\mu_{sgs}}{Sc_{sgs}}\right)\frac{\partial \widetilde{pv}}{\partial x_j}\right] + \overline{\dot{\omega}}_{pv}. \tag{4.28}$$

Regarding the RANS framework, similar approaches have been applied and the reader is referred to the Appendix A for the summary of these resolved equations.

4.3 Summary

This chapter presents main features of turbulence-combustion interaction and its modeling approaches. In the first section, the different characteristics of the accepted turbulent combustion diagrams were presented through the description of the different regimes for both premixed and non-premixed flames. Furthermore, in order to solve the different governing equations and determine the unclosed terms specifically the mean chemical source term, PDF methods are specified referring to the applied turbulence-chemistry interaction modeling approaches. Two techniques have been adopted: the presumed PDF based on β-function and the transported PDF which follows the Eulerian Stochastic fields methodology. The latter approach, in conjunction with the FPV chemistry reduction technique, stands for the newly hybrid proposed model which is the center of our research interest in the present work. By applying this method, the unclosed chemical terms can be calculated without further assumptions which reflects the accuracy of the proposed method in terms of prediction capability in reproducing the main turbulent flame properties.

Regarding the FPV chemistry approach, a look-up table is generated based on the kinetics computation of non-premixed flamelets. Also a pre-integrated table is established to be accessed once the presumed PDF is applied.

Chapter 5

Numerical Implementations

The governing equations, listed in section 2.1, involve spatial partial derivatives of first and second order along with time derivatives. Therefore, the application of numerical methods in order to discretize and solve these equations is mandatory since analytical solutions can not be used. Specific numerical treatments should be considered in the current study since challenging three dimensional turbulent combustion cases, which include different initial and boundary limits and specific physical conditions, are investigated.

In this work, open-source CFD code OpenFOAM (Open Field Operation And Manipulation), in the version 2.3.0, was utilized and further developed for all simulations. In this C++ libraries based code, the formalism of Finite Volumes discretization is implemented and is used for the numerical calculations that were established for both RANS and LES frameworks. As reported in [113] an overview of many of the accessible standing discretization techniques and numerical solution methods are described and documented in the thesis of Jasak in [80], and more recent techniques can be found in the official OpenFOAM documentation in [117; 118]. Furthermore, the numerical tools that are proposed and described in previous sections, are implemented in OpenFOAM code according to *reactingFoam* which is a transient solver primarily designed to treat non-premixed turbulent combustion. The names of the developed solvers are *stochasticFieldsFPVFoam* and *FPVFoam* that treat the ESF/FPV method and the β-PDF/FPV approach respectively. Main focus will lie on the development and the implementation of the *stochasticFieldsFPVFoam* solver since it reflects the newly improved hybrid ESF/FPV method that is currently investigated. Moreover, the solver was implemented as part of extending the in-house developed OpenFOAM libraries in order to treat turbulent combustion problems.

The three-dimensional numerical grids employed for the LES investigations are generated applying the mesh-generator software ANSYS-ICEM CFD [3]. These grids consist on block-structured hexahedral meshes where the O-grid arrangement was employed for local refinements and better grid-resolution. However, the two-dimensional meshes, that were applied in the RANS framework, were simply generated with the standard *blockMeshDict* utility that comes within OpenFOAM packages.

In the first part of this chapter, the methodology for solving the Navier-Stokes equations is detailed where discretization tools are described in order to treat fluid-flow problems. In this respect, spatial and time discretization techniques and the pressure-velocity coupling method are explained for the solution domain. Moreover, in the subsequent part, the numerical treatment of the applied solvers is outlined and the focus is devoted to the solver with the Eulerian stochastic fields approach and its overall solution procedure.

5.1 General solution procedure

As mentioned above, analytical solutions are difficult to be applied in order to solve the Navier Stokes equations. Therefore, the alternative approach is to use efficient numerical techniques which are based on the Finite Volume Method (FVM) [112]. In the computational fluid dynamics, the FVM is generally the most adopted discretization method of the transport equations.

In the coming subsection, the general solution procedure for the different discretization aspects of the considered equations is demonstrated according to the implementations in the OpenFOAM framework [80]. Hence, the first part concerns the spatial discretization of the computational domain while the temporal discretization is addressed in the second part. Then, the pressure-velocity coupling procedure is detailed in the ensuing subsection, followed by the numerical treatment of the initial and boundary conditions.

5.1.1 Spatial discretization

As documented in [70] and following the description in [145], in OpenFOAM code and based on the FVM, the solution domain is discretized spatially over a numerical grid that is composed of finite number of cells or the so-called control volumes. Giving more flexibility regarding the topology of the control volumes, the fluid-flow variables such as velocity and pressure are described at the same set of discrete locations which are usually the geometric center of the grid control volumes [63; 145].

The utilized grid notations and arrangements describing the control volumes within OpenFOAM platform are described in Figure 5.1, where P and N are the cell centroid of two adjacent control volumes and d_i stands for the vector between two cells geometric centers. S_{fi} represents one specific flat surface among a set of flat surfaces that are bordering the control volume. These flat faces can be classified as internal faces relating 2 control volumes or as boundary faces.

In order to describe the discretization procedure and the interpolation tools by applying the finite volume method, a generic equation of a scalar Φ exemplifying the general form of the governing balance equations is expressed as follows:

$$\underbrace{\frac{\partial}{\partial t}(\rho\Phi)}_{\text{time derivative part}} + \underbrace{\frac{\partial}{\partial x_i}(\rho u_i \Phi)}_{\text{convection part}} = \underbrace{\frac{\partial}{\partial x_i}\left(\frac{\partial \Phi}{\partial x_i}(\rho D_\Phi)\right)}_{\text{diffusion part}} + \underbrace{\dot{\omega}_\Phi}_{\text{source term}} \quad . \tag{5.1}$$

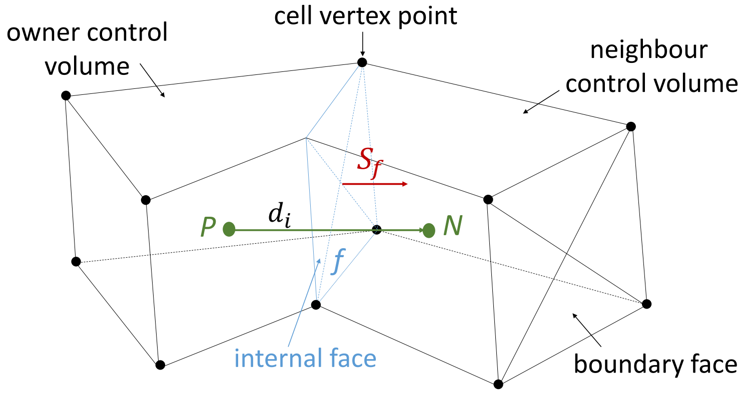

Figure 5.1: Basic schematic of control volume including the numerical grid nomenclature according to OpenFOAM.

Starting from the left side of the equation, the different terms demonstrate the time derivative or the temporal change, convection part, diffusion part with the diffusion coefficient D_Φ and the source term $\dot{\omega}_\Phi$ of the quantity Φ. The conversion of the equation (5.1) to its integral form over a random control volume V is necessary to be numerically resolved which leads to the following expression:

$$\int\limits_V \frac{\partial}{\partial t}(\rho\Phi)\,\mathrm{d}V + \int\limits_V \frac{\partial}{\partial x_i}(\rho u_i \Phi)\,\mathrm{d}V = \int\limits_V \frac{\partial}{\partial x_i}\left(\frac{\partial \Phi}{\partial x_i}(\rho D_\Phi)\right)\mathrm{d}V + \int\limits_V \dot{\omega}_\Phi \mathrm{d}V. \tag{5.2}$$

With the application of the Gauss's theorem [40], the volume integrals ($\mathrm{d}V$) of the convective and diffusive fluxes parts can be reconstructed into surface integrals ($\mathrm{d}S$) with S is the surface bounding the control volume and n_i is the unity vector normal to the surface S. Hence the equation (5.2) is transformed to:

$$\int\limits_V \frac{\partial}{\partial t}(\rho\Phi)\,\mathrm{d}V + \int\limits_S \rho u_i \Phi n_i \mathrm{d}S = \int\limits_S \left(\frac{\partial \Phi}{\partial x_i}\rho D_\Phi\right) n_i \mathrm{d}S + \int\limits_V \dot{\omega}_\Phi \mathrm{d}V, \tag{5.3}$$

As stated in [145], the volume integral of quantity Φ over the corresponding control volume can be evaluated by applying the midpoint rule once the value of this variable is estimated to a suitable average value of the quantity Φ at the cell center P and over the entire control volume. Hence the volume integral reads:

$$\int\limits_V \rho\Phi \mathrm{d}V \approx \rho_P \Phi_P \int\limits_V \mathrm{d}V = \rho_P \Phi_P V. \tag{5.4}$$

where the quantity Φ_P stands for the value of Φ at the cell center P. Analogously, and with f is the considered face, the surface integrals approximation is obtained as:

$$\int\limits_S \rho\Phi u_i \mathrm{d}S \approx \rho_f \Phi_f u_i \int\limits_{S_f} \mathrm{d}S_f = \rho_f \Phi_f u_i S_f. \tag{5.5}$$

Furthermore, the surface integral estimation can be established by considering the sum of the integrals of all flat faces that are bounding the grid cell (six faces for each hexahedron control volume). Thereby, the new form of the equation (5.3) reads:

$$\left(\frac{\partial(\rho_p \Phi_p)}{\partial t}\right)_P V + \sum_f \rho_f \Phi_f u_i S_f = \sum_f \left(\frac{\partial \Phi}{\partial x_i}\right)_f (\rho D_\Phi)_f S_f + \int_V \dot{\omega}_\Phi \mathrm{d}V. \tag{5.6}$$

Besides the estimation of the value of the quantity Φ on the cell face, the approximation of the corresponding derivatives at the same locations by interpolation of variable values at the cell center P and neighboring points is required to evaluate the convective and diffusive fluxes (see [145]). Also, the last term of the previous equation which stands for the source term, has to be discretized.

5.1.1.1 Convective Fluxes

As already shown in the previous subsection, the convection (or advection) term is integrated over a control volume and can be linearized according to:

$$\int_V \frac{\partial}{\partial x_i}(\rho u_i \Phi)\,\mathrm{d}V = \int_S (\rho u_i \Phi)\mathrm{d}S \approx \sum_f \Phi_f \underbrace{(\rho u_i)_f S_f}_{\mathcal{F}}. \tag{5.7}$$

where according to the description and notations in [118], $\mathcal{F}$ expresses here the mass flux through the surface f. The variable value of Φ_f on cell-face f can be approximated via several schemes. Mainly three schemes are often applied:

- **Central differencing (CD)**: is unbounded interpolation for the convection scheme and defined with:

$$\Phi_f = \frac{\overline{fN}}{\overline{PN}}\Phi_P + (1 - \frac{\overline{fN}}{\overline{PN}})\Phi_N \tag{5.8}$$

  where $\overline{fN}$ is the distance separating the cell-face f and the centroid N and $\overline{PN}$ is the distance separating the cell-centers P and N.

- **Upwind differencing (UD)**: is bounded and Φ_f value can be determined based on the flow direction according to:

$$\Phi_f = \begin{cases} \Phi_P & for \quad \mathcal{F} \geqslant 0 \\ \Phi_N & for \quad \mathcal{F} < 0 \end{cases} \tag{5.9}$$

- **Blended differencing (BD)**: blends the two previous schemes ((CD)(UD) in order to keep the boundedness.

In the current work, the (UD) and (BD) interpolation schemes are applied in order to estimate the bounded scalar and vector fields respectively. Among these schemes, the total variation diminishing (TVD) scheme is also used.

5.1.1.2 Diffusive Fluxes

Analogously to the advection fluxes approximation and following the same OpenFOAM documentation [118], the diffusion (or Laplacian) term is integrated over a control volume and can be linearized according to:

$$\int_V \frac{\partial}{\partial x_i}\left(\frac{\partial \Phi}{\partial x_i}(\rho D_\Phi)\right)\mathrm{d}V = \int_S \frac{\partial \Phi}{\partial x_i}(\rho D_\Phi).\mathrm{d}S = \sum_f (\rho D_\Phi)_f \left(\frac{\partial \Phi}{\partial x_i}\right)_f S_f. \tag{5.10}$$

The numerical meshes are considered orthogonal in case that the length vector d_i separating the centroids P and N is parallel to S_f. For this type of grids, face gradient is implicitly discretized as:

$$S_f(\frac{\partial \Phi}{\partial x_i})_f = |S_f|\frac{(\Phi_N - \Phi_P)}{|d_i|}. \tag{5.11}$$

However, according to OpenFOAM discretization schemes, additional correction term is explicitly included in the case of non-orthogonal meshes. Regarding the last point, the interested reader is referred to Ries in [145] for further details.

5.1.1.3 Source term discretization

In this study, the last term $\dot{\omega}_\Phi$ in the generic balance equation (5.1) stands for the chemical source term which is characterized by the non-linear relation with the quantity Φ. Hence,the source term can be linearized as:

$$\dot{\omega}_P(\Phi) = \dot{\omega}_P^c + \dot{\omega}_P^p \Phi_P. \tag{5.12}$$

where the letter c stands for constant so the term $\dot{\omega}_P^c$ is the constant part of the source term and $\dot{\omega}_P^p$ represents the coefficient of variable Φ_P [119; 145]. Therefore, an approximation of the volume integral of the source term can be obtained as follows:

$$\int_V \dot{\omega}_P(\Phi)\mathrm{d}V = (\dot{\omega}_P^c + \dot{\omega}_P^p \Phi_P)V. \tag{5.13}$$

5.1.2 Time discretization

Besides the spatial discretization of the source term, the advection and the diffusion parts of the generic balance equation (5.1), the time derivative requires also to be numerically approximated. This is established in this work according to two time integration schemes that are classified here as implicit methods: the Euler method and the second-order backward-differencing scheme that were used for RANS and LES simulations respectively. These two techniques are implemented in the standard OpenFAOM framework and will be described in the following passages.

But let's consider first, the semi-discretized form of the generic equation which reads:

$$\left(\frac{\partial}{\partial t}(\rho_P \Phi_P)\right)_P = \mathcal{R}_\Phi \tag{5.14}$$

$$\text{with} \quad \mathcal{R}_\Phi = \frac{1}{V}\left[-\sum_f \mathcal{F}_f \Phi_f + \sum_f (\rho D_\Phi)_f \left(\frac{\partial \Phi}{\partial x_i}\right)_f S_f + (\dot{\omega}_P^c + \dot{\omega}_P^p \Phi_P)V)\right]. \tag{5.15}$$

For shortness reasons, the quantity $\mathcal{R}_\Phi$ expresses here all the spatial terms that were so far discretized and it has to be evaluated in conjunction with the temporal change term in order to determine the cell's value Φ_P. Contrary to explicit methods where the quantity Φ_P is estimated based on solving a simple linear system that includes only the current time level values, the discretization of $\mathcal{R}_\Phi$ in the implicit methods depends on solving a system of ordinary differential equations including current and previous time levels to calculate Φ_P. Thereby, despite the fact that implicit methods are computationally more expensive, the time step criterion known as Courant-Friedrichs-Lewy (CFL) number [25] can reach higher values.

The description of the proposed techniques of the temporal term discretization is reported below, where three time levels are introduced as:

$$\underbrace{\Phi^n \equiv \Phi(t+\Delta t)}_{\text{solving time level}}, \qquad \underbrace{\Phi^{(n-1)} \equiv \Phi(t)}_{\text{previous time level}}, \qquad \underbrace{\Phi^{(n-2)} \equiv \Phi(t-\Delta t)}_{\text{previous to the last time level}}, \tag{5.16}$$

Euler implicit scheme

It is a first order scheme where the time derivative at the current time step is approximated following equation 5.17 which creates a system of ordinary differential equations that has to be determined for $(\rho_P \Phi_P)^n$:

$$(\mathcal{R}_\Phi)^n = \frac{(\rho_P \Phi_P)^n - (\rho_P \Phi_P)^{(n-1)}}{\Delta t}. \tag{5.17}$$

Backward differencing scheme

It is a second order accurate scheme which, analogously to Euler implicit method, generates a system of ordinary differential equations that has to be defined for $(\rho_P \Phi_P)^n$. Hence, the time derivative at the current time step is estimated as following:

$$(\mathcal{R}_\Phi)^n = \frac{3(\rho_P \Phi_P)^n - 4(\rho_P \Phi_P)^{(n-1)} + (\rho_P \Phi_P)^{(n-2)}}{2\Delta t}. \tag{5.18}$$

Ries in [145] states an important notice regarding the numerical performance of the previous method in OpenFOAM and the approximation of the value of $(\rho_P \Phi_P)^n$ at first time steps of the calculations. In fact, the implicit backward-differencing method in Eq 5.18 needs the value $(\rho_P \Phi_P)$ at previous time levels to estimate $(\rho_P \Phi_P)^n$ and later $(\rho_P \Phi_P)^{n+1}$. According to the implementations of OpenFOAM these values are obtained first by employing the Euler method then, once necessary information are gathered, the implicit backward-differencing scheme is applied for the rest of the calculations.

5.1.3 Pressure Velocity coupling

The solution procedure of the Navier-Stokes equations involves the determination of the pressure and velocity fields in a simultaneous way or in segregated manner since they correct each other and the calculated velocity must fulfill the mass conservation equation. The good numerical treatment of the velocity-pressure coupling reduce certain instabilities and divergence possibilities. Thereby, in order to solve the pressure velocity coupling, the so-called PIMPLE method is adopted in the current study. It is in fact a combination of PISO (Pressure Implicit Split Operator) and SIMPLE (Semi Implicit Method of Pressure Linked Equations) methods that are implemented in OpenFOAM and frequently used in many numerical investigations. The SIMPLE algorithm is generally applied for steady-state cases whereas the PISO method is realized for transient simulations. Merging these two algorithms introduces more efficient transient solver that is applicable for unsteady problems. The PIMPLE method is not restricted to low values of CFL numbers once compared to PISO method [41].

Additionally, the solvers (*stochasticFieldsFPVFoam*, *FPVFoam*) applied in this study are pressure based solvers operating with PIMPLE algorithm. In the pressure-based solvers, the pressure equation can be solved and corrected, then the density can be updated from the equation of state. Hence, within the PIMPLE loop and for better numerical stabilities, certain corrector iterations, so-called Outer and Inner correctors, can be considered. The number of outer correctors determines how many iterations to be executed to solve the system of equations between two successive time steps whereas the number of the inner correctors define the number of times the pressure is corrected within one single iteration. In the current study, the LES calculations were performed with 2 outer correctors and 4 inner correctors which are the recommended values in PIMPLE guide [20].

For more details, the flowchart depicted in Figure 5.2 describes the included main loops and the solution procedure of the PIMPLE algorithm implemented in OpenFOAM [174]. According to this schematic presentation, the algorithm can be outlined as follows:

1. *The initialization* : The first instruction presents the loop over all time steps.
2. *Density predictor*: The mass conservation equation is solved from values of pressure p and psi ψ that were estimated in previous time steps. In this level the density can be then approximated and updated.
3. *Momentum predictor*: The momentum equation is solved in order to approximate the new velocity field based on the finite volume discretization and the values of the pressure p and density ρ that were updated in previous time steps.

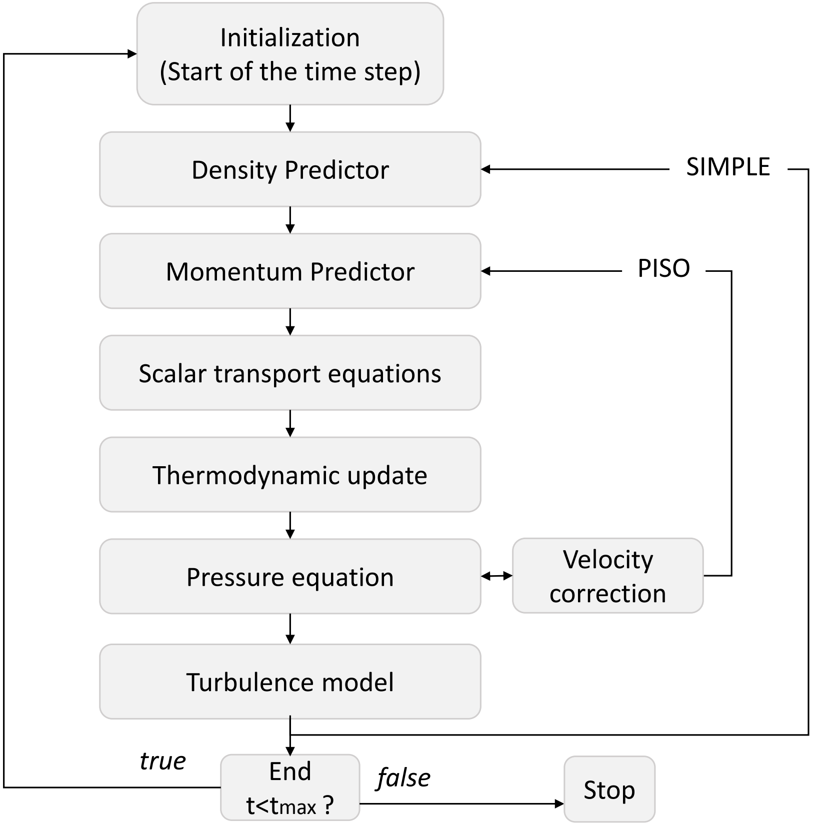

Figure 5.2: Flowchart of the PIMPLE (PISO/SIMPLE) solution algorithm according to OpenFOAM.

4. *Scalar transport equations*: In this step and depending on the turbulent combustion model applied, the scalar transport equations are solved.

5. *Thermodynamics update*: No iterative procedure is performed in this level because of the tabulated numerical modeling applied in the current work. The thermodynamic state including the temperature T is retrieved from the look up-table and updated to solve the next step.

6. *Pressure equation*: At this stage the pressure equation is solved and the velocity field is consequently corrected with the new approximation of the pressure field as far as it is not divergence-free.

7. *Turbulence model*: The last step in this algorithm is the solving of the turbulent equations according to the applied turbulent model. (sub-grid quantities for LES framework and k-ε variables in RANS context).

Notice to remind that the Mach numbers of the current cases are small with ($\mathcal{M}_a < 0.3$), so even that the compressible-based solvers are used, their applications did not present intolerable numerical issues with the described procedures.

5.1.4 Boundary conditions

For the calculations performed in the current study, standard boundary conditions implemented in OpenFOAM [112], have been used as follows:

1. *Inlet* : At the inlets, most scalars were specified with the Dirichlet condition (fixed value), except the pressure field which was initialized with Neumann type boundary (zero gradient). But, for turbulence generation in LES context, the digital filter of Klein in [90] was employed.
2. *Outlet*: The Neumann type boundary condition (zero gradient) was adapted for most scalar and velocity fields at the outlets. The pressure boundary condition was specified as wave transmissive even that the investigated cases are low $\mathcal{M}_a$ number cases, but some numerical instabilities were avoided.
3. *Wall*: The Neumann condition was used for all variables, aside from some turbulence depending-scalars (ε and k for RANS) where certain OpenFOAM standard wall functions were applied.
4. *Symmetry*: The Neumann type (zero gradient) was applied for the symmetry parts of the configurations.

5.2 Numerical implementations

5.2.1 StochasticFieldsFPVFoam

In the current section, the focus lies mainly on the implementation of the *stochasticFieldsFPVFoam* solver within OpenFOAM framework. The solver was established following the proposed hybrid ESF/PVF turbulent combustion methodology described in section 4.2.3.1 where summarized balance equations are discretized employing the finite volume techniques shown in section 5.1. The solution of these equations highly depends on the tabulated chemical source term that is defined based on the controlling variables (f, PV) of the chemical look-up data. Furthermore, the numerical process includes the treatment of the raised Wiener term in the equation (4.16) which is an important topic to be treated separately.

Random stochastic term

The random stochastic term, presented in the equation (4.16), reflects the wiener process (also called *Brownian motion*) that is established for each transported field [5; 53]. It is recalled here as follows:

$$Wt^n_\alpha = \sqrt{2\overline{\rho}^2\mathcal{D}}\frac{\partial \xi^n_\alpha}{\partial x_i}\mathrm{dW}^{\mathrm{n}}_{\mathrm{i}} \tag{5.19}$$

This term is composed of two elements: (a): the stochastic field gradient which is discretized applying same finite volume tools as outlined in section (5.1), and (b): the term

$\mathrm{dW_i^n}$ which stands for the vectorial Gaussian process indicating the wiener process (also called *Brownian motion*) in i direction for the n^{th} field. This last term is spatially uniform (space-independent) and is computed with different values for each stochastic field in each time step. Furthermore, the wiener term is not differentiable in time which is consequently the case for the different stochastic fields. This process is considered a random walk with the sum over its elements is equal to zero:

$$\frac{1}{N_s}\sum_{n=1}^{N_s}\mathrm{dW_i^n} = 0. \tag{5.20}$$

Numerically, for the N_s stochastic fields, the Wiener term is computed separately by multiplying the time-step Δt and the dichotomic vector $\mathcal{N}(0,1)$ according to the following relation:

$$\mathrm{dW_i^n} = \mathcal{N}(0,1)\sqrt{\Delta t} \quad with \quad \mathcal{N}(0,1) \approx [-1,+1] \tag{5.21}$$

where the discrete time-step Δt is defined between the temporal samples t_n and t_{n+1} and the dichotomic vector $\mathcal{N}(0,1)$ is a Gaussian random number with normal distribution, zero mean and unity variance [5]. As shown on the right side in equation (5.21), each sample involves differently positive or negative unity value for each time step. In the OpenFOAM framework, this vectorial parameter was implemented in a smooth manner.

i Within the first loop over each stochastic field N_s, the initial dichotomic vector is specified with zero value for its three components i where ($i \in \{1,2,3\}$).

ii Each vector component (i) is incremented with random value applying the random Gaussian normal distribution function. Depending on the sign of the given value, the letter will be fixed to (1)or (-1).

iii So far, the components of the dichotomic vector are within the defined sample. Hence the summation of the different components for all stochastic fields is processed.

iv The last step is to compute the mean value by dividing the calculated sum over the total number of fields.

For interested readers, other dichotomic vector approximations with different degree of complexity are available in the literature [92].

Ignition function

Among practical and useful utilities and functions that were implemented in the *stochasticFieldsFPVFoam* solver, the ignition function was additionally considered in order to treat the different oxy-fuel cases that are currently investigated. As it is treated in further detail in the chapter (7) where experimental details are described, the oxy-fuel cases are not piloted flames and it is necessary to initialize the simulations with ignition process in order to achieve the desired reacting conditions. For that purpose, the ignition utility is based on adding artificially a hot spark spot within two spatial possibilities: (a) spheric spark or (b) spark within a box. By the activation of this utility an appropriate value of the chemical source term where the combustion occurs should be included along with the temporal range that allows the good start of the reaction.

5.2.1.1 Overall solution

The global solution procedure of the developed algorithm of the *stochasticFieldsFPVFoam* solver, which is implemented as part of the current study, is outlined in this subsection and illustrated in Figure 5.3 . It was mainly established following useful implications depicted in the solution algorithm reported by Avdic in [5] where the ESF method was coupled with another chemical reduction technique and applied on different reacting cases. All involved equations are discretized following the FVM tools described above in section (5.1), and the necessary thermo-chemical properties are retrieved from the generated chemical look-up tables as explained in section (3.3).

At the simulation initialization, the stochastic fields are assumed to be equal, then as time evolves, the moments of stochastic fields are determined based on the calculated quantities from the previous time steps. For the sake of simplicity, an intermediate time loop will be itemized to explain the solution procedure of the considered numerical method. Accordingly, after including the necessary header files, the Gaussian random number with normal distribution function is applied in order to generate the dichotomic vector $\mathcal{N}(0,1)$. Notice that during this step, the sum of dichotomic random vectors should be equal to zero. Then, the density is approximated, based on previous state of both thermodynamics and pressure fields. Next, the pimple loop starts and the momentum equation is solved. At this stage, and depending on the treated turbulent reacting case (e.g oxy-fuel jet series), the ignition utility is called. Thereafter, if the condition of the number of stochastic field is fulfilled ($N_s > n > 1$), the wiener term $\mathrm{dW}_{\mathrm{i}}^{\mathrm{n}}$ is calculated individually for each created field in all spatial directions i with ($i \in \{1,2,3\}$). Then, the $N_s \times N_\alpha$ scalar transport equations are solved, recalling that N_s are the number of stochastic fields and N_α are the number of table controlling variables ($\alpha \equiv \{f, PV\}$). In case that calculated velocity does not satisfy the continuity equation, the thermo-chemical state of the fluid including temperature and chemical reaction rates are extracted from the look-up table for each stochastic field and that is based on the solutions obtained from the stochastic differential equations. Consequently, besides the filtered values of the controlling variables, other filtered quantities of the species mass fractions, the temperature and the reaction source terms are all calculated by averaging over all stochastic fields following the expression (4.18). Here, the first moment values of the table controlling variables will be used for the next time step. Thereafter, the pressure equation is solved with averaged thermo-chemical values and the velocity field is subsequently corrected with the new approximation of the pressure field as far as it is not divergence-free. Finally , the last step in this algorithm is the turbulent equations solution according to the applied turbulent model. Once the overall loop is finished, all needed quantities are stored for further post-processing.

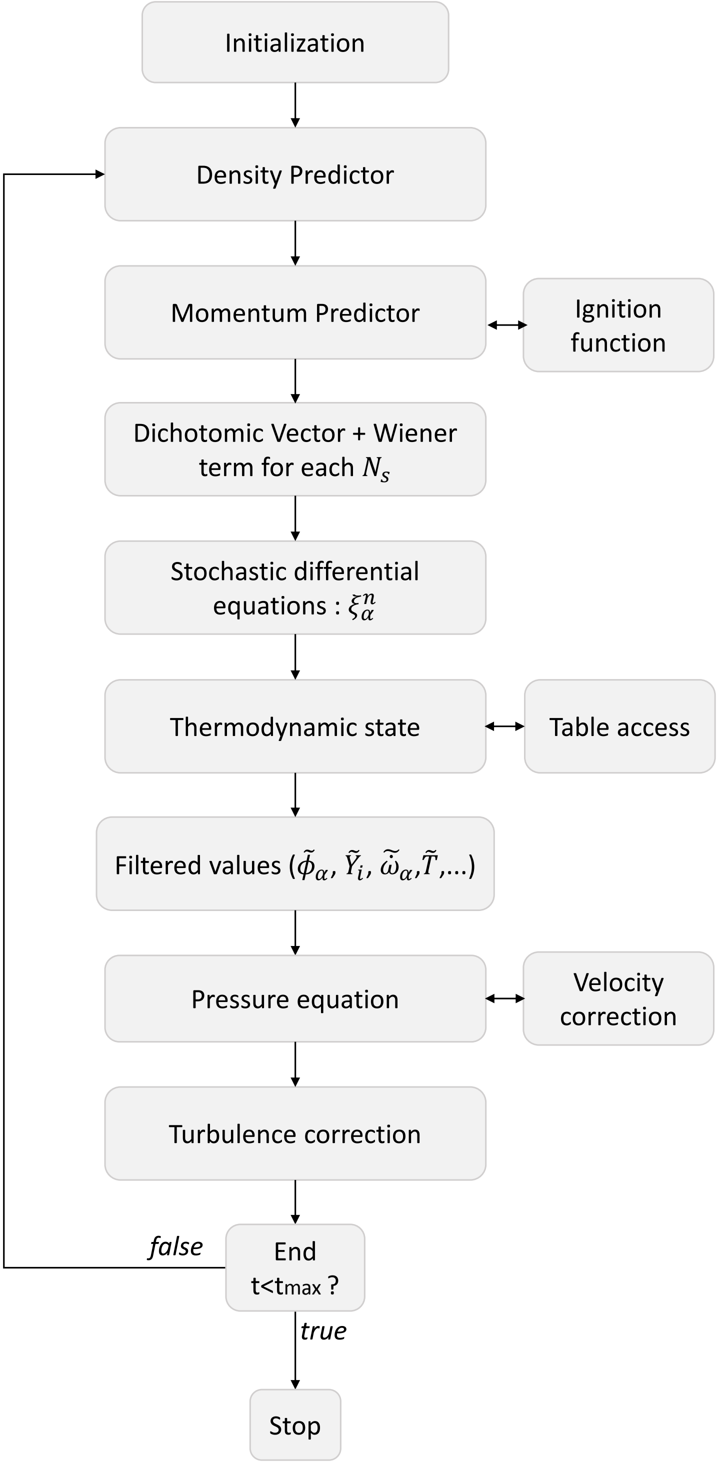

Figure 5.3: Flowchart of the global solution algorithm of one time step simulation of the turbulent reacting solver: *stochasticFieldsFPVFoam*, within OpenFOAM framework.

5.2.1.2 Generic Test Case: One-Dimensional Flame

The current subsection presents the first evaluation of the implemented turbulent reacting *stochasticFieldsFPVFoam* solver in order to assess the accuracy of the method and its prediction capability in reproducing main flame structures. Hence, one-dimensional laminar premixed flame is investigated. The obtained results of this test case are then compared to the solution of detailed chemistry computed with the flamelet generator FlameMaster. For this comparison, besides the generated FPV table, the unity Lewis number assumption ($Le = 1$) is applied also for reference data from detailed chemistry. Furthermore, within the premixed flame, the mixture fraction remains constant throughout the simulation and it is numerically fixed at its stoichiometric value while the progress variable varies. The first objective of this test case is to evaluate the performance of the stochastic fields method once coupled to the FPV approach toward the accurate description of the flame structure. Secondly, the quality of the obtained results provides an additional verification of the chemical table access implementations and the correct retrieved quantities procedure.

Description of Configuration

The description of the quasi-one-dimensional computational domain used in this test case is given in this section. The length of the domain is constant with: $L = 100\ mm$. Different grid sizes have been applied where the maximum number of control volumes reaches 1000 in order to investigate the grid dependence of the solution. Different grid spacing were involved. Regarding the initial conditions, at the fuel's inlet, the mixture fraction f of the gas mixture (methane and air) was set equal to the stoichiometric value $f_{st} = 0.055$ as already mentioned and the temperature was equal to 300 K. The inlet velocity of the gas was $u_x = 0.12\ m/s$. Furthermore, fixed value boundary conditions were set at the inlet of most scalars and symmetry boundary type for the sides of the domain. According to the applied conditions and the obtained results, the laminar flame speed of the stoichiometric mixture is approximated to 30.15 cm/s.

Results - Flame Structure

The numerical simulations of one-dimensional grids with different cell sizes were carried out and noticeably similar results were obtained toward the prediction of the flame structure, therefore only the results of one grid simulation are presented. Figure 5.4 illustrates the evolution of the temperature (T) and density (ρ) fields as well as some species mass fractions Y_α ($\alpha \equiv CO_2$,O_2,CH_4). The comparison of results obtained using the ESF/FPV approach and the solution of detailed chemistry shows a good agreement which means that the implemented method could predict main flame properties and the procedure of chemical look-up table access is correctly performed. However, this case still one-dimensional laminar simple case where turbulence characteristics and sub-grid effects can not be predicted. Hence, in order to validate the numerical approach more complicated cases should

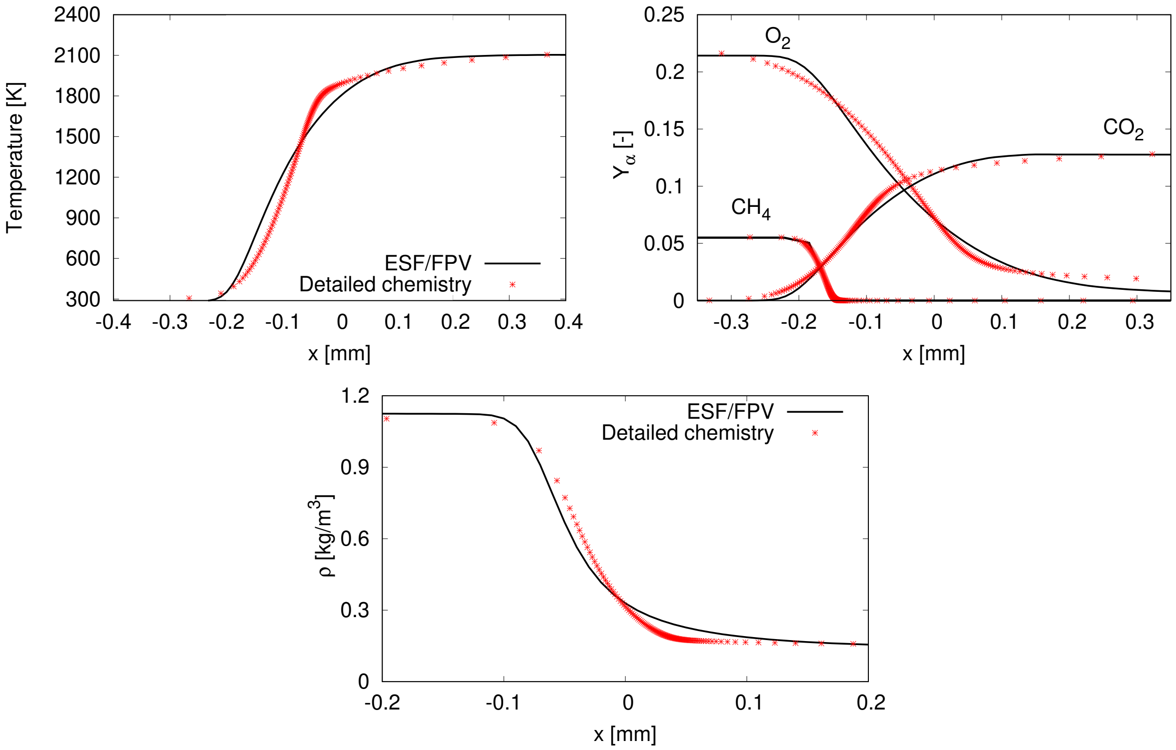

Figure 5.4: The flame structure characterized by the temperature (T), the mass fraction of certain species (CH_4, CO_2, O_2), and the density (ρ) profiles obtained by the ESF/FPV method (line). The reference solution (stars) was computed with FlameMaster code.

be addressed. In this context following chapters are devoted to investigate and discuss several turbulent reacting applications with different degree of complexity.

5.2.2 FPVFoam

The second turbulent reacting solver used in this work is the *FPVFoam* solver. It is also developed within the OpenFAOM framework based on the standard *reactingFoam* solver. The turbulence-combustion interaction model employed in this utility is the presumed PDF following the β-function and similarly to the previous described solver, the chemistry reduction technique is the Flamelet/Progress variable approach where pre-integrated chemical look-up data are computed in the pre-processing phase. As already outlined in section 4.2.3.2), besides the continuity and momentum equations, three scalar transport equations are solved. The main objective of using the *FPVFoam* which has been frequently and widely used, is to compare its numerical findings with the results obtained from the *stochasticFieldsFPVFoam* in order to assess the accuracy and the prediction capability of the Eulerian stochastic field method in characterizing different flame properties. The global solution algorithm of the *FPVFoam* solver is sketched in Figure 5.5 .

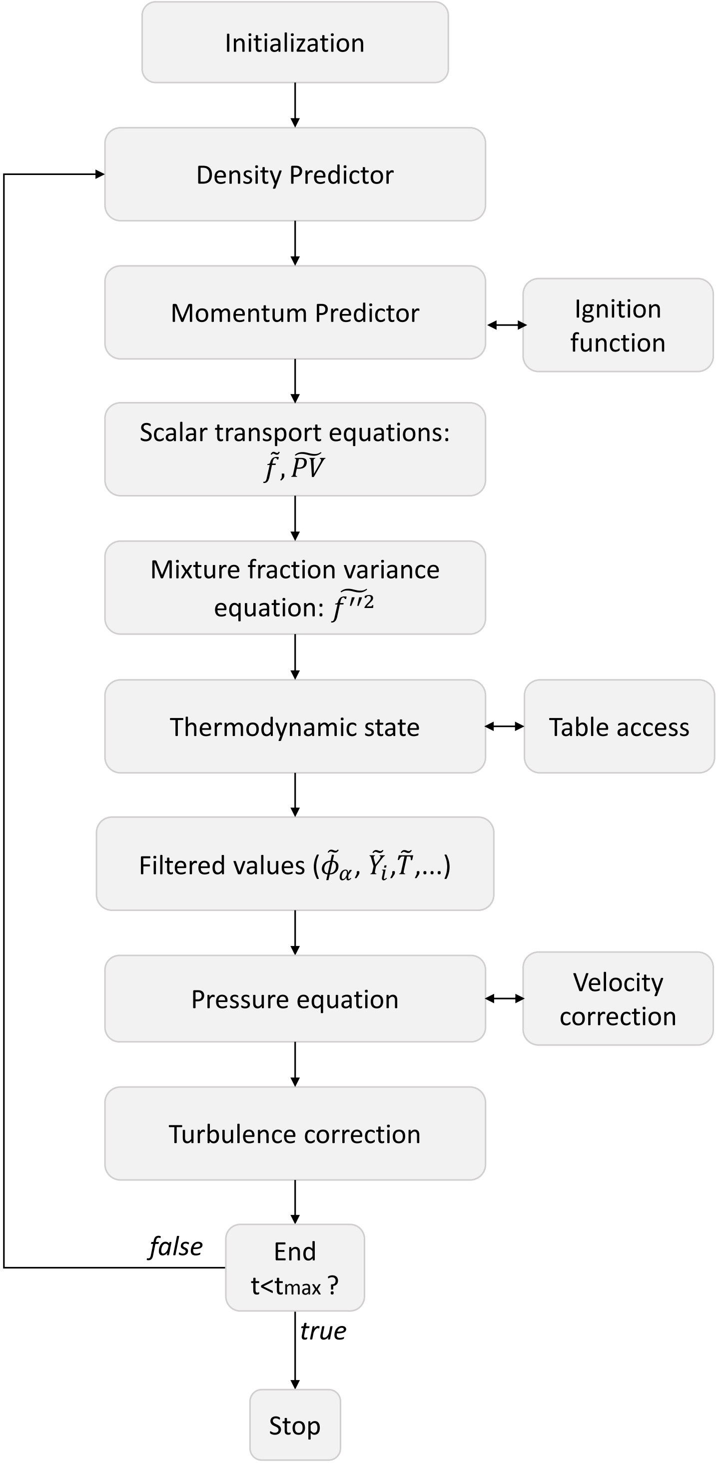

Figure 5.5: Flowchart of the global solution algorithm of one time step simulation of the turbulent reacting solver: *FPVFoam*, within OpenFOAM framework.

5.3 Parallelization

In the current investigation, many simulations have been carried out using different numerical grid sizes within the framework of RANS and LES turbulent models and by applying the Eulerian stochastic fields method. Consequently, the computational resources and memory capacity were highly demanding which explains the necessity of exploiting the parallel computing. For that purpose, OpenFOAM employs domain decomposition and can be used with any MPI library. For the concrete implementations and applications within this work, the scaling of the used solvers has been assessed on the Lichtenberg High Performance **Phase 1** infrastructure of the Technical University of Darmstadt .

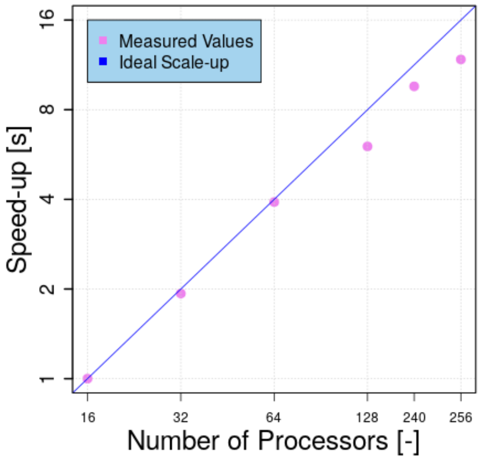

Figure 5.6: Parallel scalability for employed solution procedures while running LES calculations on the Lichtenberg high performance computer (Phase1, 2018) of TU Darmstadt.

The speed-up of the code was measured up to **256** cores applying a strong scaling test. The latter test signifies that the code performance is evaluated based on testing one constant problem size with increasing the number of cores at each simulation. The evaluation was performed for a turbulent Sandia flame-D with 3 million cells grid which is in the average of investigated cases in this study. With a speed factor normalized to 16 processors according to cluster **Phase 1** characteristics, the scaling results are illustrated in Figure 5.6. The speed-up behavior in the corresponding plot, clearly illustrates that the scaling factor is largely acceptable and that the code is able to exploit the full capacity of the machine.

5.4 Summary

This chapter reported in the first section the different techniques applied to solve numerically the partial differential equations describing the turbulent reacting flows. Within OpenFOAM framework, the discretization procedure based on the finite volume method was outlined. Especially spatial and temporal discretization tools were given with details. The pressure velocity coupling method was described, and a summarizing flowchart that illustrates the global Pimple algorithm solution was illustrated to clarify main steps involved. The second part of this chapter was devoted to reveal main implementation instructions that were applied to develop the Eulerian stochastic solver. Essential properties of the Wiener term were addressed followed by the overall solution of the Eulerian stochastic method coupled to the Flamelet/Progress variable which was minutely described. The generic one-dimensional laminar flame case was selected to verify at first insight the numerical implementation of the proposed hybrid approach and evaluate its prediction capability in reproducing the flame structures which reflects the correct procedure toward the chemical look-up tables access. Finally, the details about the parallel scaling of the applied solution procedures were presented.

Chapter 6

Validation: Piloted Jet Flame Sandia-D

In this chapter, the proposed Eulerian Stochastic Field method coupled to the FPV approach is verified and validated by investigating the famous Sandia flame D experimentally studied in [127; 163]. The objective is to evaluate the new approach using two turbulence modeling concepts, namely RANS and LES in terms of performance and capability in capturing and reproducing the turbulent flame properties. With respect to validation, the obtained numerical results are compared to appropriate benchmark of scalar and velocity measurements that has been made available by both Laboratories of Sandia National [154] and the EKT/Technical University of Darmstadt. For both modeling frameworks, the study consists of many reacting simulations using different number of stochastic fields in order to assess the convergence of the method. Regarding the FPV tables, they were generated by applying the constant Lewis number assumption $Le = 1$. Although, as reported in the thesis of Künne [95], by applying a constant Le number approach, the mixture fraction remains constant through the flame, while considering a variable Le yields to a very slight variation of the mixture fraction at the flame front since the differential diffusion phenomena is not neglected. However, Jesch in [81] reported that in similar reacting cases (Sandia flame D), "the discrepancy of applying the constant $Le = 1$ assumption among other numerical uncertainties should be a minor one".

In this work, all these features are conferred in increasing order of complexity, starting with the Sandia flame D. Note that this chapter includes some results that are already published by the author in [106].

6.1 Description of the experimental configuration

The piloted coaxial Sandia flame D [127; 163] is a reacting methane-air jet flame which was designed among other series of flame configurations in Sandia Laboratories. The CH_4/air diffusion flame is well known case and has been extensively numerically studied to validate novel approaches due to available large experimental data base. The measurements for the scalar fields were carried out by applying Raman/Rayleigh/LIF (Laser Induced Fluorescence) [6] techniques in Sandia National Laboratories, while velocity measurements were obtained using LDA (Laser-Doppler Anemometry) [15] technique at the Technical

University of Darmstadt. All experimental data are available in the Proceedings of the International Workshop on Measurement and Computation of Turbulent Non-premixed Flames (TNF) [127; 163].

The experimental configuration of the piloted methane/air jet flame is illustrated in Figure 6.1. The burner consists of 3 inlet streams: main, pilot and co-flow jets. The inside diameter of the central nozzle is $d_f = 7.2\ mm$. The fuel jet consists of a mixture of 25% methane and 75% air by volume which correspond to a mixture fraction of $f_f = 0.156$ with bulk velocity is $u_f = 49.6\ m/s$, and fluid temperature is $T_f = 294\ K$. The pilot nozzle which is surrounding the main jet has an inside diameter $d_{p,i} = 7.7\ mm$ with wall thickness equal to 0.25 mm and an outside diameter $d_{p,o} = 18.2\ mm$. It consists of hot burnt gases with temperature of $T_p = 1880\ K$, and with a lean mixture of C_2H_2 ,H_2 ,CO_2 ,N_2 and air. This mixture is with the same nominal enthalpy and equilibrium composition as methane/air at this equivalence ratio (phi=0.77) [127]. The pilot stream with a mixture fraction $f_p = 0.043$ plays a significant role in stabilizing the flame. The burner outer wall diameter is equal to 18.9 mm (wall thickness = 0.35 mm) and the co-flowing pure air surrounding the burner has a bulk velocity $u_c = 0.9\ m/s$ and temperature of $T_c = 291\ K$.

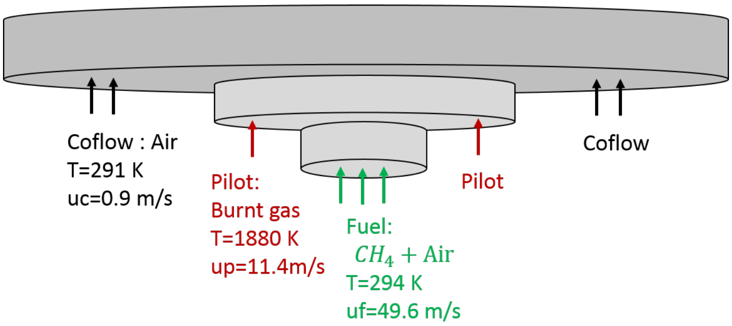

Figure 6.1: Schematic diagram of Sandia flame D with inlet conditions

As reported in [127], the flame length is reduced without any local extinction regions due to the partial premixing with air in the main jet, and the mixing percentages are high enough leading the flame to burn as diffusion flame. The Reynolds number of the corresponding flame is equal to $Re = 22400$. The experimental data present different radial profiles along many axial positions as illustrated in Figure 6.2, and they include averaged values and root mean square fluctuations.

6.2 RANS Simulation

In the engineering applications, RANS based turbulence models in particular k-ε and its variant are used to carry out the design and the optimization tasks to reduce the associated development time. The RANS model offers a relatively acceptable mean profile of flow properties (eg. velocity, temperature etc.). It also allows to carry out steady state simulations on coarse mesh and sometimes axi-symmetric configurations. This way,

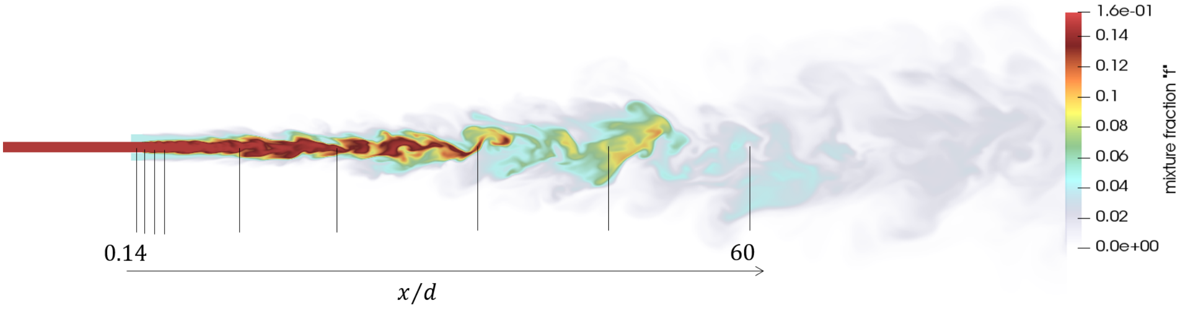

Figure 6.2: Schematic of measurement locations for the Sandia flame D.

it reduces considerably the simulation and the design analysis task. To exploit these inherent advantages of RANS models and to assess numerically the hybrid ESF/FVP and its ability in capturing the flame properties, this section mainly focuses on the numerical investigation of the Sandia flame D configuration by employing the k-ε RANS model with the hybrid ESF/FVP by considering various number of stochastic fields.

6.2.1 Numerical set-up

Two computational domains will be used. First, a 3D domain is employed (see Figure 6.3a) in order to gain results for being compared to LES findings later (see section 6.3.2.1). The computational domain is discretized using a 3D block-structured mesh composed of 1,606,440 control volumes. The dimensions of the smallest cell within the computational domain is 0.30 mm in the central jet and for the largest one, it is approximately 2.40 mm in length and 1 mm in width in region close to the outlet. The choice of the size and other characteristics of the corresponding numerical domain was based on the study of Miranda [19], where the same configuration, Sandia flame D case, was investigated using Smagorinsky model and including a grid independence study. Thus, this used mesh as in [19] reflects an acceptable compromise between accuracy and affordable computational costs. The length of the principal jet is equal to 13 d_f and the cells are extended approximately to $x = 80d_f$ in length towards the outlet plane. More detailed dimensions are illustrated in Figure 6.8.

Second, due to the symmetry characteristics of the configuration, a two-dimensional numerical grid is used to reduce the computational costs and to be compared to 3D RANS case. This will allow to assess the 2D simulations for different sensitivity studies. Using uniform mesh option, the 2D grid is discretized into 32,000 control volumes which is sufficient to ensure grid-independence. As shown in Figure 6.3b, the fuel and pilot jets are extended to 13 d_f upstream in order to obtain fully developed flow at fuel exit. To avoid the influence of the outlet boundary condition the combustion chamber is sufficiently extended to 80 d_f downstream to fuel exit.

For both 2D and 3D RANS calculations, the waveTransmissive condition is imposed for the pressure at the outlet plane with $P = 101.325kPa$, while other variables have a zero gradient boundary condition. The simulation is carried out for the physical time of 1 s in order to achieve the acceptable averaged results. A constant time step of $1 \cdot 10^{-6}$ s is chosen to maintain the CFL < 1 throughout simulations. The FPV tables were generated based on the flamelet solutions obtained with the GRI.3.0 mechanism by applying the constant unity Lewis number assumption ($Le = 1$) and the correct fuel-oxidizer compositions. Among many definitions of the progress variable pv as reported in section 3.3.1, the following definition of pv is adopted :

$$pv = \frac{Y_{CO_2}}{\mathcal{M}_{CO_2}} + \frac{Y_{CO}}{\mathcal{M}_{CO}} + \frac{Y_{H_2O}}{\mathcal{M}_{H_2O}}. \tag{6.1}$$

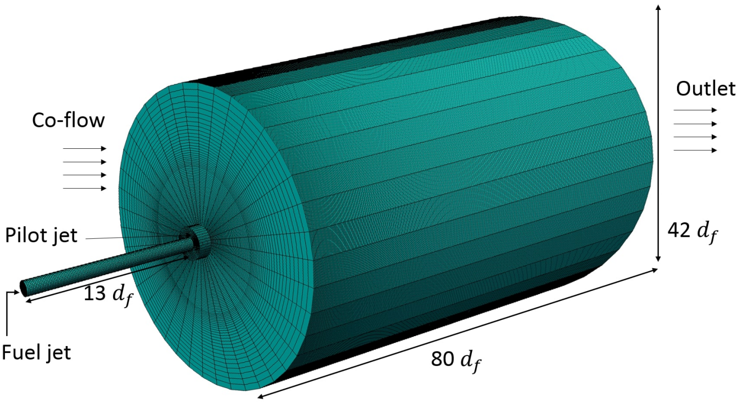

(a)

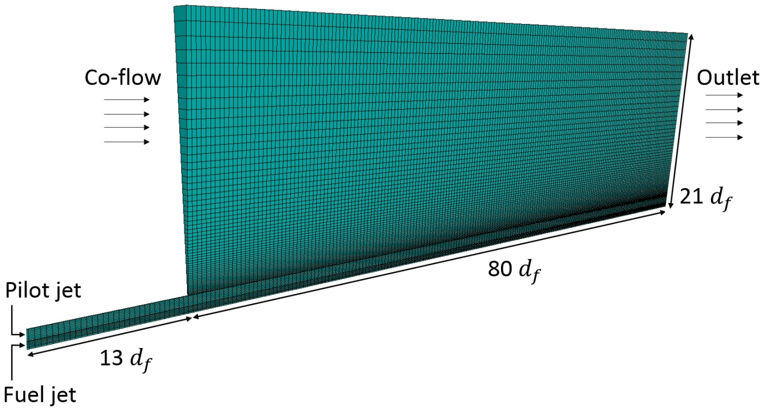

(b)

Figure 6.3: Three-dimensional (a) and two-dimensional (b) numerical block structured grids of the Sandia Flame-D configuration.

The 2D RANS parallel calculations are realized by using 16-64 processors as increasing the number of stochastic fields from 1 to 128 SF_i imposing an increase demand of computational resources. However, the 3D RANS simulations are carried out with 48 SFi using 160-192 processors.

6.2.2 Results

Since one of the focus of the present study is to evaluate the hybrid ESF/FPV approach with two turbulence modeling frameworks namely RANS and LES, in this section the results obtained using standard k-ε are presented.

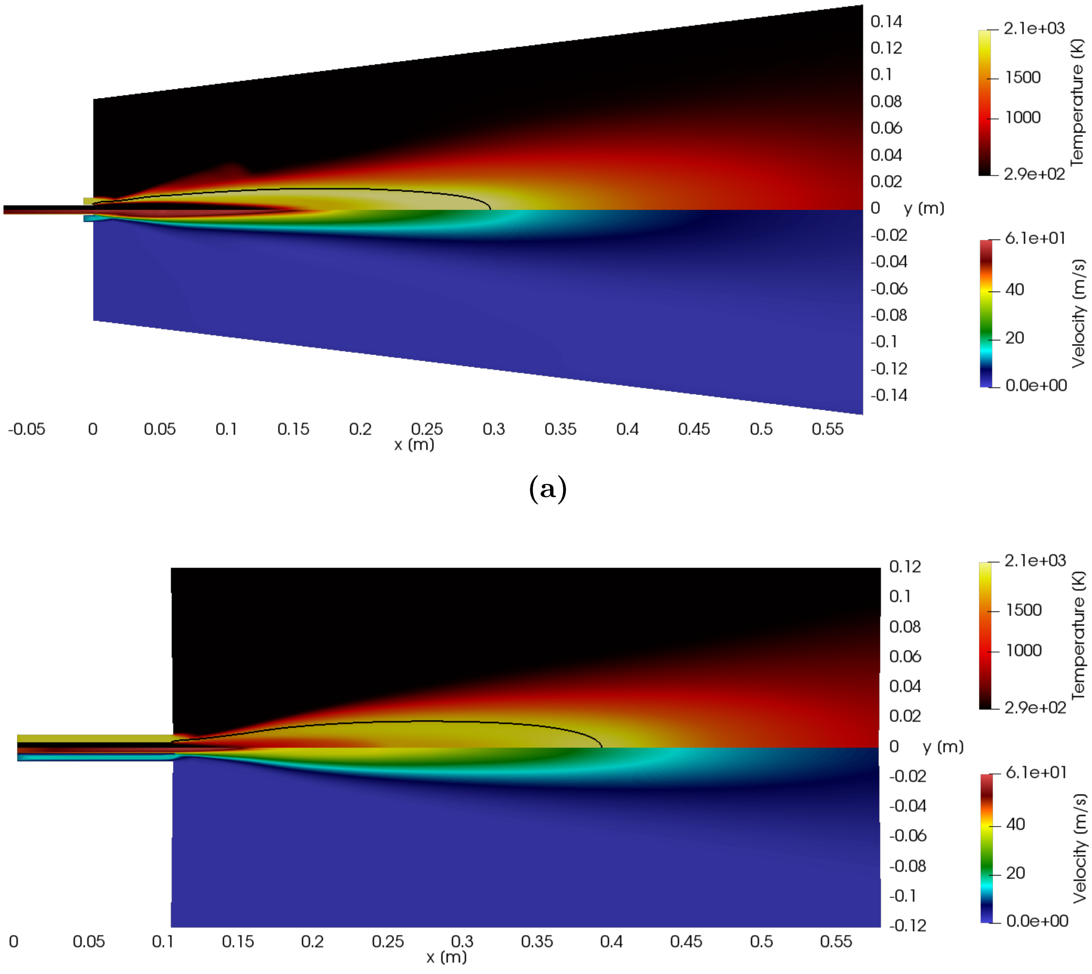

(a)

(b)

Figure 6.4: Temperature and velocity profiles of Sandia flame D configuration obtained with the simulations of 3D RANS (a) and 2D RANS (b). The traced solid black lines on the temperature snapshots represent the stoichiometric mixture fraction $f_{st} \approx 0.055$.

In order to provide the global features of Sandia flame D configuration, qualitative results for the flame obtained using 2D and 3D RANS simulations are provided for temperature and velocity in Figure 6.4. A mixture of fuel and air (CH_4+air) enters with ambient temperature (294K) through central tube and mixes with burnt gases with temperature 1880K issuing from concentric pilot tube in order to stabilize the flame (see top half parts of Figure 6.4). The higher temperature close to the fuel jet tip signifies the onset of combustion, which diffuses in chamber further downstream. A respective higher velocity profile can be observed as seen in bottom half parts of Figures 6.4a and 6.4b due to expansion of the burnt gases during combustion.

In order to determine the flame interface, a solid black line is also plotted along the temperature representing the stoichiometric mixture fraction $f_{st} \approx 0.055$ line for CH_4 flame. This way, it allows to calculate numerically obtained flame lengths and compare them with measurements as $f_L = 0.345(\approx 48\ d_f)$. For 2D RANS case, the flame length is approximated as $f_L = 0.38(\approx 52.77\ d_f)$, however for 3D case, $f_L = 0.310(\approx 43.05\ d_f)$. The results show that 2D RANS slightly over-estimates the flame length with a difference of 0.035, while 3D RANS marginally under-estimates the flame length, but, with the same difference of 0.035. Thereby, the error percentage towards the experimental value of the flame length is small and is the same for both 2D and 3D RANS findings. As the comparison between 3D and 2D RANS simulations shows, these slight discrepancies are mainly explained by the use of a k-ε RANS turbulent model with very well-known weaknesses [132].

After considering the qualitative observations of the flame, the obtained results are now compared with the experimental data ([127; 163]). Figure 6.5 shows the comparison of numerically obtained temperature and CO_2 mass fraction evolution against the measurements along various axial locations.

The influence of the stochastic field numbers can be clearly seen in the 2D RANS results showing relatively better agreement when increasing the number of stochastic fields. However, there is noticeable deviation in simulated results beyond 15 d_f region for all N_s. This can be attributed to the adopted rather simple RANS k-ε turbulence model.

Next, the axial and radial velocities obtained from 2D RANS-ESF/FPV are compared with experimental data in Figure 6.6. The observed two peaks in the axial-velocity close to the fuel jet exit are associated to the flows from the central and co-pilot jets.

These peaks subsequently transform into single peak in the downstream direction. However, in case of radial velocity the peak is observed first along the flame surface and then moved towards the central jet location. Here, the results obtained from RANS-ESF/FPV can be seen in good agreement with measurements especially for the axial velocity, while noticeable disagreement for radial velocity is recorded. These discrepancies can be attributed to the RANS k-ε turbulence model together with the 2D ax-symmetric computational domain applied.

Additionally, with respect to the number of stochastic fields applied, it can be clearly observed that a higher applied number of SF_i leads to better results that are closer to the experimental data. The illustrated profiles show similar behavior in the fuel/pilot inlet zone where varying the number of SF_i clearly affects the evolution of these quantities except for the mixture fraction profile (Figure 6.7) where very slight deviation was observed. However, for higher axial locations and beyond $x = 3d$, the results obtained with $SF_i = 48$ and $SF_i = 128$ are in better agreement with the measurement data. At the axial positions $x > 30d$, the influence of increasing the number of stochastic fields is not so pronounced where no reaction is taking place.

Therefore, in order to simulate similar turbulent reacting cases using the ESF/FPV approach in the RANS modeling context, the use of $SF_i > 48$ provides satisfactory results in

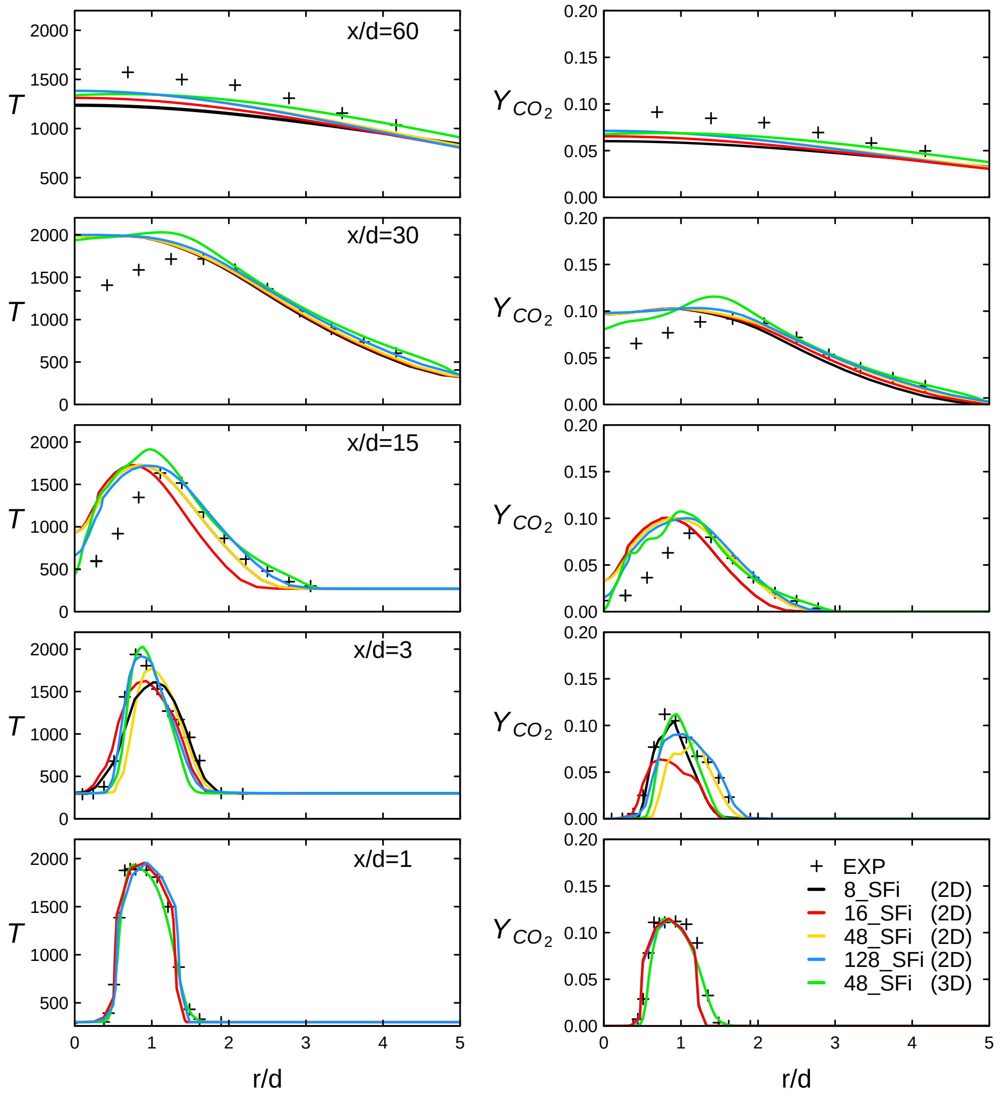

Figure 6.5: Temperature and CO_2 mass fraction profiles calculated at different axial positions ($x = 1d, 3d, 15d, 30d, 60d$) with 2D and 3D RANS-ESF/FPV method using different number of SF_i, and compared to experimental data (+) .

contrast to the observations reported in [5; 54]. In fact, Avdić stated in [5] that simulation within RANS modeling leads to the necessity of using a large number of stochastic fields, e.g. 500. Garmory in [54] used from 100 to 500 fields in the simulation of a reacting plume in grid turbulence and he found that only small change in mean results were observed but the use of higher number of fields (500) had slightly minimized statistical errors. For this reason, the 3D RANS simulations of flame D were carried out using 48 SF_i and obtained results were compared to 2D RANS findings where approximately similar behavior for all presented quantities at different axial positions is observed.

Finally, the calculated mixture fraction and its corresponding variance are found to be in overall good agreement with experimental data as illustrated in Figure 6.7. However, some deviations are observed for mixture fraction variance in middle axial positions.

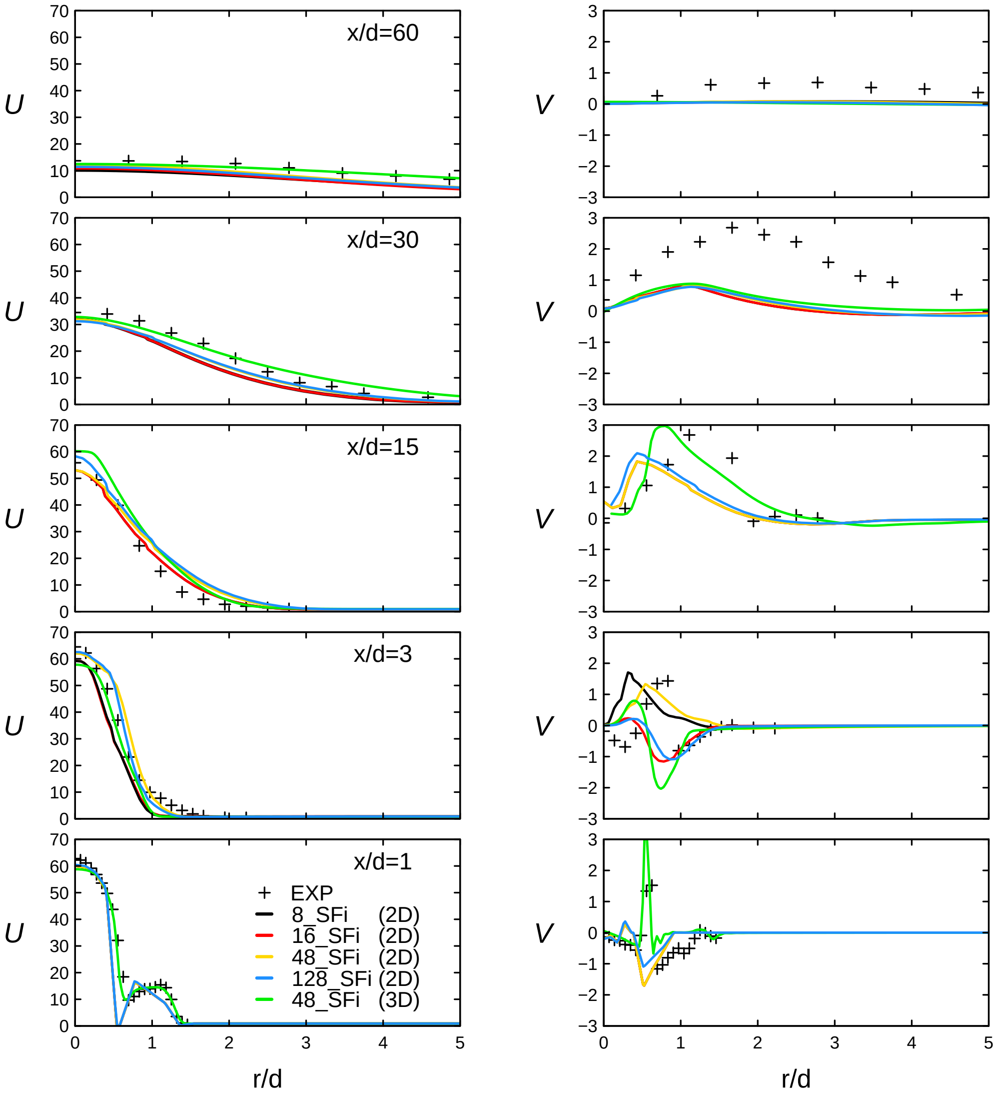

Figure 6.6: Axial and radial velocity profiles calculated at different axial positions ($x = 1d, 3d, 15d, 30d, 60d$) with 2D and 3D RANS-ESF/FPV method using different number of SF_i, and compared to experimental data (+).

6.3 LES with ESF/FVP approach

In the previous section, the application of the implemented hybrid ESF/FVP model in RANS context which is rather a simple turbulent model was analyzed and its limitations in reproducing combustion properties were thoroughly discussed. Now, the evaluation of the proposed approach with a more advanced turbulent model is carried out. Thereby, to simulate the Sandia flame D, the Smagorinsky LES model is employed for the sgs flow field together with a linear eddy-diffusivity model for the sgs scalars flux vector.

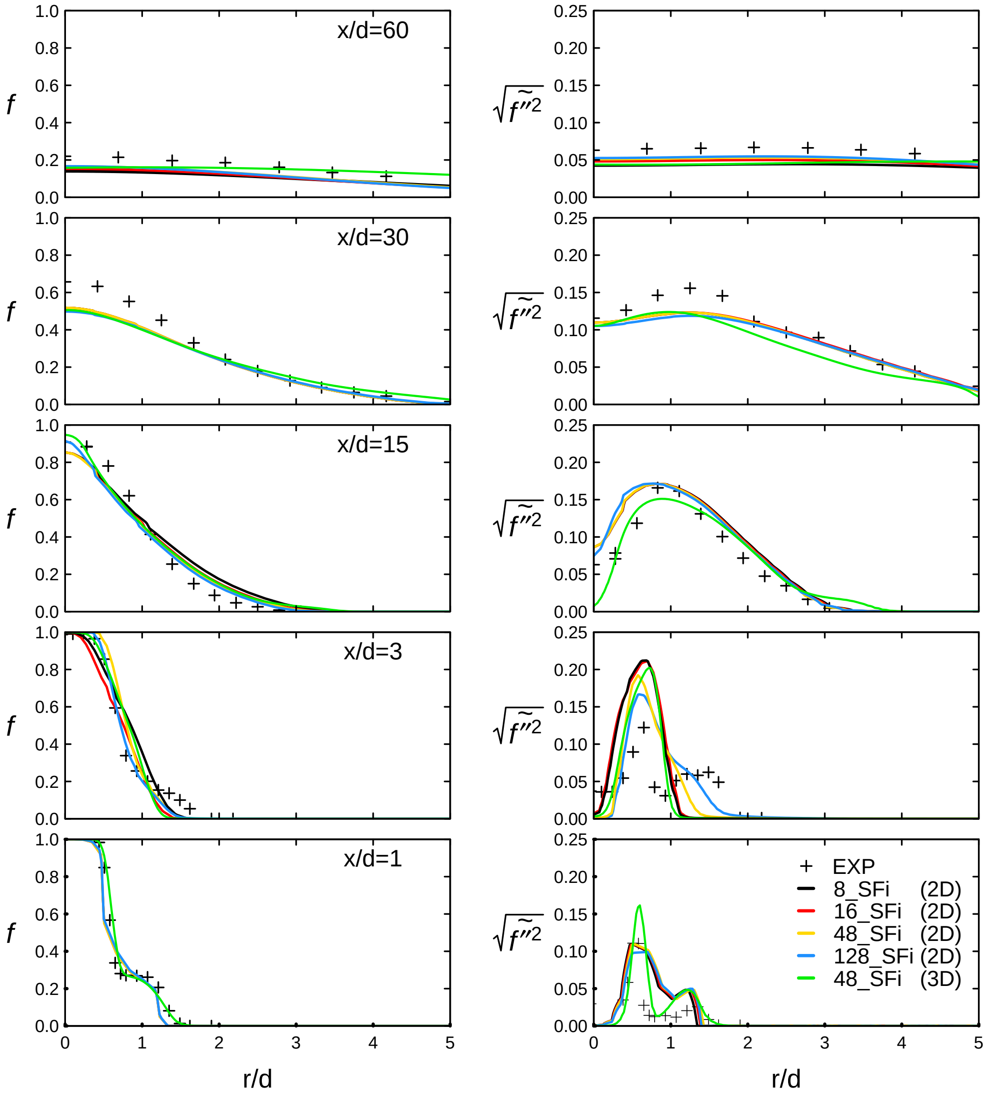

Figure 6.7: Mixture fraction and its corresponding variance profiles calculated at different axial positions ($x = 1d, 3d, 15d, 30d, 60d$) with 2D and 3D RANS-ESF/FPV method using different number of SF_i, and compared to experimental data (+).

6.3.1 Numerical set-up

In order to capture well the turbulence and related properties with LES, the same computational domain, as used in section 6.2.1 and shown in Figure 6.8 is employed for this part of the study. As previously mentioned, the dimensions of the smallest cell within the computational domain is 0.30 mm in the central jet and the largest ones are located near the outlet plane and are approximately 2.40 mm in length and 1 mm in width. The size of the corresponding numerical domain including different control volumes was chosen based on the study of Miranda [19]. Thereby the applied mesh as stated in [19] reflects an acceptable compromise between accuracy and affordable computational costs.

In the direction of being consistent with the numerical domain designed in the previous section, the central jet has a length of $13d_f$ and the cells are extended approximately to

$x = 80d_f$ in length towards the outlet plane. More detailed dimensions are illustrated in Figure 6.8. The waveTransmissive condition was used for the outlet where the pressure value was initialized with $P = 1$ atm as fixed value. Other boundary conditions were set to zero gradient. In order to asses the convergence of the number of SF_i in LES context, simulations were performed also using different numbers of stochastic fields N_s 4 , 6 and 8 SF_i. The LES is carried out for the physical time of 0.85 seconds by using the constant time step of $3 \cdot 10^{-7}$ seconds.

In order to provide fully turbulence velocity boundary conditions at the inlets, an in house turbulence inflow generator according to the method reported by Klein et al. [90] was applied where artificial turbulent fluctuations are generated and added to the velocity field at respective in-flow parts of the burner. This requires a description of turbulence length and time scales based on the isotropic turbulence hypothesis. Subsequently, the velocity fluctuations are calculated for each mesh vertex and then superposed with mean velocity obtained using the power law profile. The FPV tables applied in this context are the same tables used in the RANS context with the same definition of pv.

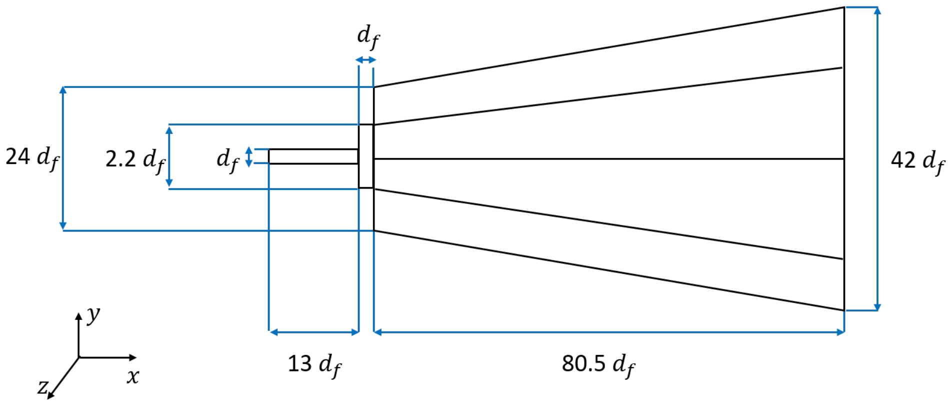

Figure 6.8: LES: The schematic of the computational domain of Sandia flame D configuration. (d_f = 7.2 mm).

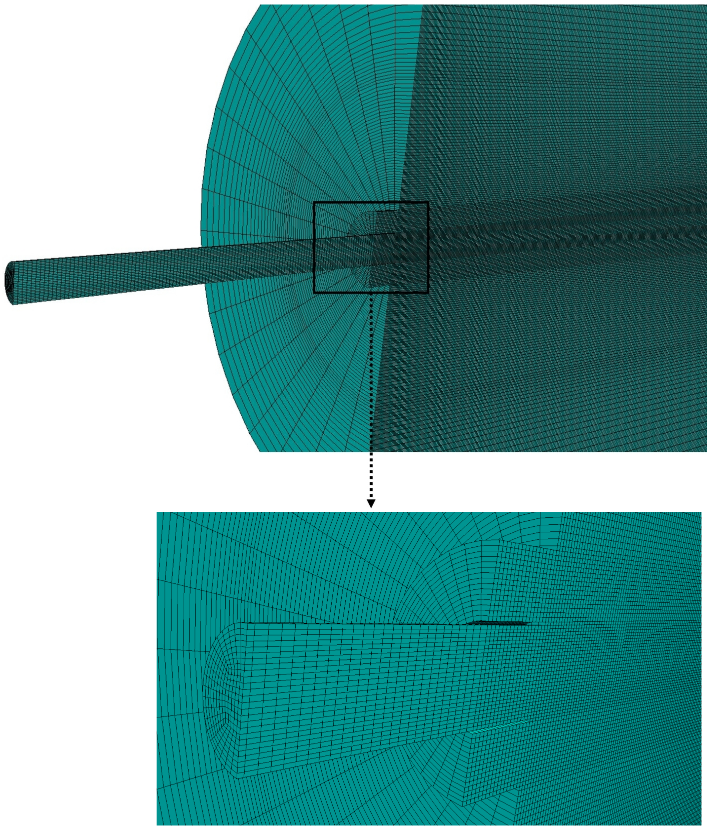

Figure 6.9: Block structured 3D numerical grid for the Sandia flame D configuration: longitudinal plane of numerical grid (top), a zoomed view of the inlet region of fuel and oxidizer nozzles (bottom).

6.3.2 Results

In contrast to RANS, LES features a reasonably resolved turbulence structures with inherent transient flow properties. Therefore, in order to compare with the experimental data, the flow properties are generally averaged over sufficiently long physical time to get statistically independent results. In this study, the averaged flow properties are obtained for 0.8 seconds.

In order to provide the evidence of highly turbulent and chaotic flow occurred in case of Sandia flame D, instantaneous flow, mixing and temperature fields are first provided. Then associated fields from Q-criteria are delivered. Thereby, following the definition in [158]:

$$Q = \frac{1}{4}\left(|\widetilde{S}|^2 - |\widetilde{\Omega}|^2\right). \tag{6.2}$$

where $|\widetilde{S}|$ is the resolved strain rate with $|\widetilde{S}| = \sqrt{\left(2\widetilde{S}_{ij}\widetilde{S}_{ij}\right)}$ and the expression of the strain rate $\widetilde{S}_{ij}$ is recalled in Eq 2.48. The term $|\widetilde{\Omega}|$ stands for the rotation rate $|\widetilde{\Omega}| = \sqrt{\left(2\widetilde{\Omega}_{ij}\widetilde{\Omega}_{ij}\right)}$ where $\widetilde{\Omega}_{ij} = \frac{1}{2}\left(\frac{\partial \widetilde{u}_j}{\partial x_i} - \frac{\partial \widetilde{u}_i}{\partial x_j}\right)$.

Instantaneous velocity contour along the middle-sectional plane is plotted in Figure 6.10 with uniformly sized vectors showing the flow directions in the flame region.

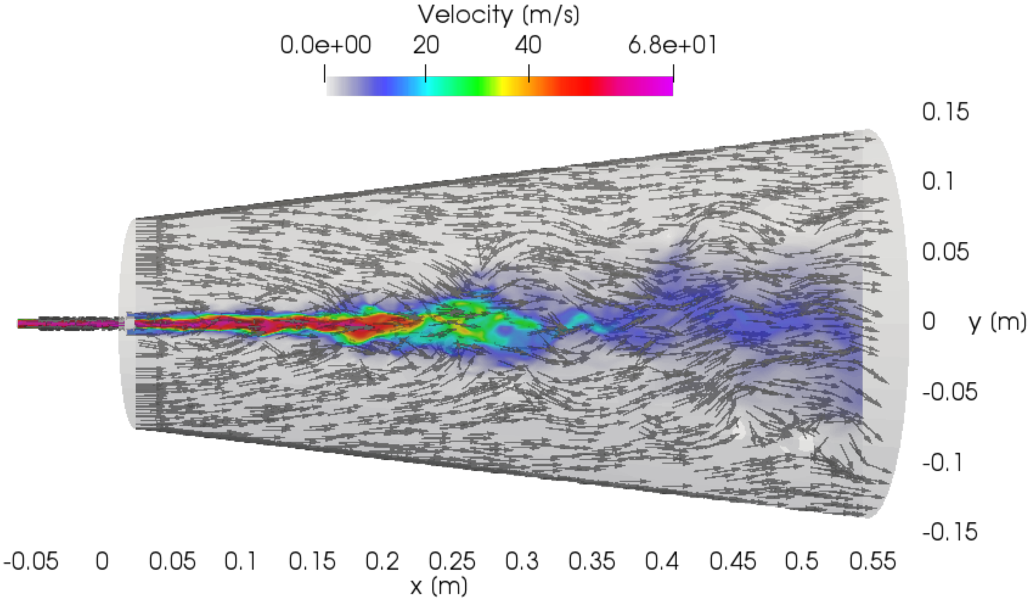

Figure 6.10: Snapshot of the instantaneous velocity field calculated with the LES hybrid ESF/FPV approach using 8 SF_i illustrated with uniformly sized vectors identifying the flow directions.

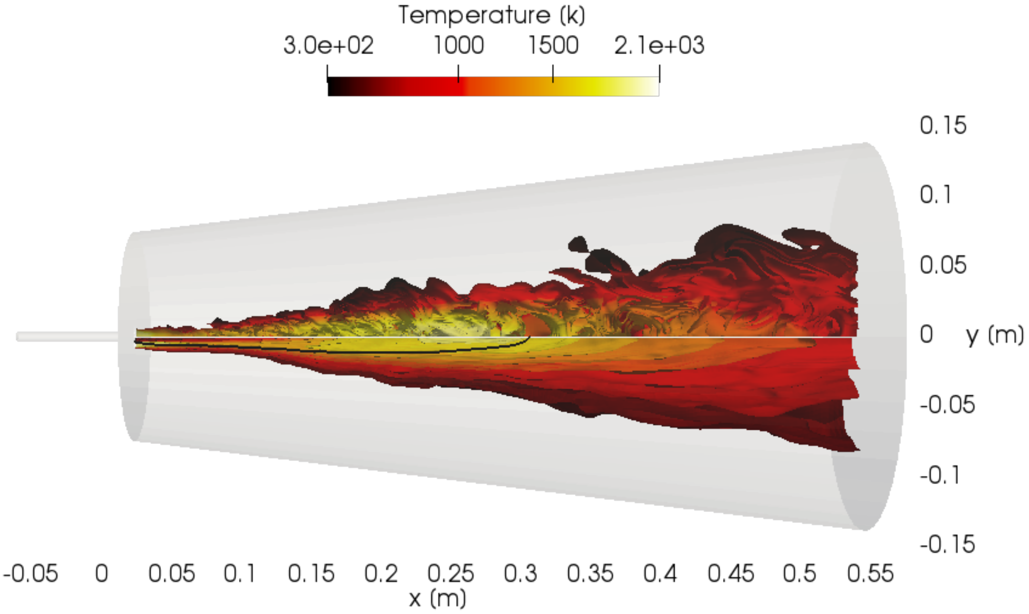

Figure 6.11: Snapshot of the instantaneous (top) and time-averaged value (bottom) of the temperature field calculated with the LES hybrid ESF/FPV approach using 8 SF_i .

This figure also reflects the velocity boundary conditions imposed at the different inlets and the surrounding pilot jet and co-flow region. A maximum instantaneous velocity of 75 m/s can be observed very close to the fuel nozzle exit.

Next, the temperature profile is depicted in Figure 6.11 with instantaneous snapshots (top half) and mean fields (bottom half) of the temperature distribution. The instantaneous profile further highlights the highly transient temperature profile during combustion, while the mean temperature looks very similar to the RANS approach discussed in previous section.

In line with Figure 6.11, the traced black line corresponds to the stoichiometric value of the mixture fraction ($f_{stoich} \approx 0.055$) which reveals the LES estimated flame length of $f_L = 0.325(\approx 45.14 d_f)$ in contrast to the RANS obtained flame lengths of $f_{L,2D} = 0.38(\approx 52.77\ d_f)$ and $f_{L,3D} = 0.310(\approx 43.05\ d_f)$ for 2D and 3D RANS, respectively. By comparing these calculated values, one can clearly notice that the LES result provides more accurate predictions of the flame length closer to the measured value of $f_L = 0.345(\approx 48 d_f)$. The instantaneous (top half) and mean profile (bottom half) for mixture fraction are illustrated in Figure 6.12. The evidence of fuel mixing due to very high shear flow is clearly visible in instantaneous mixture fraction profile, while the mean profile looks very similar to the results obtained using RANS model. A fuel rich mixture can be seen issuing from the central fuel jet, and presence of fuel becomes progressively leaner towards the downstream direction suggesting the fuel is being consumed during the combustion processes.

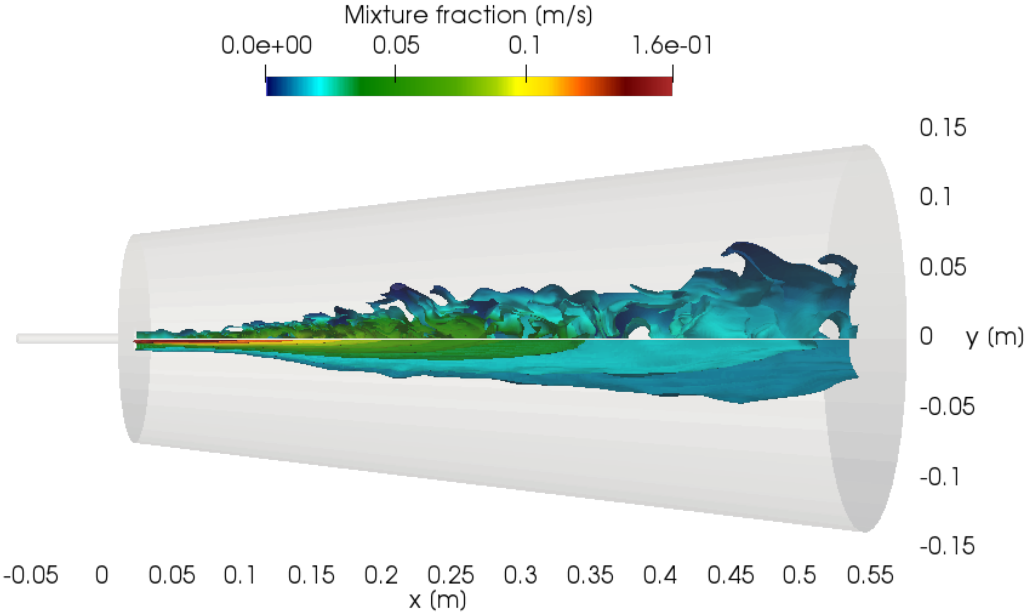

Figure 6.12: Snapshot of the instantaneous (top) and time-averaged value (bottom) of the mixture fraction calculated with the LES hybrid ESF/FPV approach using 8 SF_i .

As previously pointed out, the mixing is inherently enhanced by high shear flow which in turn influences the combustion process. In order to better understand and analyze the system flow, visualizing and identifying the individual vortices and their interaction during mixing and combustion processes can provide very good insight about the system design and performance. In this regard a criterion based on the second invariant of velocity gradient tensor which is frequently called the "Q-criterion" is used to visualize the vortical structures of the turbulent flow.

Figure 6.13 shows the iso-surface of the Q-criterion obtained using the LES hybrid ESF/FPV approach with 8 SF_i. The illustrated Q-criterion is contoured and colored by the axial velocity where the instantaneous vortical flow features are depicted and the turbulent structures of different sizes are visualized. Multiple vortex rings are clearly visible, especially in the region near the fuel nozzle which refers to toroidal vortex structures that have been generated due to very high shear flow and velocity gradient at the pipe outlet edges.

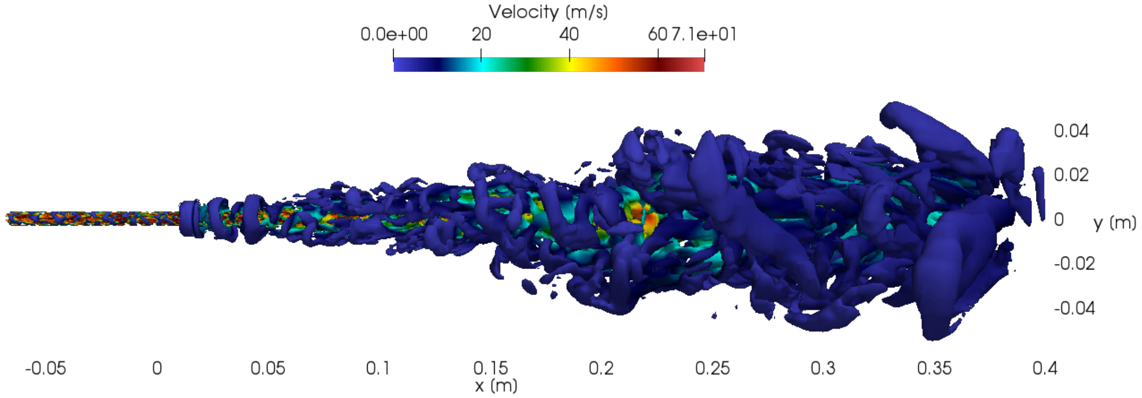

Figure 6.13: Snapshot of the instantaneous Q-criterion ($Q = 10^9\ s^{-2}$) contoured with Velocity field calculated with the LES hybrid ESF/FPV approach using 8 SF_i.

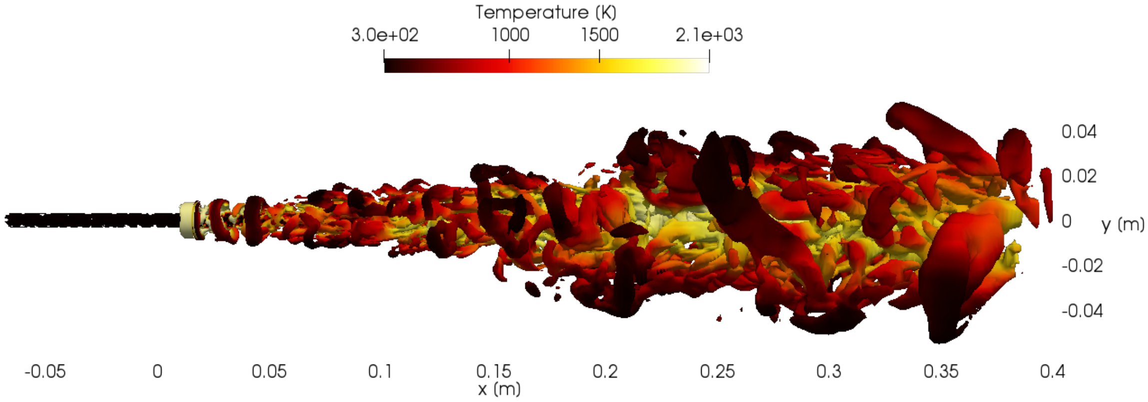

Figure 6.14: Snapshot of the instantaneous Q criterion contoured with temperature field calculated with the LES hybrid ESF/FPV approach using 8 SF_i .

It is interesting to note the qualitative similarity between Figure 6.13 and results reported in the LES study by Frolov in [158] where two other approaches for turbulent combustion modeling have been employed (the mixture fraction probability density function method and the eddy dissipation model). This suggests that the applied approach is capable at this stage of reproducing not only the main flame characteristics but also describing the flow structures.

Figure 6.14 illustrates the same view of the Q-criterion in Figure 6.13 but colored by the temperature field. This leads to the observation that, starting from the nozzle outlet, the presence of weakly fluctuating low temperature core around the jet axis is visible, while the core is surrounded by the high-temperature flame zone featuring high vorticity and turbulent pulsation magnitude.

In order to further evaluate the adopted LES hybrid ESF/FPV approach, a quantitative comparison against the experimental data is carried out at different axial locations ($x = 1d, 3d, 15d, 30d, 60d$) for various flow parameters (axial and radial velocity, temperature, mixture fraction) and their respective variances.

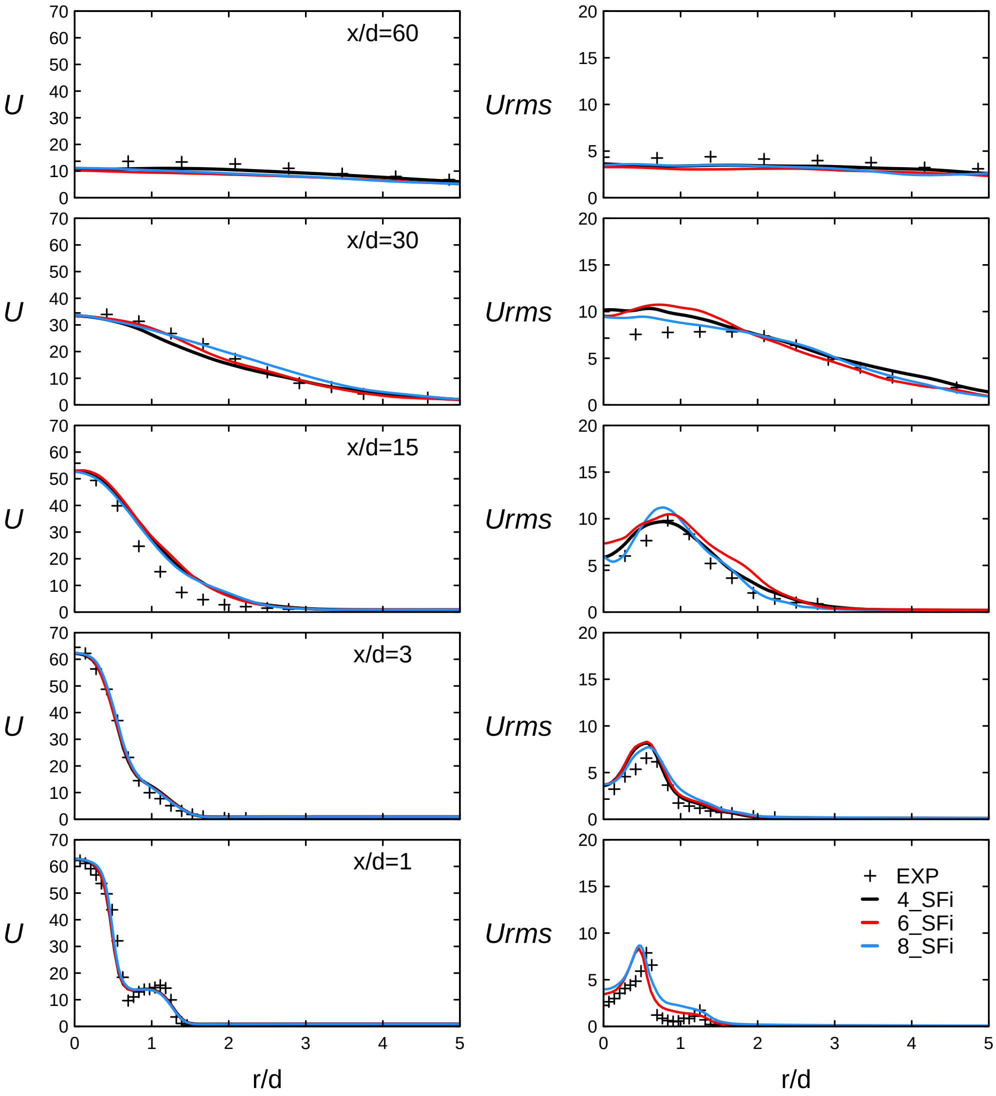

Figure 6.15: Comparison between experimental data for Sandia flame D [127; 163] and LES numerical results of the velocity field for various numbers of SF_i at different axial positions; $x = 1d, 3d, 15d, 30d, 60d$.

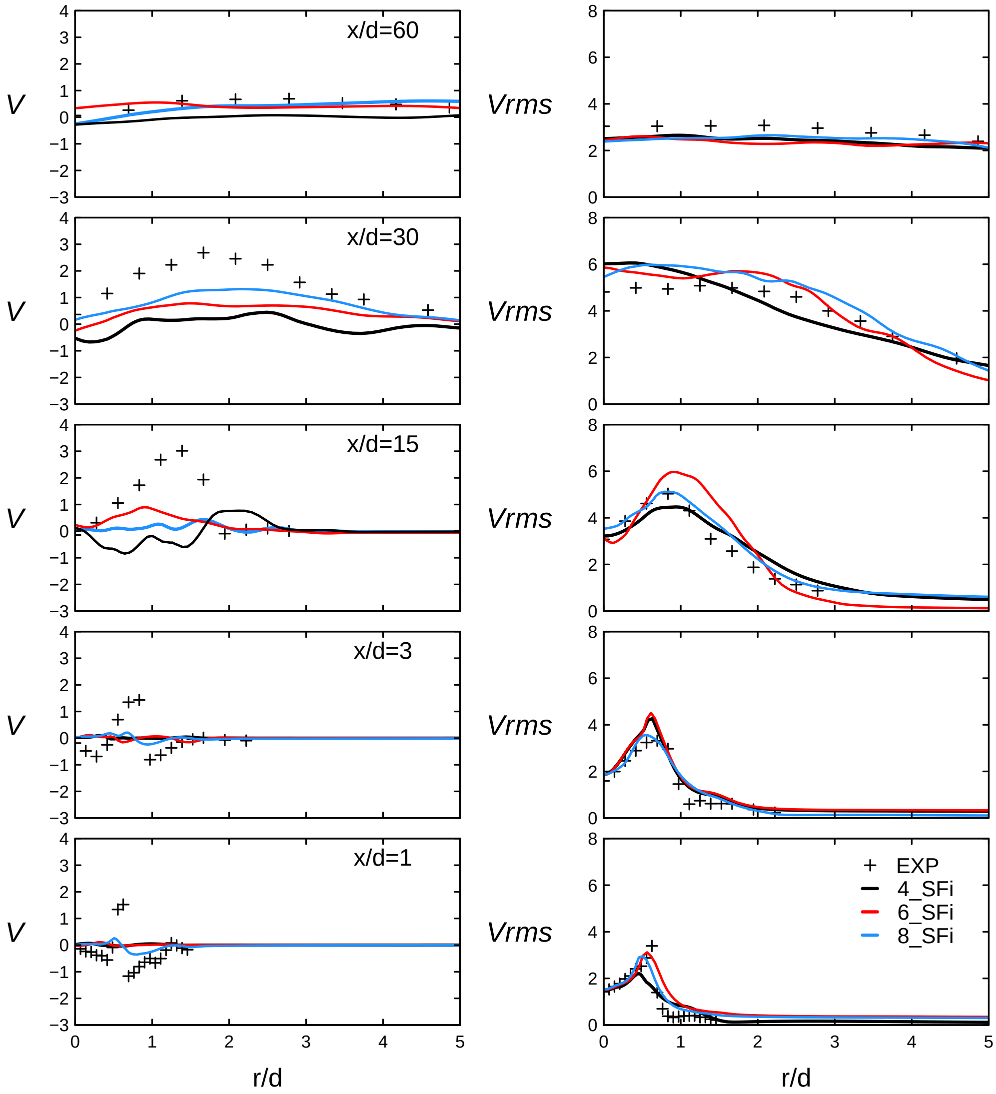

Figure 6.16: Comparison between experimental data for Sandia flame D [127; 163] and LES numerical results of the velocity field for various numbers of SF_i at different axial positions; $x = 1d, 3d, 15d, 30d, 60d$.

First, the axial velocity and its variance are plotted in Figure 6.15 featuring very good agreement with experiments, especially the LES with hybrid ESF/FPV approach is able to reproduce well the two-peaks in mean velocity profile close to the fuel jet exit. The calculated variance also shows good agreement with experimental values with slight deviation in downstream regions. However, a clear discrepancy can be observed when LES is compared with measurements for radial velocity at these locations. This is not the case for the variance depicted in Figure 6.16 where only relative good agreement is achieved. These observations are also in coherence with the finding of other researchers for this Sandia flame D configuration. Vreman et al. in [169] reported that the discrepancies are high at the locations immediately close to the nozzle exit, but the results improve further downstream. The similar behavior is also reported in [81]. These deviations can be attributed to two facts: first, the provided turbulent velocity boundary conditions especially at pilot jet, and second, the pilot jet's length and resolution used in the current

LES study.

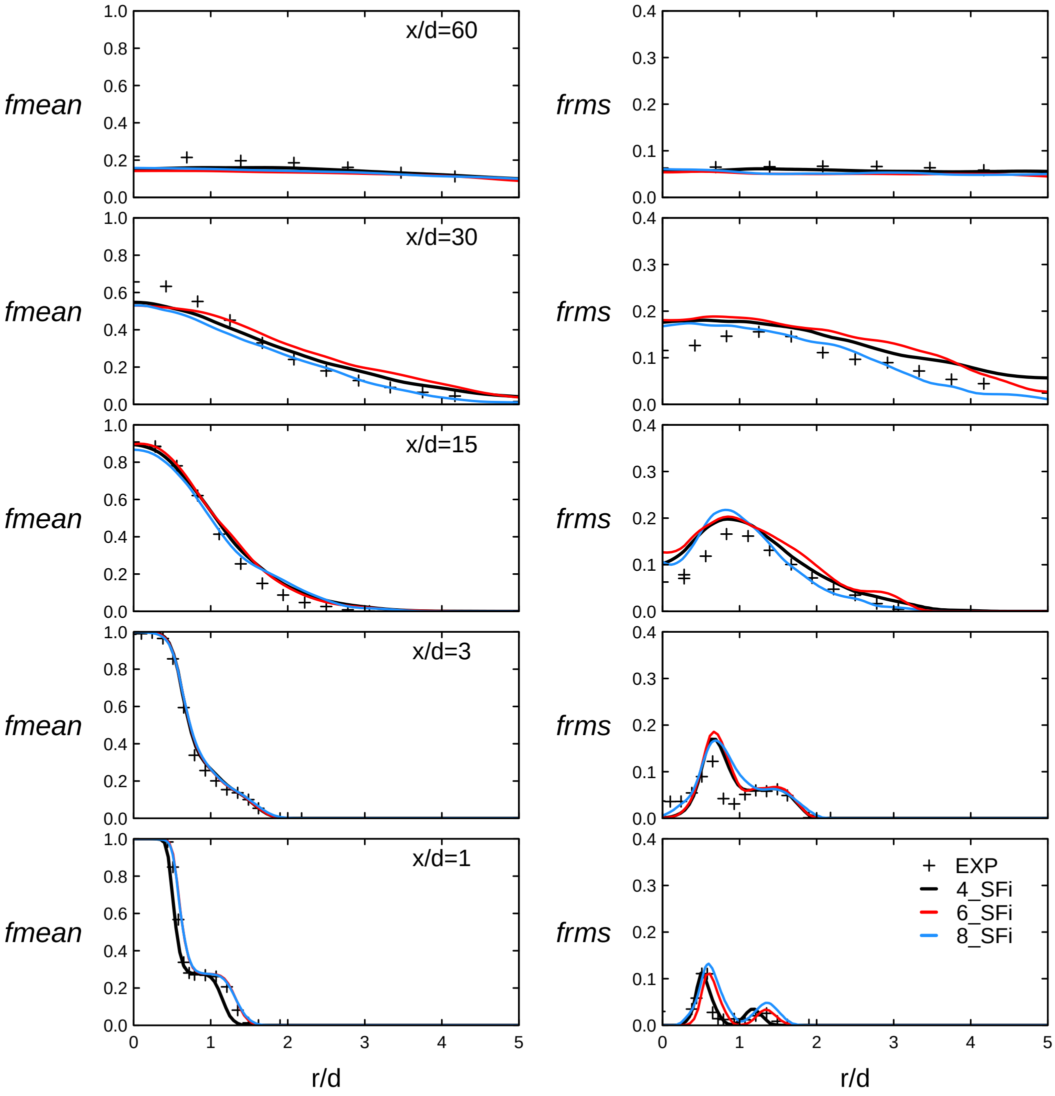

Figure 6.17: Comparison between experimental data for Sandia flame D [127; 163] and LES numerical results of the mixture fraction for various numbers of SF_i at different axial positions;$x = 1d, 3d, 15d, 30d, 60d$

The numerical results of the radial profiles of the mixture fraction field in Figure 6.17 indicate mostly an excellent agreement for both mean and variance values with slight under-estimation at the middle axial location ($x = 30d$) especially at the centerline. These observations are made for both mean and variance of the mixture fraction.

Finally, the temperature evolution is compared with measurements in Figure 6.18. The LES with hybrid ESF/FPV approach reproduces very well the temperature close to nozzle exit regions. In particular, the LES is able to retrieve nicely the mean temperature gradient up to $x/d < 30$. However beyond $x/d \geq 30$ there is a clear deviation in the predicted mean temperature and variances which can be contributed to the mixture fraction deviations.

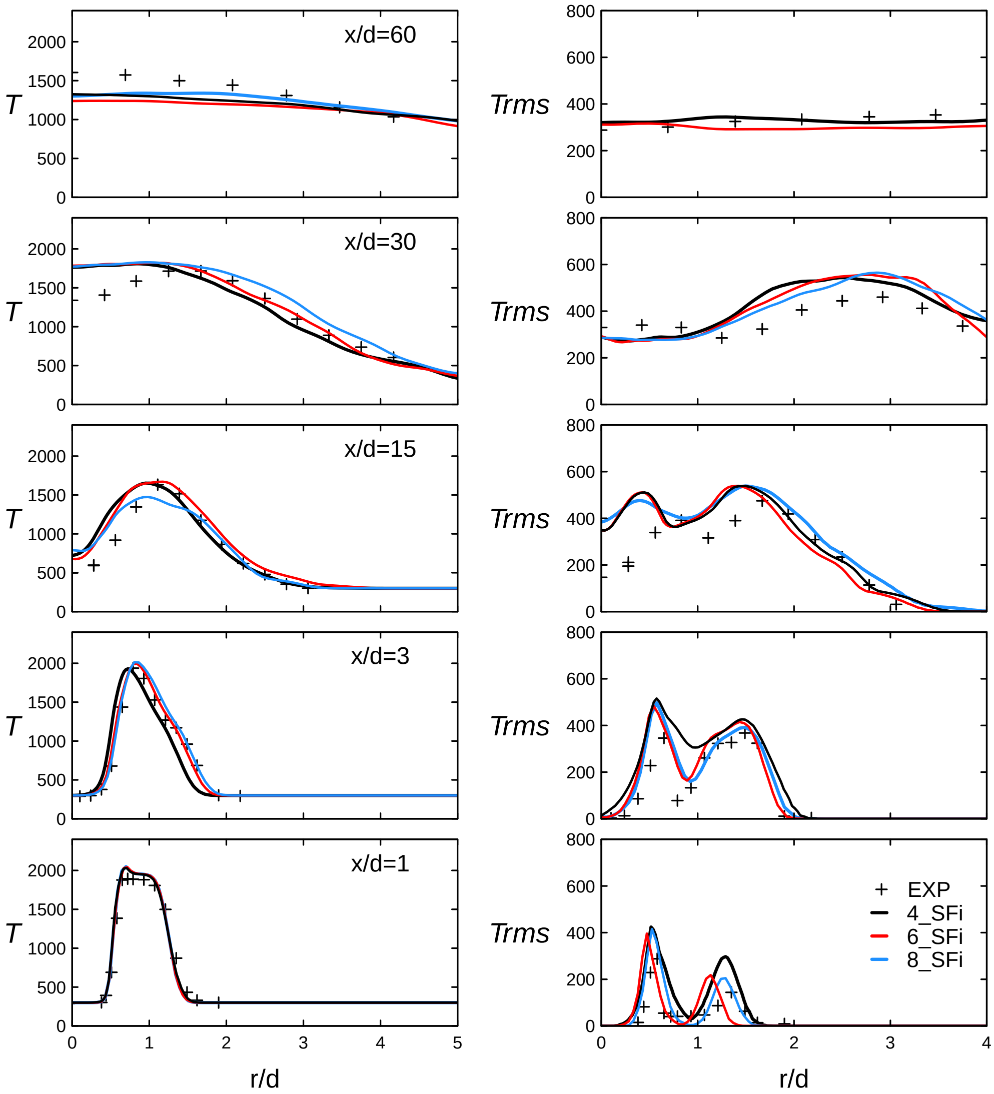

Figure 6.18: Comparison between experimental data for Sandia flame D [127; 163] and LES numerical results of temperature for various numbers of SF_i at different axial positions; $x = 1d, 3d, 15d, 30d, 60d$

Regarding the assessment of the convergence with respect to the applied number of SF_i, it broadly appears that the calculations using higher SF_i provides relatively better results, which is in line with other numerical investigations where the Eulerian stochastic field methodology was employed to simulate the Sandia flame D (see [31]). The influence of using different stochastic field numbers can be addressed by comparing results for various flow properties (e.g. temperature and its variance). It clearly shows that results obtained with 8 SF_i allows for an overall better prediction especially at positions close to the fuel nozzle ($x/d = 1$, $x/d = 3$). This also agrees well with the observations of Jones et al. in [84]. However, results obtained with lower number of fields in particular $SF_i = 6$ yield also to an acceptable agreement with experimental data which can be considered a good balance between accuracy and computational costs. Note that calculations with 6 SF_i requires 192 CPU while with 8 SF_i 224 CPU are needed.

As the reported outcome proves the efficiency and applicability of the proposed novel method once compared to available experimental data, it is worth highlighting the findings from other previous numerical investigations in which different flamelet approaches coupled to the FPV model have been employed. Regarding the different computational setups applied in the case of Sandia flame D, Coclite et al. in [21] used the statistically most likely distribution model (SMLD) coupled to the FPV technique and found the mixture fraction profiles at different axial positions rather slightly under-predicted near the centerline. In the work of di Renzo et al. [143], the mean temperature profiles were slightly over-predicted in some axial positions far from the centerline. Moreover, in [81] where the correlation set by simulated annealing (CSSA) and the FGM models were employed, the rms values of the radial velocity profile were over-predicted in low and middle axial positions.

Another essential quantity to evaluate numerical combustion approaches in predicting the flame properties is the probability density function (PDF). Figure 6.19 and Figure 6.20 illustrate the PDF of the temperature at two axial locations further downstream from the fuel inlet; $x/d = 15$ and 30. The PDF is obtained numerically by applying different SF_i numbers in comparison with experimental results.

The corresponding PDF was determined for a narrow band of the mixture fraction around the normalized stoichiometry value according to: $0.30 < f_{st,norm} < 0.40$. The PDFs obtained and simulated by applying 8 SF_i, are displaying better behavior compared to other numerical results simulated with less number of fields and better agreement with the experimentally measured PDFs at both axial positions ($x/ = 15$, $x/d = 30$). In particular, the probability of the presence of the temperature ranging from 1650K to 2150K is comparable to the measurements at selected axial locations.

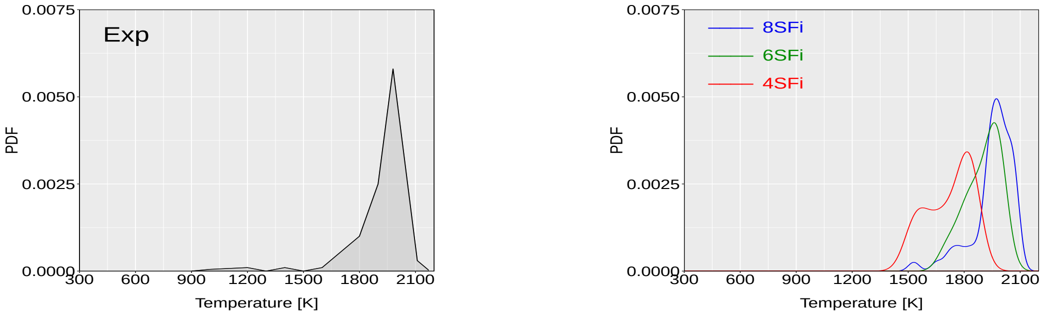

Figure 6.19: Probability density function of temperature within a mixture fraction range $\Delta_f = 0.1$ at the axial position $x = 15d$. Left: experimental results. Right: results obtained with the LES hybrid ESF/FPV approach using 4, 6 and 8 SF_i .

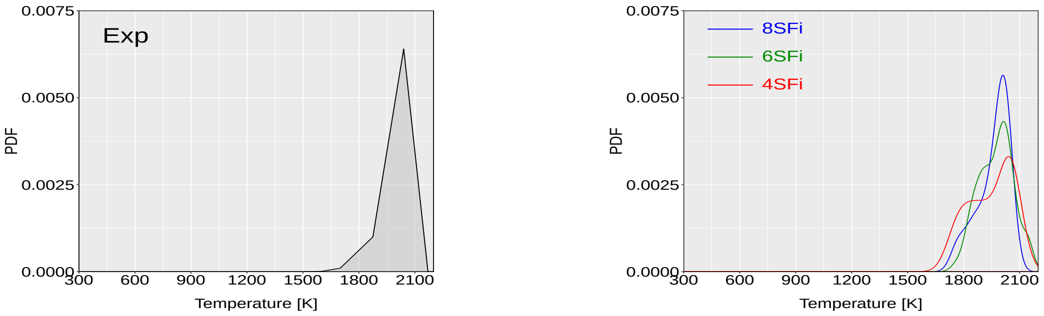

Figure 6.20: Probability density function of temperature within a mixture fraction range $\Delta_f = 0.1$ at the axial position $x = 30d$. On the left: experimental results. On the right: results obtained with the LES hybrid ESF/FPV approach using 4, 6 and 8 SF_i .

Figure 6.21 illustrates two series of instantaneous scatter plots of the temperature distribution. The first series (Figure 6.21, left) display the reference instantaneous scatter plots ([127; 163]) with respect to the instantaneous mixture fraction quantities at three different axial positions ($x = 7.5d$, $x = 15d$, $x = 30d$). The second series (Figure 6.21, right) exhibit the numerical scatter plots of the temperature field calculated with 8 SF_i which provide better results than using less fields number.

By comparing the numerical results with the experimental scatter plots, it turns out that the calculated maximum temperature corresponding to the stoichiometric mixture fraction is well predicted for all selected positions except the first axial location where it is slightly overestimated with small deviations. Some local extinction values could not be predicted numerically in the region close to the centerline. However, one can observe the presence of few unrealistic structures of temperature in the mixture fraction range $0.80 < f < 0.90$ for both axial positions $x/d = 7.5$ and $x/d = 15$. This could be due to the standard mixing model applied in this study which is based on the Interaction by Exchange of Mean (IEM) method. In fact, the IEM is known, by nature, to be not local in composition space which may lead to nonphysical events (see Subramaniam and Pope in in [160]). According to the study of Jaishree and Haworth [77] who compared the Lagrangian Monte Carlo and the ESF methods in RANS framework, two different mixing models (IEM and EMST (Euclidean minimum spanning tree)) have been evaluated for all piloted Sandia flames including the flame D, from which the IEM approach is revealed unable to capture perfectly the conditional temperature distribution. This model leads to similar nonphysical trend within the same mixture fraction range as in the present work. This behavior was also observed in the work by Hinz in [69].

6.3.2.1 Comparison with RANS

In order to reasonably compare results obtained within LES and RANS contexts, let us use the RANS results obtained from the same 3D grid (section 6.2.1) and LES calculations (see section 6.3.1). Thereby, LES results of major flame quantities are compared to those obtained with both 2D and 3D-RANS findings. The main goal of this comparison that is pictured in Figures 6.22 and 6.23, is to analyze the development of the obtained results

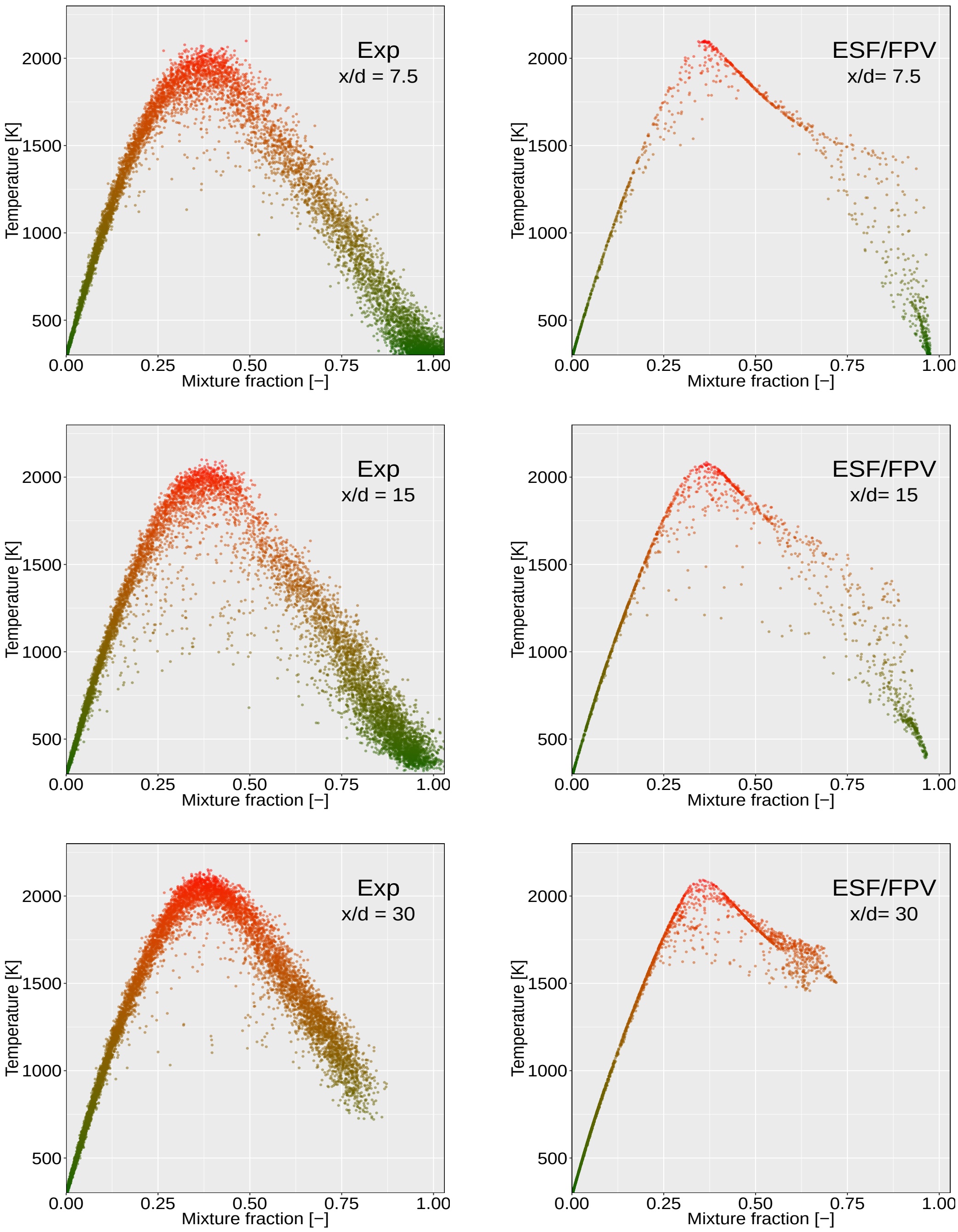

Figure 6.21: Instantaneous scatter plots of temperature versus mixture fraction for different axial ($x/d =$ 7.5 (top), $x/d = 15$(middle) and $x/d = 30$ (bottom). Measurements (Left) ([127; 163]) and results calculated using LES hybrid ESF/FPV with 8 SF_i (Right) ([107]).

using the hybrid ESF/FPV approach employing sub-grid-scale model. Firstly, it is clear that results of 2D and 3D RANS-ESF/FPV are found to be almost similar and in overall agreement with experimental data at different axial positions, except slight discrepancies that are observed at $x/d = 15$ which could be due to the turbulent modeling used in this study. It should be recalled that in the previous RANS study, the observed discrepancies pronounced at middle axial locations were mainly caused by the applied simple k-ε model.

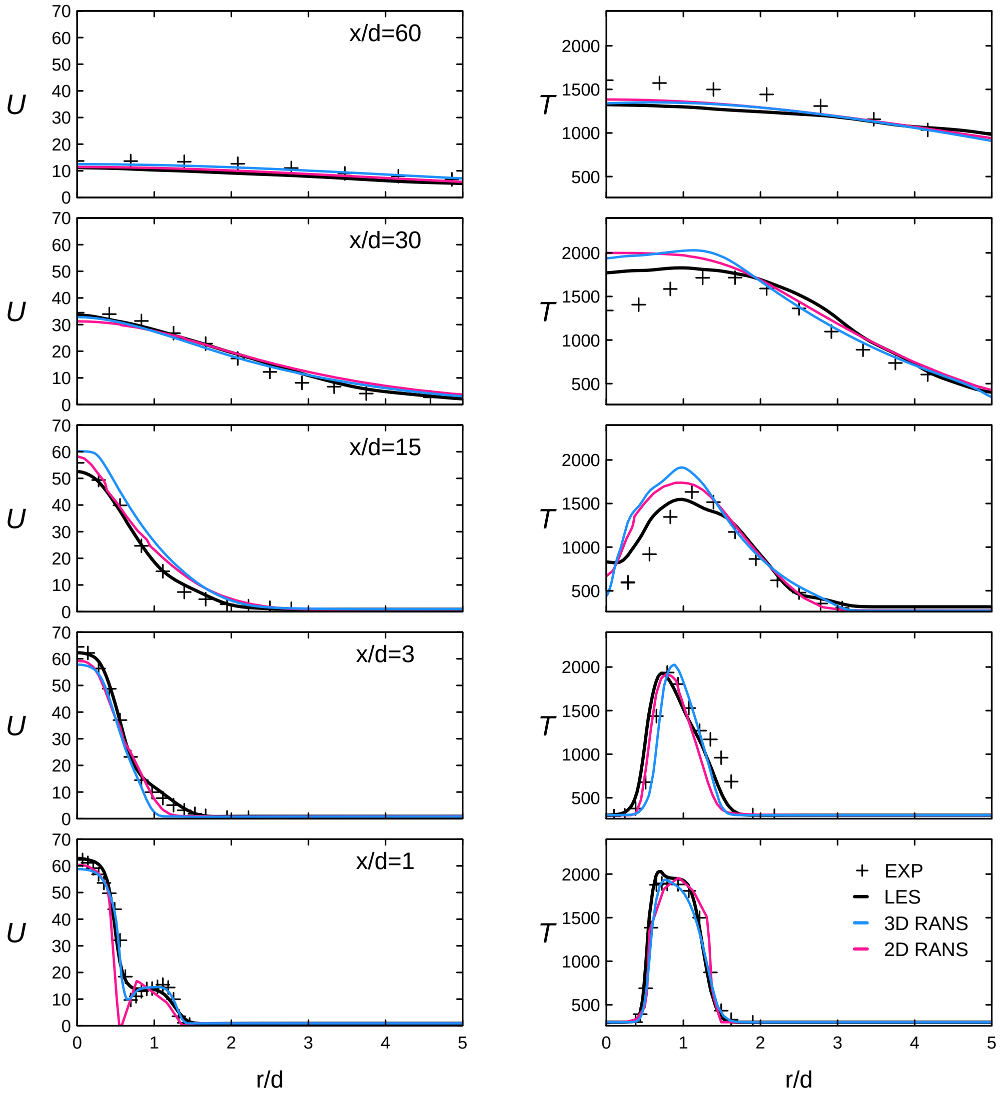

Figure 6.22: Velocity field (left) and temperature (right) profiles of Sandia flame D, calculated with LES-ESF/FPV method, and compared to RANS-ESF/FPV obtained results and to experimental data (+) [127; 163] at different axial positions: $x = 1d, 3d, 15d, 30d, 60d$.

Regarding the LES-ESF/FPV results, they are found to be slightly better than findings obtained from RANS simulations at some axial positions ($x/d = 15$ and $x/d = 30$) where temperature profiles obtained with RANS are slightly over-predicted. Hence, although that applying three-dimensional mesh with acceptable quality in the LES simulations is relevant in order to accurately predict the species evolution, the different quantities profiles obtained with 2D RANS are overall in good agreement over the entire domain with LES and experimental data.

Concerning the number of CPU applied for all calculations, as previously mentioned, the LES parallel simulations are realized by using 192 CPUs and 224 CPUs for calculations employing 6 SFi and 8 SFi, respectively. For the 3D RANS case, 160-192 processors were required to carry out the calculations using 16 SFi. However, only 16-64 processors are needed as increasing the number of stochastic fields from 1 to 128 SF_i to carry out 2D RANS calculations which emerged as an optimal compromise between prediction accuracy and computational efforts compared to 3D RANS.

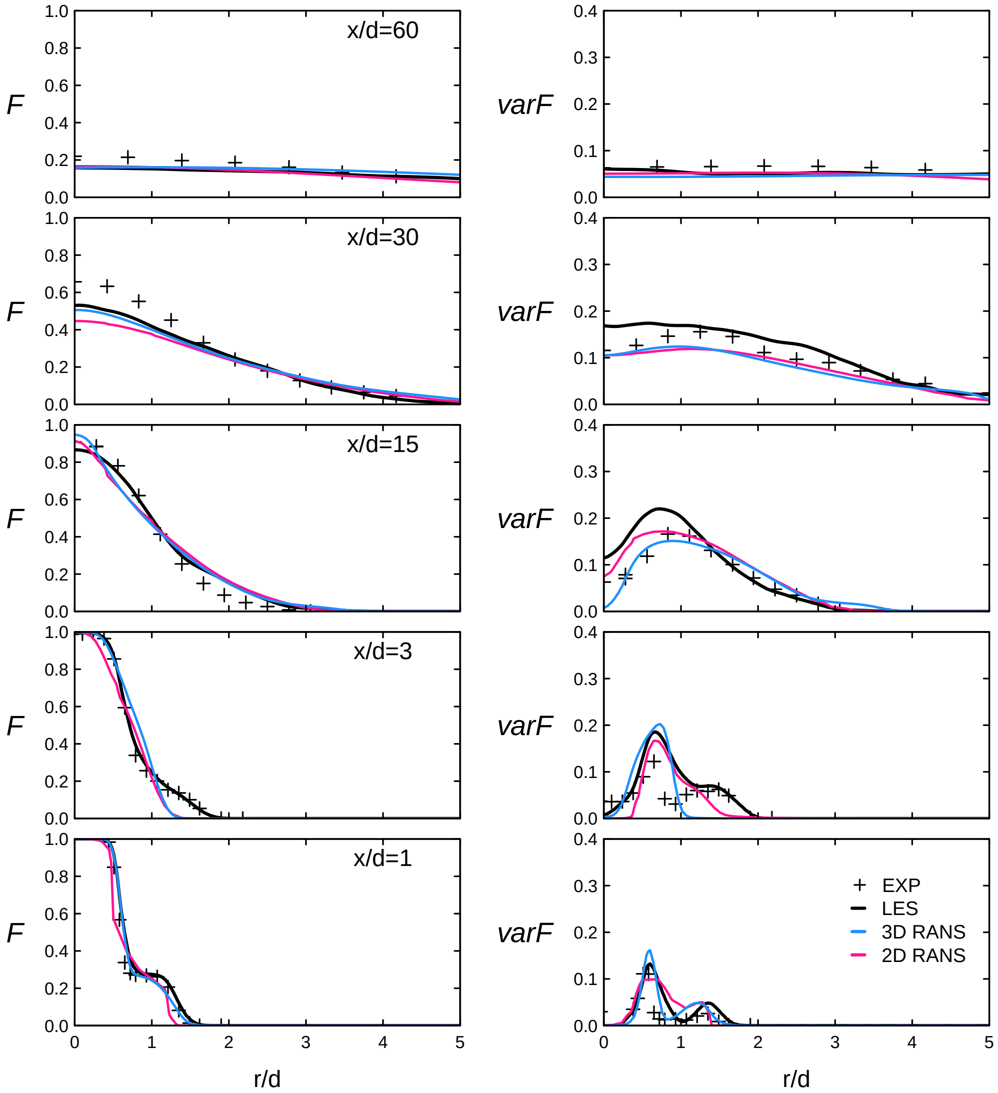

Figure 6.23: Mixture fraction (left) and mixture fraction variance (right) profiles of Sandia flame D, calculated with LES-ESF/FPV method, and compared to RANS-ESF/FPV obtained results and to experimental data (+) [127; 163] at different axial positions: $x = 1d, 3d, 15d, 30d, 60d$.

6.4 Summary

In this chapter, the validation of the hybrid ESF/FPV methodology has been achieved. Thereby, the prediction capability of the method in reproducing the main flame properties within different turbulence frameworks, namely RANS and LES has been assessed. In the first part, RANS based investigations of the Sandia flame D configuration were carried out where different numbers of stochastic fields have been employed to evaluate the SF_i number convergence. The obtained results were analyzed qualitatively and quantitatively by comparing them to the available experimental data. Based on the observed results, it turned out that calculations with 48 SF_i emerged as a very good compromise between prediction accuracy and computational costs. The second part was devoted to the application of LES with the proposed hybrid ESF/FPV approach. Apart from the mean flow properties, this model also allows to retrieve transient turbulence parameters such as variance/RMS. In particular, a very satisfactory prediction of different experimental and various fields was reported demonstrating the good capability of the method in reproducing main flow and flame characteristics. Furthermore, the importance of choosing the optimal number of stochastic fields is highlighted for both RANS and LES based ESF/FPV approach. It was found that 48 SF_i for RANS and 8 SF_i for LES provide a good trade off between the satisfactory accurate results and required computational costs. Finally, 3D RANS-ESF/FPV simulations have been carried out and obtained results were compared to previous 2D RANS and LES findings. An overall agreement was observed over the entire domain expect few discrepancies at middle axial positions. It revealed that applying 3D grid in the RANS context imposed an increase demand of computational resources without strongly affecting the behavior of major flame quantities evolution.

Chapter 7

Applications: Oxy-fuel Flames

In this chapter the implemented hybrid ESF/FVP method is used to simulate more complex combustion configurations based on non-premixed oxy-fuel combustion process. Although simpler in terms of burners geometry, the chosen application cases reproduce relevant complex physical processes and represent important oxy-combustion systems that are highly demanded in industrial applications [155].

As pointed out in the "Introduction", oxy-fuel combustion processes are of high interest nowadays since they have significant advantages over conventional combustion concepts where fossil fuel is oxidized with air, affecting the environment in terms of emission increase of CO_2 and NO_x gases [48; 141]. The choice of test cases in this work was settled responding to the recent favorable policies intending in diminishing the carbon dioxide emissions following the carbon capture and storage (CCS) technologies. In the recent review in reference [175], three main techniques are reported, namely, the pre-combustion capture, post-combustion capture and during-combustion which is referred to as oxy-fuel combustion. Only the last approach is addressed here where natural gas is involved.

Thereby, as reported in [154] and following the studies by Bolland et al. [10; 11] and Tan et al. [161], the methane gas is applied as a CO_2 removal option in the design of oxy-fuel burners and a mixture of CO_2/O_2 is adopted instead of air in the oxidizer part. The fuel combustion ideally yields flue gas which is composed of carbon dioxide and water vapor, from which the CO_2 can be easily separated applying condensation process permitting its capture,then its storage or further recycling. This technique is characterized by a faster chemical reaction and burning velocity, and the adiabatic flame temperature is much higher once compared to air-fuel combustion. Therefore, it is highly relevant to investigate, better predict and subsequently control and optimize such combustion processes.

The main objective of this chapter is to appraise the capability of the method, in both RANS and LES frameworks, in reproducing main oxy-combustion features and to investigate the emerging flame structure and flame-turbulence interaction. Similar to the studied case in the previous chapter, the burners for oxy-fuel flame series are operated under adiabatic conditions where the pressure $p = 1\ bar$ and the ambient temperature T=299 K. In terms of validation, the obtained results are analyzed and compared to available experimental data [154]. Both RANS and LES based approaches coupled to ESF/FPV are applied where various simulations using different number of stochastic fields are carried out.

7.1 Description of the Configuration

The burners under investigation correspond to that experimentally studied in [154]. Thereby, the measurements were carried out applying the simultaneous line imaging of Raman/Rayleigh scattering developed at Sandia National Laboratories to produce single-shot profiles of many parameters including temperature and mass fraction of major species (CO_2, O_2, CO, N_2, CH_4, H_2O, H_2). The measurements were performed for two oxy-flame series where each series consists of three flames: namely series A (A1, A2, A3) and series B (B1, B2 ,B3). The difference between the two flame series is summarized in table 7.1 and follows mainly two features:

- *Fuel mixture composition:*

The burner fuel inlets of all investigated flames are composed mainly with methane enriched with hydrogen. The flames in this series are characterized by the change of the CH_4/H_2 ratio keeping the Reynolds number $Re = 15,000$ constant for the main jet exit. For the first series, the molar fraction of hydrogen is varied from 37% to 55% . Three flames are denoted in the experimental work with series A (A1, A2, A3).

- *Jet exit Reynolds number Re :*

In the second flame series, while keeping the enrichment of H_2 in the fuel inlet constant with a percentage of 55%, the jet exit Reynolds number was the changing parameter varying from $Re = 12,000$ to $Re = 18,000$. These three flames are denoted as series B (B1, B2, B3).

For both flame series, the oxidizer part consists of a gas-mixture of CO_2 and O_2 instead of air to facilitate the CO_2 capture and storage/recycle as already mentioned above. Besides that, many numerical and experimental studies in references [24; 29] have been reported that “the molar percentage of oxygen in the oxidant should be around 30% to reach air-flame stability”. Herein, in the numerical set up following the experimental cases, all flames were operated with 32% of oxygen and 68% of diluted carbon dioxide in the oxidizer mixture. In the present work, only 3 flames, as listed in table 7.2, from both series are investigated numerically in order to study three important physical aspects. These aspects are summarized as below:

- The impact of varying CH_4/H_2 ratio by the enrichment of H_2 in the fuel stream. Thereby only 2 flames from the first series (A1 and A3) are involved in this study.
- The impact of varying the Reynolds number Re by comparing 2 cases chosen from each series (A1 and B3).
- The influence of the addition of CO_2 in the oxidizer inlet for the considered flames.

According to the experimental study in [154], the oxy-flame burner consists mainly of three jets: fuel, oxidizer and co-flowing air jet. These jets are constructed co-axially as depicted

Flame name	$\%_{mol}$ H_2 *in fuel* (-)	$\%_{mol}$ CH_4 *in fuel* (-)	$\%_{mol}$ O_2 *in oxidizer* (-)	$\%_{mol}$ CO_2 *in oxidizer* (-)	Re_{Fuel} (-)	*Jet speed* (m/s)	*Coflow speed* (m/s)
A1	55	45	32	68	15.000	98.2	0.778
A2	45	55	32	68	15.000	84.5	0.755
A3	37	63	32	68	15.000	75.8	0.739
B1	55	45	32	68	12.000	78.6	0.622
B2	55	45	32	68	15.000	98.2	0.778
B3	55	45	32	68	18.000	117.8	0.933

Table 7.1: Compositions of of the oxy-fuel jet flame series with inlet conditions.

in Figure 7.1. The main jet for fuel stream has an inside diameter $d_f = 5\ mm$ with wall thickness equal to 0.5 mm. In order to ensure fully developed flow of the fuel mixture, the tip of the fuel jet is placed at 40 mm above both oxidizer and co-flowing air inlets. The fuel jet is surrounded by a laminar co-flow with diameter equal to $d_c = 96.5\ mm$. This laminar co-flow or oxidizer is first discharged over many perforated plates and honeycomb in order to ensure a uniform distribution of the considered stream. The total experimental set-up was constructed at the top of a 25 cm x 25 cm square-section wind tunnel. From this tunnel the air was discharging for purely experimental reasons namely to avoid the intrusion of nitrogen by preventing early mixing with ambient air, and to protect the oxidizer mixture from being polluted with undesired gases. Moreover, in order to help the flame to be attached to the fuel nozzle, the main jet tip was squared-off end, but in this context, also the addition of H_2 in the fuel gas mixture plays the role of a pilot for maintaining the flame attached to the fuel nozzle.

All information concerning the initial conditions for the different streams of the investigated oxy-fuel flames, are summarized in table 7.2. The velocity of the fresh air entering the domain as a co-flow is set to $u_c = 0.5\ m/s$.

Flame name	$\%_{mol}$ H_2 *in fuel* (-)	$\%_{mol}$ CO_2 *in oxidizer* (-)	Re_{Fuel} *speed* (-)	*Jet speed* (m/s)	*Stoichiometric mixture fraction* (-)	*Temperature at stoichiometry* (K)
A1	55	68	15.000	98.2	0.0535	2250
A3	37	68	15.000	75.8	0.0565	2236
B3	55	68	18.000	117.8	0.0535	2250

Table 7.2: Compositions of the oxy-fuel jet flames $A1$, $A3$ and $B3$ with inlet conditions.

All measurements were taken at different positions above the fuel tip to ensure that all probe volumes do not include fresh air and consequently no nitrogen is found in the mixing and reacting zones. These positions were set from x=1 d_f to x=20 d_f.

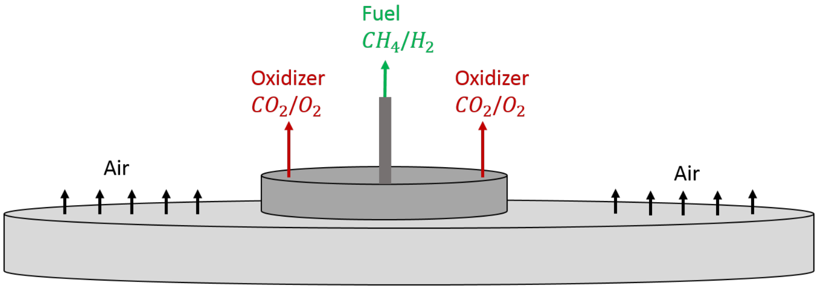

Figure 7.1: Schematic diagram of the oxy-fuel jet flame with inlet conditions

7.2 Sensitivity studies using RANS Simulation

As previously reported in section 6.2, the RANS turbulence model presents several advantages with respect to reducing the computational time and offering acceptable mean profile for the most quantities. Thereby it emerges as the compromise between acceptable results and computational efforts. In this context, this section is mainly focusing on RANS simulations employing the k-ε model in order to evaluate the capability of the hybrid ESF/FVP method in reproducing chemical and physical features of the turbulent oxy-fuel flames.

7.2.1 Numerical set-up

Due to the symmetry characteristics of a 2D computational domain applied for this case as illustrated in 7.2, a simplified uniform mesh is designed with 28,000 control volumes which is sufficient to ensure grid-independent solutions. In order to avoid the influence of the outlet boundary condition, the combustion chamber is sufficiently extended to 150 d_f downstream the oxidizer inlet as it is displayed in Figure 7.2. The waveTransmissive condition is imposed at the outlet plane with $P = 101.325\ kPa$, while other variables have a zero gradient boundary conditions. The temperature is initially uniformly distributed with 300 K.

The calculations are carried out for the physical time of 1.2 s in order to achieve the acceptable averaged results. In order to control the CFL number throughout calculations (CFL $<$ 1), the time step of t_s = 2.10e-6 s is chosen. Different FPV tables were generated based on the flamelet solutions obtained from the flamelet generator FlameMaster [46]. These flamelets are calculated with the GRI.3.0 mechanism by using the constant unity Lewis number assumption ($Le = 1$) and the correct fuel-oxidizer compositions for each oxy-flame. The objective of using $Le = 1$ even though H_2 takes place is to assess its effect on the general prediction of the oxy-fuel flame structure, stability and emissions. In this case the definition of the progress variable pv is set as:

$$pv = \frac{Y_{H_2O}}{\mathcal{M}_{H_2O}}. \tag{7.1}$$

This progress variable definition is chosen based on the findings of Gierth et al. [58; 59] demonstrating that it gives a unique mapping from the scalar dissipation rate to the progress variable.

Parallel simulations are carried out considering 16-64 processors, since increasing the number of stochastic fields applied from 1 to 128 SF_i leads to an increase demand of computational resources.

Other numerical details for the operating conditions are depicted in the Table 7.3 where they are set similarly for all considered flames A1, A3, B3.

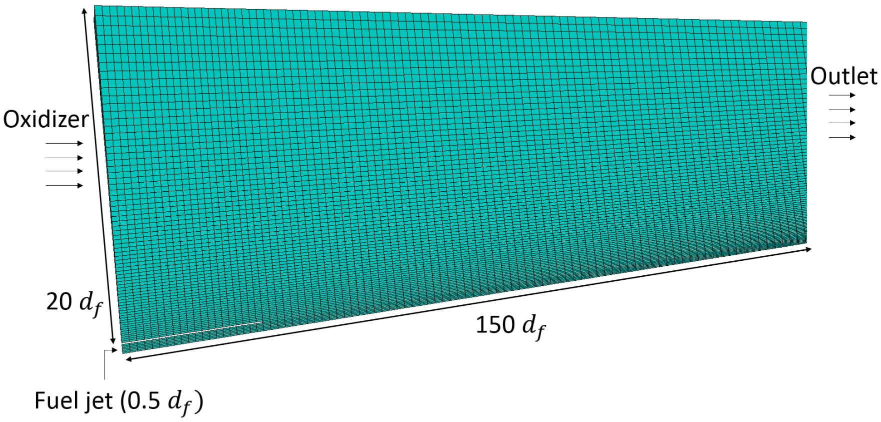

Figure 7.2: 2D numerical block structured grid for the oxy-fuel configurations.

Mixture fraction f (-)	*Progress variable* pv (-)	*Temperature* T (K)	*Kinematic viscosity* ν (m^2/s)
1	0	299	$3.271 \cdot 10^{-5}$

Table 7.3: Numerical inlet conditions of oxy-fuel flame cases

7.2.2 Results

The three flames $\{A1, A3, B3\}$ from the oxyflame series have been simulated in order to highlight the effect of CO_2 and O_2 dilution and of $H_2\%$ enrichment as well as the impact of the Reynolds number on the flow field and the flame structure. For comparison purposes, two methods are applied in this study, namely the novel proposed hybrid ESF/FPV approach and the classical presumed β-PDF technique. Thereby, the ESF/FPV obtained results are compared not only to experimental data but also to solutions collected using the classical β-PDF method in order to numerically examine the capabilities and limitations of the suggested approach.

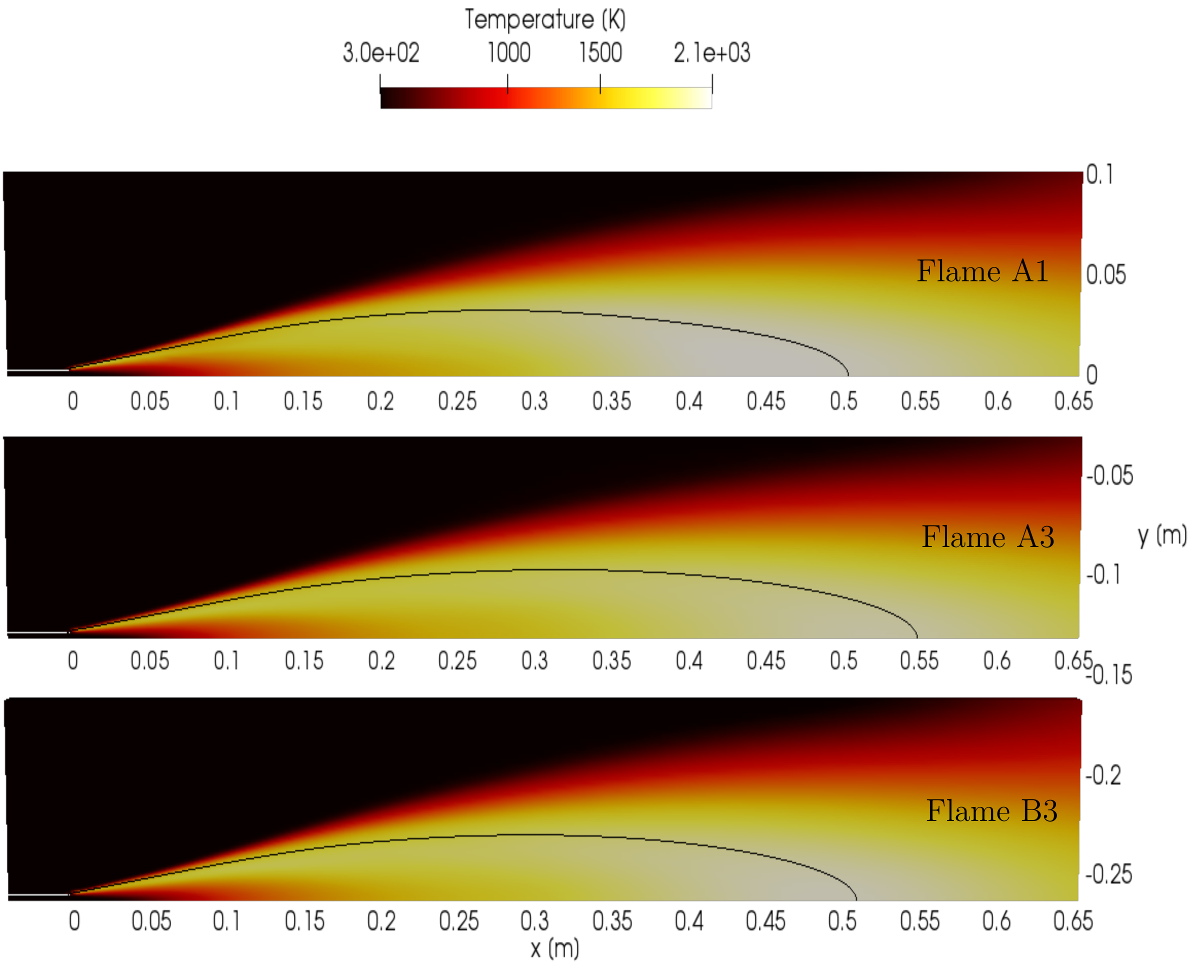

Figure 7.3: Temperature profile of the three oxyflame configurations ($A1$, $A3$, $B3$). The traced solid black lines present the stoichiometric mixture fraction values: Flame A1: $f_{st} \approx 0.0535$, Flame A3: $f_{st} \approx 0.0565$, Flame B3: $f_{st} \approx 0.0535$.

At first, in order to qualitatively compare the results obtained using the ESF/FPV approach of the three oxyflames $\{A1,\ A3,\ B3\}$, Figure 7.3 presents the snapshots of the mean temperature profiles of different cases along the centerline. All three cases feature similar trend of temperature profile displaying smooth and continuous distributions of the temperature evolution. However, once comparing the flame lengths which are highlighted by the solid black line in temperature plots in Figure 7.3, a clear distinction can be observed.

In the experiment, only the heights of the flames can be visually observed through the flame series pictures, even though, measured values of flame lengths are not reported. Thence, the comparison of the flame lengths is limited only to numerical findings of three cases. Accordingly, in Figure 7.3 (Flame A1) the representative line of the stoichiometric mixture fraction indicates a flame length of about $f_{LA1} = 0.5 (\approx 100 d_f)$. This value is slightly lower than the flame length of the flame B3 which is approximately equal to $f_{LB3} = 0.51 (\approx 102 d_f)$. Nevertheless, the flame length for the A3 case is clearly higher with about $f_{LA3} = 0.55 (\approx 110 d_f)$. The aforementioned values of the calculated flame lengths are exploited to understand the influence of different operating conditions on the simulated flames, see more detailed in subsections (7.2.2.2) and (7.2.2.4).

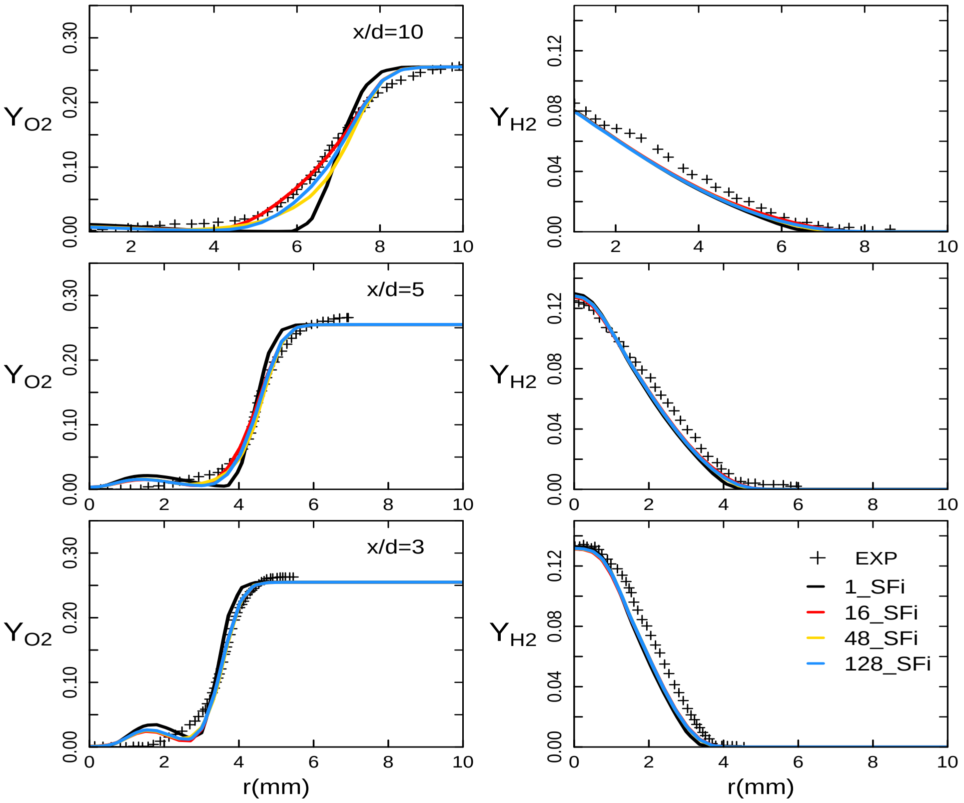

Figure 7.4: O_2 (left) and H_2 (right) mass fraction profiles of flame case $B3$ calculated at different axial positions ($x = 3d, 5d, 10d$) with RANS-ESF/FPV method using different number of SF_i, and compared to experimental data (+) [154].

7.2.2.1 Convergence with respect to N_s

A quantitative analysis of the oxyflame simulation results is described in terms of comparison between numerical findings and measurements. Initially, parametric investigations are achieved by simulating the flame B3 in order to study the numerical convergence with respect to number of stochastic fields (SF_i) applied. The obtained numerical data are collected and compared to experimental data at different axial positions ($x = 3d$, $x = 5d$, $x = 10d$). The mass fraction profiles of O_2 and H_2 quantities are depicted in Figure 7.4 while Figure 7.5 displays the evolution of CO and H_2O mass fractions. The results of SF_i with $N_s = 1$ show clear overestimations for almost all plotted quantities at all positions. This result deviations with respect to experimental data are obviously expected since applying $N_s = 1$ SF_i for RANS calculations means employing simple laminar chemistry approach without considering any combustion modeling. This results in the similar performance as for a perfectly stirred reactor [106]. For H_2 species mass fraction profiles, an acceptable agreement is achieved for all SF_i numbers at all locations once results are compared with measurements. Similar behavior is closely reproduced for the O_2 profiles;

however an unexpected raising of the O_2 mass fraction values is pronounced near the centerline at axial positions close to the fuel inlet. This behavior can be associated with the mesh quality used alongside the RANS turbulence model applied.

Regarding the impact of employing different SF_i numbers, this is mostly detected for other mean quantities where the evolution of both CO and H_2O mass fractions are better captured with ESF/FPV calculations already using 16 SF_i, whilst under-predictions of the species mass fractions are observed for the same simulations only at the axial position $x = 10d$.

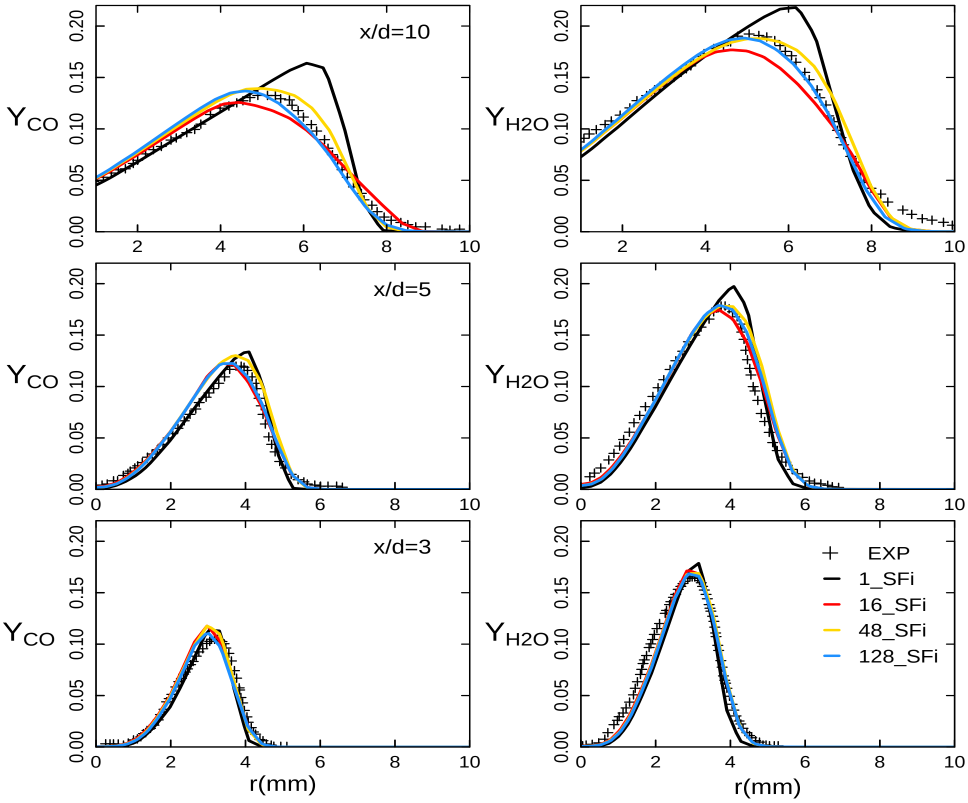

Figure 7.5: CO (left) and H_2O (right) mass fraction profiles of flame case $B3$ calculated at different axial positions ($x = 3d, 5d, 10d$) with RANS-ESF/FPV method using different numbers of SF_i, and compared to experimental data (+) [154].

Increasing the number of stochastic fields to 48 SF_i and 128 SF_i leads to very good agreement with experimental data further from the fuel nozzle. This means that, ESF/FPV simulations employing higher number of stochastic fields in the order of 128 provide almost identical results with experiments and closely similar solutions to the calculations using 48 SF_i. Hence, 48 fields emerge as a good compromise between good results reproduction and computational costs. It is important to mention that simulations with 128 SF_i necessitated 64 CPUs while those with 48 SF_i required 32 CPUs.

7.2.2.2 Effect of H_2 enrichment

After the detailed description of the parametric study related to the convergence with respect to the stochastic fields numbers, the effect of the H_2 enrichment is addressed in this subsection. As described in Table 7.2, the reacting cases $A1$ and $A3$ operating with the same value of Reynolds number ($Re = 15.000$) exhibit different CH_4/H_2 ratios where the H_2 enrichment in the fuel part is equal to 55% for $A1$ and 37% for $A3$. These particular inlet conditions showed an important influence on the flame structures. Analogously to flame B3, the other oxyflames $A1$ and $A3$ have been simulated with the ESF/FPV approach using 48 SF_i. The obtained results are extracted according to the selected axial locations ($x = 3d, 5d, 10d$) and compared to the experimental data. Figure 7.6 illustrates the mass fraction distributions of O_2 and H_2 species while Figure 7.7 displays the evolution of CO and of the transported H_2O species mass fractions.

Regarding the flame $A1$ calculations, although small discrepancies at the lower position are observed, all reproduced quantities reasonably match the experiments. Similar acceptable agreement is noticed in the case of flame $A3$, except some slight under-predictions for the species CO and H_2O remarked in the central axial position.

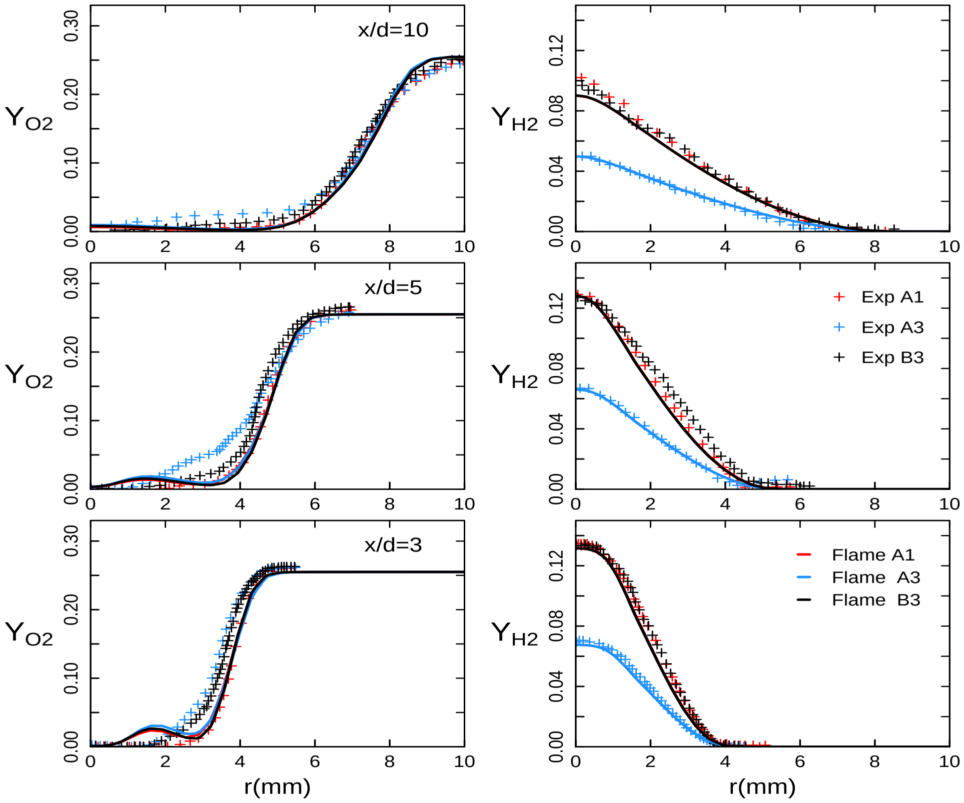

Figure 7.6: O_2 (left) and H_2 (right) mass fraction profiles of flame series: $A1$, $A3$,$B3$, calculated at different axial positions ($x = 3d, 5d, 10d$) with RANS-ESF/FPV method using 48 SF_i, and compared to experimental data (+) [154].

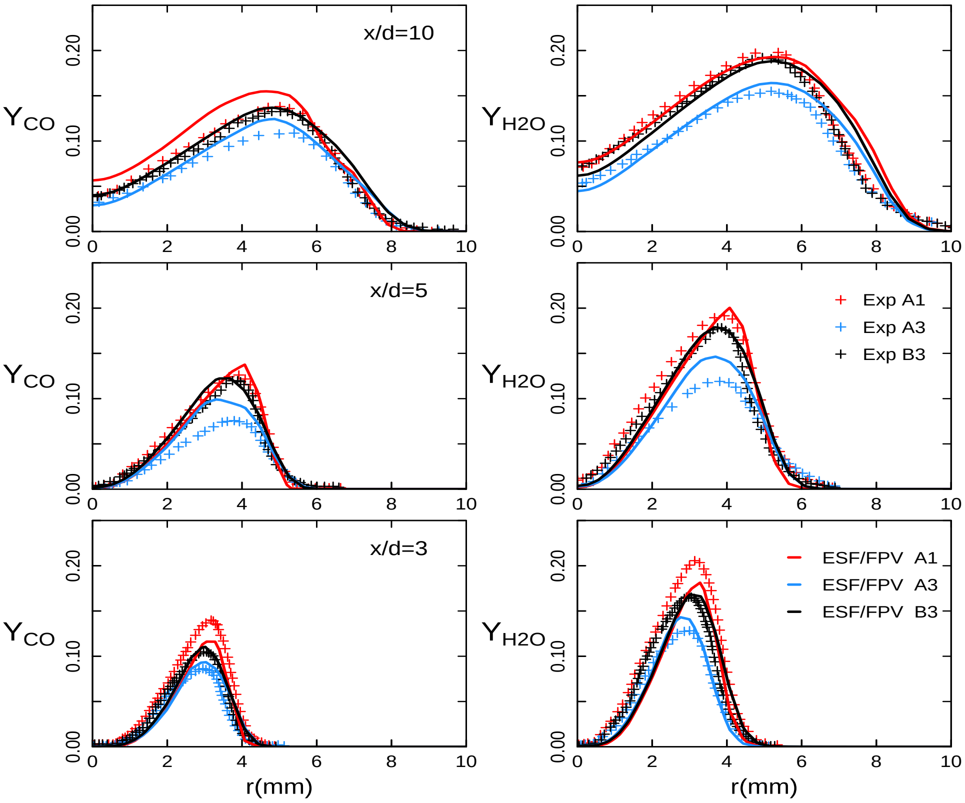

Figure 7.7: CO (left) and H_2O (right) mass fraction profiles of flame series: $A1$, $A3$,$B3$, calculated at different axial positions ($x = 3d, 5d, 10d$) with RANS-ESF/FPV method using 48 SF_i, and compared to experimental data (+) [154].

In particular, Figure 7.7 shows that both CO and H_2O species productions in flame $A1$, which has the highest CH_4/H_2 ratio, are more important than in flame $A3$ at the different axial positions in accordance with the available measurements. This is of interest despite that the Lewis number effect has not been included at the present stage since only unity Lewis number hypothesis was assumed ($Le = 1$). This means, that this method is able to reproduce major reacting species of oxy-fuel flames and H_2 induced differential diffusion effect is not important in the investigated area.

Moreover, the temperature evolution profiles of both flames are also affected by the H_2 enrichment change. According to Sevault et al. [154], the extinction level increased from flame $A1$ to $A3$ and its effect was reported together with the reduction of the mean temperature values around the stoichiometric mixture fraction. This behavior is successfully numerically predicted in Figure 7.8 at both axial locations $x = 3d$ and $x = 5d$ with difference of temperature approximately equal to $200K$.

Although the increase in temperature with $H_2\%$ enrichment is observed close to the fuel inlet from flame $A1$ to flame $A3$, this temperature difference disappears at further axial locations at $x = 10d$ where the numerical prediction of the temperature profile of both flames leads to similar results. Unfortunately, experimental results of temperature at further positions, $x/d \geq 10$, are not available. Decreasing the percentage of $H_2\%$ enrichment in the fuel side of the flame $A3$ does not affect only the temperature's peak value nearby the stoichiometric mixture fraction but also the maximum adiabatic temperature that is deviated from stoichiometry towards rich side.

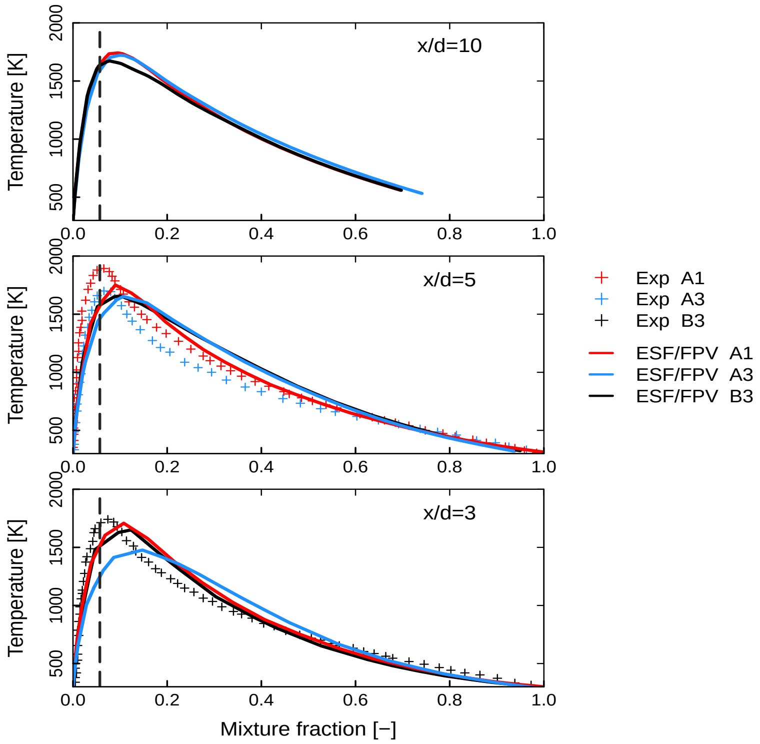

Figure 7.8: Temperature profiles of flame series: $A1$, $A3$,$B3$, calculated at different axial positions ($x = 3d, 5d, 10d$) with RANS-ESF/FPV method using 48 SF_i, and compared to experimental data (+) [154].

By further looking into the Figure 7.3 where the different flame lengths are illustrated, another important observation can be highlighted in order to emphasize the effect of varying the H_2% enrichment. It appears that, the flame $A3$ corresponding to the case with lower CH_4/H_2 ratio in the main jet side, reveals a higher value of flame length in comparison with other two cases. This is explained by the fact that exceeded amount of H_2 in the fuel nozzle advances the faster production of combustion products leading the reactions to occur at closer downstream positions.

7.2.2.3 Effect of Reynolds Number

The flame details in Table 7.2 show that both jet flame cases $A1$ and $B3$ have similar CH_4/H_2 ratio in the fuel nozzle with H_2 enrichment equal to 55%, but they are operated under different Reynolds numbers ($Re_{A1} = 15.000, Re_{B3} = 18.000$). These particular inlet conditions lead to important influences on the flame properties. The effect of different Reynolds numbers can be observed in 7.7, where there is a clear augmentation in the production of mean mass fraction of both CO and H_2O species for the flame operated with lower Re-number ($A1$) and that is in particular at the lower axial location $x = 3d$.

The difference of both mentioned formation quantities is reduced progressively far from the nozzle. It turns out that the mixing state near the nozzle with lower jet Reynolds number likely leads to higher formation level of CO and H_2O species.

Regarding the effect of the Reynolds number on the temperature distribution, Figure 7.8 shows that the maximum adiabatic temperature position against the mixture fraction space is nearly the same for both jet flames at all axial positions. This note can be affirmed from the analysis of the flame length line values delineated in Figure 7.3. It appears that with various Reynolds numbers, the flame lengths from oxy-fuel flames remain approximately the same with an averaged value of $f_L \approx 101 d_f$. This confirms a previous finding by Ditaranto in [30].

It is highly important to mention that the hybrid ESF/FPV approach is able at this stage to reproduce satisfactorily numerically mentioned trends.

7.2.2.4 Effect of CO_2 enrichment

The oxidizer sides of all jet oxyflame series (A and B) are enriched with a considerable quite high level of CO_2 which is a constant amount of about 68%. This results in the high level of production of CO and H_2O mass fractions as it can be observed in Figure 7.7. For the jet flames $A1$ and $B3$ which include both the same H_2% enrichment in fuel side and same CO_2 dilution amount, the CO mass fraction locally reaches at $x = 5d$ an amount of 0.14 and increases further at $x = 10d$ reaching the value of 0.16, which is not a common value for cases with air-diluted flames. This confirms a previous finding by Masri et al. in [108] who presumed that the CO_2 diluted in oxidizer is not inert and CO high level formation is the result of the reaction of CO_2 with H to form CO species. Therefore, the production level of CO in flames $A1$ and $B3$ is manifestly higher than in $A3$ at all axial locations. The various simulations applying the hybrid ESF/FPV approach could reproduce this trend.

Furthermore, the high CO_2 amount diluted within the oxidizer streams does not only raise the production level of some combustion species but also lead to a slight reduction of the temperature profile in the zone closer to the inner fuel jet once values compared to the air/methane flame outcomes.

7.2.2.5 Comparison with β-PDF approach

As previously mentioned, apart from the ESF, a combustion sub-model based on the presumed probability density function using the β-function (β-PDF) is also applied. In fact, studying the efficiency of the β-PDF method is not in the focus of this numerical investigation, but it was quite compulsory to compare the hybrid ESF/FPV model to another approach that was widely frequently employed in the combustion community [81; 91; 116; 142]. For this purpose, the equations set Eq (4.26) - Eq (4.28) along with Eq (4.21) has been utilized.

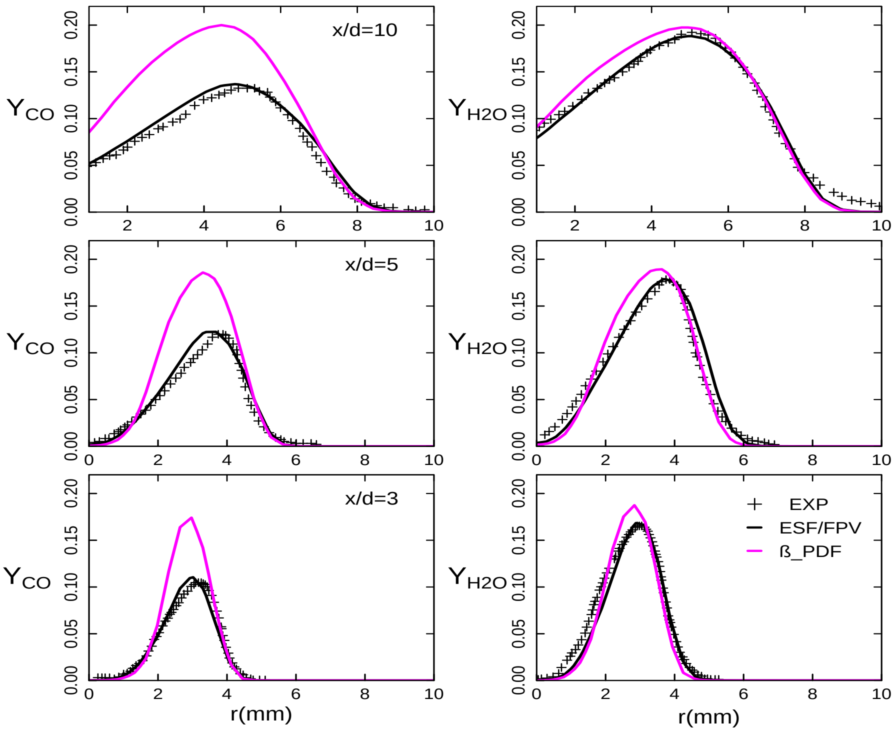

Figure 7.9: CO (left) and H_2O (right) mass fraction profiles of oxy-flame *B*3, calculated with RANS-ESF/FPV method, and compared to β-PDF obtained results and to experimental data (+) [154].

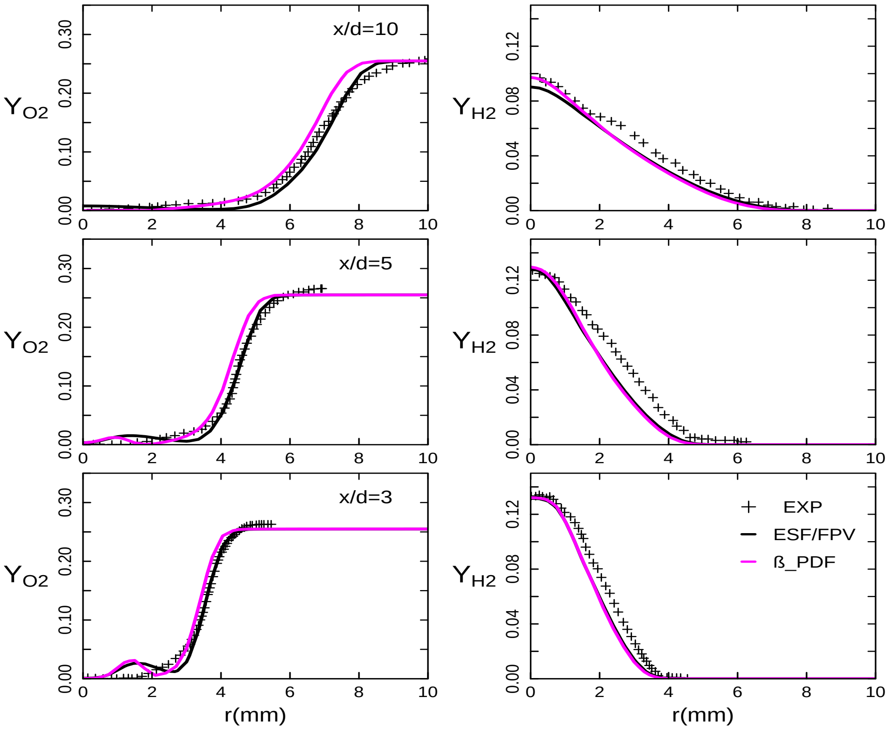

Figure 7.10: O_2 (left) and H_2 (right) mass fraction profiles of oxy-flame *B*3, calculated with RANS-ESF/FPV method, and compared to β-PDF obtained results and to experimental data (+) [154].

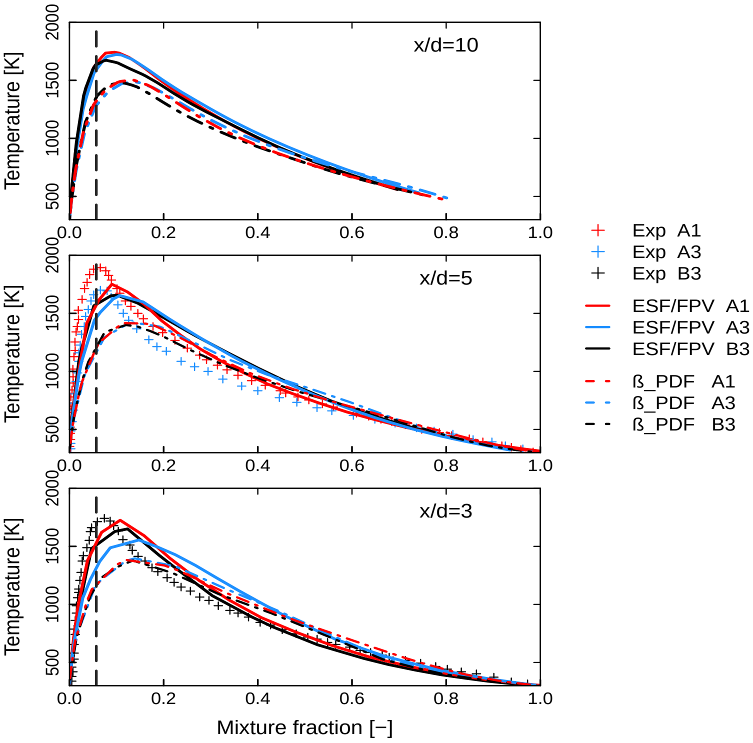

Figure 7.11: Temperature profiles of flame series: $A1$, $A3$,$B3$, calculated at different axial positions ($x = 3d, 5d, 10d$) with RANS-ESF/FPV method using 48 SF_i, and compared to β-PDF approach and to experimental data (+) [154].

Thereby, the application of both approaches to the oxyflames $A1$, $A3$ and $B3$, deliver different prediction results regarding the production of various combustion species. With the application of both combustion sub-models (ESF/FPV and β-PDF), Figure 7.9 represents the obtained distribution of CO and H_2O mass fractions of flame $B3$ whilst Figure 7.10 illustrates the evolution of O_2 and H_2 species. All calculated solutions were compared to experimental data. The hybrid ESF/FPV reproduces closely the reference experimental data of the species, while visible discrepancies can be observed in solutions that were obtained using the assumed β-PDF approach. This can be explained by the intrinsic assumptions associated, like the consideration of statistical independence between single PDF along with the modeling applied to the source term during its estimation.

A further evaluation of the prediction capability of the applied ESF/FPV approach comparing to the presumed β-PDF method is also confirmed by the evolution of the mean temperature as function of the mixture fraction which is depicted in Figure 7.11. It clearly shows that the β-PDF approach under predicts the temperature profile at almost all axial locations. As stated in the work of Sevault et al. in [154], the stoichiometric mixture fraction is reported as 0.056 with maximum adiabatic temperature around T=1750 K. The hybrid ESF/FPV calculations reproduces a value of T=1700 K for both simulations with 48 and 128 SF_i. In contrast, the β-PDF results clearly under-estimates the temperature evolution with a maximum value of T=1300 K.

Regarding the results of species evolution of flames $A1$ and $A3$ using the same procedure, corresponding plots are shown in Appendix B, and similar behavior of the applied numerical combustion methods is reproduced as well in predicting the different species mass fractions.

It appears clearly that the hybrid ESF/FPV approach overcomes the limitations of the presumed β-PDF by accurately characterizing the influence of turbulent fluctuations on the flame structure and on combustion properties, along with the TCI, also for oxyflame configurations.

The comparison of the proposed ESF/FPV approach with other re-examined presumed PDF combustion models employing the statistically most likely distribution (SMLD) (see [73; 125]) is out of the scope of the current work. However, a further study in this context can be addressed in order to examine the performance of various combustion models in terms of prediction capability of main turbulent flame properties and required computational efforts.

7.3 LES simulation: Oxy-flame B3

Note that a part of this chapter is based on [107]. In the preceding section the focus was put on the application of the suggested hybrid ESF/FVP method in RANS context analyzing its general prediction capability in reproducing main oxy-combustion characteristics. In the current section, the hybrid ESF/FVP is appraised in the LES context by simulating the oxy-fuel flame $B3$ [154]. Comparing to other oxy-fuel flames, the $B3$ flame has a considerably high Reynolds number with a value of $Re = 18.000$ and an important enrichment of H_2 and CO_2 with percentage of 55% in the fuel inlet and 68% in the oxidizer inlet, respectively. These challenging features made this case highly interesting for LES investigations. The sub-grid scale model adopted in this part is the Smagorinsky model to close the Navier-Stokes filtered equations, while ESF is treated according to the stochastic differential equations Eq (4.24) and Eq (4.25).

Dealing with oxy-combustion LES modeling, Hidouri et al. in [68] employed in the LES framework an alternative method based on the joint PDF method coupled to the FGM technique based on the mixture fraction and the reaction progress variable in order to investigate the behavior of two reacting separated oxy-fuel jets. Thereby the sub-grid PDF shape is described by the presumed beta-PDF assumption. However, according to [94], not all transported scalar properties could be appropriately reproduced using presumed-PDF approaches. Nevertheless, the conditional moment closure (CMC) combustion model has been applied for different turbulent studies, including the characteristics of turbulent combustion of natural gas flame in oxy-fuel combustion environments by Kim et al. in [89], and also the oxy-fuel coaxial jets by Garmory et al. in [55]. However, very few contributions dealt with oxy-combustion using the FPV approach. One of the early turbulent simulations incorporating the FPV approach in the LES framework has been reported in [58], where it was shown that the LES-FPV approach possesses in turbulent regimes a potential promise in addressing the issue of differential diffusion. Similar to FPV, the FGM method has been used in [68] with $Le = 1$ to tackle oxy-fuel combustion process in twin-jets.

As mentioned above, the hybrid ESF/FPV approach enables to accurately characterize the influence of the sgs fluctuations on the flame structure and on combustion properties. The objectives of this section are:

1. To evaluate the prediction capability of the novel approach in LES context.
2. To assess the impact of generating the FPV chemistry tables under the constant unity Lewis number assumption ($Le = 1$) even when H_2 dilutions in the fuel stream and CO_2 dilution in the oxidizer are present with high percentages.

7.3.1 Numerical set-up

The computational domain of the reacting turbulent oxy-fuel burner is depicted in Figure 7.12 where the dimensions are presented as a function of the diameter of the flame burner d_f. The three-dimensional block structured grid generated for the LES calculations is illustrated in Figure 7.13. It consists of $2, 800, 770$ control volumes arranged in 89 blocks. For the fuel pipe jet, 8450 cells are used with minimum cell size equal to $5.31 \cdot 10^{-12}\ m^3$ and maximum cell size located in the outlet region with $1.09 \cdot 10^{-10}\ m^3$. In order to carry out a good and fine resolution for the mesh, the O-grid technique implemented in the ICEM-CFD grid generator was called and wisely applied.

Similar to the previous set-up, the outlet plane was defined at 150 d_f, where waveTransmissive condition was imposed with fixed pressure $P = 101.325\ kPa$. The boundary conditions were set to zero gradient while other variables and temperature were set initially uniform. The other details for the operating conditions are defined similar to the RANS simulations where they as depicted in Table 7.3. Applying the same FPV tables used in the RANS context following the definition of the pv in Eq 7.1, multiple calculations have been carried out to study the convergence with respect to the number of stochastic fields $(4, 8, 16\ SF_i)$ in order to give the closest estimation of the optimal number of stochastic fields that should be employed. The time step used for all considered LES simulations was set to $t_s = 2.55 \cdot 10^{-7}\ s$ which ensures a CFL number below one. High performance computer was used to run all cases with number of processors varying between 192 and 240.

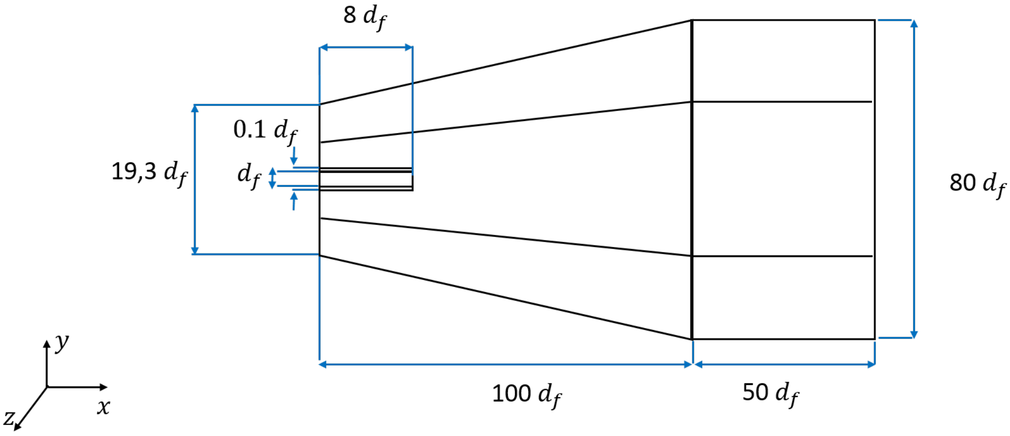

Figure 7.12: The schematic of the computational domain of oxy-fuel flame configuration.

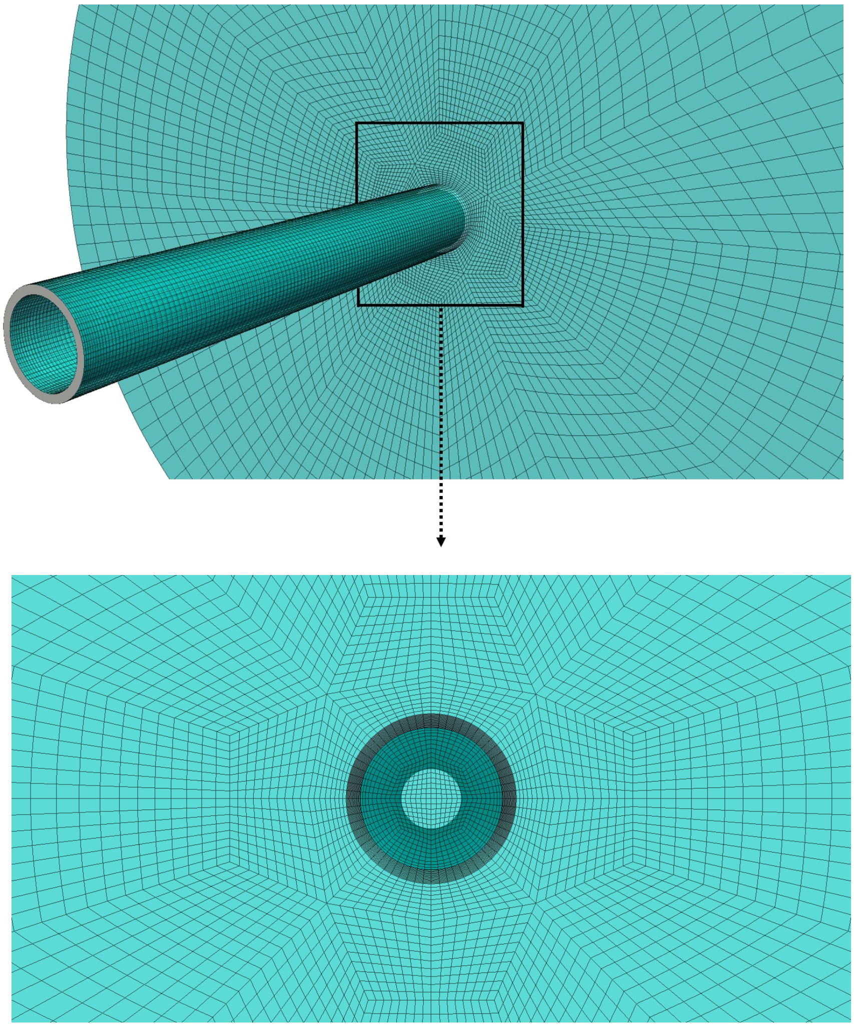

Figure 7.13: Block structured 3-D numerical grid for the oxy-fuel flame case: all configuration inlets (top), a zoomed view on the fuel nozzle (bottom).

Similarly to the previous LES case, the inlet turbulent flow field velocity of the current case was generated employing an in house turbulence inflow generator which was developed according to Klein et al in [90].

7.3.2 LES quality

Regarding the LES, various approaches are available in the literature which are leading to evaluate the quality of LES results (see Ries et al [146]). Among the criteria which can be found in [25; 146], the selected approach proposed by Hanjalic et al. in [66] and Pope in [132] is chosen for use in this study. This approach states that the LES quality can be evaluated by comparing the ratio of the applied LES mesh size Δ where $\Delta = (\Delta_x \Delta_y \Delta_z)^{1/3}$, to the Kolmogorov length scale η calculated from previous RANS solutions to a specific value of 12. This prescribed value reflects that approximately 80% of the turbulent kinetic energy are resolved. We should here note that Kolmogorov length scale η is estimated according to the following expression:

$$\eta = (\mu^3/\rho^3\epsilon)^{1/4}. \tag{7.2}$$

where μ is the dynamic molecular viscosity, ρ is the density and ϵ is the dissipation rate. The snapshot depicted in Figure 7.14 illustrates an estimation of the defined ratio Δ/η calculated for the oxy-fuel $B3$ grid. It is clear that in almost the entire domain $\Delta/\eta \leq 12$, especially for the most part of the flame region. Therefore, this numerical grid can be considered sufficient for the LES calculations reported in this work.

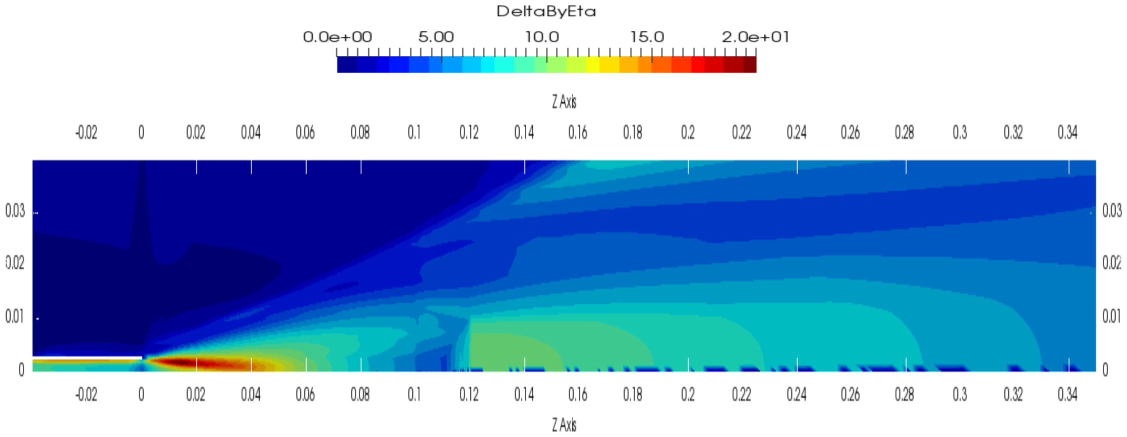

Figure 7.14: Estimated ratio Δ/η of the numerical grid of the oxy-fuel flame $B3$

7.3.3 Results

In this section, numerical solutions obtained from the simulation of the oxy-fuel jet flame $B3$ using the hybrid ESF/FPV approach within LES framework are analyzed and compared to the available measurements. The upper part of Figure 7.15 represents qualitatively the mean (top half) and the instantaneous (bottom half) temperature field for the oxy-flame $B3$. Moreover, similarly to the experimental observation, the flame is shown attached to the burner nozzle which is due to the important percentage of H_2 enrichment in the fuel mixture. Besides, the lower part of the same illustration depicts the instantaneous temperature contour radial planes at various axial locations ($x/d \in \{3, 5, 10, 20, 40, 60, 80\}$) showing how the temperature distribution is spreading radially and toward the outlet of the burner.

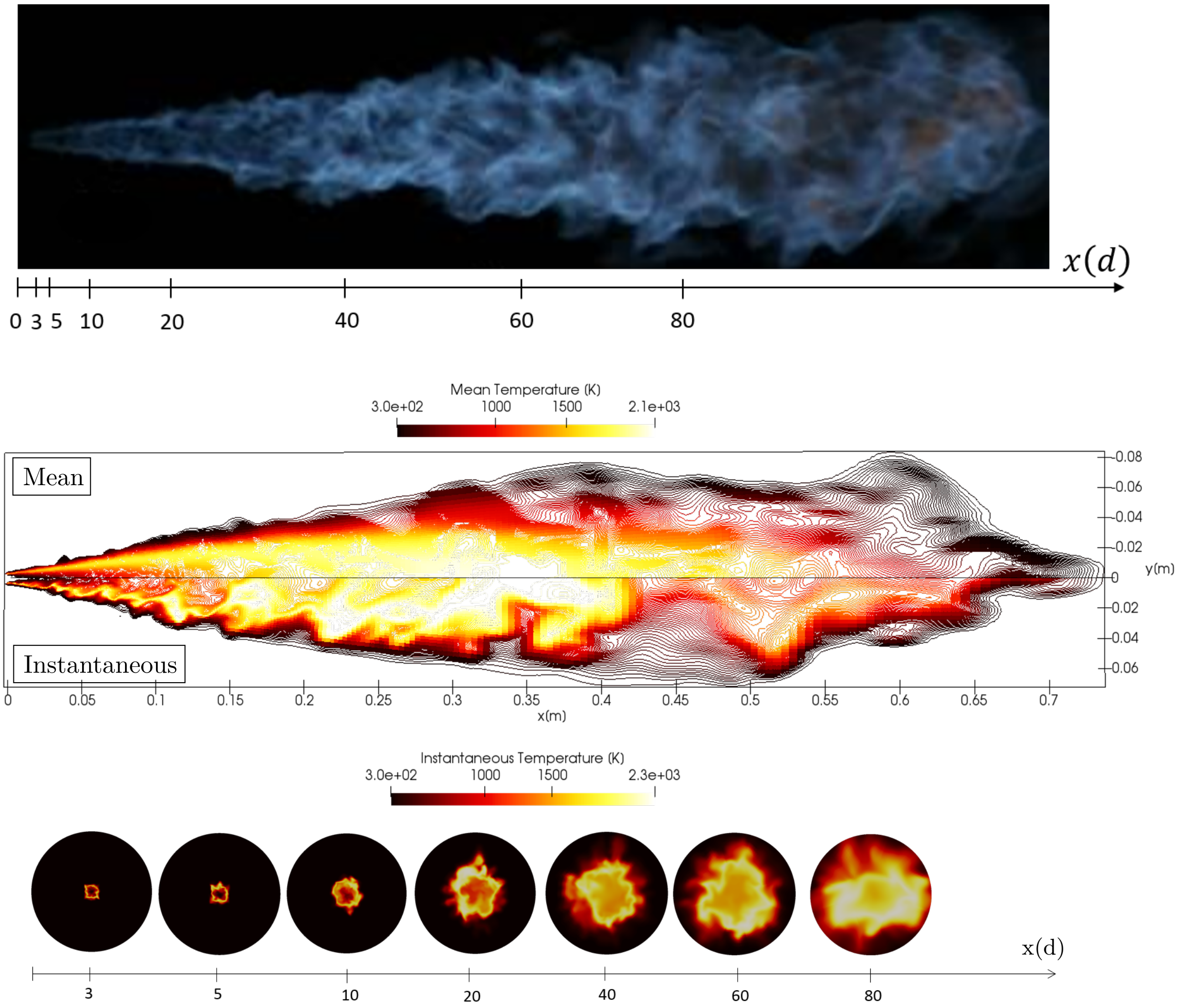

Figure 7.15: Temperature profiles of the oxy-flame $B3$ configuration. **Top**: Measurements. **Middle**: Longitudinal profile with time-averaged (top half) and instantaneous (bottom half) values calculated with the LES hybrid ESF/FPV approach using 8 SF_i. **Bottom**: 2D contours on radial planes at various axial positions.

As previously indicated, high shear flow significantly improves the mixing process within the combustion systems. Thereby, in order to have first insights about the system design and performance of the current case, individual vortices and their interaction during mixing are identified through the "Q-criterion" which allows the visualization of the multi-sized turbulent flow vortices.

In this regard the iso-surface of the Q-criterion calculated using the LES hybrid ESF/FPV approach with 8 SF_i are represented in Figure 7.16. The illustrated Q-criterion is contoured and colored by the axial velocity where the multi-sized instantaneous vortical structures of the turbulent flow are sketched. some vortex rings are visualized in the region close to the fuel tip which refers to toroidal vortex structures that have been generated due to very high shear flow and the velocity gradient at the pipe outlet edges. Figure 7.17 illustrates the same view of the Q-criterion in Figure 7.16 but contoured and colored by the temperature field.

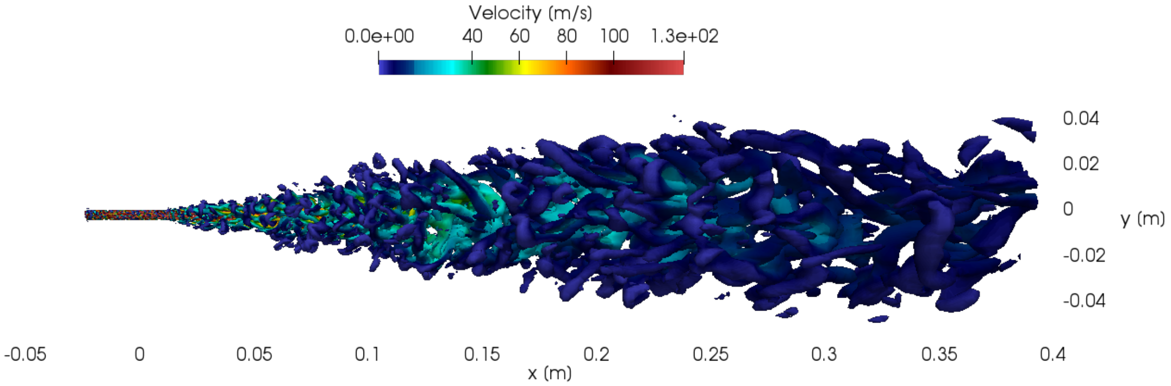

Figure 7.16: Snapshot of the instantaneous Q criterion of flame B3 contoured with temperature field calculated with the LES hybrid ESF/FPV approach using 8 SF_i .

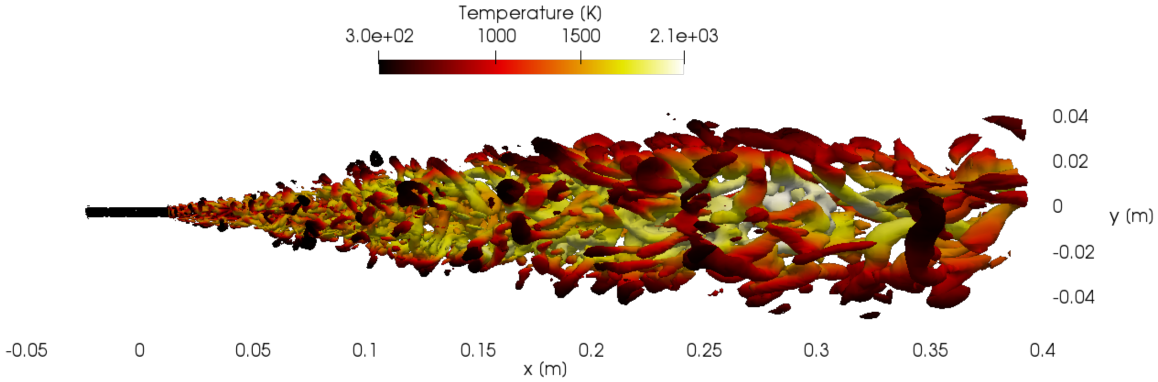

Figure 7.17: Snapshot of the instantaneous Q criterion of flame B3 contoured with temperature field calculated with the LES hybrid ESF/FPV approach using 8 SF_i .

7.3.3.1 Convergence with respect to N_s

To evaluate the convergence with respect to the number of the applied stochastic fields in the LES context, many numbers of stochastic fields $N_s \in \{4, 8, 16\}$ were used for all calculations. Figures 7.18 and 7.19 exhibit the quantitative validation of the numerical solutions obtained by applying the ESF/FPV approach using different stochastic fields. The mass fraction evolution of major combustion species are compared to the experimental data at various axial positions ($x = 3d$, $x = 5d$, $x = 10d$). Analyzing Figure 7.18 which depicts the evolution of the mean values of CO and H_2O species mass fractions at different axial locations, notably higher amounts of CO and H_2O mass fractions are observed once compared to values generally obtained with air diluted flame cases [138]. This trend is considerably perceived close to the inner fuel jet. The CO and H_2O mass fractions are equal to 0.11 and 0.18, respectively, which increased to almost 0.16 and 0.21 at higher axial positions. In this way, the present LES results confirm the RANS findings of previous chapter, and agree with Masri et al. [108], who reported that the 68% diluted CO_2 with pure oxygen in the oxidizer inlet is not inert. This plays an important role in increasing CO and H_2O gases formation.

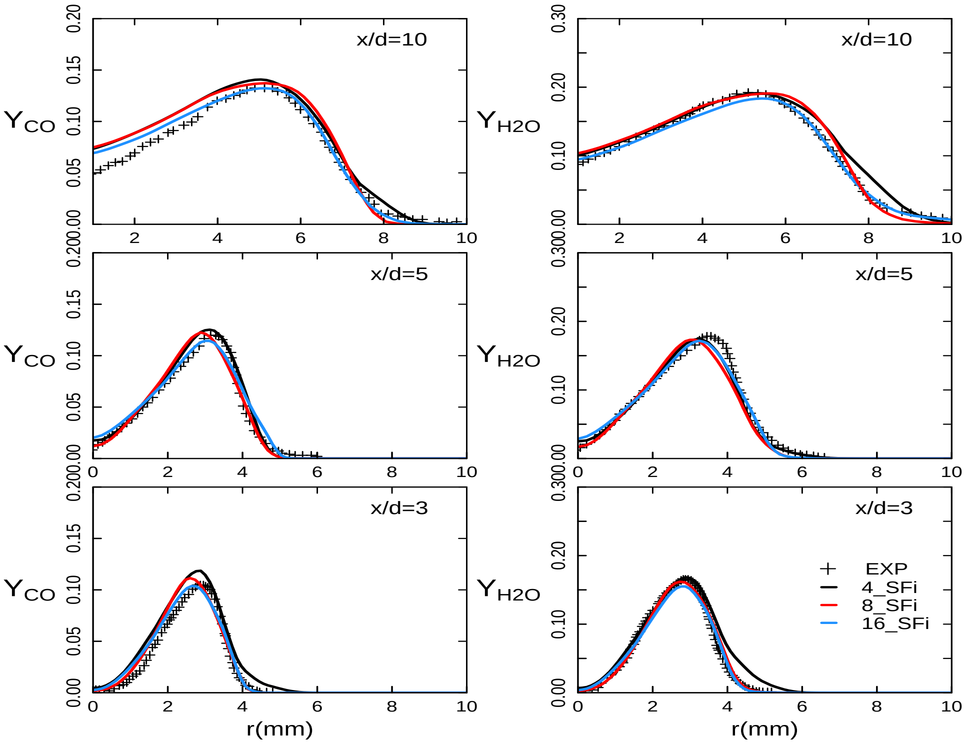

Figure 7.18: CO (left) and H_2O (right) mass fraction profiles of oxy-flame $B3$, calculated with LES hybrid ESF/FPV method using 16 SF_i, and compared to experimental data (+) [154].

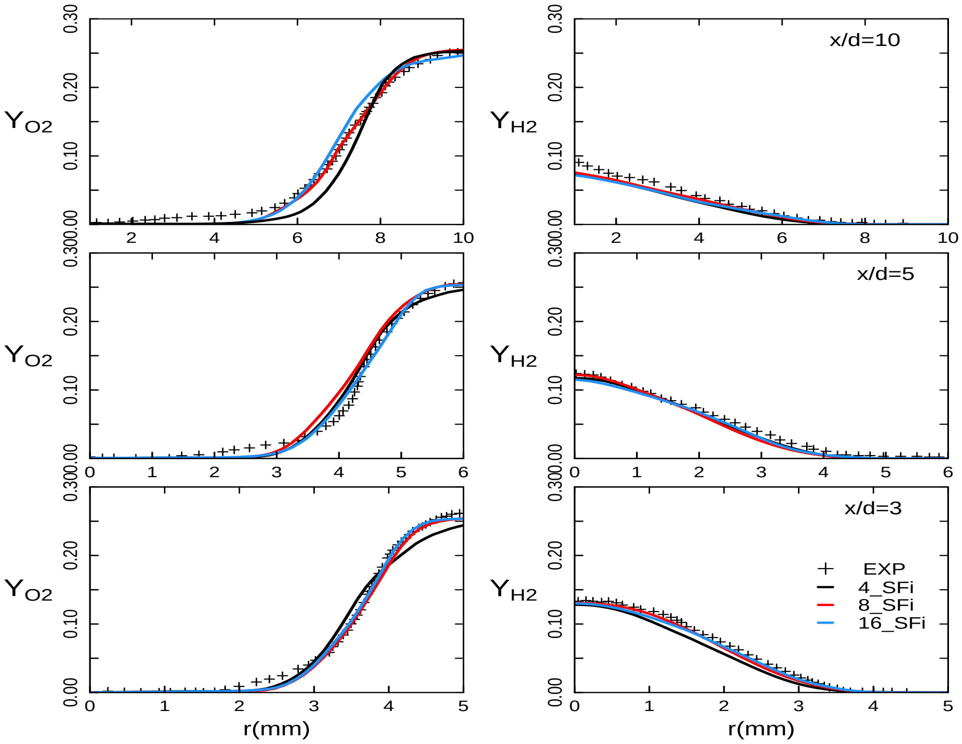

Figure 7.19: O_2 (left) and H_2 (right) mass fraction profiles of oxy-flame $B3$, calculated with LES hybrid ESF/FPV method using 16 SF_i, and compared to experimental data (+) [154].

Generally all results are well reproduced with respect to experiments using different N_s. However, the results obtained from calculations using 8 SF_i and 16 SF_i achieve better agreements at radial profiles once compared to results with 4 SF_i. This is not surprising, since 4 stochastic fields are not sufficient to reproduce the exact evolution of measured quantities in accordance to the outcomes shown in the previous chapter (see section 6.3).

Moreover, very slight under-prediction of calculated mean quantities of CO species mass fractions is pronounced at the centerline only at further downstream positions $x \geq 10d$. The same observation can be made for the mean mass fraction of H_2 quantities which is illustrated in Figure 7.19.

Figures 7.20, 7.21, 7.22 compare the probability density function calculated using different numbers of N_s with those obtained from measurements at the different axial positions ($x = 3d$, $x = 5d$, $x = 10d$).

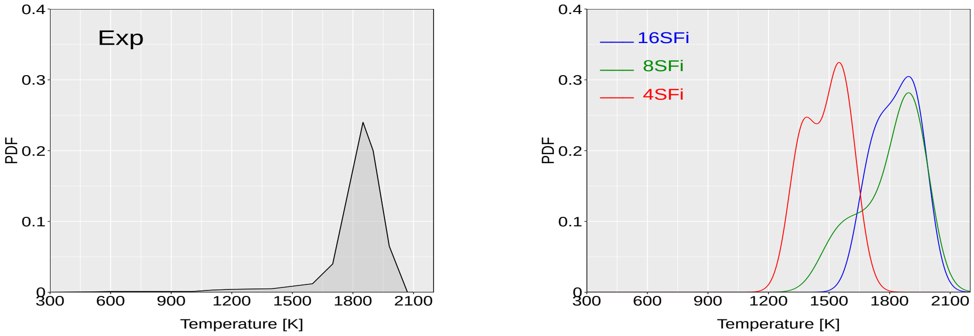

Figure 7.20: Probability density function of temperature within a mixture fraction range $\Delta_f = 0.04$ at the axial position $x = 3d$. Left : The experimental results. Right: The results obtained with the LES hybrid ESF/FPV approach using 4,8 and 16 SF_i.

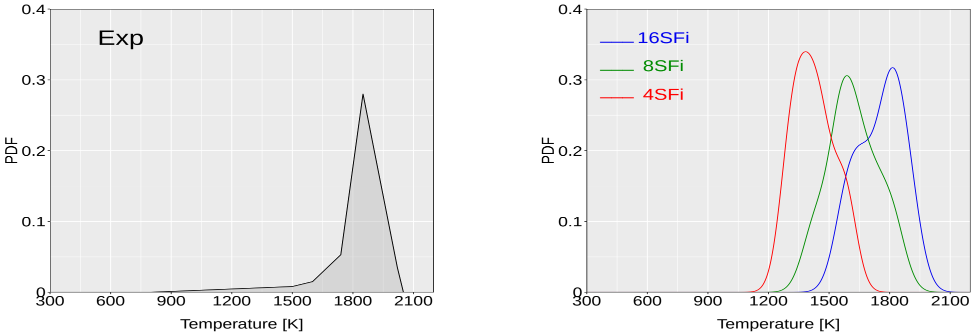

Figure 7.21: Probability density function of temperature within a mixture fraction range $\Delta_f = 0.04$ at the axial position $x = 5d$. On the left: On the left : The experimental results. On the right: The results obtained with the LES hybrid ESF/FPV approach using 4,8 and 16 SF_i.

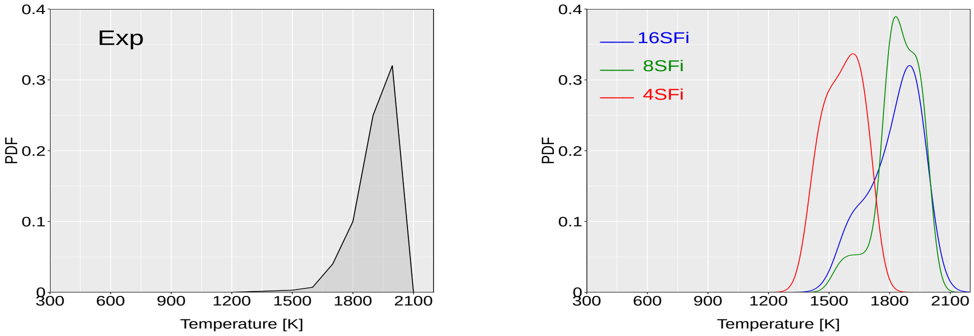

Figure 7.22: Probability density function of temperature within a mixture fraction range $\Delta_f = 0.04$ at the axial position $x = 10d$. On the left: On the left : The experimental results. On the right: The results obtained with the LES hybrid ESF/FPV approach using 4,8 and 16 SF_i.

For both sets, the PDF was estimated for a narrow band of the mixture fraction around the stoichiometry where $\Delta = 0.04$. In most locations, the shape of the PDF of the temperature could be reproduced only with simulation results using 16 SFi, but slight differences were noticed at higher axial positions where few values of temperature in the range of $1500K$ and $1700K$ were over-predicted. Nevertheless, the probability of the presence of the temperature range from $1800K$ to $2100K$ is successfully matching the values obtained experimentally for all positions.

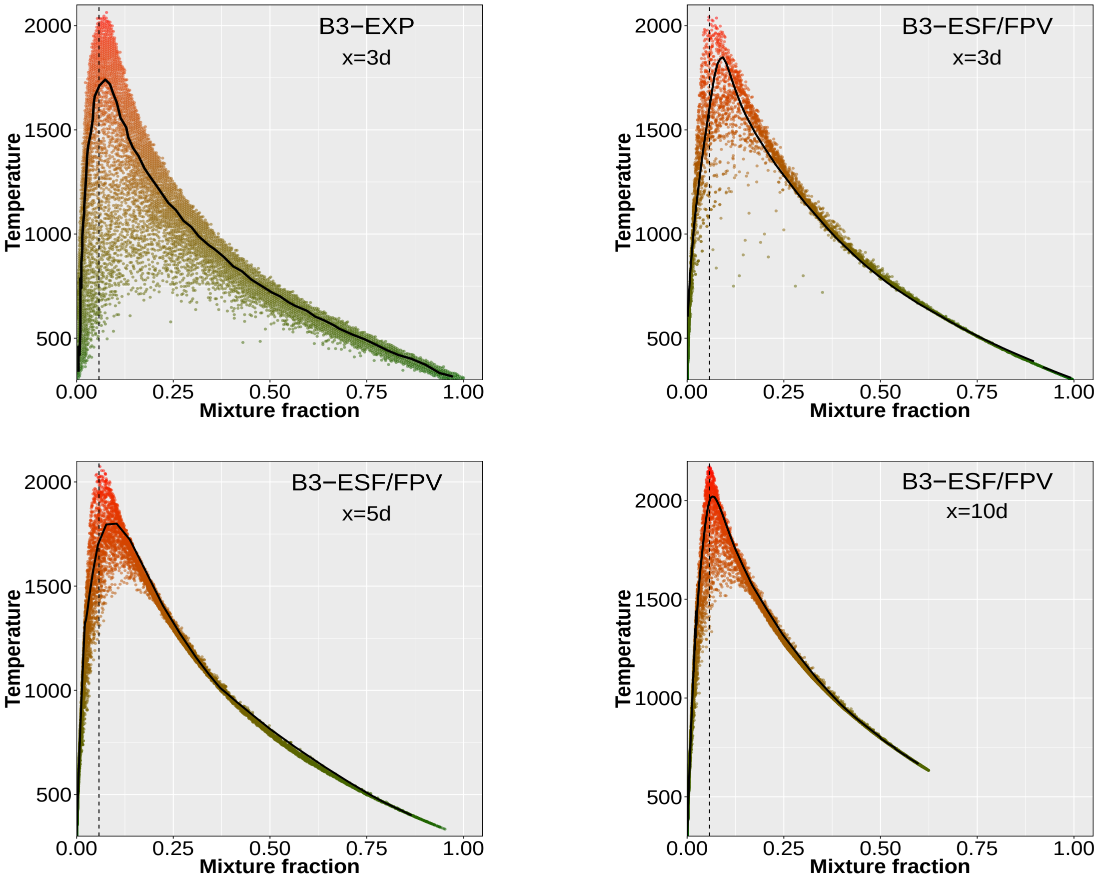

Figure 7.23: Instantaneous scatter plots of temperature versus mixture fraction of the oxy-fuel flame $B3$ at different axial positions ($x = 3d, 5d, 10d$). Top left: Measurements ([154]). Top right and bottom: Numerical results calculated using LES hybrid ESF/FPV with 16 SF_i ([107]).

The instantaneous scatter plots of the temperature distribution at different axial positions ($x = 3d, 5d, 10d$) are depicted in Figure 7.23 where only results near the fuel nozzle ($x = 3d$) are compared with experimental data since the latter are available only at this location. The vertical black line drawn in all plots corresponds to the stoichiometric mixture fraction value. At region close to the fuel inlet ($x/d = 3$), the maximum reached value of the temperature distribution was $2100K$, which closely matches the experimental data as shown in the plot. This value is slightly increased at the further axial positions $x/d = 5$ and $x/d = 10$ to reach approximately $2150K$ and $2200K$, respectively. However, although mean values of temperature profiles near stoichiometry region are well reproduced especially at the axial position further downstream from the fuel nozzle ($x/d = 10$), the mean temperature is slightly overestimated once compared with the measured one at $x/d = 3$.

Furthermore, on the top-left side of Figure 7.23, the localized extinctions, which take place when turbulent mixing rates come to be comparable to major chemical reaction rates [171], are represented with colored points scattered in the lower part of the measured temperature band. Although the values referring to the localized extinctions were properly reproduced numerically close to stoichiometric mixture fraction, a notably lower probability of localized extinction further from the stoichiometry region is observed. Similar behavior is noticed for the instantaneous temperature scatter plots illustrated at locations $x/d = 5$ and $x/d = 10$.

Additionally, the lowest value predicted with the simulation reads $750K$, while experimentally it is $500K$. This behavior could mainly be related to two reasons: the turbulent approach applied for all calculations and the standard IEM mixing model adopted. It has been reported in [160], where two different mixing models (IEM and EMST (Euclidean minimum spanning tree)) have been employed on all piloted Sandia flames, the IEM approach could not capture perfectly the conditional temperature distribution leading to a similar unphysical trend within the same mixture fraction range as observed also in [69]. This means, that in LES the choice of the mixing model plays an important role.

7.4 Summary

The hybrid ESF/FPV methodology has been applied in order to investigate the jet flame series ($A1$, $A3$, $B3$) which features challenging oxy-combustion conditions that fundamentally differ from air-fired combustion. These jet flame series are considered more complex cases comparing to the piloted jet-flame Sandia D which was discussed in the previous chapter. Generally the hybrid ESF/FPV approach could once again reproduce the main flame properties and obtained results in very good agreement with the experimental data.

In the first part of the chapter, the numerical study of the oxy-flame cases within RANS turbulent model was reported. The evaluation of the optimal SF_i numbers where very good agreements between calculated solutions and measurements is addressed (48 SF_i). The main focus was devoted to the impact of different inlet conditions of the flame series on the flame structure. This includes the effect of H_2 and CO_2 enrichments in fuel and oxidizer inlets and also the effect of varying the Reynolds number.

In the second part, LES investigation of the oxy-fuel jet flame $B3$ was reported with details. The main flame properties were analyzed through comparison with measurements for different critical reacting species. The comparative study includes also the RANS solutions in order to assess the performance of the ESF/FPV method within both turbulence modelling frameworks. Moreover, PDF distribution plots and instantaneous scatter plots were provided.

Finally, with only minor differences that could be observed between numerical solutions of RANS/LES simulations and experimental data, the performance analysis of the ESF/FPV method in reproducing major oxy-flame combustion properties like major species mass fractions, shows satisfactory prediction capability and proves good potential of the proposed methodology to accurately describe the TCI.

Chapter 8

Conclusions and Outlook

The present thesis dealt with the development and application of a novel well-designed numerical method enabling to accurately simulate flames in non-premixed combustion regime while capturing appropriately TCI processes. This was referred to as hybrid ESF/FPV method. For validation purposes, both oxy-fuel and air-diluted flames have been considered and thoroughly studied. In particular, the oxy-combustion cases were represented by the oxy-fuel flame series A and B while the turbulent air diluted case was the Sandia flame D .

The proposed numerical method is based on the joint scalar probability density function (PDF) transport method following the Eulerian Stochastic Field (ESF) solutions approach. This is combined with the detailed chemistry tabulation technique according to the Flamelet Progress Variable (FPV) method.

Up to now, employing the proposed strategy to investigate oxy-fuel flames has not been reported yet. That is why the oxy-fuel flame series have been selected and addressed in the current work. They feature quite challenging combustion systems as they are operating under different Reynolds numbers and considering highly diluted conditions of CO_2 and H_2 in oxidizer and fuel streams, respectively.

The proposed hybrid ESF/FPV method has been implemented within a turbulent reacting solver in the OpenFOAM code and was verified on one-dimensional laminar premixed flame as first evaluating test case. It was demonstrated that the implemented scheme could reproduce the main properties of the one-dimensional flame once the calculated results converge correctly towards the exact chemical reference solution. Subsequently, the proposed methodology was employed to different configurations with increasing complexity, namely the flame D and the oxy-fuel flames $A1$, $A3$ and $B3$.

First, the hybrid ESF/FPV approach was used to numerically simulate the piloted air-methane jet flame Sandia D serving as a validation test case. The simulations have been carried out within both RANS and LES modeling contexts applying various number of stochastic fields. For validation, the obtained results of both RANS and LES turbulent models were compared to experimental data at different positions. Satisfactory predictions of the main flow properties and flame characteristics were achieved for flow field variables, species mass fractions and temperature profiles.

Second, the combustion behavior of more complex configurations featuring oxy-fuel jet flame series has been analyzed in order to evaluate the prediction capability of the hybrid ESF/FPV approach in reproducing the flame structure. Initially, RANS calculations of oxy-flames ($A1$, $A3$, $B3$) were carried out using different numbers of stochastic fields. These flames exhibit different CH_4/H_2 and O_2/CO_2 ratios in the fuel and oxidizer inlets, respectively, and are characterized by different Reynolds numbers. This study allowed for tracing the impact of these properties on the temperature profiles and the CO and H_2O species formation. Accordingly, it was demonstrated that with lower H_2 % enrichment in fuel side, fixed O_2/CO_2 ratio and constant Reynolds number, the maximum adiabatic temperature value decreases in a significant manner near the fuel nozzle and its location in the mixture fraction space is shifted toward the reach side of the fuel. Moreover, results with lower Reynolds number, constant O_2/CO_2 and CH_4/H_2 ratios, the CO formation is considerably intensified near the fuel inner part.

In all cases, the comparison between the numerical results and the experimental data exhibit a very good agreement. Furthermore, the obtained solutions were also compared to achievements accomplished by using a classical presumed β-PDF based FPV combustion model. It turned out that the hybrid ESF/FPV clearly showed superiority in better predicting the temperature, H_2O and especially CO mass fraction, while the presumed β-PDF model under-estimated the maximum adiabatic temperature and over-predicted the CO formation level at different positions above the fuel nozzle downstream. By comparing RANS and LES results, it appeared that the utilization of both turbulent models could accurately reproduce the major reacting species except some discrepancies at the lower position close to the fuel jet for RANS while LES could better predict the distribution of O_2 mass fraction.

The third application of the hybrid ESF/FPV methodology consists in investigating the oxy-flame $B3$. In this setting, numerical simulations were carried out applying different numbers of stochastic fields. Very good agreements between numerical findings and measurements have been reported after comparison of obtained results. However, some derivations to experiments were noticed due probably to turbulence sub-model applied and standard mixing model adopted. Moreover, although previous RANS results were close to measurements, the LES hybrid ESF/FPV model provides more accurate predictions in some specific locations. Focusing on the effect of the important amount of CO_2 diluted in the oxidizer stream. It resulted in high level of production of CO and H_2O mass fraction species confirming previous findings by Masri et al in [108]. Regarding the general prediction of the oxy-flame stability and emissions, it turns out that 68% molar percentage of additional CO_2 enrichment in the oxidizer side leads to 0.39% of CO formation near the burner fuel inlet and to 0.62% above the nozzle at $x = 10d_f$. These amounts of CO-formed gases are clearly high compared to ordinary flame cases with air-diluted conditions. Overall, the LES hybrid filtered ESF/FPV approach demonstrated its potential in reproducing main flame and flow properties in the oxy-flame configuration, using FPV chemical tables based on the unity Lewis number assumption ($Le = 1$). This indicates that H_2 induced differential diffusion effect was negligible in the investigated area of the oxy-flame $B3$. The H_2 induced differential diffusion might be significant if different investigation areas of oxy-flames would be treated. In this case, the $Le \neq 1$ shall be considered.

Regarding the convergence of the stochastic field number (N_s), the optimal applied number strongly depends on the complexity of the combustion case. Even though more N_s could help to achieve fully complete convergence, saving the computational costs is always desirable. It turned out that starting the calculations with 48 SF_i emerged as the compromise between accurate prediction and computational costs fo all configurations operating within RANS modeling. However in the LES framework, calculations with at least 8 stochastic fields lead to an accurate prediction in Sandia flame D and at least 16 stochastic fields allow achieving better results in accordance with measurements once complex configuration like the oxy-fuel flame $B3$ is investigated.

Despite encouraging results provided by the hybrid ESF/FPV approach, the suggested model needs to be further evaluated by using FPV or FGM based tabulated chemistry with non-unity Lewis number assumption to better consider the importance of the $H2$ differential diffusion effect which may affect the prediction of other minor species.

An additional interesting improvement of the implemented novel combustion model shall be to consider more advanced micro-mixing models coupled to the LES/RANS hybrid ESF/FPV since the applied standard interaction by exchange of mean method is prone to well-known limitations.

An extension of the method to spray is also an interesting aspect. This is fortunately an ongoing research at the institute.

Appendix A

Set of averaged equations solved within RANS framework

In the framework of LES, the set of equations [(2.40)-(2.42)] together with [(4.24) (4.25)] from the hybrid ESF/FPV method along with equations [(2.40)-(2.42)] together with [(4.26)-(4.28)] for the presumed β-PDF approach are solved respectively.

By using the hybrid ESF/FPV approach with RANS, N_s stochastic differential equations for the mixture fraction and the progress variable are added to the governing equation system [(2.31) (2.32)] and [(2.34) (2.35)] as sketched in the flowchart in Figure 5.3.

Thereby, for $1 \leqslant n \leqslant N_s$, the corresponding differential equations implemented are as follows:

$$\begin{aligned} \overline{\rho}\mathrm{d}(\xi_f^n) + \overline{\rho}\widetilde{u}_j \frac{\partial(\xi_f^n)}{\partial x_i}\mathrm{dt} - \frac{\partial}{\partial x_i}\left[(\frac{\mu}{Sc} + \frac{\mu_t}{Sc_t})\frac{\partial \xi_f^n}{\partial x_i}\right]\mathrm{dt} &= -\frac{\overline{\rho}C_\zeta}{2\tau}(\xi_f^n - \widetilde{\phi}_f)\mathrm{dt} \\ &+ \sqrt{2\overline{\rho}(\frac{\mu_t}{Sc_t})}\frac{\partial \xi_f^n}{\partial x_i}\mathrm{dW_i^n}. \end{aligned} \tag{A.1}$$

$$\begin{aligned} \mathrm{d}(\overline{\rho}\xi_{pv}^n) + \frac{\partial(\overline{\rho}\widetilde{u}_j\xi_{pv}^n)}{\partial x_i}\mathrm{dt} - \frac{\partial}{\partial x_i}\left[(\frac{\widetilde{\mu}}{Sc} + \frac{\mu_t}{Sc_t})\frac{\partial \xi_{pv}^n}{\partial x_i}\right]\mathrm{dt} &= \overline{\rho}\dot{\omega}_{pv}^n(\xi_{pv}^n)\mathrm{dt} \\ -\frac{\overline{\rho}}{2\tau}(\xi_{pv}^n - \widetilde{\phi}_{pv})\partial t &+ \sqrt{2\overline{\rho}(\frac{\mu_t}{Sc_t})}\frac{\partial \xi_{pv}^n}{\partial x_i}\mathrm{dW_i^n}. \end{aligned} \tag{A.2}$$

By using the classical β-PDF approach coupled to FPV technique, averaged transport equations for the mixture fraction f, the variance of mixture fraction f''^2 and the reaction progress variable pv have to be solved together with the set of equations [(2.31) (2.32)] and [(2.34) (2.35)] as sketched in the flowchart in Figure 5.5

These equations read:

$$\frac{\partial\overline{\rho}\widetilde{f}}{\partial t} + \frac{\partial\overline{\rho}\widetilde{u}_j\widetilde{f}}{\partial x_j} = \frac{\partial}{\partial x_j}\left[\overline{\rho}\left(\frac{\mu}{Sc} + \frac{\mu_t}{Sc_t}\right)\frac{\partial\widetilde{f}}{\partial x_j}\right]. \tag{A.3}$$

$$\begin{aligned}\frac{\partial \overline{\rho}\widetilde{f''^2}}{\partial t} + \frac{\partial \overline{\rho}\widetilde{u}_j\widetilde{f''^2}}{\partial x_j} =& \frac{\partial}{\partial x_j}\left[\overline{\rho}\left(\frac{\mu}{Sc} + \frac{\mu_t}{Sc_t}\right)\frac{\partial \widetilde{f''^2}}{\partial x_j}\right] + \\ & 2\overline{\rho}D_t\left(\frac{\partial \widetilde{f}}{\partial x_j}\right)^2 - \overline{\rho}\frac{C_\zeta\widetilde{\varepsilon}}{\widetilde{k}}\widetilde{f''^2}.\end{aligned} \tag{A.4}$$

$$\frac{\partial \overline{\rho}\widetilde{pv}}{\partial t} + \frac{\partial \overline{\rho}\widetilde{u}_j\widetilde{pv}}{\partial x_j} = \frac{\partial}{\partial x_j}\left[\overline{\rho}\left(\frac{\mu}{Sc} + \frac{\mu_t}{Sc_t}\right)\frac{\partial \widetilde{pv}}{\partial x_j}\right] + \overline{\dot{\omega}}_{pv}. \tag{A.5}$$

Appendix B

RANS Results for oxy-fuel flames A1 and A3

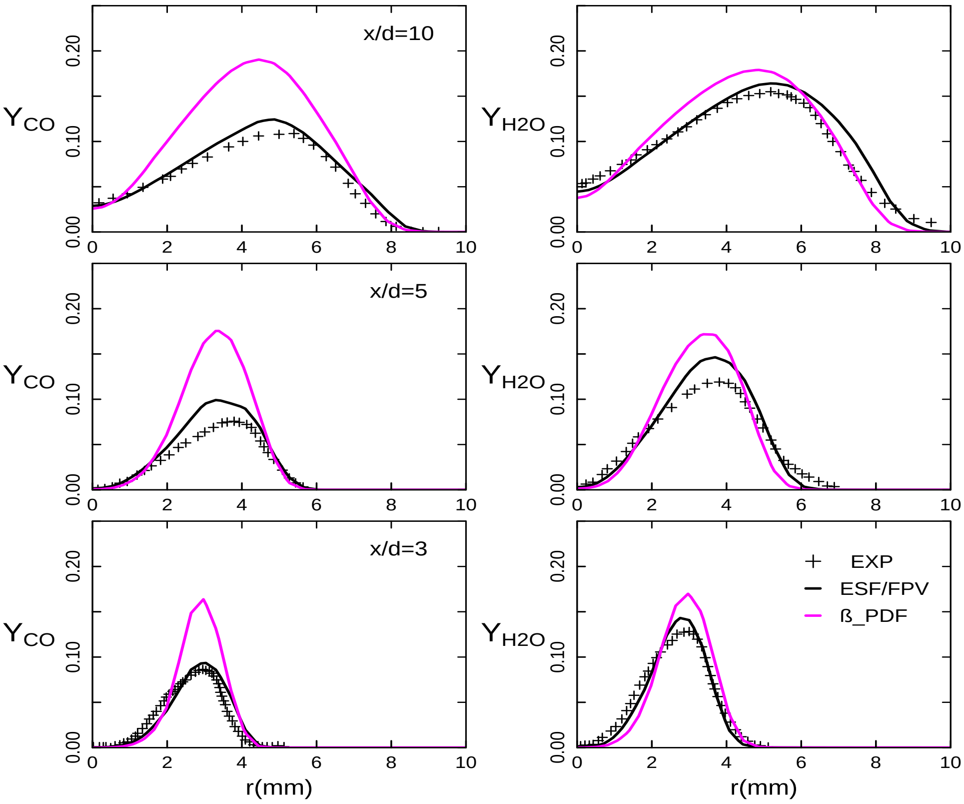

Figure B.1: CO (left) and H_2O (right) mass fraction profiles of oxy-flame $A3$, calculated at different axial positions ($x = 3d, 5d, 10d$) with RANS-ESF/FPV method using 48 SF_i, and compared to β-PDF findings and to experimental data (+) [154].

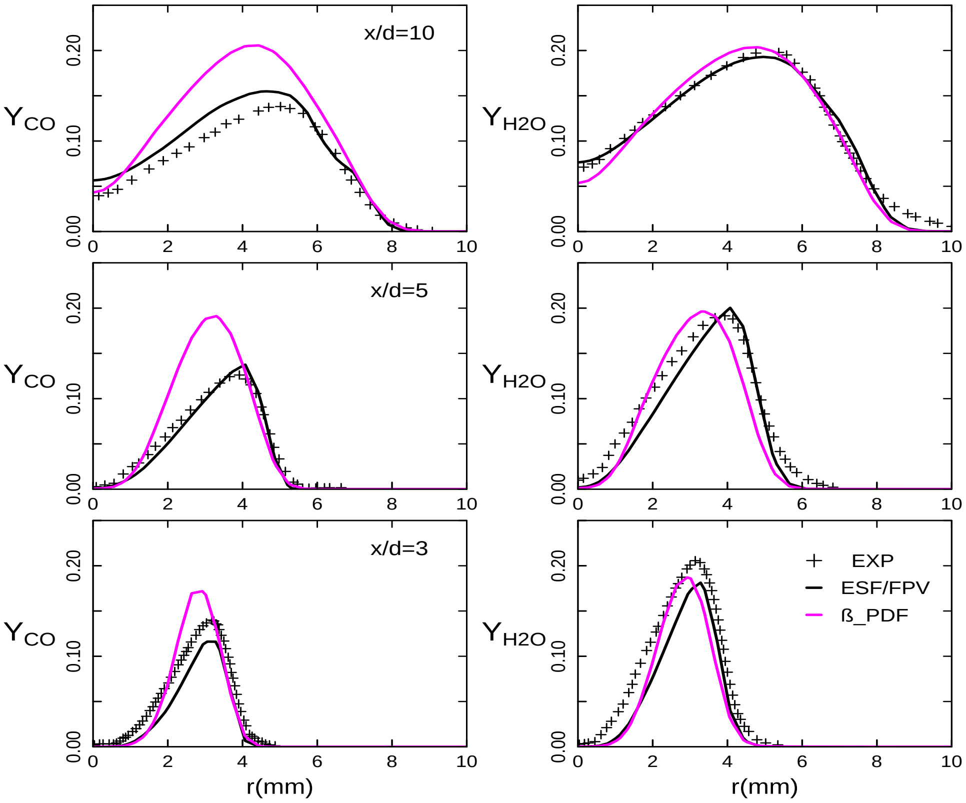

Figure B.2: CO (left) and H_2O (right) mass fraction profiles of oxy-flame $A1$, calculated at different axial positions ($x = 3d, 5d, 10d$) with RANS-ESF/FPV method using 48 SF_i, and compared to β-PDF findings and to experimental data (+) [154].

Appendix C

Abstract

In the prevailing situation of unsustainable fossil fuel resources and the elevated levels of air pollutant emissions, the state-of-the-art of combustion investigations confronts primarily two challenges. These are on the one hand the optimization of the fossil fuel combustion efficiency and on the other hand the development and the application of robust strategies to reduce the amount of the released pollutant gases with respect to the new emission standards in accordance with the global energy policies. Within this context, the carbon dioxide capture and storage (CCS) technologies play an important role as an accepted strategy towards the mitigation of CO_2 emissions. One of the important aspects of the CCS techniques is the oxidation of natural gas under oxy-fuel combustion conditions. However, very few scientific contributions have been devoted to research of these systems, so that there is a lack of understanding the oxy-combustion processes. The present work aims at the development and the application of an advanced numerical approach for the simulation of oxy-fuel combustion in which the TCI is adequately accounted for within non-premixed combustion regimes using the OpenFOAM platform. The suggested model which is designed for both RANS and LES applications, consists of a combination of a transported probability density function approach following the Eulerian Stochastic field methodology and the flamelet progress variable (FPV) chemistry reduction mechanism. In the LES framework, the proposed method accurately represents the effect of the sub-grid fluctuations on the flame structure and on combustion characteristics along with the interaction between turbulence and chemistry. The implemented developed combustion model is first verified, and then validated and applied to different turbulent non-premixed combustion configurations featuring an increasing order of complexity. In particular, Sandia flame D which consists of a turbulent piloted methane-air jet flame [127], is first employed for model validation in both RANS and LES contexts. The next flames are more challenging cases, namely the non-premixed Sandia oxy-flame series (A & B), which are operated under different Re numbers and characterized by various CO_2 and H_2 enrichments in the oxidizer and fuel streams, respectively [154]. All investigated cases are well documented with available experimental measurements. The comparison of the obtained results with experimental data in terms of temperature, scalar distributions, PDFs and scatter plots agree satisfactorily, essentially in LES context. This work finally reveals that the hybrid ESF/FPV approach removes the weaknesses of the presumed probability density function based FPV modeling (β-PDF).

Zusammenfassung

Aufgrund schwindender Ressourcen an fossilen Brennstoffen und strengen Abgasnormen stehen neue Verbrennungstechnologien heutzutage vor zwei groβen Herausforderungen. Diese sind angesichts verschärfter Emissionsvorschriften und gemäβ globaler energiepolitischer Maβnahmen zum einen die Steigerung des Verbrennungswirkungsgrades und zum anderen die Entwicklung und Anwendung von brauchbaren Strategien zur Reduzierung von Schadgasen. In diesem Zusammenhang spielen Kohlenstoffabscheidungs und Kohlenstoffspeicherungs Technologien (CCS) eine entscheidende Rolle zur Verringerung des Ausstoβes von CO_2. Ein wichtiger Aspekt der CCS-Technik ist hierbei die Oxidation von Erdgas unter Oxyfuel-Verbrennungsbedingungen. Trotz deren Relevanz gibt es derzeit jedoch nur sehr wenige wissenschaftliche Beiträge zu dieser Technologie, weshalb Verbrennungsprozesse unter Oxyfuel-Bedingungen noch weitgehend unverstanden sind. Das Ziel der vorliegenden Arbeit besteht in der Entwicklung und Anwendung eines fortschrittlichen numerischen Verfahrens zur Simulation von Verbrennungsprozessen unter Oxyfuel-Bedingungen. Dieses wurde in die OpenFOAM-Umgebung integriert und ist in der Lage die Interaktion zwischen der turbulenten Strömung und der Verbrennung für nicht vorgemischte Verbrennungsregime korrekt wiederzugeben. Das vorgeschlagene Verfahren ist geeignet für numerische Strömungssimulation welche auf der Lösung der Reynolds-Gleichungen (RANS) oder auf Grobstrukturansätzen (LES) basieren. Es besteht aus einer transportieren Wahrscheinlichkeitsdichtefunktion (PDF) im Kontext der Eulerschen stochastischen Felder Methode (ESF) kombiniert mit einem Chemiereduktionsmechanismus welcher auf einer Flamelet-Fortschrittsvariabel (FPV) basiert. Im Zusammenhang mit LES, ermöglicht die vorgeschlagene Methode eine präzise Beschreibung des Einflusses von Feinstrukturfluktuationen auf die Flammenstruktur sowie auf Verbrennungscharakteristika mitsamt der einhergehenden Turbulenz-Chemie-Interaktion. Das entwickelte Verbrennungsmodell wird zunächst verifiziert, dann validiert und angewendet auf verschiedene turbulente nicht vorgemischte Verbrennungskonfigurationen, welche eine zunehmende Komplexität aufweisen. Der erste Testfall zur Validierung der Methode im Kontext von RANS und LES ist die sogenannte Sandia flame D, welche aus einer turbulenten, pilotierten Methan-Luft Jet-Flamme [127] besteht. Die darauf folgenden Testflammen sind die sogenannten nicht vorgemischte Sandia oxy-flame series A & B, welche bei unterschiedlichen Reynolds-Zahlen betrieben werden und charakterisiert sind durch eine CO_2- und H_2-Anreicherungen im Oxidatorstrom bzw. im Brennstoffstrom [154]. Alle untersuchten Validierungsfälle sind hierbei gut dokumentiert, wobei experimentelle Messdaten zur Verfügung stehen. Ein Vergleich zwischen den erhaltenen Simulationsergebnissen und den experimentellen Daten bezüglich Temperatur, skalaren Verteilungen, PDFs und Streudiagrammen zeigt eine gute Übereinstimmung, insbesondere im Kontext von LES. Die vorliegende Arbeit legt letztendlich dar dass der hybride ESF/FPV-Ansatz potentielle Schwachstellen eines FPV basierten Modellierungsansatzes mit vorausgesetzter PDF (β-PDF) beheben kann.

Résumé

Vue la situation actuelle de ressources en combustibles fossiles menacées d'épuisement et des niveaux élevés d'émissions de polluants atmosphériques, l'état de l'art des recherches sur la combustion est confronté à deux défis principaux. Il s'agit d'une part d'optimiser l'efficacité de la combustion des combustibles fossiles et d'autre part du développer et d'appliquer des stratégies puissantes pour réduire la quantité de gaz polluants rejetés dans l'air tout en respectant les nouvelles normes d'émission conformément aux politiques énergétiques mondiales. Dans ce contexte, les technologies de captage et de stockage du dioxyde de carbone (CSC) jouent un rôle important en tant que stratégie énergétique adapteée en vue de l'atténuation des émissions de CO_2. L'un des aspects importants des techniques de CSC est l'oxydation du gaz naturel dans les conditions d'oxycombustion. Cependant, très peu de contributions scientifiques ont été consacrées à la recherche de ces systèmes de combustion, de sorte que les processus d'oxycombustion ne sont pas assez compris. L'objectif du présent travail est de développer et d'appliquer une méthode numérique avancée pour la simulation de l'oxycombustion. Cette approche a été intégrée dans la platforme numérique OpenFOAM et est capable de reproduire correctement l'interaction chimie-turbulence (ICT) pour les régimes de combustion non prémélangés. Le modèle proposé, qui est conçu pour les applications de RANS et LES, consiste en une fonction de densité de probabilité de transport (PDF) dans le contexte de la méthodologie du champ stochastique eulérien (ESF) combiné à un mécanisme de réduction chimique basé sur la variable d'avancement de la flamme (FPV). Dans le cadre la simulation des grandes échelles (LES), la méthode proposée permet une description précise de l'influence des fluctuations de la structure fine (sous-maille) sur la structure de la flamme et sur les caractéristiques de la combustion, y compris l'intéraction turbulence-chimie associée. Le modèle de combustion développé a été d'abord vérifié, puis validé et appliqué à diverses configurations de combustion turbulente, non prémélangée et de complexité croissante. Le premier cas d'essai pour la validation de la méthode dans le contexte du RANS et du LES est la flamme Sandia D, qui consiste en flamme turbulente de méthane pilotée [127]. Les flammes d'essai suivantes sont des flammes Sandia non prémélangées A & B, qui fonctionnent à diffèrents nombres de Reynolds et sont caractérisées par un enrichissement important de CO_2 et de H_2 dans les flux d'oxydant et du combustible, respectivement [154]. Toutes les configurations de validation et d'application étudiés sont bien documentés avec des données expérimentales disponibles. Une comparaison entre les résultats des simulations obtenus et les données expérimentales concernant la température, les distributions scalaires, les PDFs et les diagrammes de dispersion montre un bon accord, en particulier dans le contexte de la LES. Enfin, ce travail démontre que l'approche hybride FSE/FPV peut éliminer les faiblesses associées à la méthode numérique β-PDF qui est basée sur l'approche FPV.

Bibliography

[1] T. Ajayi, J.S. Gomes, A. Bera, A review of CO2 storage in geological formations emphasizing modeling, monitoring and capacity estimation approaches, Petroleum Science 16 (2019) 1028–1063.

[2] J.D. Anderson, J. Wendt, Computational fluid dynamics, Mcgraw-Hill Professional, New York, USA, (1995).

[3] ANSYS ICEM CFD version 18.1 (2017).

[4] A. Avdić, G. Künne, F. di Mare, J. Janicka, LES combustion modeling using the Eulerian stochastic field method coupled with tabulated chemistry, Combustion and Flame 175 (2017) 201–219.

[5] A. Avdić, Development and Application of Numerical Methods for the Simulation of Advanced Combustion Processes within Complex Devices, Ph.D. thesis, TU-Darmstadt, Darmstadt, 2014.

[6] R.S. Barlow, C.D. Carter, Raman/Rayleigh/LIF measurements of nitric oxide formation in turbulent hydrogen jet flames, Combustion and Flame 97 (1994) 261–280.

[7] R.S. Barlow, G. Magnotti, H.C. Cutcher, A.R. Masri, On defining progress variable for Raman/Rayleigh experiments in partially-premixed methane flames, Combustion and Flame 179 (2017) 117–129.

[8] R.W. Bilger, Turbulent reactive flows, Springer Verlag, (1980).

[9] R.W. Bilger, The structure of turbulent nonpremixed flames, Proceedings of the Combustion Institute 22 (1988) 475–488.

[10] O. Bolland, P. Mathieu, Comparison of two CO2 removal options in combined cycle power plants, Energy Conversion and Management 39 (1998) 1653–1663.

[11] O. Bolland, S. Seather, New concepts for natural gas fired power plants which simplify the recovery of carbon dioxide, Energy Conversion and Management 33 (1992) 467–475.

[12] R. Borghi, Recent advances in aeronautical science, Pergamont, London, UK, (1984).

[13] BP Statistical Review of World Energy, `https://www.bp.com/en/global/corporate/energy-economics/statistical-review-of-world-energy.html`, Accessed: 20-05-2020.

[14] N. Branley, W.P. Jones, Large eddy simulation of a turbulent non-premixed flame, Combustion and Flame 127 (2001) 1914–1934.

[15] P. Buchhave, K. William, Jr. George, The measurement of Turbulence with the Laser-Doppler Anemometer, Annual Review of Fluid Mechanics 11 (1979) 443–503.

[16] T.D. Butler, P.J. O'Rourke, A numerical method for two-dimensional unsteady reacting flows, Symposium (International) on Combustion 16 (1977) 1503–1515.

[17] S. Bürkle, Laser-based Investigation of Gas and Solid Fuel Combustion under Oxy-Fuel Atmosphere, BoD-Books on Demand, 2019.

[18] V. Bykov, U. Maas, The extension of the ILDM concept to reaction Diffusion manifolds, Combustion Theory and Modelling 11 (2007) 839–862.

[19] F. Cavalcanti Miranda, Large Eddy Simulation of Turbulent Reacting Flows With Radiative Heat Transfer, Ph.D. thesis, TU-Darmstadt, Darmstadt, 2018.

[20] CFD: PIMPLE Algorithm, https://www.simscale.com/forum/t/cfd-pimple-algorithm/81418, Accessed: 07-04-2020.

[21] A. Coclite, G. Pascazio, P. de Palma, L. Cutrone, M. Ihme, An SMLD Joint PDF Model for Turbulent Non-Premixed Combustion Using the Flamelet Progress Variable Approach, Flow Turbulence and Combustion 95 (2015) 97–119.

[22] Combustion Theory and Applications in CFD (Prof. H. Pitsch), https://cefrc.princeton.edu/sites/cefrc/files/2018_pitsch_lecture1.pdf, Accessed: 20-05-2020.

[23] A.W. Cook, J.J. Riley, G. Kosály, A laminar flamelet approach to subgrid-scale chemistry in turbulent flows., combustion and Flame 109 (1997) 332–341.

[24] F.H.V. Coppens, A.A. Konnov, The effects of enrichment by H2 on propagation speeds in adiabatic flat and cellular premixed flames of CH4 + O2 + CO2, Fuel 81 (2008) 2866–2870.

[25] R. Courant, K. Friedrichs, H. Lewy, Über die partiellen differenzengleichungen der mathematischen physik, Mathematische Annalen 100 (1928) 32–74.

[26] G.Z. Damköhler, Turbulente flammenstruckturen 46 (1940).

[27] L. Davidson: Fluid mechanics, turbulent flow and turbulence modeling, http://www.tfd.chalmers.se/ÌČlada/postscriptfiles/solids-and-fluidsturbulent-flowturbulence-modelling.pdf, Accessed: 20-05-2020.

[28] J.W. Deardorff, A numerical study of three-dimensional turbulent channel flow at large Reynolds numbers, Fluid Mechanics 41 (1970) 453–480.

[29] M. Ditaranto, J. Hals, Combustion instabilities in sudden expansion oxy-fuel flame, Combustion and Flame 146 (2006) 493–512.

[30] M. Ditaranto, T. Oppelt, Radiative heat flux characteristics of methane flame spheres, Experimental Thermal and Fluid Science 35 (2011) 1343–1350.

[31] I.A. Dodoulas, S.N. Martinez, Large Eddy Simulation of Premixed Turbulent Flames Using the Probability Density Function Approach, Flow Turbulence and Combustion 90 (2013) 645–678.

[32] A.S. Doost, F. Ries, L.G. Becker, S. Burkle, S. Wagner, V. Ebert, A. Dreizler, F. di Mare, A. Sadiki, J. Janicka, Residence time calculations for complex swirling flow in a combustion chamber using large-eddy simulations, Chemical Engineering Science 156 (2016) 97–114.

[33] C. Dopazo, Probability density function approach for a turbulent axisymmetric heated jet. Centerline evolution Physics of Fluids 18 (1975) 397–404.

[34] C. Dopazo, E.E. O'Brien, An approach to the autoignltlon of a turbulent mixture, Acta Astronautica 1 (1974) 1239–1266.

[35] V. Driest, On Turbulent Flow near a Wall, Journal of the Aeronautical Sciences 23 (1956) 1007–1011.

[36] Emission Database for Global Atmospheric research EDGAR, European Commission, `https://edgar.jrc.ec.europa.eu`, Accessed: 20-07-2020.

[37] A. Favre, Statistical equations of turbulent gases, Problems of hydrodynamics and continuum mechanics (1969) 231–266.

[38] S.A. Ferraris, J.X. Wen, LES of the Sandia Flame D Using Laminar Flamelet Decomposition for Conditional Source-Term Estimation, Flow Turbulence and Combustion 81 (2008) 609–639.

[39] M. Ferrarotti, Z. Li, A. Parente, On the role of mixing models in the simulation of MILD combustion using finite-rate chemistry combustion models, Proceedings of the Combustion Institute 37 (2019) 4531–4538.

[40] J.H. Ferziger, M. Perić, Computational Methods for Fluid Dynamics, Springer, 2002.

[41] D.R.A. Fikri, Modeling Non-premixed Turbulent Combustion in Industrial Rotary Kiln: Application in OpenFOAM, M.Sc. thesis, Delft University of Technology, Delft, Netherlands, 2017.

[42] B. Fiorina, R. Baron, O. Gicquel, D. Thevenin, S. Carpentier, N. Darabiha, Modelling non-adiabatic partially premixed flames using flame-prolongation of ILDM, Combustion Theory and Modelling 7 (2003) 449.

[43] B. Fiorina, O. Gicquel, L. Vervisch, S. Carpentier, N. Darabiha, Approximating the chemical structure of partially premixed and diffusion counterflow flames using FPI flamelet tabulation, Combustion and Flame 140 (2005) 147–160.

[44] B. Fiorina, D. Veynante, S. Candel, Modeling Combustion Chemistry in Large Eddy Simulation of Turbulent Flames, Flow Turbulence and Combustion 94 (2015) 3–42.

[45] B. Fiorina, R. Vicquelin, P. Auzillon, N. Darabiha, O. Gicquel, D. Veynante, A filtered tabulated chemistry model for LES of premixed combustion, Combustion and Flame 157 (2010) 465–475.

[46] FlameMaster v3.3.10, `https://web.stanford.edu/group/pitsch/FlameMaster.htm`, Accessed: 10-05-2020.

[47] C.A.J. Fletcher, Computational Techniques for Fluid Dynamics, Springer Berlin Heidelberg, 1998.

[48] P. Friedlingstein, S. Solomon, Contributions of past and present human generations to committed warming caused by carbon dioxide, PNAS 102 (2005) 10832–10836.

[49] J. Fröhlich, Large Eddy Simulation turbulenter Strömungen, Teubner Verlag, Wiesbaden, Deutschland, (2006).

[50] C. Galletti, G. Coraggio, L. Tognotti, Numerical investigation of oxy-natural-gas combustion in a semi-industrial furnace: Validation of CFD sub-models, Fuel 109 (2013) 445–460.

[51] S. Ganter, Verbrennung in Wandnähe: Numerische Analyse von Phänomenen und Modellentwicklung, Ph.D. thesis, TU-Darmstadt, Darmstadt, 2019.

[52] F. Gao, E.E. O'Brien, A large-eddy simulation scheme for turbulent reacting flows, Physics of Fluids A: Fluid Dynamics 5 (1993) 1282–1284.

[53] C.W. Gardiner, D.C. Haworth, Handbook of Stochastic Methods for Physics, Chemistry and the Natural Sciences, Springer Berlin/Heidelberg, Germany (2009).

[54] A. Garmory, R.E. Britter E. Mastorakos, Simulation of the evolution of aircraft exhaust plumes including detailed chemistry and segregation, Geophysical Research 113 (2008).

[55] A. Garmory, E. Mastorakos, Numerical simulation of oxy-fuel jet flames using unstructured LES-CMC, Proceedings of the Combustion Institute 35 (2014) 1207–1214.

[56] E. Garnier, N.A. Adams, P. Sagaut,Large eddy simulation for compressible flows, Springer, (2009).

[57] O. Gicquel, N. Darabiha, D. Thevenin, Laminar premixed hydrogen/air counterflow flame simulations using flame prolongation of ILDM with differential diffusion, Proceedings of the Combustion Institute 28 (2000) 1901–1908.

[58] S. Gierth, F. Hunger, S. Popp, H. Wu, M. Ihme, C. Hasse, Assessment of differential diffusion effects in flamelet modeling of oxy-fuel flames, Combustion and Flame 197 (2018) 134–144.

[59] S. Gierth, F. Hunger, S. Popp, H. Wu, M. Ihme, C. Hasse, Supplementary Material to: Assessment of differential diffusion effects in flamelet modeling of oxy-fuel flames, Combustion and Flame 197 (2018) 134–144.

[60] S.S. Girimaji, Assumed β-pdf Model for Turbulent Mixing: Validation and Extension to Multiple Scalar Mixing, Combustion Science and Technology 78 (2007) 177–196.

[61] V.I. Golovitchev, N. Nordin, R. Jarnicki, J. Chomiak, 3-D Diesel Spray Simulations Using a New Detailed Chemistry Turbulent Combustion Model, CEC/SAE, International Spring Fuels Lubricants Meeting Exposition (2000).

[62] C. Gong, M. Jangi, X.S. Bai, J.H. Liang, M.B. Sun, Large eddy simulation of hydrogen combustion in supersonic flows using an Eulerian stochastic fields method, Hydrogen Energy 42 (2017) 1264–1275.

[63] C.J. Greenshields, H.G. Weller, L. Gasparini, J.M. Reese, Implementation of semidiscrete, non-staggered central schemes in a colocated, polyhedral, finite volume framework, for highspeed viscous flows, International Journal for Numerical Methods in Fluids 36 (2010) 1–21.

[64] Gri-Mesh3.0, `http://www.me.berkeley.edu/gri_mech/`, Accessed: 20-05-2020.

[65] M. Hallaji, K. Mazaheri, Numerical simulation of turbulent non-premixed combustion in diluted hot coflow using PaSR combustion model 7th Mediterranean Combustion Symposium (2004).

[66] K. Hanjalic, M. Popovac, M. Hadziabdic, A robust near-wall elliptic-relaxation eddy-viscosity turbulence model for CFD, International Journal of Heat and Fluid Flow 25 (2004) 1047–1051.

[67] D.C. Haworth, Progress in probability density function methods for turbulent reacting flows, Progress in Energy and Combustion Science 36 (2010) 168–259.

[68] A. Hidouri, M. Chrigui, T. Boushaki, A. Sadiki, J. Janicka, Large eddy simulation of two isothermal and reacting turbulent separated oxy-fuel jets, Fuel 192 (2017) 108–120.

[69] A. Hinz, Numerische Simulation Turbulenter Methan-Diffusionsflammen Mittels Monte Carlo PDF Methoden, Ph.D. thesis, TU-Darmstadt, Darmstadt, 2000.

[70] C. Hirsch, Numerical Computation of Internal & External Flows: Fundamentals of Computational Fluid Dynamics, John Wiley & Sons, (2007).

[71] F. Hunger, M. Zulkifli, B. Williams, F. Beyrau, C. Hasse, A combined experimental and numerical study of laminar and turbulent non-piloted Oxyfuel jet flames using a direct comparison of the Rayleigh signal, Flow Turbulence and Combustion 97 (2016) 231–262.

[72] M. Ihme, H. Pitsch, Prediction of extinction and reignition in non-premixed turbulent flames using a flamelet/progress variable model: 2. Application in LES of Sandia flames D and E, Combustion and Flame 15 (2008) 90–107.

[73] M. Ihme, H. Pitsch, Prediction of extinction and reignition in non-premixed turbulent flames using a flamelet/progress variable model: 1. A priori study and presumed PDF closure, Combustion and Flame 155 (2008) 70–89.

[74] International Energy Agency, World Energy Outlook, 2019.

[75] The Intergovernmental Panel on Climate Change, `https://www.ipcc.ch/`, Accessed: 20-05-2020.

[76] F.A. Jaberi, P.J. Colucci, S. James, P. Givi, S. Pope, Filtered mass density functionfor Large eddy simulation of turbulent reacting flows, Journal of Fluid Mechanics 401 (1999) 85–121.

[77] J. Jaishree, D.C. Haworth, Comparisons of Lagrangian and Eulerian PDF methods in simulations of non-premixed turbulent jet flames with moderate-to-strong turbulence-chemistry interactions, Combustion Theory and Modelling 16 (2012) 435–463.

[78] M. Jangi, C. Li, Modelling of Methanol Combustion in a Direct Injection Compression Ignition Engine using an Accelerated Stochastic Fields Method, Energy Procedia 105 (2017) 1326–1331.

[79] M. Jangi, M. Zhao, D.C. Haworth, X.S. Bai, Stabilization and liftoff length of a non-premixed methane/air jet flame discharging into a high-temperature environment: An accelerated transported PDF method, Combustion and Flame 162 (2015) 408–419.

[80] H. Jasak, Error analysis and estimation for the finite volume method with applications to fluid flows, Ph.D. thesis, Imperial College, London, UK, 1996.

[81] D. Jesch, Large Eddy Simulation of Turbulent Combustion: A Novel Multivariate Probability Density Function Approach, Ph.D. thesis, TU-Darmstadt, Darmstadt, 2016.

[82] W.P. Jones, A. Marquis, V.N. Prasad, LES of a turbulent premixed swirl burner using the Eulerian stochastic field method, Combustion and Flame 159 (2012) 3079–3095.

[83] W.P. Jones, S.N. Martinez, Numerical Study of n-heptane auto-ignition using LES-PDF methods, Flow Turbulence and Combustion 83 (2009) 407–423.

[84] W.P. Jones, V.N. Prasad, Large Eddy Simulation of the Sandia Flame Series (D, E and F) using the Eulerian stochastic field method, Combustion and Flame 157 (2010) 1621–1636.

[85] V.M. Jordi, Numerical Simulation of Turbulent Diffusion Flames Using Flamelet Models on Unstructured Meshes, Ph.D. thesis, Centre Tecnologic de Transferencia de Calor Departament de Maquinesi Motors Termics Universitat Politecnica de Catalunya, Terrassa, Spain, (2015).

[86] A. Kassinos, C. Langer, G. laccarino, P. Moin,Complex Effects in Large Eddy Simulations, Springer-Verlag Berlin/Heidelberg (2007).

[87] A. Kempf, A. Sadiki, J. Janicka, Prediction of finite chemistry effects using large eddy simulation, Proceedings of the Combustion Institute 29 (2003) 1979–1985.

[88] A. Ketelheun, G. Künne, J. Janicka, Heat transfer modeling in the context of large eddy simulation of premixed combustion with tabulated chemistry, Flow Turbulence and Combustion 91 (2013) 867–893.

[89] G. Kim, Y. Kim, Y.J. Joo, Conditional Moment Closure for Modeling Combustion Processes and Structure of Oxy-Natural Gas Flame, Energy Fuels 23 (2009) 4370–4377.

[90] M. Klein, A. Sadiki, J. Janicka, A digital filter based generation of inflow data for spatially developing direct numerical or large eddy simulations, Journal of Computational Physics 186 (2003) 652–665.

[91] T.C. Klenke, Hybride numerische Simulation von Verbrennungslärm und thermoakustischen Instabilitäten in technischen Verbrennungssystemen, Ph.D. thesis, TU-Darmstadt, Darmstadt, 2014.

[92] P.E. Kloeden, E. Platen, Numerical solution of stochastic differential equations, Springer Berlin/Heidelberg, 1992.

[93] J. Kühne, Analysis of Combustion LES using an Eulerian Monte Carlo PDF Method, Ph.D. thesis, TU-Darmstadt, Darmstadt, 2011.

[94] J. Kühne, A. Ketelheun, J. Janicka, Analysis of sub-grid PDF of a progress variable approach using a hybrid LES/TPDF method, Proceedings of the Combustion Institute 33 (2011) 1411–1418.

[95] G. Künne, Large Eddy Simulation of Premixed Combustion Using Artificial Flame Thickening Coupled with Tabulated Chemistry, Ph.D. thesis, TU-Darmstadt, Darmstadt, 2012.

[96] T. Landenfeld, A. Sadiki, J. Janicka, A Turbulence-Chemistry Interaction Model Based on a Multivariate Presumed β-pdf Method for Turbulent Flames, Flow, Turbulence and Combustion 68 (2002) 111–135.

[97] B.E. Launder, B.I. sharma, Application of the Energy-Dissipation Model of Turbulence to the Calculation of Flow Near a Spinning Disc, Letters in Heat and Mass Transfer 1 (1974) 131–138.

[98] A. Leonard, Energy cascade in Large-eddy Simulatins of Turbulent Fluid Flows, Advances in Geophysics 18 (1975) 237–248.

[99] D.Y.C. Leunga, G. Caramannab, M.V.M. Mercedes, An overview of current status of carbon dioxidecapture and storage technologies, Renewable & Sustainable Energy Reviews 39 (2014) 426–443

[100] M.T. Lewandowski, J. Pozorski, Assessment of turbulence-chemistry interaction-models in the computation of turbulent non-premixed flames, Journal of Physics: Conference Series 760 (2016) 012–015.

[101] Z. Li, M. Ferrarotti, A. Cuoci, A. Parente, Finite-rate chemistry modelling of non-conventional combustion regimes using a Partially-Stirred Reactor closure: Combustion model formulation and implementation details, Applied Energy 225 (2018) 637–655.

[102] D.K. Lilly, The representation of small-scale turbulence in numerical simulation experiments, Proceedings of IBM Scientific Computing Symposium on Environmental Sciences (1967) 195–210.

[103] G. de Luca, T. Schmitt, D. Veynante, Investigation of the thickened flame model behavior for non-premixed flames, 17th International Conference on Numerical Combustion, Aachen (2019).

[104] U. Maas, S.B. Pope, Simplifying chemical kinetics: Intrinsic low-dimensional manifolds in composition space, Combustion and Flame 88 (1992) 239–264.

[105] B. Magnussen, On the structure of turbulence and a generalized eddy dissipation concept for chemical reaction in turbulent flow, Proceedings of the AIAA, Aerospace Sciences Meeting (1981).

[106] R. Mahmoud, M. Jangi, B. Fiorina, M. Pfitzner, A. Sadiki, Numerical Investigation of an Oxyfuel non-premixed combustion using a Hybrid Eulerian Stochastic Field/Flamelet Progress Variable approach: Effects of H2/CO2 enrichment and Reynolds number, Energies 11 (2018) 3158.

[107] R. Mahmoud, M. Jangi, F. Ries, B. Fiorina, J. Janicka, A. Sadiki, Combustion Characteristics of a Non-Premixed Oxy-Flame Applying a Hybrid Filtered Eulerian Stochastic Field/Flamelet Progress Variable Approach, Applied Sciences 9 (2019) 1320.

[108] A.R. Masri, R.W. Dibble, R.S. Barlow, Chemical kinetic effects in non-premixed flames of H2/CO2 fuel, Combustion and Flame 91 (1992) 285–309.

[109] S. McAllister, J.Y. Chen, A. Carlos Fernandez-Pello, Fundamentals of Combustion Processes, Springer, 2011.

[110] J.M. Mejia, A. Sadiki, A. Molina, F. Chejne, P. Pantangi, Large Eddy Simulation of the Mixing of a Passive Scalar in a High-Schmidt Turbulent Jet, Journal of Fluids Engineering 137 (2015) 31301–31311.

[111] J.M. Mejia, F. Chejne, A. Molina, A. Sadiki, Scalar Mixing Study at High-Schmidt Regime in a Turbulent Jet Flow Using Large-Eddy Simulation/Filtered Density Function Approach, Journal of Fluids Engineering 138 (2016) 021205.

[112] F. Moukalled, L. Mangani, M. Darwish, The finite volume method in computational fluid dynamics: An advanced introduction with OpenFOAM and Matlab (fluid mechanics and its applications), Springer, (2015).

[113] H. Müller, Simulation turbulenter nicht vorgemischter Verbrennung bei überkritischen Drücken, Ph.D. thesis, Universität der Bundeswehr München, München, Germany, 2016.

[114] P. Obando Vega, A. Parente, A. Coussement, A. Sadiki, Evaluation of the non premixed Filtered Tabulated Chemistry for LES model on a turbulent non premixed piloted methane jet flame 17th International Conference on Numerical Combustion, Aachen (2019).

[115] J.A. van Oijen, A. Donini, R.J.M. Bastiaans, J.H.M. Ten-Thije-Boonkkamp, L.P.H. de Goey, State-of-the-art in premixed combustion modeling using flamelet generated manifolds Science 57 (2016) 30–74.

[116] J.A. van Oijen, L.P.H. de Goey, Modelling of premixed laminar flames using FGM, Combustion Science and Technology 161 (2000) 113–137.

[117] OpenFOAM User Guide, `http://www.openfoam.org/docs/`, Accessed: 10-05-2020.

[118] OpenFOAM Programmer's Guide, `http://foam.sourceforge.net/docs/Guides-a4/ProgrammersGuide.pdf`, Accessed: 10-05-2020.

[119] S.V. Patankar, Numerical heat transfer and fluid flow, Hemisphere Publishing Corporation, 1980.

[120] N. Peters, Local quenching due to flame stretch and non-premixed turbulent combustion, Progress in Energy and Combustion Science 31 (1983) 1–17.

[121] N. Peters, Laminar diffusion flamelet models in non-premixed turbulent combustion, Progress in Energy and Combustion Science 10 (1984) 319–339.

[122] N. Peters, The turbulence burning velocity for large scale and small scale turbulence, Journal of Fluid Mechanics 384 (1999) 107–132.

[123] N. Peters, Turbulent Combustion, Cambridge University Press, 2000.

[124] C.D. Pierce, Progress Variable Approach for Large Eddy Simulation of Turbulent combustion, Ph.D. thesis, stanford university, California, USA, 2001.

[125] C.D. Pierce, P. Moin, Progress variable approach for large-eddy simulation of non-premixed turbulent combustion, Fluid Mechanics 504 (2004) 73–97.

[126] J.H. Peric, M. Ferzieger, Numerische Strömunsgmechanik, Springer Verlag, (2008).

[127] Piloted CH4/air flames C, D, E, and F., `http://www.sandia.gov/TNF/DataArch/FlameD/SandiaPilotDoc21.pdf`, Accessed: 20-05-2020.

[128] H. Pitsch, M. Chen, N. Peters, Unsteady flamelet modeling of turbulent hydrogen-air diffusion flames, Proceedings of the Combustion Institute 27 (1998) 1057–1064.

[129] H. Pitsch, H. Steiner, Large eddy simulation of a turbulent piloted methane/air diffusion flame (Sandia flame D) Physics of Fluids 12 (2000) 2541–2554.

[130] T. Poinsot, D. Veynante, Theoretical and numerical combustion, 2nd ed, Edwards, (2005).

[131] T. Poinsot, D. Veynante, S. Candel, Quenching processes and prremixed turbulent combustion diagrams, Journal of Fluid Mechanics 228 (1991) 561–606.

[132] S.B. Pope, Turbulent Flows, Cambridge University Press, Cambridge, UK, (2000).

[133] S.B. Pope, PDF methods for turbulent reacting flows, Progress in Energy and Combustion Science 11 (1985) 119–192.

[134] S.B. Pope, A Monte Carlo method for the PDF equations of turbulent reacting flow, Combustion Science and Technology 25 (1981) 159–174.

[135] V.N. Prasad, K.H. Luo, W.P. Jones, LES-PDF Simulation of a highly sheared turbulent piloted premixed flame, Proceedings of the 7th Mediterranean Combustion Symposium (2011) 1–12.

[136] F. Proch, P. Domingo, L. Vervisch, A. Kempf, Flame resolved simulation of a turbulent premixed bluff-body burner experiment. Part II: A-priori and a-posteriori investigation of sub-grid scale wrinkling closures in the context of artificially thickened flame modeling, Combustion and Flame (2017) 340–350.

[137] E. Quadarella, A. Stagni, A. Cuoci, A. Parente, T. Faravelli, H.G. Im, A partially stirred reactor model for turbulent combustion closure using detailed chemical time scales, Joint Meeting German and Italian sections of the Combustion Institute (2018).

[138] W.J.S. Ramaekers, J.A. van Oijen, L.P.H. de Goey, A Priori Testing of Flamelet Generated Manifolds for Turbulent Partially Premixed Methane/Air Flames, Flow Turbulence and Combustion 84 (2010) 439–458.

[139] V. Raman, H. Pitsch, A consistent LES/filtered density function formulation for the simulation of turblent flames with detailed chemistry, Proceedings Combustion Institute 31 (2007) 1711–1719.

[140] V. Raman, H. Pitsch, R. Fox, Eulerian transported probability density function sub-filter model for LES simulations of turbulent combustion, Combustion Theory and Modelling 10 (2007) 439–458.

[141] V. Ramanathan, Y. Feng, On avoiding dangerous anthropogenic interference with the climate system: Formidable challenges ahead, PNAS 105 (2008) 14245–14250.

[142] M. di Renzo, LES of the Sandia Flame D Using an FPV Combustion Model, Energy Procedia 82 (2015) 402–409.

[143] M. di Renzo, A. Coclite, M.D. de Tullio, P. de Palma, G. Pascazio,LES of the Sandia Flame D Using an FPV Combustion Model, In Proceedings of the 70th Conference of the ATI Engineering Association, Energy Procedia (2015) 402–449.

[144] O. Reynolds, An experimental investigation of the circumstances which determine whether the motion of water shall be direct or sinuous, and of the law of resistance in parallel channels, Proceedings of the Royal Society of London 35 (1883) 84–99.

[145] F. Ries, Numerical Modeling and Prediction of Irreversibilities in Sub- and Supercritical Turbulent Near-Wall Flows, Ph.D. thesis, TU-Darmstadt, Darmstadt, (2018).

[146] F. Ries, K. Nishad, L. Dressler, J. Janicka, A. Sadiki, Evaluating large eddy simulation results based on error analysis, Theoretical and Computational Fluid Dynamics 32 (2018) 733–752.

[147] V. Sabelnikov, C. Fureby, Extended LES-PaSR Model for Simulation of Turbulent Combustion, Progress in Propulsion Physics 4 (2013) 539–568.

[148] V. Sabelnikov, O. Soulard, Rapidally decorrelating velocity-field model as tool for solving one-point Fokker-Planck equations for probability density functions of turbulent reactive scalars, Physical Review E 72 (2005).

[149] F.L. Sacomano Filho, Novel approach toward the consistent simulation of turbulent spray flames using tabulated chemistry, Ph.D. thesis, TU-Darmstadt, Darmstadt, (2017).

[150] F.L. Sacomano Filho, M. Chrigui, A. Sadiki, J. Janicka, LES-Based Numerical Analysis of Droplet Vaporization Process in Lean Partially Premixed Turbulent Spray Flames, Combustion Science and Technology 186 (2014) 435–452.

[151] A. Sadiki, S. Agrebi, M. chrigui, A.S Doost, R. Knappstein, F. Di Mare, J. Janicka, A. Massmeyer, D. Zabodiec, J. Hees, R. Kneer, Analyzing the effects of turbulence and multiphase treatments on oxy-coal combustion process predictions using LES and RANS, Chemical Engineering Science 166 (2017) 283–302.

[152] A. Sadiki, J. Janicka, Large Eddy Simulation of Turbulent Combustion Systems, Proceedings of the Combustion Institute 30 (2005) 537–547.

[153] P. Sagaut, Large Eddy Simulation for Incompressible Flows, An introduction, Springer, Heidelberg, Germany, (2001).

[154] A. Sevault, M. Dunn, R.S. Barlow, M. Ditaranto, On the Structure of the Near Field of Oxy-Fuel Jet Flames Using Raman/Rayleigh Laser Diagnostics, Combustion and Flame 159 (2012) 3342–3352.

[155] A. Sevault, Investigations of the strcuture of Oxy-Fuel flames using RAMAN Laser Diagnostics, Ph.D. thesis, Norwegian University of Science and Technology, Trondheim-Norway, (2012).

[156] A. Shiryaeva, V. Sabelnikov, Critical Analysis of Classical Turbulent Combustion Experiments on the Basis of RANS Simulations, International Conference on the Methods of Aerophysical Research, AIP (2018).

[157] J. Smagorinsky, General Circulation Experiments with the Primitive Equations. Part I, the Basic Experiment, Monthly Weather Review 91 (1963) 99–164.

[158] A.Y. Snegirev, A.S. Frolov, The Large Eddy Simulation of a Turbulent Diffusion Flame, High Temperatire 49 (2011) 690–703.

[159] M. Staufer, Large Eddy Simulation of Premixed and Partially Premixed Flames, Ph.D. thesis, TU-Darmstadt, Darmstadt, 2009.

[160] S. Subramaniam, S. Pope, A mixing model for turbulent reactive flows based on Euclidean minimum spanning trees, Combustion and Flame 115 (1998) 487–517.

[161] Y. Tan, M.A. Douglas, K.V. Thambimuthu, CO2 capture using oxygen enhanced combustion strategies for natural gas power plants, Fuel 8 (2002) 1007–1016.

[162] H. Tennekes, J. Lumley, A First Course in Turbulence, MIT Press, 1972.

[163] TNF Workshop, `https://tnfworkshop.org/`, Accessed: 20-05-2020.

[164] S.R. Turns, An Introduction to Combustion: Concepts and Applications, Mc Grow Hills, (2012).

[165] L. Valiño, A field Monte Carlo formulation for calculating the probability density functions of a single scalar in turbulent flow, Flow Turbulence and Combustion 60 (1998) 157–172.

[166] D. Veynante, L. Vervisch, Turbulent combustion modeling, Progress in Energy and Combustion Sciences 28 (2002) 193–266.

[167] R. Vicquel, Tabulated Chemistry for Turbulent Combustion Modelingand Simulation, Ph.D. thesis, Laboratoire d'Énergétique Moléculaire et Macroscopique, Combustion (EM2C) du CNRS et de l'ECP, Ecole centrale Paris, Paris, France, 2010.

[168] J. Villermaux, J.C. Devillon, Représentation de la coalescence et de la redispersion des domaines de ségrégation dans un fluide par un modòle d'interaction phénoménologique, Proceedings of the 2nd International symposium on chemical reaction engineering (1972).

[169] A.W. Vreman, B.A. Albrecht, J.A. van Oijen, L.P.H. de Goey, R.J.M. Bastiaans, Premixed and nonpremixed generated manifolds in large-eddy simulation of Sandia Flame D and F, Combustion and Flame 153 (2008) 394–416.

[170] J. Warnatz, U. Maas, R.W. Dibble, Combustion: Physical and Chemical Fundamentals, Modeling and Simulation, Experiments, Pollutant Formation, Springer, Berlin, Germany, (2009).

[171] J. Warnatz, U. Maas, R.W. Dibble, Combustion, Springer, (2000).

[172] V. White, L. Torrente-Murciano, D. Sturgeon, D. Chadwick, Purification of Oxyfuel-derived CO2, In Proceedings of the 9th International Conference on Greenhouse Gas Control Technologies 2 (2008) 399–406

[173] F.A. Williams, Combustion Theory, Benjamin Cummings, Menlo Park, CA (1985).

[174] O. Winter, P. Sváček, Numerical Simulation of Flow Induced Airfoil Vibrations with Large amplitudes, Proceedings of Seminar Hejnices (2019) 186–194.

[175] L. Zheng, Oxy-Fuel Combustion for Power Generation and Carbon Dioxide (CO2) Capture, Woodhead Publishing series in energy; Elsevier, Cambridge, UK, (2011).

Curriculum Vitae

Rihab Mahmoud

Education

University studies	09/2008 - 06/2010	Preparatory Institute for Engineering Studies of Nabeul.
	09/2010 - 06/2013	Engineering Degree in Chemical Process Engineering National Engineering School of Gabes.
	09/2013 - 09/2015	PhD Student National Engineering School of Gabes & Faculty of Science of Gafsa 'MEER' research institute.
	11/2015 - 11/2020	PhD Student Technical university of Darmstadt Department of Energy and Power Plant Technology CentraleSupelec, University of Paris-Saclay. 'EM2C' research institute.

Internships, Research Projects

PhD secondment	10/2017 - 08/2018	CentraleSupelec, University of Paris-Saclay 'EM2C' research institute
Scientific visitor	03/2018 - 04/2018	Birmingham University Mechanical Engineering Department
Scientific visitor	08/2017 - 08/2017	Newcastle University Mechanical Engineering Department

This project has received funding from the European Union's Horizon 2020 Program for research, technological development, and demonstration under grant agreement no.643134-CLEAN-Gas.